Summer 8-5-2019

Organic-Inorganic Hybrid Composites: Superhydrophobic Polymer Coatings with Photoreactive Perfluorinated Phthalocyanines

Abdul Azeez
abdul.azeez@shu.edu

Organic-Inorganic Hybrid Composites: Superhydrophobic Polymer Coatings with Photoreactive Perfluorinated Phthalocyanines

A Dissertation submitted to Seton Hall University in partial fulfillment of the requirements for the degree of Doctorate of Philosophy

By:

Abdul Azeez

August 2019

Department of Chemistry and Biochemistry
Seton Hall University
South Orange, NJ, USA

DISSERTATION COMMITTEE APPROVALS

We certify that we read this dissertation and that in our opinion it is adequate to scientific scope and quality as a dissertation for the degree of Doctor of Philosophy.

APPROVED BY:

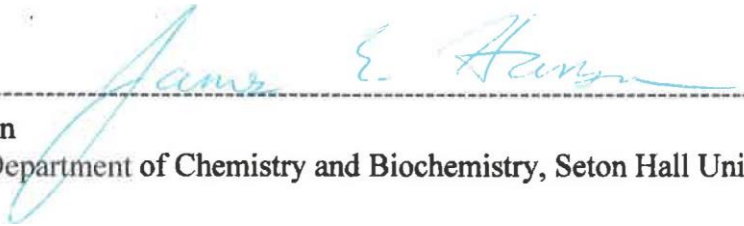

Dr. James E. Hanson
Research Mentor, Department of Chemistry and Biochemistry, Seton Hall University

Dr. Sergiu M. Gorun
Research Mentor, Department of Chemistry and Biochemistry, Seton Hall University

Dr. Joseph J Badillo
Reader, Department of Chemistry and Biochemistry, Seton Hall University

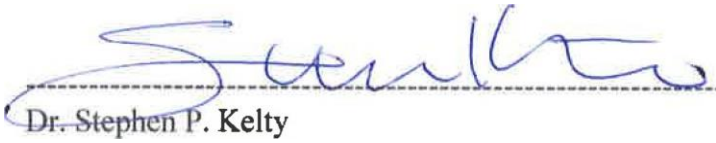

Dr. Stephen P. Kelty
Chair, Department of Chemistry and Biochemistry, Seton Hall University

ABSTRACT

We report partly fluorinated and silicon-based polymers that incorporate inorganic/organic materials capable of generating reactive oxygen species (ROS) using only visible light and air. Polyvinylidene fluoride (PVDF), which incorporated a known perfluorinated phthalocyanine photosensitizer, $F_{64}PcZn$, supported on silicon and titanium oxides was further modified via chemical surface roughening to exhibit enhanced hydrophobicity when used as a coating. Water contact angles as high as ~159° have been observed, vs. ~ 92° for the unmodified polymer. The polymer matrix, however, does not resist the ROS it produces as evidenced by spectroscopic and SEM data. A polysiloxane matrix was similarly produced and, unlike the PVDF, resists ROS. This polymer hybrid produces singlet oxygen $^1O_2$ by visible light illumination and decomposes efficiently several organic dyes present in aqueous solutions in contact with the polymer surface. The new materials may have broad applications in solid-state based degradation of undesired organic contaminants.

Dedicated to my beloved parents:

Alhaja. Iyah Ikoko and Alhaji. Ibrahim Ikoko.

ACKNOWLEDGMENTS

I am forever grateful to all those whom I have had the opportunity to work under and work with during my journey as a Ph.D. as a graduate student at Seton Hall University. I would sincerely like to thank my, mentors, Dr. Sergiu M. Gorun and Dr. James E. Hanson, for words can't describe their academic contribution they made toward my research program and for introducing me to an innovative, cutting edge field of Photocatalysis and Superhydrophobicity, I couldn't have asked for any discipline in Chemistry better than the current. They introduced me to the principles of these branches of Chemistry that shaped my research project: Inorganic, Polymer, and Surface Chemistry. I was always very enthusiastic about my research project, it is of great interest to know that you are a part of an upcoming area of Green Chemistry, certainly the future of a clean source of energy. My mentors always kept my focus and also explore little details of the research, for that is where great answers always lay. Nevertheless, the research project was very challenging and we were always thinking of ways to navigate through these challenges, moreover, scientific literatures and reviews were very helpful.

I will also use this opportunity to thank my Ph.D. matriculation committee members, firstly, I am grateful to Dr. Alexander Fadeev for been my matriculation committee member and the extensive use of his laboratory for my research project and special thanks to Dr. Wyatt Murphy and Dr. Monica Raj for been part of my matriculation committee. I am also thankful to Dr. Joseph J Badillo for been my Ph.D. dissertation reader. I would also like to acknowledge all four undergraduate research students: Lauren Polio, Prabh Jassal, Jazmine Bandala and Nancy Jimenez who worked very hard and spent long hours, including some weekends to the success of my research project, their contributions were very valuable as a result of the volume of work done; we made lots of materials and also we did lots of analytical characterizations.

I would also like to thank Dr. Stephen Kelty, Dr. Cecilia Marzabadi, Dr. Nicholas Snow, Dr. Yuri Kazakevich, Dr. Cosimo Antonacci, Dr. Tin-Chun Chu, and Dr. David Laviska. Rafael Rivera, James Lampe, and Jose Alvarez are also acknowledged for their help. Special acknowledgment goes to all current and formal members of Dr. Gorun's research group, notably Marius Pelmus, Mufeda Zhort, and Mary Okorie, these individuals were always by-my-side, much thanks. Special thanks to James Sullivan, Dr. Karpagavalli Ramji, Razi Abbas, Marta G Suazo, Olivia C Xiao and also Dr. Gorun's formal students, Dr. Hemant Patel and Dr. Erik Carrion for supplying me with phthalocyanines (F_{64}PcZn) for my research. Also, I would like to acknowledge the members of Dr. Hanson's research group for their contributions and support: namely Daniel Goldman, Usha Kalra, and Miguel Medico. I would also like to acknowledge Members of the Education Opportunity Fund (EOF), remarkably, Sandra Vanegas, Musa Manneh, Dr. Maurice Ene, Professor Bernadette Wilkowski and Dr. Hasani Carter now Executive Director of NJ State EOF for their assistance and generosity during my period as a Chemistry Graduate Assistant with the program. Special thanks goes to Andy Ajayi and Daniel E. Guerrero for their contributions.

I would also like to give special acknowledgments for financial support to the Department of Defense (US Air Force) and our Center for Functional Materials and thank Princeton University PRISM Imaging and Analytical Center (IAC) for access to state of the art instruments for surface characterization. Daniel Gregory of IAC is thanked for his technical assistance.

Finally, I would sincerely like to thank my family for their support and encouragement, Habib Bello, Nera Adiele, Dr. Muhammed Lecky, Mrs. Mary Tsedi and Mr. Vincent Tsedi, Alhaja. Iyah Ikoko and Alhaji. Ibrahim Ikoko. Most importantly, my mother Alhaja. Iyah Ikoko for her strict and disciplined upbringing.

TABLE OF CONTENTS

Chapter **Page**

LIST OF FIGURES

Figures **Pages**

LIST OF TABLES

Table **Page**

Chapter 1

A Study of Photoreactive Surfaces

1.1. An Introduction to Phthalocyanines.

Environmental remediation is an important issue of our generation because of global growth and industrialization. These issues have created serious environmental problems such as wastewater and freshwater industrial as a result of the use of fossil fuel and industrial chemical. [1] Alternative remediation solutions of these environmental pollutants are currently of interest to researchers in both academic and industrial sectors. [2] Catalysts of various kind of materials are currently at the forefront of research in solving some of these problems of pollution from a broader perspective. [3] The abundance of solar radiation is of great interest, due to its availability and the ability of some catalytic materials to harness photons for effective use at a low cost. Taking advantage of the photons of the solar radiation has proven to be a great challenge as a result of different radiation energy levels, for example, ultraviolet and visible at different energy levels and availability of use. Designing photosensitizers that incorporate metals or are based on metal oxides have been explored extensively. [4 - 8] These transition metals and their oxides are either too expensive or not very efficient catalysts due to limitations in the visible region of the electromagnetic spectrum, some can become toxic to the environment. Titanium dioxide (TiO_2), a well-studied photocatalyst, with a proven record of accomplishments and thus has been of great interest. [7] The major drawback of TiO_2 is its absorbance restriction to the ultraviolet region of the electromagnetic spectrum, which only accounts for 5% of the solar energy. [6 - 9] Visible light accounts for more than 50% of the solar energy, taking advantage of this abundance can be of great advantage. Photoreactive materials that are active in this region without polluting the environment can help solve some the problems of our time as the world strives for renewable energy. The good news is that there are photoreactive materials that are active in the visible region of the solar spectrum.

The family of phthalocyanines (Pcs) has been a topic of great interest to researchers in various fields of science since their discovery. In 1928, Braun and Tscherniac, while experimenting with *o*-cyanobenzamide in an iron reactor, accidentally came across what is now known as Pcs. [10, 11] Pcs dianions are composed of four isoindole units with delocalized 18 π-electron in an aromatic cloud over nitrogen and carbon atoms. [12] The bright-dark blue-green color of Pcs was of great interest in the dye and paper industries initially, but these interest did not stop there, further research into the compounds continued. [13] Pcs exhibit distinctive bands in the electromagnetic spectrum: B and Q band, the Q-band absorbs strongly in the visible region of the spectrum at wavelength 620-700 nm with. [14] **Figure 1.1 and 1.2**, shows the representation of two Pcs structures: first-generation H_{16}PcM and a second-generation F_{16}PcM, (M represents a metal at the center of the structure) as advancement in structural modifications resulted due to tailored interest in applications.

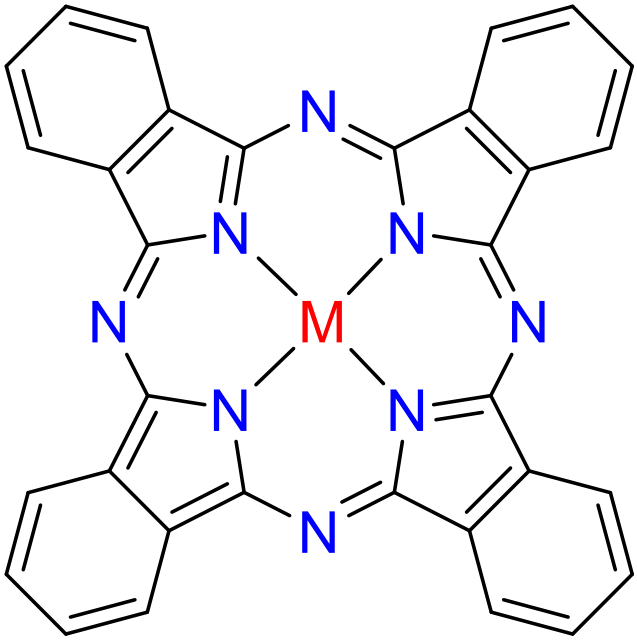

Figure 1. 1. The general structure of the metal phthalocyanines, depicting (A) H_{16}PcM.

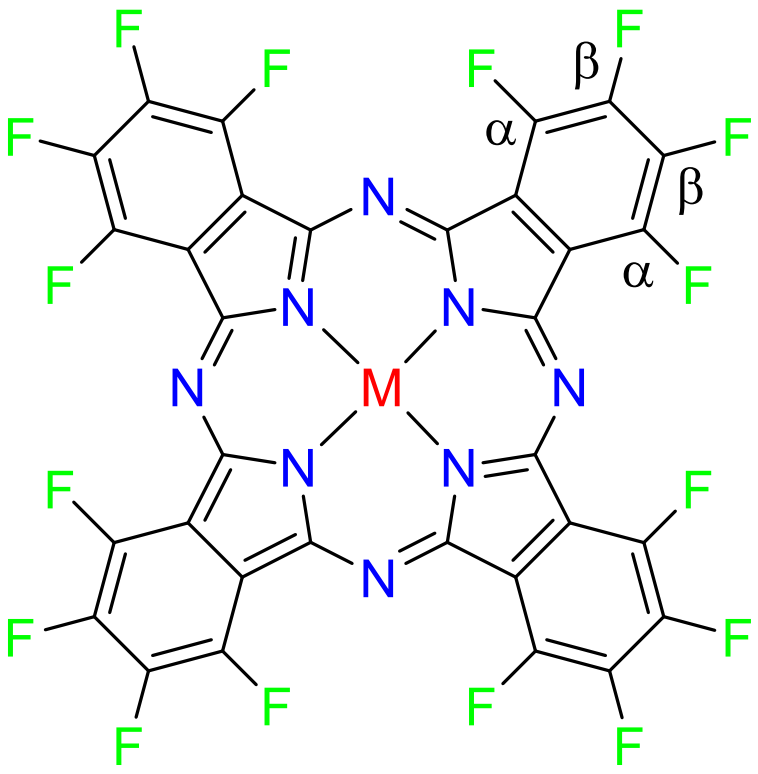

Figure 1. 2. The general structure of the metal phthalocyanines, depicting (B) F_{16}PcM.

The emergence of Pcs in the fields of material science and nanoscience [15] can be attributed to their diverse properties such as electrical, chemical and thermal stability and most importantly their strong absorption of light in the visible region. The substitution of various transition metals, example: Mg^{2+}, Zn^{2+}, Fe^{2+}, Cu^{2+}, Ru^{2+} and more in the central cavity (macro center) replaces the two hydrogen atoms located in the center of the compound. Furthermore, the peripheral substitution and the axial position with a different compound is known as ligands such as sulfonate, alkyl, amino, halogen, carboxylic acid, and thiol resulted to advancement in photochemical and

photophysical properties of Pcs. Substituting the macro center of Pcs with these metals and/or ligands contributes to the diverse physical and chemical properties; these modification methods fine-tune the molecules for use in different applications. These diverse properties elevated Pcs applications in the areas of electrochromic devices, semiconductor, information storage units, and liquid crystal, to name a few. [16] The integration of these functional Pc complexes into an active molecular network, such as a polymer of interest to material scientist and researchers. Successful incorporation of Pcs into polymer complex requires a fine-tuning of the micro/nano-scale morphology of the host material, in this case, the polymer, the fabrication can enhance or as a cooperator for the design of Pcs-polymer or Pcs-device complex. [17] Pcs can also be used as standalone complexes for example as a photosensitizer for photodynamic therapy with a delivery agent. [18] Phthalocyanines are classified as an organic compound, never been reported in nature because their precursors are not found in nature, therefore, they are only synthesized in the laboratory. [16] The reaction process of phthalonitrile or diiminoisoindoline precursors which undergo self-assembly or self-rearrangement to form four-isoindole units consisting of a macrocenter, [12, 16] these isoindole units are joined together at their 1,3-positions by aza-bridges to for Pcs. [19 - 20]

1.2. Fluorinated Phthalocyanines.

The primary focus from here on is photoreactive third-generation fluorinated phthalocyanines, F_{64}PcM (M represents metal) and the geneses of the third generation Pcs is the fluorinated, F_{16}PcM. F_{16}PcM are good photoactive catalysts with some drawbacks, the reactivity of the C-H bond leads to thermal degradation, [20] and prone to aggregation π–π stacking, [21] these drawbacks limit H_{16}PcM ability as an effective catalyst. [22] The susceptibility of H_{16}PcM extends to photo-instability and

poor solubility; these effects drastically reduce their ability for redox and photo-catalysis capability. [20] The improvement of the peripheral properties by substituting H-16 atoms with F-16 atoms, replacing the C-H bonds with C-F bonds created a new class of Pcs, F_{16}PcM. [21] This class of Pcs has improved thermal stability and excellent redox and photocatalysis properties. [20 - 23] Although, these Pcs are photoreactive and have improved thermal stability, the C-F bonds along the peripheral (β-positions) possess uncertain characteristic properties, [24 - 25] leading to aggregation due to π–π stacking and nucleophilic susceptibility, replacing the peripheral fluorine groups; these are huge drawback for the robustness of F_{16}PcM. [26] These questions resulted to further studies for an all-round robust catalyst capable of overcoming the drawbacks of its predecessors. A robust class of Pcs introduced by Dr. Gorun's research group has addressed the primary issues of the earlier Pcs; H_{16}PcM and F_{16}PcM. [27-28] F_{64}PcM class of Pcs derived its robustness from the replacement of the majority of the C-F bonds with bulky aliphatic *i*-C3F7 groups, these modifications have contributed to its exceptional thermal stability above 300 ^{o}C. [26] Structure represented below in **Figure 1.3.**

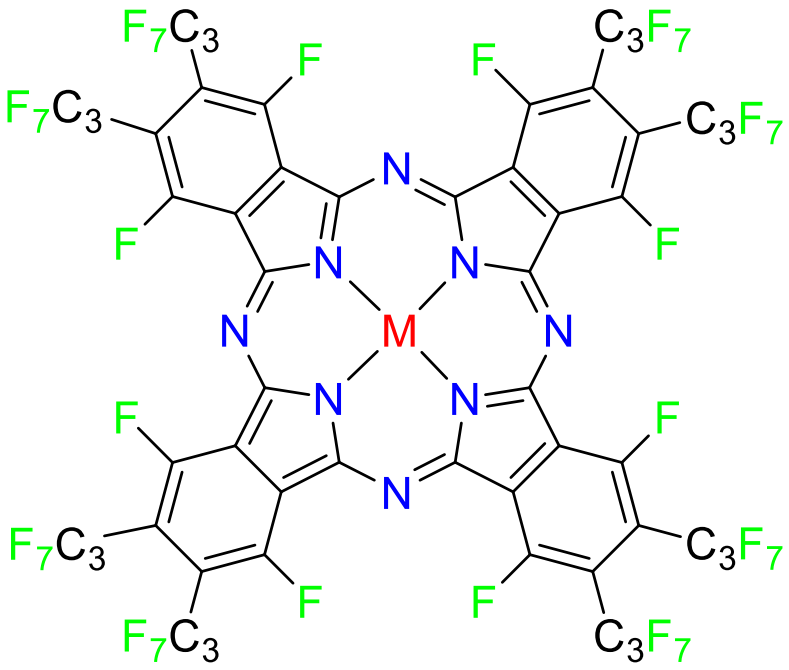

F64PcM

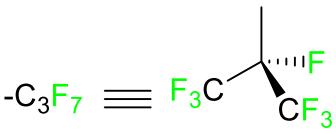

Figure 1. 3. The general structure of the metal phthalocyanines, depicting F_{64}PcM. M represents metals.

The improvement of these class of catalysts extended to wider solubility range in organic solvents, non-aggregation properties eliminating the π–π stacking due to the bulky aliphatic *i*-C3F7 groups and excellent chemical stability; these superior characteristics makes F_{64}PcM a class of catalysts material suitable for redox and photoreactive chemistry. The present research study is primarily focused on Zinc (Zn) as the metal-centered transition metal (F_{64}PcZn) for a photooxidative reaction. [27 - 29] Metal-center catalyst coated or anchored on different solid-supports can take advantage of the solid support high surface area. The photocatalyst hybrid complex formed with solid support may interact in the form of van der Waals interaction and or other forms of

interaction. This photocatalyst hybrid complex will be embedded in a polymer network (the catalyst hybrid either in the matrix of the polymer and/or some of the hybrid catalyst will be partially exposed to the surface) for photooxidative application. The creation of channels on the polymer matrix will provide added advantages for the singlet oxygen produced by the photocatalyst hybrid, as species are diffused through the channels to the surface of the polymer for reactivity.

1.3. Fluorinated Phthalocyanines/Support as Photoreactive Hybrid.

For optimal production of singlet oxygen, the Pcs is indeed desired to be deposited on a solid support with large surface area: titania (TiO_2), silica (SiO_2) and alumina (Al_2O_3) are some of the materials commonly used as solid support. Metal centered Pcs previously adsorbed onto porous silica for water treatment has been demonstrated for thermal stability. [26] Further studies are needed to determine the success of these photoactive materials and their robustness and susceptibility to thermal degradation under broadband spectrum continuous irradiation and the ability for the photocatalyst to withstand the singlet oxygen/ROS they produce. The advantage of some fluorinated phthalocyanines like the once containing the perfluoroalkyl groups on the peripheral, constitute bulky groups, proved toughness. [27] These robust periphery groups protect the molecule from chemical, radical, electrophilic and nucleophilic attack, and also from the singlet oxygen and ROS they produce.

1.4. Semiconductors: Properties and Photoreactivity.

Solid-state material can be divided into three class: insulators, semiconductors, and conductors. A semiconductor is crystalline solids material [30] that possess transitional electrical conductivity with

characteristically unique properties between an insulator and a conductor. Semiconductors materials have been studied extensively for different purposes, the study of these materials started in the early 19th century and the greater part of these materials are incessantly involving in the field of nanotechnology and material science. [30 – 32] Semiconductors can be categorized into two class: single-element semiconductors and the multi-element semiconductors, those with more than one types of atoms in its structure. [33]

One of the most important properties of semiconductors is their energy bandgap (E_g). [33, 36] Strong interaction of orbitals results in energy band gap defined by the conduction band (CB) and valence band (VB) of the semiconductor. [33] The CB and VB are the basis for the electronic structure of semiconductors (TiO_2, SiO_2, Al_2O_3 and so on). [35] The difference between CB and VB are the presence and absence of electrons, filling the orbitalis at the bed. It can be noted that between the two bands, there is an energy difference characterized as the bandgap, the energy difference between VB as the highest energy level and CB lowest energy level. [36] In the absorption of photons by a semiconductor, electrons are promoted from the electron-rich VB, leaving a positively charged hole (h^+) in the VB, this can only occur when photons equal or energy greater than the bandgap of the semiconductor are absorbed. [37] The CB retained the negatively charged electron (e^-) as a result of the promotion from the VB to the CB.

TiO_2, a well-modeled semiconductor, can breakdown pollutant through a photocatalytic e^-/h^+ process. The oxidation and reduction (redox) reaction occur on the surface of the photocatalyst concurrently, by adsorbing the pollutant onto the surface of the photocatalyst in the presence of atmospheric oxygen (O_2). The process of photo-mineralization shown in **equation 1** can lead to

the total breakdown of organic pollutant in aqueous media to form water, carbon dioxide, and other less harmful hydrocarbon products.

$$\text{Organic pollutant} + O_2 \rightarrow TiO_2\ (h\nu) \rightarrow CO_2 + H_2O \qquad 1$$

The mechanism of this degradation process results from surface hydroxyl (OH) groups undergoing photooxidation to surface hydroxyl radicals (•OH), the oxidized hydroxyl radicals [38, 39] promotes the oxidation of pollutant adsorbed on the surface of the photosensitizer, this is classified as one method of mineralizing pollutant through an oxidation process. The second method, a reduction process takes place in the presence of water, superoxide anion (O_2^-) species are generated leading to the formation of hydroxide radicals, [39] the radical formed, further promotes mineralization of the pollutants on the surface of the semiconductor. The schematic shown below **Figure 1.4**, represents the photo-mineralization of organic pollutant on the surface of TiO_2. [33]

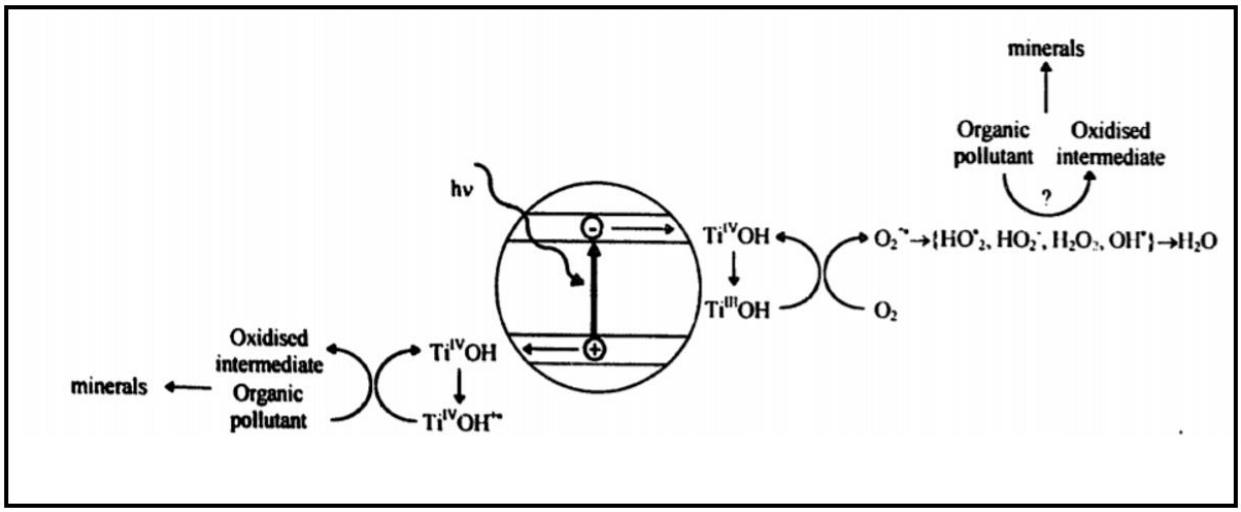

Figure 1.4. TiO_2 photosensitizer photo-mineralization organic pollutant in the presence of atmospheric oxygen. Reproduced with permission from Elsevier. "*Reproduced with permission from Elsevier".* [33]

TiO_2 semiconductor is an active sensitizer with air and light inert in the dark or anaerobic conditions, non-toxic, cheap and absorb wavelength in the UV region below 387 nm resulting in large energy bandgap (3.0 - 3.2 eV) [34 - 36] depending on the type of TiO_2 in question. Although TiO_2 is an efficient/effective catalyst, it only absorbs in the UV region, this region is only responsible for less than 5% of the solar spectrum. [31] This major drawback experienced by TiO_2 has limited its large-scale usability and has been a subject of intense research. [31, 32] One approach to this limitation is shifting the TiO_2 optical capability towards the visible light region by adding impurities, a process called doping. Researchers have explored this approach extensively, doping methods can be done in different ways and not limited to either cationic or anionic forms. [30, 40] Coupling TiO_2 with another semiconductor with a shorter band gap can stretch TiO_2 optical properties into the visible light region, such coupling as, TiO_2/WO_3, TiO_2/ZnO, and TiO_2/CdS have all been explored extensively and with promising results. [40] Another approach currently under study in doping technique is the combination of p-orbital elements with TiO_2, such elements as carbon, sulfur, nitrogen [41] are able to shift TiO_2 optical capability toward the visible light region by lowering the overall bandgap for optimal photoactivity. These modifications to TiO_2 can also prevent fast recombination of the electron/hole pair a major defect, a process of electron demotion back down to the valence band during the photoreactivity process can be repelled. [40] **Table 1.1**, shows the band gaps, wavelengths, and redox potential in normal hydrogen electrode of commonly studied semiconductors.

Table 1.1. Semiconductors and their Optical Properties**.**

Semiconductor	Wavelength (nm)	Band gap (eV)	Absorption	CB (V vs NHE)	VB(V vs NHE)
WO_3	443	2.8	visible	+0.4	+3.0
ZnO	387	3.2	-	-0.2	+3.0
CdS	496	2.5	-	-0.4	+2.1
TiO_2	387	3.2	UV	-0.1	+3.1

Even though TiO_2 and ZnO are the most studied semiconductors for photodegradation of organic compounds, both are disadvantageous due to the wide bandgap (3.2 eV for TiO_2 anatase type and 3.4 eV for ZnO). [42, 43] The properties of CB and VB can also be defined by other parameters like the absence of a small amount of oxygen, Ti^{3+} centers, this only defines the n-type TiO_2 semiconductor. [40] The d^3 orbital of Ti^{4+} consists of the lower section of CB while the VB is consistence of the overlapped 2p orbitals of oxygen. [34]

1.5. Electronic Structure of Singlet Oxygen.

Singlet oxygen liberated from the chemiluminescent reaction of hypochlorite-peroxide was first interpreted by Khan and Kasha (1994), [44] even though, singlet molecular oxygen was discovered in 1924. [44] The physical, chemical and biological properties of these energy-rich form of oxygen have been explored in-depth for reactivity purpose. Substantial research focused on the molecule has been in the areas of polymer science, photooxidation and photodynamic therapy. [45, 46]

Molecular oxygen consist of three electronic states, two singlet state $^1\sum^+_g$, and $^1\triangle_g$ respectively and the lower energy triplet state $^3\sum^-_g$ lower in energy state, [47a,b] represented in **Figure 1.5**.

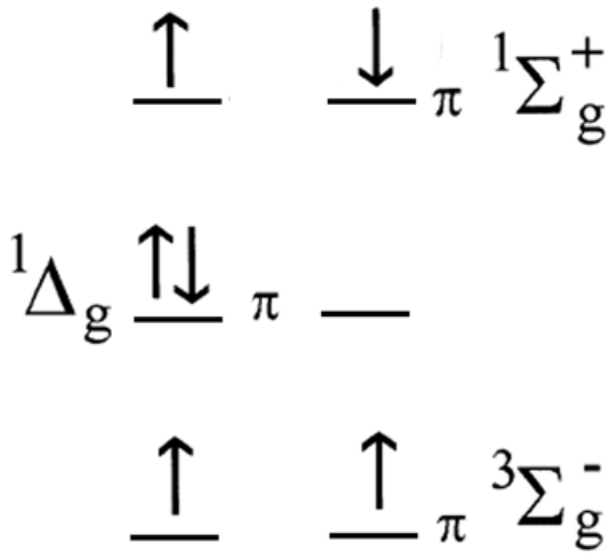

Figure 1.5. Representations of dioxygen molecule in both singlet and triplet states. *"Image courtesy of Abdul Azeez"*.

The orbitals are the same, but electrons are filled differently. The triplet state and the second excited singlet state are similar except for their spin states, in the case of triplet state, $^3\sum^-_g$ electrons are an anti-parallel forbidden state in the orbital, while the second excited singlet state $^1\sum^+_g$ electrons are a parallel state in its orbital. The transition from the second excited state to triplet state is spin allowed, has a short live spin state. While the transition from the first excited state to triplet state is spin forbidden with longer life span, this is because of the arrangement of electrons in triplet state are antiparallel, while in the second excited state electrons are arranged parallel in the orbital.

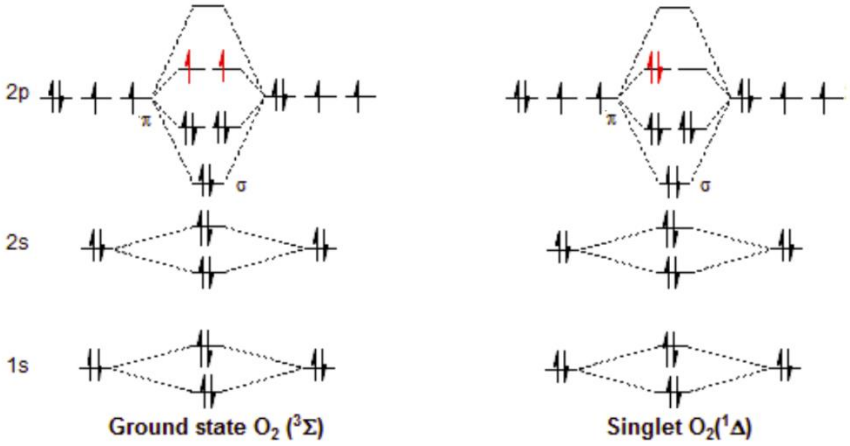

Figure 1.6. Representations of dioxygen molecule in both singlet and triplet states. *"Image courtesy of Abdul Azeez"*.

The meta-stability of these states is represented in radiative lifetimes measurements, the first singlet state is between 10^{-9} – 10^{-6} sec, while the triplet state is 10^{-3} – 100 sec respectively. [47b, 48] Quenching of singlet excited oxygen can be deactivated in two ways; physical and chemical process. The **physical quenching** [49] process does not involve oxygen and no product formation; the singlet oxygen is deactivated by the following process, **equation 2**.

$$^1O_2 + A \rightarrow kp \rightarrow {}^3O_2 + A \qquad 2$$

The second process, **chemical quenching** [49] reactions, involving oxygen in the reaction to produce a new product as seen in **equation 3**.

$$^1O_2 + A \rightarrow kc \rightarrow P \qquad 3$$

The properties of singlet oxygen make it a stronger oxidizing agent than the normal atmospheric oxygen (O_2), it is a strong electrophile, has the capability to attack conjugated C-C bonds during a reaction process. [50] Singlet oxygen can be generated through several processes, one way, by

photosensitization a simple and controlled process because it can be tailored to a particular wavelength and appropriate photon energy. [50] One photon transition is required to excite a ground state molecule S_0 to an excited singlet state S_n, where, internal conversion (IC) of the excited S_n where $n > 0$. Therefore, as stated by Kasha's rule, [44] photon emission is only expected from the lowest or first excited state (S_1) as a result, S_{n-1} from the S_n to S_1 state, the lowest excited S_n state is expected to take place for the photon to be emitted or proceed to the triplet state through the intersystem crossing (ISC). At this stage, if the molecule relaxes back down, two things can happen; either radiation relaxation or none radiation relaxation of the photon energy. Another photochemical process that can happen is when the molecule moves to the triplet state through ISC, a different spin state from the singlet state configuration. Excited triplet state reaction has a longer life spin (μs) than excited singlet state (ns) due to the spin forbidding process, this type of reaction follows Type I or II reaction mechanisms. Type I process involves electron transfer between the excited molecules, while Type II process involves the transfer of energy from the triplet state sensitizer (^3S) to a triplet state oxygen ($^3O_2$) as both molecules collide in the state. The reaction scheme is shown in **Figure 1.7**.

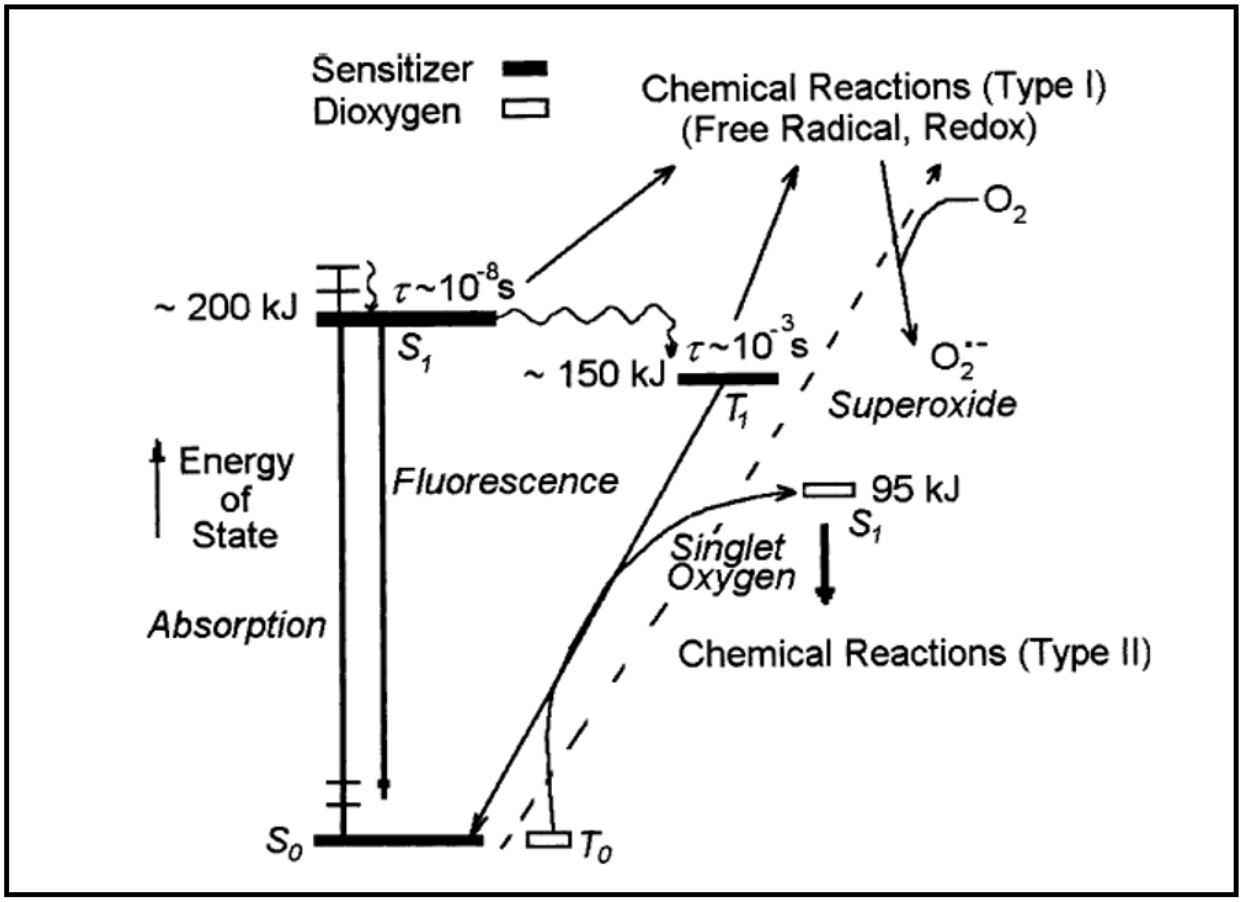

Figure 1.7. Excited-state photosensitizer and triplet state oxygen in Type I and II reaction. *"Reproduced with permission from Royal Society of Chemistry"* [51]

$$P(S_0) + h\nu \longrightarrow P(S_1) \longrightarrow k_{ISC} \longrightarrow P(T_1) \qquad 4$$

$$P(T_1) + {}^3O_2 \longrightarrow k_{en} \longrightarrow P(S_0) + {}^1O_2 \qquad 5$$

Representation: photosensitizer (P), singlet ground state (S_0), singlet excited state (S_1) excited triplet state (T_1), rate constant of electron transfer (k_{et}), rate constant of energy transfer (k_{en}), rate constant of intersystem crossing (k_{ISC}), singlet oxygen ($^1O_2$) and ground state triplet oxygen ($^3O_2$).

$$P(T_1) \longrightarrow k_r \longrightarrow P(S_0) + h\nu'' \quad (6)$$

$$P(T_1) \longrightarrow k_{nr} \longrightarrow P(S_0) \quad (7)$$

$$P(T_1) + O_2 \longrightarrow k_{dO2} \longrightarrow P(S_0) + O_2 \quad (8)$$

$$P(T_1) + O_2 \longrightarrow k_{et} \longrightarrow P(S_0) + O_2^{\bullet -} \quad (9)$$

The pathways above reflect the transition from ground state singlet state of the sensitizer to triplet excited state of energy transfer. Quantum yield dictate the amount of singlet oxygen produced by photosensitizer in a photo reactive process, this yield is due to quenching followed by the pathways through a photochemical process.

1.6. Introduction to Polymers at Surfaces: Properties and Energies.

Bulk and surface properties of polymers [52 - 54] are the foundation for the potential performance of any surface coating material. These fundamental properties, such as thermal stability, the strength of the material, molecular composition, durability, and functionality [55 - 59] of the coated surfaces, are crucial to coating applications. The chemical and physical properties of coated surfaces cannot be overemphasized due to surface wettability, oxidation, corrosion, surface abrasion, strength and durability of the surface. [60 - 62]

The chemical structure of a polymer governs the intermolecular forces within. [63 - 67] The chemical backbone, such as an aliphatic hydrocarbon-based polymer (C-C) or silica-based polymer (Si-O-Si), plays a critical role as well. [68] These backbone properties determine the strength and durability

of coated surfaces from oxidation, thermal stress, irradiation and the ultimate longevity of coated surfaces. [56, 59, 68] Polymer and copolymer architectures, such as random, block, linear, branched and cross-linked, can contribute to strength and durability. [69] Although these characteristics constitute great advantages, some can also come with some disadvantages, [59] not limited to micro-phase separation, challenging preparatory methods for coating surfaces and the ability to manipulate these polymers. [65] All can be a significant challenge to researchers and scientists.

Surface tension [70 - 72] primarily describes the force on a surface [72] as a result of surface interaction with other molecules making contact with the surfaces. These tensions represent the energies exhibited by the coated surface [70] with respect to contact; the unit of this energy can be represented as J/m^2 or commonly N/m. This difference can be interpreted with respect to the intermolecular forces [63] of the surroundings of the molecule; these intermolecular forces balance the forces of attraction and repulsion, [64] between the surrounding molecules or atoms are shown in **Figure 1.8.**

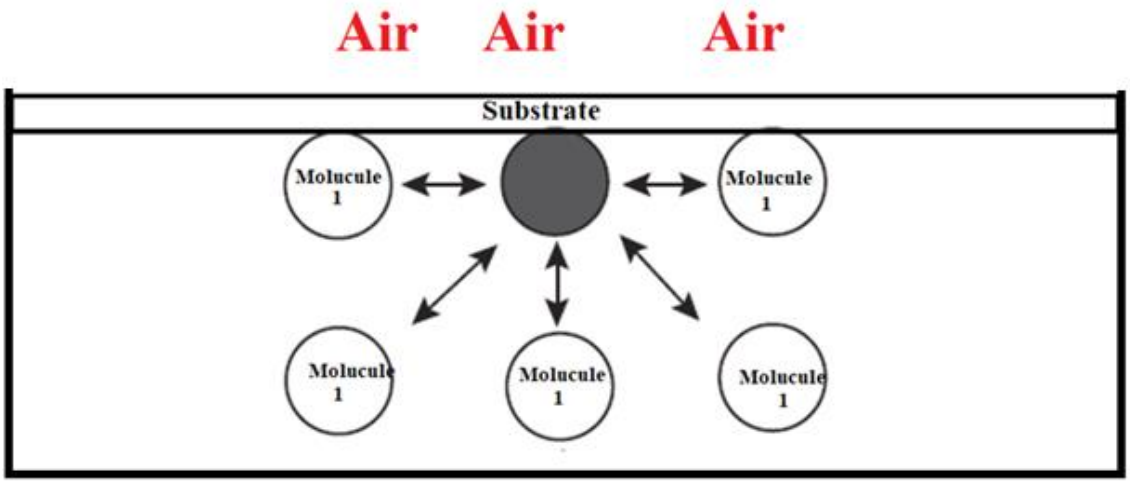

Figure 1.8. Schematic representation of intermolecular interaction and surface interaction. *"Image courtesy of Abdul Azeez"*.

There is a close relationship between surface tension and intermolecular forces as represented in **Table 1.2.** Stronger intermolecular forces (hydrogen bonding, ion-dipole, and dipole-dipole) are known to increase surface tensions. [64 - 66] The sum of these surface tensions or energies can be the sum of total polar forces and dispersive forces expressed in a given polymer network. [64 - 65] In the data shown in **Table 1.2**, poly(acrylic acid) (PAA) has the highest polar force, 36.6 mN/m, this should not come as a surprise because PAA includes a polar carboxylic group, with strong hydrogen bonding. [67, 68] PAA also has dispersive energy of 18.4 mN/m and with a high surface energy of 54.7 mN/m. Polydimethylsiloxane (PDMS) has very low surface energy, 19.8 mN/m, because of the methyl groups are arranged along the (Si-O) backbone. [68,] Dispersive forces contribute most of the energy, 19.0 mN/m, with only small polar fraction energy of 0.8 mN/m. [68 - 71] This contribution of 0.8 mN/m, comes from the polar nature of Si-O-Si backbone, [17] but the arrangement is a huge contributing factor to the highly, non-polar ($Si-CH_3$) groups, making PDMS lower in surface energy compared to other polymers. [69] This low surface tension has contributed to a wide range of industrial applications for PDMS, [70] positioning them as excellent materials for designing superhydrophobic surfaces. Although PDMS has a low energy surface, [68] substituting some of the methyl groups with long-chain alkyl groups or with fluorinated groups will further reduce the surface energy of the polymer and improve hydrophobicity- substitution of methyl group from PDMS with trifluoropropyl ($CF_3CH_2CH_2$) will reduce surface tension of the siloxane compound to 13.6 mN/m. [68] The strong electron-withdrawing CF_2 group and perfluoroalkyl groups may be attributed to the electronegativity of fluorine atoms and can promote the reduction of organic polymer surface energy. **Table 1.2**, revealed polyethylene (PE) has a high surface tension of 35.7 mN/m, with zero polar energy can be but high dispersive energy of 35.7 mN/m. PVDF, with alternating CH_2 and CF_2 groups, reduces the surface energy to 30.3 mN/m, with a

reduction of more than 5 mN/m. Completely replacing all the hydrogen atoms with fluorine atoms to generate polytetrafluoroethylene (PTFE, Teflon), reduces the surface energy to 20.0 mN/m, making PTFE one of the lowest surface energy polymers.

Table 1.2. Polymer Surface Energies and their Dispersive and Polar Energies.

Polymer	Surface Energy (mN/m)	Dispersive Energy (mN/m)	Polar Energy (mN/m)
Polypropylene (PP)	30.1	33.6	0
Polyethylene (PE)	35.7	35.7	0
Polystyrene (PS)	40.6	34.5	6.1
Poly(methyl methacrylate) (PPMA)	41.1	29.6	11.5
Polytetrafluoroethylene (PTFE)	20.0	18.4	1.6
Polyvinylidene fluoride (PVDF)	30.3	23.3	7
Polydimethylsiloxane (PDMS)	19.8	19.0	0.8
Poly(acrylic acid) (PAA)	54.7	18.4	36.3

1.7. Hydrophilicity and Hydrophobicity: Wettability of Surfaces.

One of the methods for characterizing coated surfaces is through the wetting process. Liquid droplets on a surface can wet the surface partially, completely or the surface may reject the liquid,

and this phenomenon is called liquid wettability on surfaces. [73, 74] Wettability can be used to quantitatively determine the energy of the surface in question (polar energy and dispersive energy). The wettability of a surface can be measured numerically by contact angle (CA) technique from 0° to 180°. [72-77] Wettability reflects the energy difference between the coated surface and the liquid droplet resting on it.

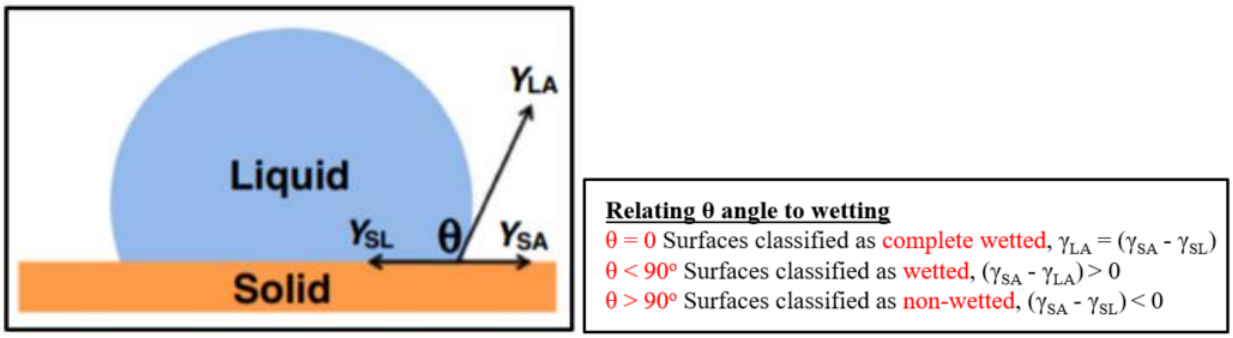

Figure 1.9. Liquid droplet at equilibrium state in contact with a smooth solid surface. *"Reproduced with permission from American Chemical Society".*[75]

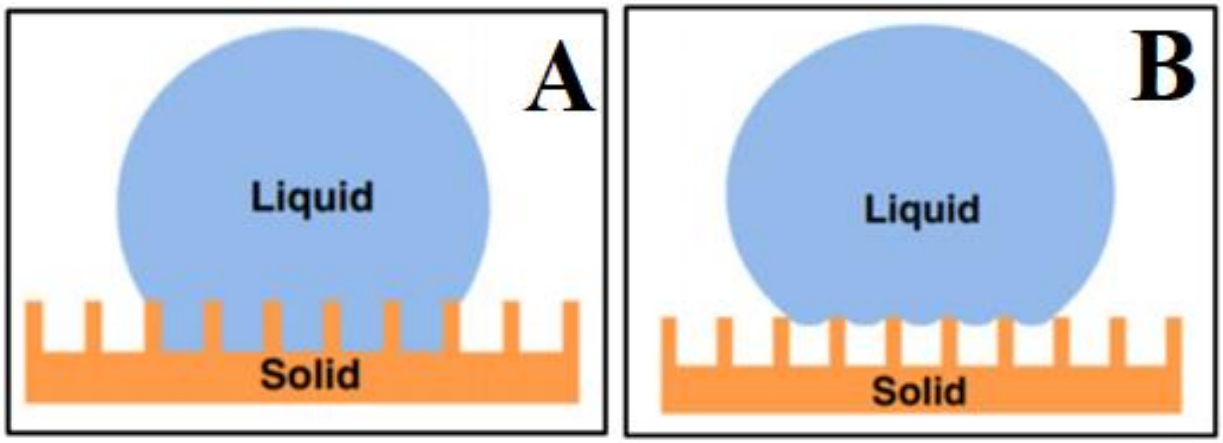

Figure 1.10. Liquid droplet on a rough surface **(a)** Wenzel state and **(b)** Cassie-Baxter state. *"Reproduced with permission from American Chemical Society".*[75]

When the contact angle of a droplet on a surface is measured, if the CA θ < 90°, the liquid making contact with the surface is classified as wetting, shown in **Figure 1.9,** alternatively, if the CA θ >

90°, the surface is classified as not wetting, the surface is rejecting the liquid droplet, shown in **Figure 1.10 b.** To explain this wettability phenomenon, liquid-liquid intermolecular forces, and liquid-solid forces, acting on the surface [63] play a great role. The strength of these forces either cohesively or adhesively is significant in determining surface wetting. [64, 65]

If the liquid cohesive forces acting within the liquid are much stronger than the adhesive forces the forces acting between the liquid and smooth solid surface and the surface will not be wetted. If the reverse is the case (adhesive stronger than cohesive), then the surface will be wetted, the water will spread out on the coated surface. Stronger cohesive forces will result to hydrophobicity, CA $\theta > 90^{o}$, while, stronger adhesive forces will result to hydrophilicity, thus can result to complete wetting depending on the degree of adhesiveness, CA $\theta < 90^{o}$. Deionized water has a surface energy of 72.6 mN/m at room temperature and is commonly used for CA determination. [79] **Table 1.2** revealed the water CA of some polymer as they follow an inverse relationship with surface energy. PMMA has a high surface energy of 41.1 mN/m and gives a hydrophilic CA with water of 70.9°. This can be attributed to its ester group which can easily hydrogen bond with water. Polyhexafluoropropylene, [80] a fluorocarbon polymer, has the lowest surface energy because of the strong electron-withdrawing group provided by the fluorine atoms; hydrogen bonding with water is not favored with this polymer at the surface. The inverse relationship of surface energy and contact angle dictate wettability, [80] surface energy lesser than 35mN/m are said to be hydrophobic as shown below in **Table 1.3**. The lowest surface energy polymers are still partially wetted. For a coated surface to completely repel water, the surface will require more than low surface energy. As can be seen from **Table 1.3** to this point, a superhydrophobic surface is far from reality.

Table 1.3. Polymer Surface Tension and CA of Water (Static).

Polymer	Surface Energy (mN/m)	Water Contact Angle (θ)
Poly(methyl methacrylate) (PMMA)	41.1	70.9
Polystyrene (PS)	40.6	87.4
Polyethylene (PE)	35.7	96.0
Polyvinylidene fluoride (PVDF)	30.3	98.2
Polypropylene (PP)	30.1	102.1
Polydimethylsiloxane (PDMS)	19.8	107.2
Polytetrafluoroethylene (PTFE)	20.0	109.2
Polyhexafluoropropylene	14.7	112.0

1.8. Modification of Polymer Matrix and Surface Properties.

Polymer composition plays a significant role in polymer applications, therefore, it is important to improve surface hydrophobicity by choosing the appropriate polymer material with low surface energy to prevent corrosion of the underlying metal. [81, 82] PTFE has unique properties, not limited to a high melting temperature of 327 °C, this property makes it very expensive and difficult to process. The lowest surface materials are not always the first option [82] when designing surfaces. The replacement of the hydrogen atoms with fluorine atoms try contributes to its strong thermal properties. Nevertheless, after melting, PTFE does not flow like a liquid; instead, it forms a thick viscous gelation adhesive material, therefore, it is not useful in a wide variety of application, despite superior thermal stability.

It is necessary to augment the properties of polymers for better corrosion resistance. [83] Modification of bulk and surface polymers can be classified into two categories: the bottom-up approach and the top-down approach. These two approaches are dependent on the type of surface application in question, although the top-down approach involves mainly surface re-engineering of the polymer, while the bulk or matrix of the polymer are left unmodified. Superhydrophobic surfaces can be achieved with the process of tailoring the topography of the surface to the desired shape and achieving small-scale size (nano-micro range). [83 - 86] Bottom-up approach employs a different strategy from the top-down; bottom-up technique requires the construction of polymer matrix and surface topography from the beginning to the finished product on the coated substrate. [87] It is challenging to achieve superhydrophobicity with this technique because of the difficulty in controlling the surface topography and the matrix during the design process. [88, 89]

1.8.1. Top-down Approach.

Lithographic methods, a common printmaking technique, are an easy way to achieve superhydrophobicity, since surface topography can be manipulated easily with this method. [90] There are different types of lithography; soft lithography is commonly used for designing superhydrophobic surfaces. It is an easy process has drawbacks such as susceptibility to thermal degradation and low resistance to solvent attack according to study by Miyamura *et al*. [91] Another technique of interest is the colloidal lithography, superhydrophobicity was easily achieved with polystyrene with WCA 150 º reported by Sun *et al*. [92] The drawback for this technique can come from loss of reflectance demonstrated by Li *et al*, [93] and Tseng *et al*, [94] in their research studies. Electron beam lithography (EBL) is another important technique, this technique can be used to produce ordered hierarchical surface, and high WCA was reported by Li *et al*. [93] In general,

lithographic techniques are good for ordered surface design but not easily scalable to large scale industrial usage, they tend to be limited to relatively small surface areas.

Chemical and Plasma Etching method, a common way of polymer surfaces engineering as a result of method reproducibility were demonstrated by Guo *et al*, [95] the use of this technique for precise tailoring or surface topography showed great success. Gupta *et al*, [96] reported superhydrophobic surfaces with chemical and plasma etching method. Plasma etching can be combined with other techniques such as the template method for achieving superhydrophobicity. Palumbo *et al*, [97] reported the use of this combined method to achieve superhydrophobicity. Chemical etching is mainly used for the modification of metal surfaces for hydrophobic purposes, this etching promotes roughness on surfaces commonly used in metal applications.

1.8.2. Bottom-up Approach.

Hydrothermal method, the technique involves a process of aqueous solution at higher temperature and pressure. Superhydrophobic nano-lamellar structures were achieved with PDMS modified with vinyl-terminal through a spin coating process initially prepared by a hydrothermal method. Sun *et al*, [98] reported the use of a hydrothermal method for hydrophobic surfaces with low cost and easy to use. High WCA above 150^{o} was reported through the hydrothermal method on a number of the substrate by Guo *et al*. [95] Guo *et al*, [44] also reported superhydrophobic coatings with a hydrothermal method on magnesium alloy, a template-free method, although, with the combination of fluoroalkylsilane (FAS) coating, high WCA can easily be attained.

Chemical Vapor Deposition (CVD) method, a thin film or powder is deposited on the surface of a substrate through the process of inducing volatile precursors transformed from the vapor phase

during the process. Choi *et al*, [99] reported CVD surface growth control as a result of manipulating the growth restriction of the polymer deposited on the substrate. Electrospinning method can be combined with CVD, a process where continuous fabrication of nanoscale material can be attained through a process of electro-fluid-dynamics (EFD). Therefore, the induced charged fibers within the nano/micrometer range are made from the polymer material. These fiber materials are highly flexible and highly porous, with ordered nano-range and high volume to surface aspect ratio.

Layer-by-Layer Assembly method, a very simple and convenient process whereby polymer of desired types are arranged on a substrate for application purpose. This arrangement can pave ways for superhydrophobic surfaces through well-tailored film growth of the polymer on the surface of the substrate. Li *et al*, [100] reported using layer-by-layer film growth assembly method for attaining a superhydrophobic surface. Silver nanoparticles deposited as a monolayer generated a superhydrophobic surface due to the topographic arrangement of the nanocomposite.[100]

Sol-gel method, a wet-chemical technique for the fabrication of gel-like components with the representation of both solid phase and liquid phase all in a single reaction network. This process includes the modification of the sol-gel network through the hydrolysis and polycondensation reaction process. The process of hydrolysis and polycondensation is a very common practice in sol-gel chemistry, this technique was used to design high WCA surfaces in excess of 160 ^{o} reported by Xiang *et al*. [101] Sol-gel methods have wide uses in areas of metals, stainless steel, textile, and other large scale applications. Methyltriethoxysilane (MTES), a silane-based colorless polymer precursor, has been used to enhance substrates, also to act as a crosslinker. This material was prepared through hydrothermal method for prevention of surface corrosion reported by Rao *et al*. [102] Tetraethoxysilane (TEOS) a silica-based monomer polymer with characteristic flexibility was

used for the improvement of adhesion and corrosion prevention reported.[102] The advantages of the sol-gel method compared to other methods is the ability to control the surface roughness of coating materials during the coating process. Low temperature, resulting to a superior degree of homogeneity of the coated surfaces, showing the impact of temperature control by this technique has been observed, also superhydrophobicity through nano-sized cavities formed within pores during the process of hardening, a process of controlling the desired matrix formatted with the sol-gel method.

1.9. Theory of Wettability on Smooth Surfaces: Young's Equation.

Liquid droplets on a solid surface measure the wettability in an equilibrium state. This state of equilibrium provides a quantitative analysis of the liquid through contact angle measurement. Contact angle measurement can be accurately predicted from the surface energy of the substrate and the liquid in contact at a determined temperature. Contact angle measurement is a function of temperature due to changes in intermolecular/intramolecular forces governing the substrate surface and the water droplet in contact. A rigid solid surface "ideal solid", can be qualified as a homogenous surface, if the surface perfectly exhibits smoothness and is chemically inert under a pure liquid, this can be expressed with Young's equation. [102, 103] Therefore, the surface of the solid can be determined by measuring the contact angle as related to free energy. Although most liquids are under atmospheric condition, an interfacial boundary with three phases is mostly formed on a surface: solid-air, solid-liquid, and liquid-air. This relationship can be expressed by (air-solid-liquid) interfaces and can be represented independently as liquid-air (γ_{LA}), solid-air (γ_{SA}) and solid-liquid (γ_{SL}) interface as shown in **Figure 4.1** below.

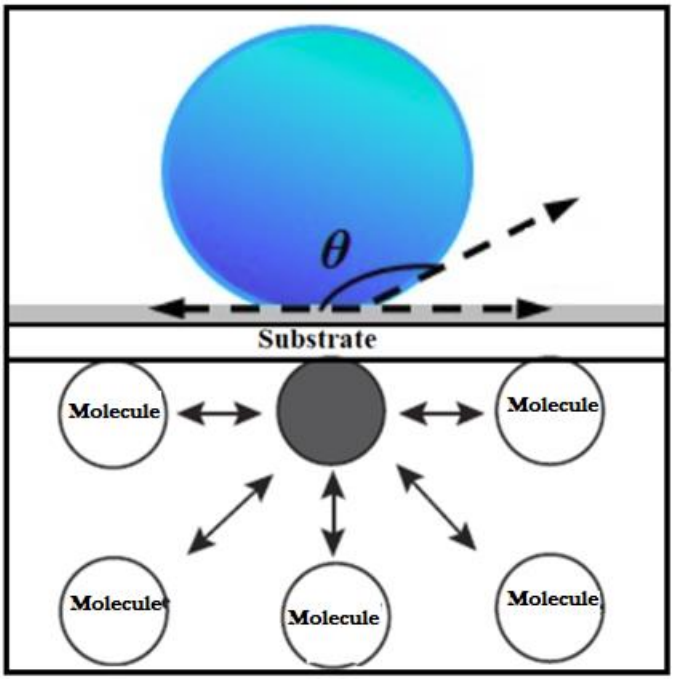

Figure 1.11. Static liquid droplet on a solid surface with interfacial forces. *"Image courtesy of Abdul Azeez"*.

As the liquid spreads outward on the surface of the solid, the air is displaced giving further room for liquid as this spread cause loss of solid-air interface [104] and simultaneously as the solid-liquid interface is gained on the surface area at equilibrium, [104] shown above in **Figure 1.11**. Interfacial energy plays a role during the force of attraction if the cohesiveness in water molecules is lesser than the force of adhesion with water molecules and the surface in contact. Dupre', 1869 proposed the concept of work done on the solid surface due to adhesion, therefore the attraction of various phases as a result of surface tension of the solid in contact, the expression by Dupre' is illustrated in **equations 10** below. [103]

$$W_{SL} = \gamma_{SA} + \gamma_{LA} - \gamma_{SL} \qquad 10$$

Work of adhesion (W_{SL}) and the other symbols expressed above as interfacial forces. [51]

In 1805, Thomas Young expressed that the surface tension between solid-air should not surpass the combined surface tension of solid-liquid and liquid-air. This expression by Young represents **equation 11** below.

$$\text{Cos } \theta = (\gamma_{SA} + \gamma_{LA})/ \gamma_{SL} \qquad 11$$

Although cos θ expresses the infinitesimal change (*dx*) of the triple line as expressed by **equation 11**, CA is determined by the various interfacial energies acting on solid-liquid-air, which represents the angle formed by the liquid on the solid surface. Therefore, expressed as $\theta < 90^o$ can be classified as wetted and $(\gamma_{SA} - \gamma_{LA}) > 0$. If $\theta = 0$ can represent complete wetting of the surface by the liquid, therefore, $\gamma_{LA} = (\gamma_{SA} - \gamma_{SL})$. If $\theta > 90^o$, it is determined to be a non-wetting surface at equilibrium as $(\gamma_{SA} - \gamma_{SL}) < 0$. When CA is at 90^o $(\gamma_{SA} - \gamma_{SL}) = 0$, this becomes an intermediate between the non-wetted and wetted surface. [54] These two equations can be combined together to form the Young-Dupre' equation [105] for interfacial energies of solid surface in contact with liquid and air, **equation 12**.

$$W_{SL} = \gamma_{LA} + \gamma_{LA} \times \text{Cos } \theta = \gamma_{LA} \times (1 + \text{Cos } \theta) \qquad 12$$

In the case of complete wetting on the solid surface, if $\theta = 0$, then the Young equation can be expressed in the following way as shown in **equation 13** below.

$$\gamma_{SA} = (\gamma_{SL} + \gamma_{LA}) \qquad 13$$

Solid surfaces are not ideally smooth in practical applications, and not homogenous in everyday usage, these effects limit Young's equation based on practicality. [105]

1.10. Theory of Wettability on Rough Surfaces: Wenzel Model.

An ideal solid surface can only be treated with the Young equation, but surfaces have different forms: smooth, ridged, heterogeneous, homogenous, etc. The irregular surfaces are more common in nature, [106] therefore, wettability on surfaces outside the defined ideal smooth solid surface are said to be apparent surfaces and characterized macroscopically. [107] In 1936, Wenzel studied the roughness effect on chemically homogenous surfaces, he defined a roughness factor (r) for complete wetting on a rough surface as the ratio of the actual area of its projected geometric area; $r = (A_{actual}/A_{projected})$ of surface roughness. The model projected the liquid size to be larger than the roughness scale of the solid surface, where $r > 1$ for rough surface and $r = 1$ for an ideally flat surface. [56] Wenzel model is shown in **Figure 1.12**.

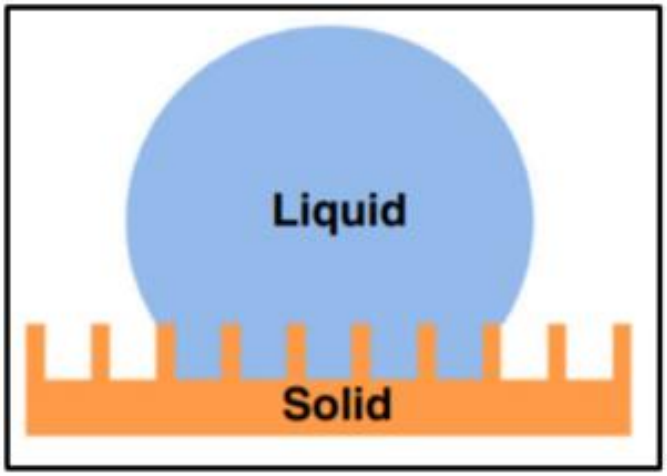

Figure 1.12. Wettability of apparent rough surface according to Wenzel Model. *"Reproduced with permission from American Chemical Society"*. [75]

The Wenzel equation is directly proportional to CA, if an intrinsically hydrophobic rough surface, where $\theta > 90°$, surface wetting is unfavorable, will continue to decrease, and the static liquid CA will increase. On the other hand, if an intrinsically hydrophilic rough surface, where $\theta < 90°$,

surface wetting is favorable, will continue to increase, and the static liquid CA will decrease. Wenzel model is defined by **equation 14** for the contact angle on a rough surface where θ is the apparent contact angle which relates to the stable state at the equilibrium position.

$$\text{Cos}\,(\theta^*) = r\cos(\theta) \qquad 14$$

Therefore, for the Wenzel model to occur, the more hydrophobic a rough surface, the higher the CA, while the more hydrophilic a rough surface the lower the CA. [106] These rationalizations are based on a dynamic liquid on a solid surface and not the surface roughness, based on the assumption that liquid spreading will fill the total area of the rough surface; therefore surface roughness will not be the primary determinant. This assumption was the basis for the Wenzel principle for surface roughness. [106, 107]

1.11. Theory of Wettability on Rough Surfaces: Cassie-Baxter Model.

In 1944, Cassie and Baxter, [108] revealed wetting phenomena on chemically heterogeneous composite solid surfaces composed of two phases with just a single CA determined. Although there are two phases, each phase gave a CA with θ_1 and θ_2 respectively. Each phase has its own fractional surface area called f_1 and f_2 respectively, these fractional areas are assumed to be very small in size and smaller than the liquid droplet. The sum of both fractional surface areas equal to unity, $f_1 + f_2 = 1$. Change in Energy (*dE*), assuming small displacement of the liquid droplet on a chemically heterogeneous surface can be significant, at equilibrium, $dE = 0$. [109] Apparent CA in Cassie-Baxter model is dependent on the cosine angle of each phase of the surface in contact. [58] The Cassie-Baxter model predicted a liquid droplet suspended on a composite surface (solid-air) would behave differently from the Wenzel predication of complete wetting of the solid surface in

contact. The Cassie-Baxter model in an appropriate state (rough surface of appropriate scale) will trap air between the solid surface and the liquid, apparent CA possibly approaching 180^{o}.

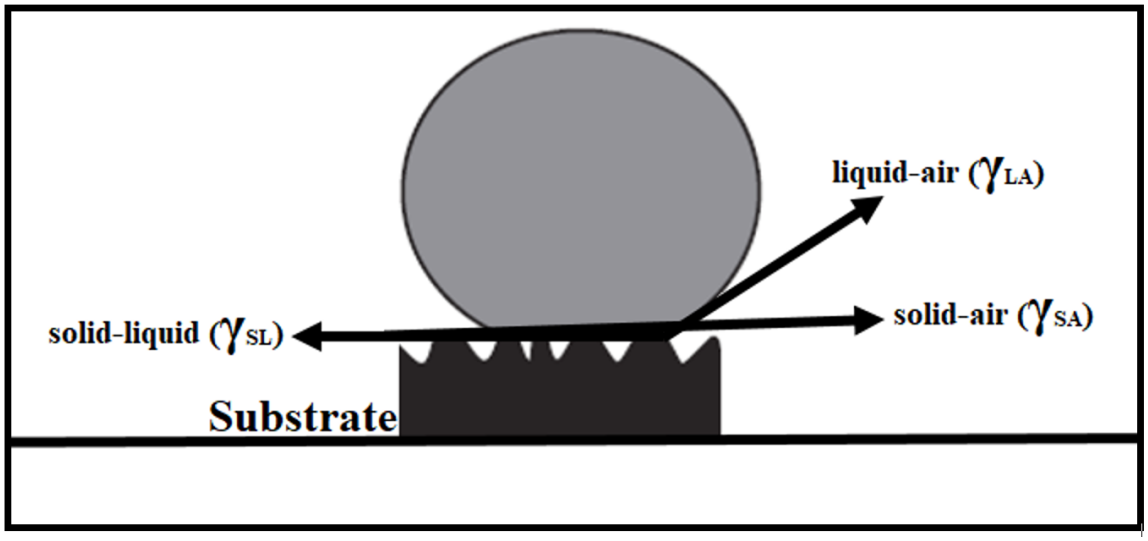

Figure 1.13. Wetting behavior of liquid droplets on a rough surface, Cassie-Baxter model. *"Image courtesy of Abdul Azeez"*.

The Cassie-Baxter equation in a simple form is shown in **equation 15**, reflecting cos θ as a function of the surface fraction of both phases:

$$\text{Cos } \theta_{CB} = f \times \cos \theta + f - 1 \qquad 15$$

Combination of the Wenzel model on a rough surface (r) with Cassie-Baxter model for apparent contact angle with a fractional part (f), and angle of roughness (θ_R) is shown in **equation 16**. The combination of both equations gives a good insight into the effect of the surface roughness, as the

surface roughness increases with this model the CA angle also increases even with surfaces that are intrinsically hydrophilic, this can be attributed to the surface roughness factor. [110]

$$\text{Cos } \theta_R = r \times f \times \cos \theta + f - 1 \qquad 16$$

The Cassie-Baxter state treats surfaces that are not completely wetted, such surfaces are tailored in a way that the depressions in the surfaces are smaller than the water droplet, suspending the water droplet on a composite surface with air. The Wenzel model treats surfaces with total wetting.

Liquid droplets on a solid surface can remain stationary or can be set in motion. A liquid droplet in motion on an inclined surface will have a CA at the front and a CA at the back. The front CA is called the advancing CA, while the back CA is called the receding CA. The advancing CA is leaning forward, will be favored to have a higher CA, while the receding CA will tend to be smaller. This phenomenon of liquid in motion on a surface is called contact angle hysteresis (CAH), [111] a second way to determine CAH is by slowly lowering and retracting a liquid droplet onto a surface through a process called the sessile drop method. The CAH of the sessile drop method can be determined by the difference between the advancing and receding CA of the droplet on the solid surface. [111] The extent of the surface tension on the solid surface by the movement of the liquid droplet can also determine the CAH. [112]

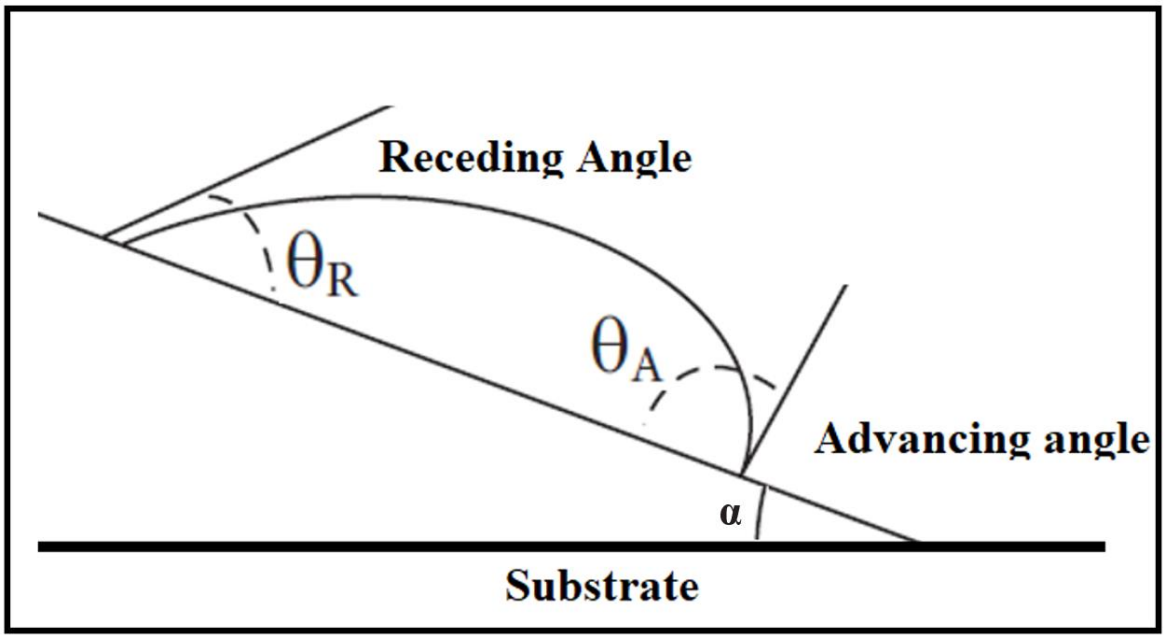

Figure 1.14. Angle hysteresis of angle α, advancing θ_A to and receding θ_R contact angle. *"Image courtesy of Abdul Azeez"*.

For a composite heterogeneous solid surface to be superhydrophobic, the liquid droplet on the surface must have a CA > 150^o and CAH < 10^o. The topographical arrangement of the surface can influence the CAH of a surface.

1.12. Nature and Surface Wettability: Self-Cleaning Surfaces.

1.12.1. Lotus Effect.

Barthlott and Neinhuis studied structures and composition of numerous plant leaves and insects, as they looked at what was behind the durable stability of water repellency for these natural species in their habitat. [112] Characterizing the morphology and topography of these plant leaves and insect were challenging, the invention of Scanning Electron Microscopy (SEM) was a major breakthrough for the study of the morphology of these natural surfaces. [113]. Lotus leaf (Nelumbo

Nucifera) stood out among all the plants studied because of its characteristic high water repellency. In 1998, the Lotus Effect was attributed to superhydrophobic effects as a result of micro-/nano-hierarchical structural surface morphology on the leaves. In a study by Barthlott and Neinhuis, two levels of hierarchical roughness were revealed with the advent of SEM, [114] as seen in **Figure 1.15**. The studies proved hierarchical roughness pattern on the leaf distributed irregularly all around the surface [112] and comprised of 5 -10 μm tall and approximately 5 μm base diameter protrusions. These protrusions are primarily responsible for the lotus leaf water repellency. [112] The surface of the lotus leaf is composed of a waxy layer on the outer epidermal cell layer [102] and this waxy layer is intrinsically hydrophobic due to its chemical composition. [102] The combination of the waxy polyester composite and hierarchical roughness pattern represents the characteristic high water repellency measured CA > 150^{o} and CAH less than 10^{o}. [115] Other forms of surface modification through artificial means to achieve superhydrophobicity and superhydrophilicity have been reported in the literature, these surface arrangements have similarities to the hierarchical structure of the lotus leaf. [115]

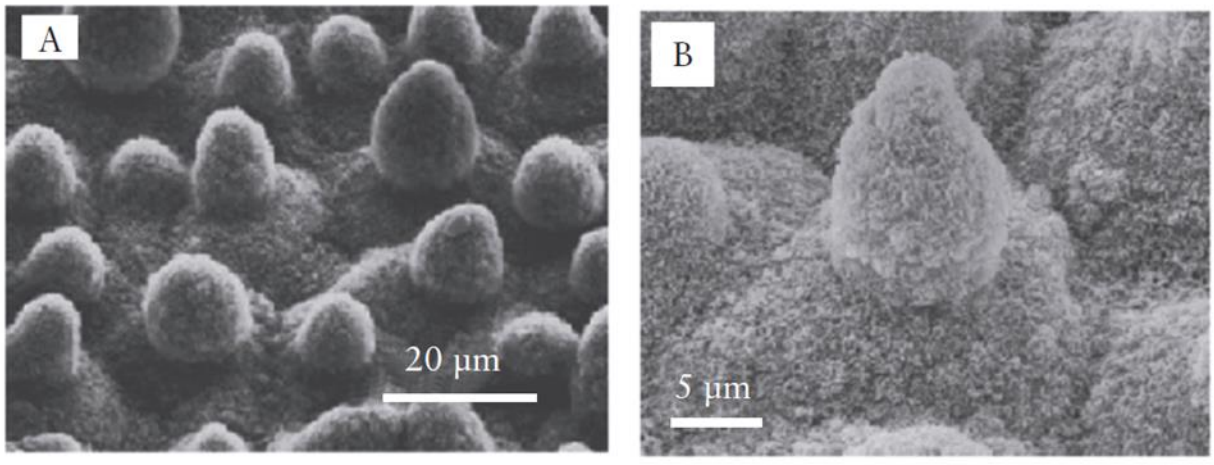

Figure 1.15. SEM images of the surface of a lotus leaf at different magnifications. *"Reproduced with permission from American Chemical Society".* [115]

Water repellency in plants is not unique to lotus leaves. Superhydrophobicity has been studied in other plants, such as rice leaves and red rose petals. Red rose petal surfaces consist of convex conical cells. [116] Rose petals quality are unique, superhydrophobic with high contact angle 152.4°, however, water droplets stick to their surfaces without rolling off. This is a unique combination, high CA with high contact angle hysteresis. This high CAH is attributed to the topographical arrangement of the rose petal surface morphology. When compared to a lotus leaf, which has high CA and low CAH, as proposed by the Cassie-Baxter model for superhydrophobicity on surfaces. The observed difference shown in the SEM images, lotus leaf above in **Figure 1.15** and rose petal below in **Figure 1.16**, the SEM images revealed rose petal micro/nanostructural surface with deep/steep pitches compared to the topography of lotus leaf surface. [117] Cassie explained the possibility of a wetting state between the microstructure and the nanostructure. Because of the hierarchal topographical structure (micro/nano) surface of rose petal, water can penetrate the microstructures and not the nanostructures giving high CAH > 10^{o} and high CA > 150^{o}. [51]

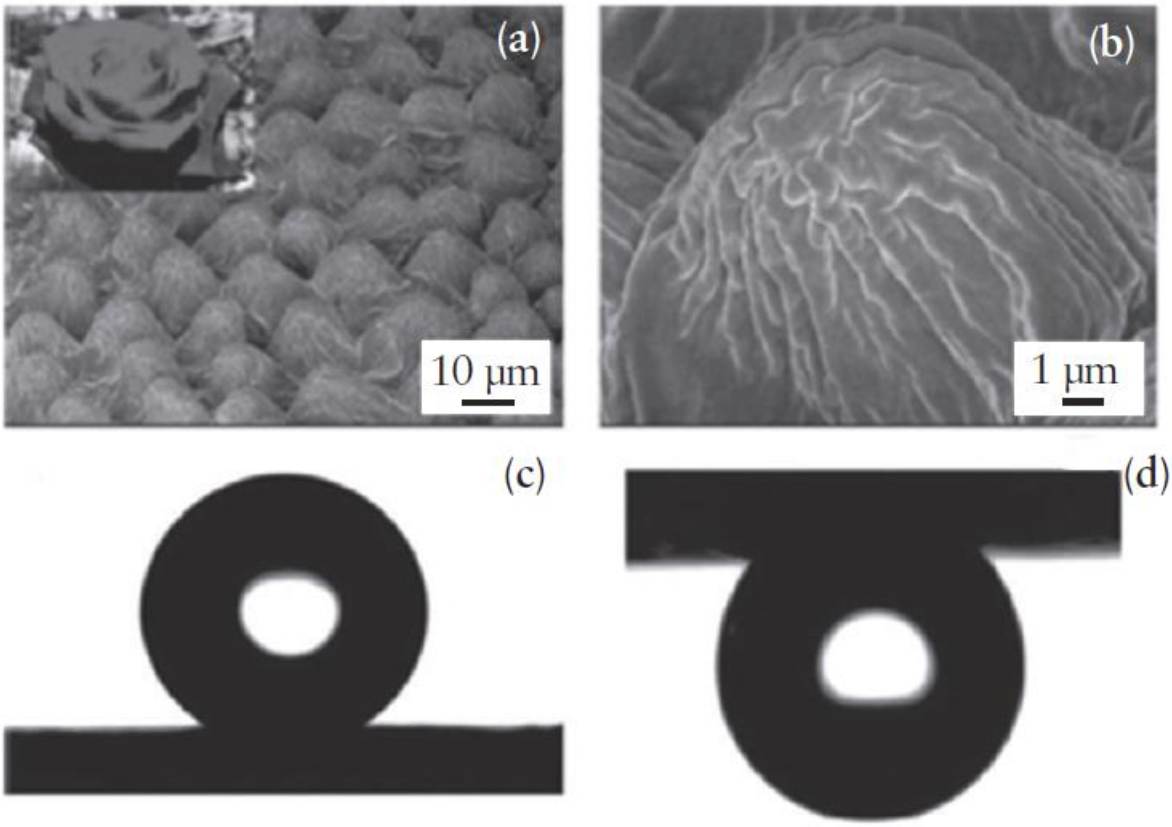

Figure 1.16. SEM images of the surface of rose petal and contact angle. *"Reproduced with permission from Springer Nature".* [117]

1.12.2. Superhydrophobic Effects in Animals.

Besides the numerous superhydrophobic effects studied in plants, superhydrophobicity has also been studied in animals, micro/nano-hierarchical structured layers studied in animals have contributed their anti-fogging capabilities, [116] a typical example is a thin layer covering the eyes of a mosquito. Mosquito eyes are covered with a hexagonal-shaped layer called ommatidia, [118] these layers are packed with micro-size hair-like structures around and within the eyes providing for

excellent vision in a waterlogged environment. [119] The wings of certain insects also have excellent water-repelling capabilities which make them superhydrophobic. The structural morphologies of many insects' wings have been studies with the aid of SEM to understand the topographical structure. The wings of butterflies repel water, studies conducted under SEM, revealed micro/nano dual-scaled topological roughness. Excellent water repellency was observed with contact angle on the surface of the wings, revealed CA > 150^{o} (46) and CAH > 3^{o}. [188, 119] The superhydrophobic nature of the legs of water striders has fascinated scientist due to its ability to walk on the surface of streams and ponds because of needle-shaped microsetae that cover the legs at an inclined angle of 20^{o} positioned on the surface. [116] The measured water CA on the legs of these insects revealed approximately 150^{o}. [116, 119] Nature has always inspired science from all perspectives, the hydrophobicity of these natural systems protect vital components in wet environments and provide greater survivability to these organisms.

1.13. An Introduction to Photochemical and Photophysical Studies.

The absorption of photons in the presence of broad-spectrum irradiation result in photophysical and photochemical reactions. [120, 121] The photons absorbed produce an electronically excited state of a molecule. First, the energy of the photon should match an energy gap within the molecule (absorber), [121] second, when the initial wave function (ψ_i) and final wave function (ψ_f) are most aligned with one another, absorption of photons are strongest. [121]

$$R + h\nu \rightarrow R^* \qquad 17$$

The amount of light absorbed by a molecule is dictated by the molar absorptivity (ε), there is an exponential relationship between the light intensity out of the molecule that is reduced than the

light intensity into a sample (I_{out} /I_{in}). [122, 123] The absorbance (A) has a linear relationship with molar absorptivity, the concentration of the substance (c) and the path length (l), the relationship is characterized as Beer-Lambert Law, expressed in **equation 18 and 19**.

$$A = \log (I_{out}/I_{in}) \qquad 18$$

$$A = \varepsilon cl \qquad \varepsilon = A/cl\ (mol^{-1}\ cm^{-1}) \qquad 19$$

Absorption spectra of molecules display the variation of Absorbance or molar absorptivity vs wavelength, the absorption information provides the wavelength (λ_{max}) as a function of the maximum absorption coefficient (ε_{max}) of the molecule. [124] To explain the total effect of electronic excitation of a molecule, the motion of the nuclei should be taken into consideration, the vibrational and rotational energy of the molecule as it is related to electronic excitation is expressed in **equation 20**.

$$E_t = E_e + E_v + E_r \qquad 20$$

Where total energy (E_t), is the sum of electronic energy (E_e), vibrational energy (E_v), and rotational energy (E_r) respectively. The Born-Oppenheimer approximation relies on the large energy gap [125] between electronic state → vibrational state → rotational state. [123] Changes in both electronic and vibration state called vibronic transitions represent the absorption of light energy in the ultraviolet and visible region of the electrospectrum. Molecules in electronically excited states due to excess energy as a result of photon absorption are short-lived, deactivation occurs through physical and chemical processes. [126, 127] A schematic representation is shown in **Figure 1.17**, represents the physical processes.

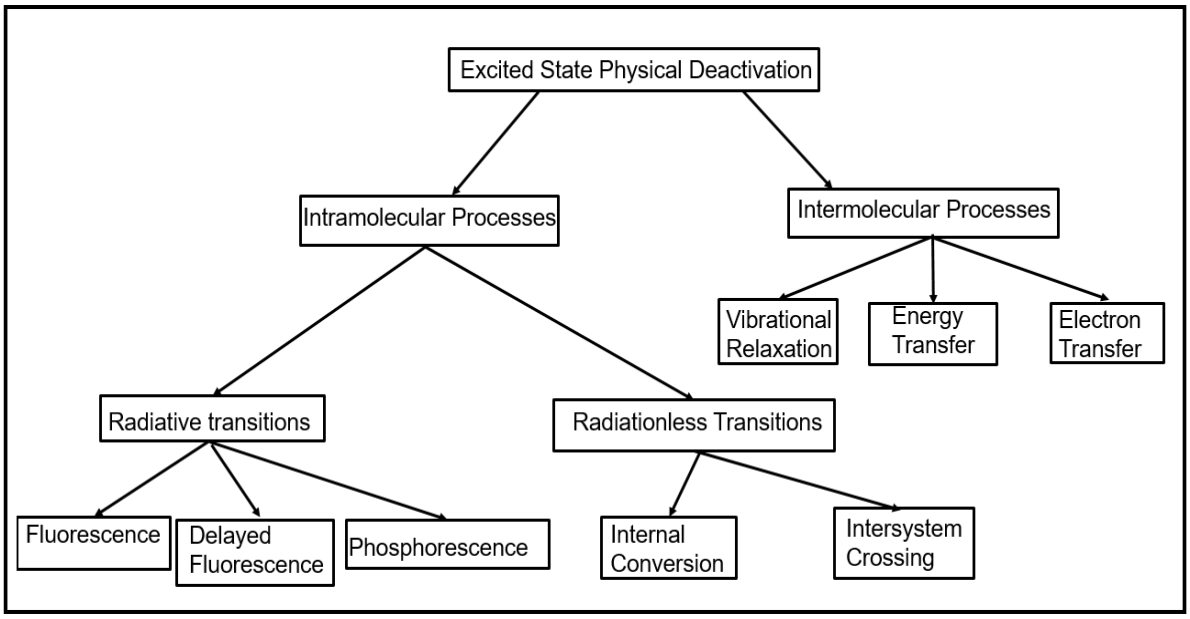

Figure 1.17. Physical deactivation of excited states of organic molecules. *"Image courtesy of Abdul Azeez"*.

Physical deactivation processes are classified into various roles; intermolecular processes: energy transfer and electron transfer. [127, 128] Intramolecular processes are categorized into two paths, radiative transitions involving the emission of electromagnetic radiation during relaxation of the excited molecule to the ground state, and radiationless transitions where relaxation occurs with no radiation. [128] During the intermolecular processes, molecules with excess vibrational energy collide with other molecules or solvent resulting in the distribution of energy and produce molecules in the lowest vibrational energy state. Energy transfer occurs when an excited molecule (sometimes called a sensitizer or donor), is deactivated as a result of the transfer of the excitation energy to another molecule (a quencher or acceptor). The acceptor molecule is promoted to a higher energy state while the donor molecule to a lower energy state as a result of energy balance. [128 - 130] Electron transfer occurs when a photo-excited molecule undergoes electron transfer with a quencher molecule. Electron transfer can be forward (where the high energy excited electron is

transferred to the quencher) or reverse (where an electron is transferred from the quencher to the hole vacated by the excited electron). The Jablonski diagram below [131] represents the characterization of excited state molecules and the relaxation processes [128, 131] as shown in **Table 1.4** and **Figure 1.18.**

Table 1.4. Photochemical and photophysical process of an excited state molecule.

Relaxation Process	Method of relaxation
Vibrational	Vibrationally excited state and electronic state (Molecular collision).
Internal conversion (IC)	Radiationless transitions between vibronic states between same multiplicities, (Isoenergetic process).
Intersystem crossing (ISC)	Radiationless transitions, spin forbidden between different multiplicities, (Isoenergetic process).
Fluorescence	Radiative transitions, spin allowed between same multiplicities, excited singlet state (Photon emission). $S_1 (v = 0) \rightarrow S_0 + h\nu$
Phosphorescence	Radiative transitions spin forbidden between same multiplicities, excited triplet state (Photon emission). $T_1 (v = 0) \rightarrow S_0 + h\nu$

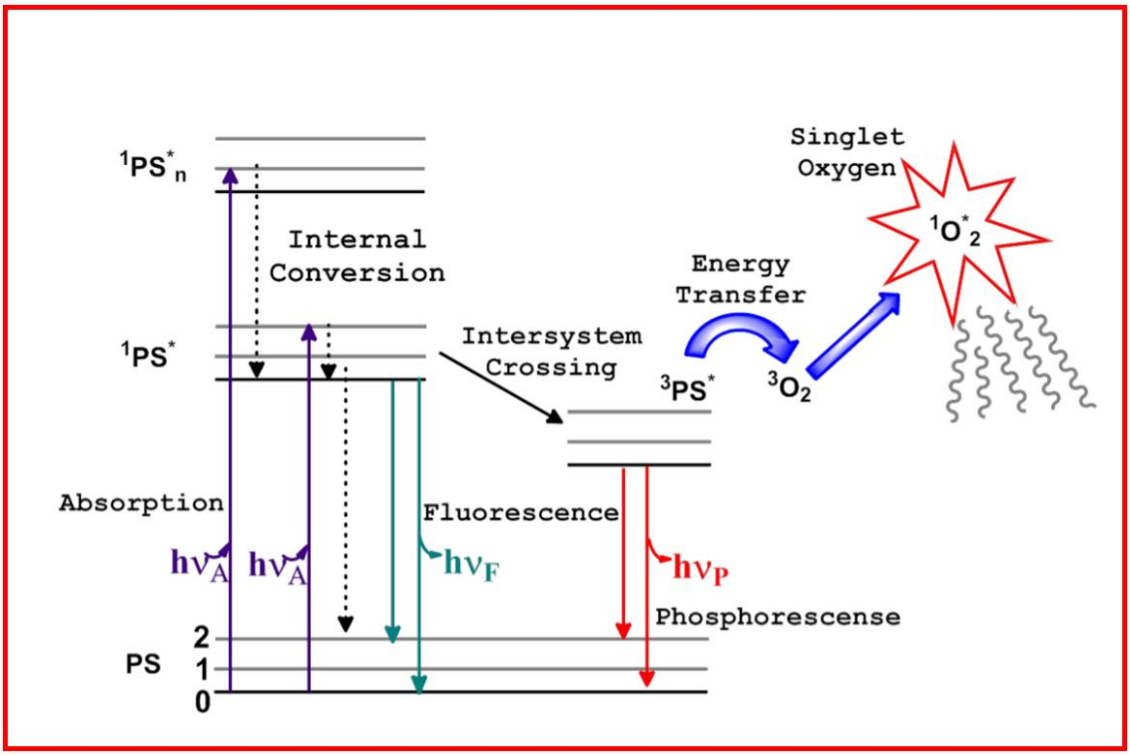

Figure 1.18. Modified Jablonski diagram of a photochemical and photophysical process. *"Open-Access Article"*. [131]

References

1. Balzani, V., Moggi, L., Manfrin, M. F., Bolletta, F., & Gleria, M. (**1975**). Solar Energy Conversion by Water Photodissociation: Transition metal complexes can provide low-energy cyclic systems for catalytic photodissociation of water. *Science*, *189*(4206), 852–856.

2. Balzani, V., Credi, A., & Venturi, M. (**2008**). Photochemical Conversion of Solar Energy. *ChemSusChem*, *1*(1-2), 26–58.

3. Armaroli, N., & Balzani, V. (**2007**). The Future of Energy Supply: Challenges and Opportunities. *Angewandte Chemie International Edition*, *46*(1-2), 52–66.

4. Service, R. F. (**2005**). Solar Energy: Is It Time to Shoot for the Sun? *Science*, *309*(5734), 548–551.

5. Meyer, T. J. (**1989**). Chemical approaches to artificial photosynthesis. *Accounts of Chemical Research*, *22*(5), 163–170.

6. Bard, A. J., & Fox, M. A. (**1995**). Artificial Photosynthesis: Solar Splitting of Water to Hydrogen and Oxygen. *Accounts of Chemical Research*, *28*(3), 141–145.

7. Eisenberg, R., & Nocera, D. G. (**2005**). Preface: Overview of the Forum on Solar and Renewable Energy. *Inorganic Chemistry*, *44*(20), 6799–6801.

8. Keeney, D. (**2009**). Ethanol USA. *Environmental Science & Technology*, *43*(1), 8–11.

9. Lewis, N. S., & Nocera, D. G. (**2006**). Powering the planet: Chemical challenges in solar energy utilization. *Proceedings of the National Academy of Sciences*, *103*(43), 15729–15735.

10. Braun, A. v.; Tcherniac, J. (**1907**). About the products of the action of acetanhydride on phthalamide. *Ber. dtsch. Chem. Ges*, *40*, 2709-2714.

11. Linstead, R. (**1934).** 212. Phthalocyanines. Part I. A new type of synthetic coloring matters. *J. Chem. Soc (Resumed).* 1016-1017.

12. Robertson, J. M. 136. (**1935).** An X-ray study of the structure of the phthalocyanines. Part I. The metal-free, nickel, copper, and platinum compounds. *J. Chem. Soc (Resumed).* 615-621.

13. Oksengendler, I.; Kondratenko, N.; Lukyanets, E.; Yagupolskii, L. (**1977)**. Trifluoro-methyl Substituted Phthalocyanines. *Zh Org Khim*. 13, 1554-1558.

14. Kobayashi, N.; Sasaki, N.; Higashi, Y.; Osa, T. (**1995).** Regiospecific and nonlinear substituent effects on the electronic and fluorescence spectra of phthalocyanines. *Inorg. Chem*. 34, 1636-1637.

15. Duro, J. A.; de la Torre, G.; Torres, T. (**1995).** Synthesis and different aggregation properties in solution of alkyl-and dialkyl amide surrounded phthalocyanines. *Tetrahedron Lett*, 36, 8079-8082.

16. Berezin, B. D.; Berezin, B. D. *Coordination compounds of porphyrins and phthalocyanine;* Wiley New York: **1981**.

17. Rodriguez-Morgade, M. S.; De La Torre, G.; Torres, T. (***2003).*** Design and Synthesis of 99 Low-Symmetry Phthalocyanines and Related Systems. *The porphyrin handbook*, 11, 125.

18. Jiang, X.; Yeung, S.; Lo, P.; Fong, W.; Ng, D. K. (**2010).** Phthalocyanine-polyamine conjugates as highly efficient photosensitizers for photodynamic therapy. *J. Med. Chem.* 54, 320-330.

19. Arishima, K.; Hiratsuka, H.; Tate, A.; Okada, T. (**1982).**Electrophotographic photoreceptor with high sensitivity in the near-infrared region. *Appl. Phys. Lett.* 40, 279-281.

20. Loas, A.; Gerdes, R.; Zhang, Y.; Gorun, S. M. (**2011)**.Broadening the reactivity spectrum of a phthalocyanine catalyst while suppressing its nucleophilic, electrophilic and radical degradation pathways. *Dalton Trans.* 40, 5162-5165.

21. Dolbier, W. R. (**2005).** Fluorine chemistry at the millennium. *J. Fluorine Chem. 126*, 157-163.

22. Chen, Y.; Hanack, M.; Blau, W. J.; Dini, D.; Liu, Y.; Lin, Y.; Bai, J. (**2006)**. Soluble axially substituted phthalocyanines: synthesis and nonlinear optical response. *J. Mater. Sci*., 41, 2169-2185.

23. Porphyrin Handbook: Applications of Phthalocyanines (**2003**), 179.

24. Birchall, J.; Haszeldine, R.; Morley, J. (**1970**). Polyfluoroarenes. Part XIV. Synthesis of halogenophthalocyanines. *J. Chem. Soc*. C. 2667-2672.

25. Umemoto, (**1996).** T. Electrophilic perfluoroalkylating agents. *Chem. Rev., 96*, 1757-1778.

26. d'Alessandro, N.; Tonucci, L.; Morvillo, A.; Dragani, L.; Di Deo, M.; Bressan, M. (**2005**). Thermal stability and photostability of water solutions of sulfophthalocyanines of Ru (II), Cu (II), Ni (II), Fe (III) and Co (II). J. Organomet. Chem. 690, 2133-2141.

27. Gorun, S. M.; Bench, B. A.; Carpenter, G.; Beggs, M. W.; Mague, J. T.; Ensley, H. E. (**1998**). Synthesis and structural characterization of non-planar perfluoro phthalonitriles. J. *Fluorine Chem*. 91, 37-40.

28. Bench, B. A.; Beveridge, A.; Sharman, W. M.; Diebold, G. J.; van Lier, J. E.; Gorun, S. M. (**2002**). Introduction of bulky perfluoroalkyl groups at the periphery of zinc perfluorophthalocyanine: chemical, structural, electronic, and preliminary photophysical and biological effects. *Angew. Chem. Int. Ed*, 41, 747-750.

29. Schwarzer, A.; Weber, E. (**2008**). Influence of fluorine substitution on the crystal packing of Nphenylmaleimides and corresponding phthalimides. *Cryst. Growth Des*. 8, 2862-2874.

30. Davis, E. A., & Mott, N. F. (**1970**). Conduction in non-crystalline systems V. Conductivity, optical absorption and photoconductivity in amorphous semiconductors. *Philosophical Magazine*, *22*(179), 0903–0922.

31. Li, Q., Kako, T., & Ye, J. (**2010**). WO3 modified titanate network film: highly efficient photo-mineralization of 2-propanol under visible light irradiation. *Chemical Communications*, *46*(29), 5352.

32. Forouhi, A. R., & Bloomer, I. (**1988**). Optical properties of crystalline semiconductors and dielectrics. *Physical Review B*, *38*(3), 1865–1874.

33. Mills, A., & Le Hunte, S. (**1997**). An overview of semiconductor photocatalysis. *Journal of Photochemistry and Photobiology A: Chemistry*, *108*(1), 1–35.

34. Vurgaftman, I., Meyer, J. R., & Ram-Mohan, L. R. (**2001**). Band parameters for III–V compound semiconductors and their alloys. *Journal of Applied Physics*, *89*(11), 5815–5875.

35. Smith, A. M., & Nie, S. (**2010**). Semiconductor Nanocrystals: Structure, Properties, and Band Gap Engineering. *Accounts of Chemical Research*, *43*(2), 190–200.

36. Robertson, J. (**2000**). Band offsets of wide-band-gap oxides and implications for future electronic devices. *Journal of Vacuum Science & Technology B: Microelectronics and Nanometer Structures*, *18*(3), 1785.

37. Zhang, S., Yan, Z., Li, Y., Chen, Z., & Zeng, H. (**2015**). Atomically Thin Arsenene and Antimonene: Semimetal-Semiconductor and Indirect-Direct Band-Gap Transitions. *Angewandte Chemie International Edition*, *54*(10), 3112–3115.

38. Rodriguez, M., Sarria, V., Esplugas, S., & Pulgarin, C. (2002). Photo-Fenton treatment of a biorecalcitrant wastewater generated in textile activities: biodegradability of the photo-treated solution. *Journal of Photochemistry and Photobiology A: Chemistry*, *151* (1-3), 129–135.

39. Li, Q., Kako, T., & Ye, J. (**2010**). WO_3 modified titanate network film: highly efficient photo-mineralization of 2-propanol under visible light irradiation. *Chemical Communications*, *46* (29), 5352.

40. The influence of transition metal doping on the physical and photocatalytic properties of titania. (**1999**). Journal *of Photochemistry and Photobiology A: Chemistry*, *121*(1), 49–53.

41. Chen, X., & Burda, C. (**2004**). Photoelectron Spectroscopic Investigation of Nitrogen-Doped Titania Nanoparticles. *The Journal of Physical Chemistry B*, *108*(40), 15446–15449.

42. Xu, J., Lu, M., Guo, X., & Li, H. (**2005**). Zinc ions surface-doped titanium dioxide nanotubes and its photocatalysis activity for degradation of methyl orange in water. *Journal of Molecular Catalysis A: Chemical*, *226*(1), 123–127.

43. Scanlon, D. O., Dunnill, C. W., Buckeridge, J., Shevlin, S. A., Logsdail, A. J., Woodley, S. M., . . . Sokol, A. A. (**2013**). Band alignment of rutile and anatase TiO_2. *Nature Materials*, *12*(9), 798–801.

44. Khan, A. U., & Kasha, M. (**1963**). Red Chemiluminescence of Molecular Oxygen in Aqueous Solution. *The Journal of Chemical Physics*, *39*(8), 2105–2106.

45. Wasserman, H.H., Murray, R.W, (Eds.), Singlet Oxygen, vol. 40, *Academic Press*, New York, (**1979)**.

46. Ranby, B., Rabek, J.F, (Eds.), Singlet Oxygen: Reactions with Organic Compounds and Polymers, *John Wiley and Sons*, New York, (**1978**).

47. (a) Herzberg, G, Molecular Spectra and Molecular Structure I: Spectra of Diatomic Molecules, 2nd ed., *VonNostrand*, New York, (**1950**).
(b) Wasserman, H. H.; DeSimone, R. W.; Chia, K. R.; Banwell, M. G. (**2001**). Singlet oxygen; In Encyclopedia of Reagents for Organic Synthesis; Charette, A., Ed.*; John Wiley & Sons, Ltd*: Chichester, U.K., 1−11.

48. Merkel, P. B., Nilsson, R., & Kearns, D. R. (**1972**). Deuterium effects on singlet oxygen lifetimes in solutions. New test of singlet oxygen reactions. *Journal of the American Chemical Society*, *94*(3), 1030–1031.

49. Bellus, D, Quenchers of Singlet Oxygen in Singlet Oxygen: Reactions with Organic Compounds and Polymers, *John Wiley and Sons*, New York, (**1978**).

50. Clennan, E.L, (**2000**). New Mechanistic and Synthetic Aspects of Singlet Oxygen Chemistry. *Tetrahedron* 56 9151-9179.

51. Bonnett, R., (**1995**). Photosensitizers of the porphyrin and phthalocyanine series for photodynamic therapy, *Chem. Soc. Rev.*, 24, 19-34.

52. Bush, B. G., Del Rio, F. W., Jaye, C., Fischer, D. A., & Cook, R. F. (**2013**). Interfacial Mechanical Properties of *n*-Alkylsilane Monolayers on Silicon Substrates. *Journal of Microelectromechanical Systems*, *22*(1), 34–43.

53. Awasthi, A. P., Grady, M. E., Kim, I. H., Sottos, N. R., & Geubelle, P. H. (**2016**). Nanoscale mechanical tailoring of interfaces using self-assembled monolayers. *Mechanics of Materials*, *98*, 71–80.

54. Bush, B. G., DelRio, F. W., Opatkiewicz, J., Maboudian, R., & Carraro, C. (**2007**). Effect of Formation Temperature and Roughness on Surface Potential of Octadecyltrichlorosilane Self-Assembled Monolayer on Silicon Surfaces. *The Journal of Physical Chemistry A*, *111*(49), 12339–12343.

55. Gilman, J. (**1999**). Flammability and thermal stability studies of polymer layered-silicate (clay) nanocomposites. *Applied Clay Science*, *15*(1-2), 31–49.

56. Zhao, W., Qian, D., Zhang, S., Li, S., Inganäs, O., Gao, F., & Hou, J. (**2016**). Fullerene-Free Polymer Solar Cells with over 11% Efficiency and Excellent Thermal Stability. *Advanced Materials*, *28*(23), 4734–4739.

57. Leszczyńska, A., Njuguna, J., Pielichowski, K., & Banerjee, J. (**2007**). Polymer/ montmorillonite nanocomposites with improved thermal properties. *Thermochimica Acta*, *453*(2), 75–96.

58. Zhu, J., Uhl, F. M., Morgan, A. B., & Wilkie, C. A. (**2001**). Studies on the Mechanism by Which the Formation of Nanocomposites Enhances Thermal Stability†. *Chemistry of Materials*, *13*(12), 4649–4654.

59. Du, M., Guo, B., & Jia, D. (**2006**). Thermal stability and flame retardant effects of halloysite nanotubes on poly(propylene). *European Polymer Journal*, *42*(6), 1362–1369.

60. De Gennes, P. G. (**1985**). Wetting: statics and dynamics. *Reviews of Modern Physics*, *57*(3), 827–863.

61. Sigal, G. B., Mrksich, M., & Whitesides, G. M. (**1998**). Effect of Surface Wettability on the Adsorption of Proteins and Detergents. *Journal of the American Chemical Society*, *120*(14), 3464–3473.

62. Wang, R., Sakai, N., Fujishima, A., Watanabe, T., & Hashimoto, K. (**1999**). Studies of Surface Wettability Conversion on TiO_2 Single-Crystal Surfaces. *The Journal of Physical Chemistry B*, *103*(12), 2188–2194.

63. Fang, T., Chang, W., Lin, S., & Fang, C. (**2010**). Interface dynamics and mechanisms of nanoindented alkanethiol self-assembled monolayers using molecular simulations. *Journal of Colloid and Interface Science*, *345*(1), 19–26.

64. Allen, G., Gee, G., Mangaraj, D., Sims, D., & Wilson, G. J. (1960). Intermolecular forces and chain flexibilities in polymers: II. Internal pressures of polymers. *Polymer*, *1*, 467–476.

65. Grady, M. E., Geubelle, P. H., Braun, P. V., & Sottos, N. R. (**2014**). Molecular Tailoring of Interfacial Failure. *Langmuir*, *30*(37), 11096–11102.

66. David, M. O., Reiter, G., Sitthaï, T., & Schultz, J. (**1998**). Deformation of a Glassy Polymer Film by Long-Range Intermolecular Forces. *Langmuir*, *14*(20), 5667–5672.

67. Granick, S., Patel, S., & Tirrell, M. (**1986**). Direct measurement of intermolecular forces between a polymer layer and mica. *The Journal of Chemical Physics*, *85*(9), 5370–5371.

68. Hutzinger, O, (**1980)**. *The Handbook of Environmental Chemistry*. Springer, Berlin.

69. Zhu, D., Handschuh-Wang, S., & Zhou, X. (**2017**). Recent progress in fabrication and application of polydimethylsiloxane sponges. *Journal of Materials Chemistry A*, *5*(32), 16467–16497.

70. Clark, D. T., Peeling, J., & O'Malley, J. M. (**1976**). Application of ESCA to polymer chemistry. VIII. Surface structures of AB block copolymers of polydimethylsiloxane and polystyrene. *Journal of Polymer Science: Polymer Chemistry Edition*, *14*(3), 543–551.

71. Hongbin, Y., Guangya, Z., Siong, C. F., Shouhua, W., & Feiwen, L. (**2009**). Novel polydimethylsiloxane (PDMS) based microchannel fabrication method for lab-on-a-chip application. *Sensors and Actuators B: Chemical*, *137*(2), 754–761.

72. Polmanteer, K. E., & Hunter, M. J. (**1959**). Polymer composition versus low-temperature characteristics of polysiloxane elastomers. *Journal of Applied Polymer Science*, *1*(1), 3–10.

73. Paria, S., & Khilar, K. C. (**2004**). A review on experimental studies of surfactant adsorption at the hydrophilic solid–water interface. *Advances in Colloid and Interface Science*, *110*(3), 75–95.

74. Bico, J., Thiele, U., & Quéré, D. (**2002**). Wetting of textured surfaces. *Colloids and Surfaces A: Physicochemical and Engineering Aspects*, *206*(1-3), 41–46.

75. He, B., Patankar, N. A., & Lee, J. (**2003**). Multiple Equilibrium Droplet Shapes and Design Criterion for Rough Hydrophobic Surfaces. *Langmuir*, *19*(12), 4999–5003.

76. Marmur, A. (**2003**). Wetting on Hydrophobic Rough Surfaces: To Be Heterogeneous or Not To Be? *Langmuir*, *19*(20), 8343–8348.

77. Wang, S., Song, Y., & Jiang, L. (**2007**). Photoresponsive surfaces with controllable wettability. *Journal of Photochemistry and Photobiology C: Photochemistry Reviews*, *8*(1), 18–29.

78. Tian, Y., & Jiang, L. (**2013**). Intrinsically robust hydrophobicity. *Nature Materials*, *12*(4), 291–292.

79. Kilpadi, D. V., & Lemons, J. E. (**1994**). Surface energy characterization of unalloyed titanium implants. *Journal of Biomedical Materials Research*, *28*(12), 1419–1425.

80. Lovejoy, E. R., Bro, M. I., & Bowers, G. H. (**1965**). Chemistry of radiation crosslinking of branched fluorocarbon resins. *Journal of Applied Polymer Science*, *9*(2), 401–410.

81. Sørensen, P. A., Kiil, S., Dam-Johansen, K., & Weinell, C. E. (**2009**). Anticorrosive coatings: a review. *Journal of Coatings Technology and Research*, *6*(2), 135–176.

82. Ji, W. G., Hu, J. M., Liu, L., Zhang, J. Q., Cao, C. N. (**2007**). Improving the Corrosion Performance of Epoxy Coatings by Chemical Modification with Silane Monomers. *Surf. Coat. Technol.*, 201 (8) 4789–4795.

83. Shon, M., Kwon, H. (**2009**). Comparison of Surface Modification with Amino Terminated Polydimethylsiloxane and Amino Branched Polydimethylsiloxane on the Corrosion Protection of Epoxy Coating. *Corros. Sci*., 51 (3) 650–657.

84. Dı´az, I., Chico, B., De La Fuente, D., Simancas, J., Vega, J., Morcillo, M. (**2010**) Corrosion Resistance of New Epoxy–Siloxane Hybrid Coatings. A Laboratory Study. *Prog. Org. Coat*., 69 (3) 278–286.

85. Canak, T. C., Serhatlı, I. E. (**2013**). Synthesis of Fluorinated Urethane Acrylate Based UV-Curable Coatings.'' *Prog. Org. Coat*., 76 (2) 388–399.

86. Wankhede, RG., Morey, S., Khanna, A., Birbilis, N. (**2013**). Development of Water-Repellent Organic-Inorganic Hybrid Sol-Gel Coatings on Aluminum Using Short Chain Perfluoro Polymer Emulsion. *Appl. Surf. Sci*., 283 1051–1059.

87. Guo, Z., Liu, W, Su, B. L. (**2011**) Superhydrophobic Surfaces: from Natural to Biomimetic to Functional. *J. Colloid. Interf. Sci*., 353 (2) 335–355.

88. Xu, X, Zhang, Z, Guo, F, Yang, J, Zhu, X. (**2011**) Fabrication of Superhydrophobic Binary Nanoparticles/PMMA Composite Coating with Reversible Switching of Adhesion and Anticorrosive Property. *Appl. Surf. Sci.,* 257 (16) 7054– 7060.

89. Momen, G., Farzaneh, M. (**2014**). Facile Approach in the Development of Icephobic Hierarchically Textured Coatings as Corrosion Barrier. *Appl. Surf. Sci.,* 299 41–46.

90. Tuteja, A., Choi, W., Mabry, J. M., McKinley, G.H., Cohen, R. E. (**2008**). Robust Omniphobic Surfaces. P. *Natl. Acad. Sci.* USA, 105 (47) 18200–18205.

91. Miyamura, Y., Park, C., Kinbara, K., Leibfarth, F.A., Hawker, C.J., Aida, T., (**2011**). Controlling volume shrinkage in soft lithography through heat-induced cross-linking of patterned nanofibers. *J. Am. Chem. Soc*. 133, 2840.

92. Rosa, L., Sun, K., Mizeikis, V., Bauerdick, S., Peto, L., Juodkazis, S., April (**2011**). 3D-tailored gold nanoparticles for light field enhancement and harvesting over visible-IR spectral range. *J. Chem. Phys. C*. 115, 5251–5256.

93. Ming, B., Li, J., Kang, F., Pang, G., Zhang, Y., Chen, L., Xu, J., Wang, X., (**2012**). Microwave–hydrothermal synthesis of birnessite-type MnO_2 nanospheres as super capacitor electrode materials. *J. Power Sources*. 198, 428.

94. Tseng, A., Kuan Chen, Chen, C., & Ma, K. (**2003**). Electron beam lithography in nanoscale fabrication: recent development. *IEEE Transactions on Electronics Packaging Manufacturing*, *26*(2), 141–149.

95. Guo, Z., Liu, W., Su, B. L., (**2011**). Superhydrophobic surfaces: from natural to biomimetic to functional. *J. Colloid Interface Sci*. 353, 335.

96. Gupta, N., Kavya, M.V., Singh, Y.R.G., Jyothi, J., Barshilia, H.C., (**2013**). Superhydrophobicity on transparent fluorinated ethylene propylene films with nano-protrusion morphology by Ar plasma etching: study of the degradation in hydrophobicity after exposure to the environment. *J. Appl. Phys*. 114, 164307.

97. Palumbo, F., Muo, R.D., Cappelluti, D., d'Agostino, R., (**2011**). Superhydrophobic and superhydrophilic polycarbonate by tailoring chemistry and nano-texture with plasma processing. *Plasma Processes Polymer*. 8, 118.

98. Sun, Q.F., Lu, Y., Li, J., Cao, J., (**2014**). Self-assembly of a superhydrophobic ZnO nanorod arrays film on wood surface using a hydrothermal method. *Key Eng. Mater.* 609, 468.

99. Choi, Y.C., Shin, Y.M., Lee, Y.H., Lee, B.S., Park, G.-S., Choi, W.B., Lee, N.S., Kim, J.M., (**2000**). Controlling the diameter, growth rate, and density of vertically aligned carbon nanotubes synthesized by microwave plasma-enhanced chemical vapor deposition. *Appl. Phys. Lett*. 76, 2367.

100. Li, Y., Wang, X., Sun, J., (**2012**). Layer-by-layer assembly for rapid fabrication of thick polymeric films. *Chem. Soc. Rev*. 41, 5998.

101. Xiang, H., Zhang, L., Wang, Z., Yu, X., Long, Y., Zhang, X., Zhao, N., Xu, J., (**2011**). Multifunctional polymethylsilsesquioxane (PMSQ) surfaces prepared by electrospinning at

the sol-gel transition: superhydrophobicity, excellent solvent resistance, thermal stability and enhanced sound absorption property. *J. Colloid Interface. Sci*. 359, 296.

102. Bhushan, B., & Jung, Y. C. (**2011**). Natural and biomimetic artificial surfaces for superhydrophobicity, self-cleaning, low adhesion, and drag reduction. *Progress in Materials Science*, *56*(1), 1–108.

103. Nosonovsky, M., & Bhushan, B. (**2009**). Superhydrophobic surfaces and emerging applications: Non-adhesion, energy, green engineering. *Current Opinion in Colloid & Interface Science*, *14*(4), 270–280.

104. R.N. Wenzel. (**1936**). Resistance of solid surfaces to wetting by water *Industrial and Engineering Chemistry*, 28, 988.

105. Ramiasa, M., Ralston, J., Fetzer, R., & Sedev, R. (**2014**). The influence of topography on dynamic wetting. *Advances in Colloid and Interface Science*, 206, 275–293.

106Hejazi, V., Moghadam, A. D., Rohatgi, P., & Nosonovsky, M. (**2014**). Beyond Wenzel and Cassie–Baxter: Second-Order Effects on the Wetting of Rough Surfaces. *Langmuir*, *30*(31), 9423–9429.

107. Bormashenko, E. (**2015**). Progress in understanding wetting transitions on rough surfaces. *Advances in Colloid and Interface Science*, *222*, 92–103.

108. A.B.D. Cassie and S. Baxter, (**1944)**. Wettability of porous surfaces. *Transactions of the Faraday Society*. 40, 546.

109. Bico, J., Thiele, U., & Quéré, D. (**2002**). Wetting of textured surfaces. *Colloids and Surfaces A: Physicochemical and Engineering Aspects*, *206*(1-3), 41–46.

110Callies, M., & Quéré, D. (**2005**). On water repellency. *Soft Matter*, *1*(1), 55.

111Papadopoulos, P., Mammen, L., Deng, X., Vollmer, D., & Butt, H. (**2013**). How superhydrophobicity breaks down. *Proceedings of the National Academy of Sciences*, *110*(9), 3254–3258.

112. Barthlott, W., & Neinhuis, C. (**1997**). Purity of the sacred lotus, or escape from contamination in biological surfaces. *Planta*, *202*(1), 1–8.

113. NEINHUIS, C. (**1997**). Characterization and Distribution of Water-repellent, Self-cleaning Plant Surfaces. *Annals of Botany*, *79*(6), 667–677.

114. Onda, T., Shibuichi, S., Satoh, N., & Tsujii, K. (**1996**). Super-Water-Repellent Fractal Surfaces. *Langmuir*, *12*(9), 2125–2127.

115. Chen, W., Fadeev, A. Y., Hsieh, M. C., Öner, D., Youngblood, J., & McCarthy, T. J. (**1999**). Ultrahydrophobic and Ultralyophobic Surfaces: Some Comments and Examples. *Langmuir*, *15*(10), 3395–3399.

116. Yu, S., Guo, Z., & Liu, W. (**2015**). Biomimetic transparent and superhydrophobic coatings: from nature and beyond nature. *Chemical Communications*, *51*(10), 1775–1794.

117. Wang, G., Guo, Z., & Liu, W. (**2014**). Interfacial effects of superhydrophobic plant surfaces: A review. *Journal of Bionic Engineering*, *11*(3), 325–345.

118. Celia, E., Darmanin, T., Taffin de Givenchy, E., Amigoni, S., & Guittard, F. (**2013**). Recent advances in designing superhydrophobic surfaces. *Journal of Colloid and Interface Science*, *402*, 1–18.

119. Wang, S., Liu, K., Yao, X., & Jiang, L. (**2015**). Bioinspired Surfaces with Superwettability: New Insight on Theory, Design, and Applications. *Chemical Reviews*, *115*(16), 8230–8293.

120. Luis, J. M., Bishop, D. M., & Kirtman, B. (**2004**). A different approach for calculating Franck–Condon factors including anharmonicity. *The Journal of Chemical Physics*, *120*(2), 813–822.

121. Atkins, Peter and Julio de Paula. Physical Chemistry for the Life Sciences. (**2006)**. New York, NY: *W.H. Freeman and Company*. p. 563-564.

122. Dallinger, R. F., Woodruff, W. H., & Rodgers, M. A. J. (**1981**). The Lifetime of the excited singlet state of β-carotene: consequences to photosynthetic light harvesting. *Photochemistry and Photobiology*, *33*(2), 275–277.

123. Spears, K. G., & Rice, S. A. (**1971**). Study of the Lifetimes of Individual Vibronic States of the Isolated Benzene Molecule. *The Journal of Chemical Physics*, *55*(12), 5561–5581.

124. Zhang, C., Du, M., Cheng, H., Zhang, X., Roitberg, A. E., & Krause, J. L. (**2004**). Coherent Electron Transport through an Azo benzene Molecule: A Light-Driven Molecular Switch. *Physical Review Letters*, *92*(15).

125. Woolley, R., & Sutcliffe, B. (**1977**). Molecular structure and the born—Oppenheimer approximation. *Chemical Physics Letters*, *45*(2), 393–398.

126. Fölling, J., Bossi, M., Bock, H., Medda, R., Wurm, C. A., Hein, B., Hell, S. W. (**2008**). Fluorescence nanoscopy by ground-state depletion and single-molecule return. *Nature Methods*, *5*(11), 943–945.

127. Valeur, B. (**2009**). Molecular Fluorescence. *Digital Encyclopedia of Applied Physics*, 477–531.

128. Raymo, F. M., & Tomasulo, M. (**2005**). Electron and energy transfer modulation with photochromic switches. *Chemical Society Reviews*, *34*(4), 327.

129. Ward, M. D. (**1997**). Photo-induced electron and energy transfer in non-covalently bonded supramolecular assemblies. *Chemical Society Reviews*, *26*(5), 365.

130. Song, L., Varma, C., Verhoeven, J., & Tanke, H. (**1996**). Influence of the triplet excited state on the photobleaching kinetics of fluorescein in microscopy. *Biophysical Journal*, *70*(6), 2959–2968.

131. James, N. S., Ohulchanskyy, T. Y., Chen, Y., Joshi, P., Zheng, X., Goswami, L. N., & Pandey, R. K. (**2013**). Comparative Tumor Imaging and PDT Efficacy of HPPH

Conjugated in the Mono- and Di-Forms to Various Polymethine Cyanine Dyes: Part - 2. *Theranostics*, *3*(9), 703–718.

Chapter 2

Engineering of Self-Cleaning Superhydrophobic and Photoreactive Coated Surfaces for Environmental Remediation.

2.1. Introduction.

Superhydrophobic and self-cleaning surfaces have received recognition from the moment they were first proven useful in applications. [1 - 3] Surface morphology plays an important role in the properties of material interfaces and the characteristics of surfaces. These characteristics are mainly controlled by surface energy and surface morphology. [4, 5] Tailoring surface morphology with low surface energy polymer materials to achieve nano-hierarchical and micro-hierarchical topography will provide the capacity to trap "air pockets" between the surface and a water droplet on the surface. [6 - 8] A variety of methods for manipulation of polymer surface morphologies have been studied for the purpose of producing superhydrophobicity. Augmentation of hierarchical topography using a volatile salt has been applied to polymer coatings for the purpose of enhancing surface roughness, according to a study by Peng *et al*. [9]

Thermoplastics and thermosets are two separate types of polymers, the properties of these polymers are based on their thermal behavior. Thermosets typically have chemical cross-links, allowing them to be molded into shape only once – after being "set" they cannot be melted again. Thermoplastic polymers can be melted and molded into shape, then melted and molded into a new shape; in theory through an infinite number of cycles. One example is polyvinylidene fluoride (PVDF), a promising polymer with a wide range of applications. [10] The characteristics of PVDF are of great interest, providing a range of claims regarding applications and uses. [11, 12]. These characteristics have been widely studied in areas of the polymer coating, membrane separation, and ferroelectric materials. [10 - 13] PVDF is superior to many (C-C) backbone polymers such as polyethylene (PE) with all (CH_2) groups, which can be susceptible to thermal degradation at elevated temperature and UV photochemical degradation. [14] polytetrafluoroethylene (PTFE) is another related fluoropolymer with a (C-C) backbone, a stable and durable polymer. Despite its

superior resistance to chemical and physical deterioration as a result of the (CF_2) groups, there are drawbacks to this polymer. One major problem is the difficulty of processing and manipulation, this problem originates from the CF_2 groups which repel other materials. PVDF remedies this issue with alternating CH_2 and CF_2 groups. [7, 14] The (CF_2) groups of the PVDF gives the polymer good hydrophobicity and chemical resistance qualities, while the (CH_2) groups give the polymer better solubility and adhesion to substrates. Between PE and PTFE in its properties, PVDF also has a variety of crystalline phases from arrangements of the alternating CH_2 and CF_2 groups. PVDF properties fall between those of PE and PTFE, with superior characteristics for many applications, not limited to surface coating. [15]

Common preparation methods for PVDF coatings include melt casting and solution casting. Methods such as phase-inversion precipitation have been explored for achieving hydrophobic PVDF surfaces. [16] Predicting the mechanism of this process is complex, the solvent-polymer interaction can be challenging as a result of the interplay of thermodynamic and kinetic processes while making the films. During film formation, the crystallization and surface morphology is influenced by the solvent-polymer interactions during the evaporation precipitation processes. The rate of this process can influence the outcome as well, along with the presence of any additives. [11] The beta-phase of PVDF has proven to be the most useful phase compared to all other phases, this is because of the alternating linear, all (trans. TTTT) conformational arrangement of the phase, compared to the alpha phase with trans-gauche conformation. [16] The position of the beta-phase H and F atoms positioned directly perpendicular to the (C-C) backbone. The alpha phase is more easily prepared and more commonly used in applications, especially thin films and coatings, It has less desirable properties due to the trans-gauche conformation, as shown by Kabir *et al*. [16] Other PVDF phases can approximate the beta-phase through the process of mechanical stretching in

order to achieve (TTTT conformation) with electroactive characteristics. [16] Different phases of PVDF are shown in **Figure 2.1**, below. The electroactive properties of PVDF can be optimized through polarizability as a result of the vibrational motions of the polymer chains, another important property of the polymer, with a high dielectric constant: 2.1 D for β-phase PVDF.

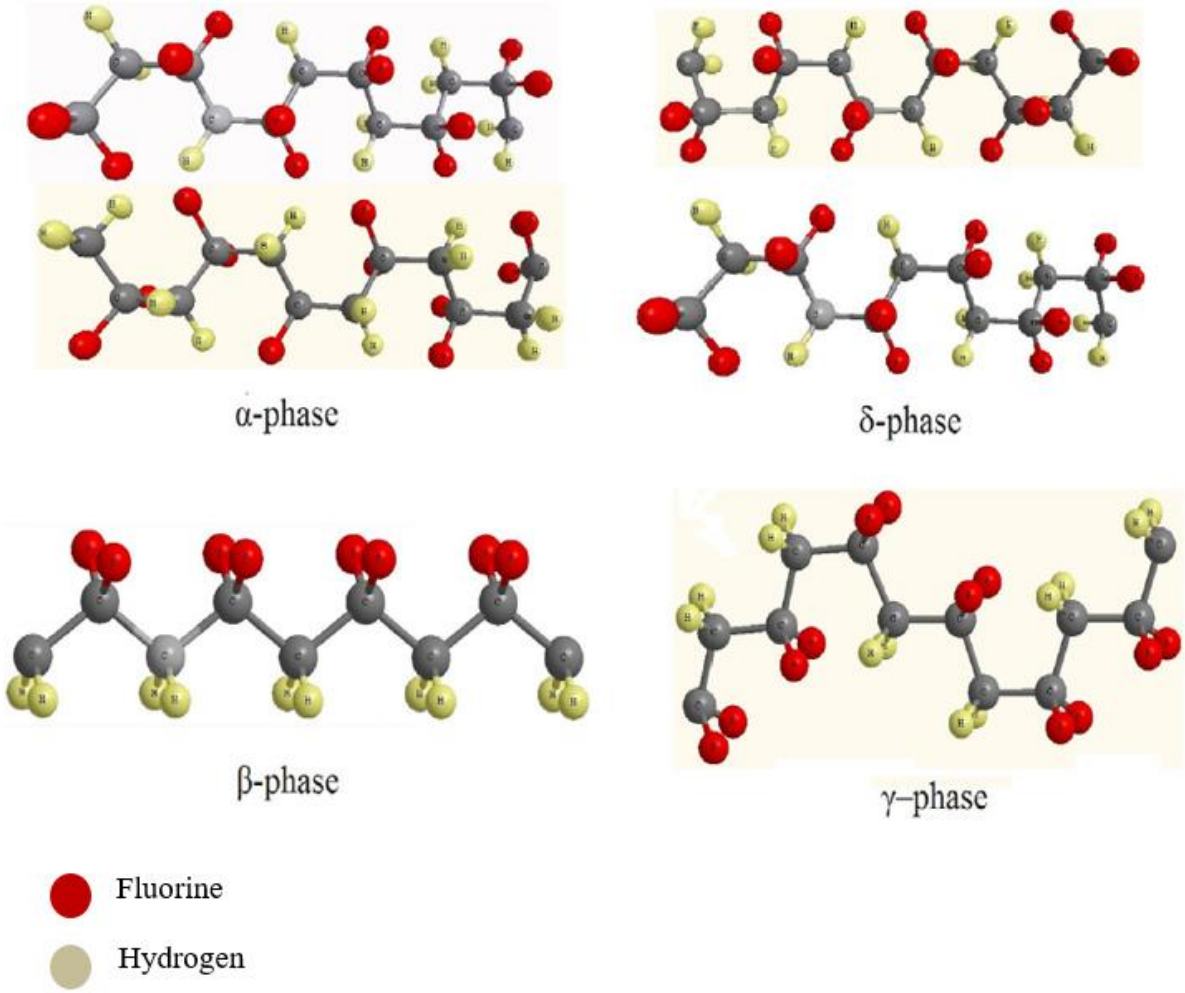

Figure 2.1. PVDF structures with different phases: α, β, δ, and γ. "*Reproduced with permission from IOP Publishing".* [16]

PVDF is naturally hydrophobic, but the films are intrinsically permeable; they are therefore widely used in membrane filtration due to their strong thermal and mechanical stability.[17-19] PVDF coatings that have been made superhydrophobic have received wide attention because of their properties and potential applications. A superhydrophobic PVDF surface was created by Peng *et al*, [9] for use as an anti-icing coating for wind-turbine blades. In the process they developed, ammonium bicarbonate (NH_4HCO_3) salt was added to the PVDF solution before coating. Upon heating, the salt volatilized to carbon dioxide, ammonia, and water vapor gases, generating a roughened PVDF surface. [9] The entire process of preparing the PVDF coatings modified with NH_4HCO_3 can influence the final surface morphology. [9]

Surfaces can be modified to prevent water but not air from penetrating through to the protected substrate, such as steel. [18, 19] Different approaches to surface modification have been reported in literature for surface preparation to achieve superhydrophobic surfaces. [20 - 22] The preparation of these desired surfaces is controlled by the bottom-up approach method for nanostructured and micro-structured surface texture. [9, 23 - 26] The Cassie-Baxter model describes air trapped in between the sessile water drop and the rough surface as a composite surface comprising of the solid-liquid-air interface. [27] This junction, when constructed/designed properly can result in superhydrophobic surfaces; these surfaces contain sufficiently features to prevent liquid water from penetrating. This is explained by equation $\cos \theta_r = f_1 \cos \theta - f_2$, [27 - 29] Where f_1 is the fraction of solid surface in contact with water droplet and f_2 is the fraction of air trapped between the solid surface and water. [27] The combination of both fractions $f_1 + f_2 = 1$, [27] these fractions increase or decrease respectively with the surface morphology, predicting the contact angle.

This observation propelled us to look closely at techniques for the preparation of superhydrophobic surfaces that are photoactive for the achievement of a true self-cleaning surface.

Most surfaces are not self-cleaning, the combination of a photoreactive catalyst with a superhydrophobic surface will prove a significant improvement in the direction of self-cleaning. [30] There are numerous studies, combining inorganic materials with PVDF for photoreactive purposes, such as Al_2O_3, ZrO_2, SiO_2, $CaCO_3$, and TiO_2. Among these compounds, TiO_2 has a proven record of accomplishment as a photosensitizer, [31 - 36] although there are drawbacks. It has limitations as a result of the wide band gap, [32, 34] limiting its ability to fully utilize the visible region of the electronic spectrum. [37] Doping is a process aimed at improving the band gap, but the limitations of doping were studied by Walsh *et al.* [38] A new class of robust fluorinated phthalocyanine photosensitizers have been developed and will be used in this research. These photosensitizers have reactivity in the visible region, [39, 40] and transfer energy to $^3O_2$ to produce reactive singlet oxygen ($^1O_2$) for degradation of organic molecules. [40] The direct and robust approach presented here will contribute to solving the problems of environmental remediation through photoreactive processes.

2.2. Materials and Methods.

2.2.1. General.

All chemicals, solvents and HPLC-grade solvents were obtained commercially and used as received unless stated otherwise. Ammonium hydrogen carbonate (NH_4HCO_3) was treated as described below. Polyvinylidene fluoride (PVDF, Mw = 180,000) was purchased from Sigma-Aldrich. Fumed titanium dioxide (TiO_2) P25 Aeroxide®, surface area (BET) 50 m^2/g) was purchased from Evonik. Deionized H_2O (Milli-Q, resistivity 15 MΩ-cm) was used for all

experiments. Fluorinated phthalocyanine, was prepared from zinc acetate in the presence of perfluoro-(4,5-di-isopropyl) phthalonitrile at about 180 °C microwave method.

2.2.2. Instruments.

Contact angles were measured with a RAMA-HART goniometer using the sessile water drop method, 5μL volume. The reported measurements are averages from five different points on the surface of each film. Uncoated glass slides with contact angle measurement $\theta = 45$ ° were used as a control. Surface morphology of the coated films was analyzed with a Verios 460 Extreme High-Resolution Scanning Electron Microscope (XHR SEM) at the Princeton University, Princeton Institute for the Science and Technology of Materials PRISM. Differential scanning calorimetry (DSC) experiments were performed aerobically with a TA model 2920 instrument. Thermogravimetric analyses (TGA) were performed with a TA model Q500 instrument. Experiments were conducted under a blanket of N_2. A 10 °C/min heating gradient was used for both DSC and TGA unless noted otherwise. PerkinElmer Fourier transform infrared spectrometer (FTIR) fitted with Universal ATR sampling accessory was used to analyze the absorption of the solid sample before and after light irradiation.

2.2.3. Sample Preparation.

The description of the composition of materials uses the union and inclusion symbols "$\cup$" and "$\in$", which mean "deposited on" and "embedded in", respectively.

2.2.4. Preparation of NH_4HCO_3 of controlled particle size.

NH_4HCO_3 particles were ground with a mortar and pestle, the finely ground particles were then sieved sequentially with a set of sieves to separate particles of different sizes as follows 707, 250, 125 and 63 μm. All the experiments were done with 63 μm maximum size as mention below.

2.2.5. Preparation of NH_4HCO_3-doped PVDF films, $NH_4HCO_3 \in$PVDF.

The film was prepared by adding 10 ml of DMF solution to 1.0 gram of PVDF pellets heated at 60 °C, the mixture was stirred mechanically at 600 rpm for 45 minutes, cooled to 25 °C, the compound formed was a sol-gel mixture and then 0.2 g NH_4HCO_3 was added. The sol-gel mixture was stirred for another 30 minutes at the same speed, the viscous mixture was coated onto glass slides, the compound was allowed to equilibrate for 6 hours and then baked in the oven at 80 °C for 48 hours to decompose and volatilize the NH_4HCO_3.

2.2.6. Preparation of $F_{64}PcZn$ coated TiO_2, $F_{64}PcZn \cup TiO_2$.

The photocatalyst was prepared by dissolving 30 mg ($1.45x10^{-5}$ moles) $F_{64}PcZn$ in 10 ml of an ethanol solution, the mixture was stirred and sonicated to form a uniform solution. P25 TiO_2 (0.10 g) was then added to the solution. The mixture was stirred for 45 minutes, then stored in the dark for 24 hours. Next, the solvent was removed *in vacuo* and the resulting greenish solid was baked at 170 °C for 24 hours. The solid was then washed with H_2O and ethanol until the ethanol was colorless. UV-Vis-NIR spectrometry quantification of the $F_{64}PcZn$ yielded the amount of $F_{64}PcZn$ bound to P25. The $F_{64}PcZn \cup TiO_2$ complex was kept in the dark until further use.

2.2.7. Preparation of TiO_2-doped PVDF films, $TiO_2 \in$PVDF.

The coating material was prepared by adding 10 ml of DMF to 1.0 g PVDF pellets, then heating at 60 ^oC with constant stirring for 45 minutes. This formed a gel-like solution. The solution was allowed to cool to room temperature before adding P25 TiO_2 (0.03 g, 3% solids) and stirring 30 minutes at 600 rpm. The resulting mixture was coated on glass slides, the coated surface was allowed to evaporate for 6 hours at room temperature, then baked at 80 °C in an oven for 48 hours.

2.2.8. Preparation of TiO_2 and NH_4HCO_3 doped PVDF films, (NH_4HCO_3&TiO_2) $\in$PVDF.

The coating material was prepared by adding 10 ml of DMF to 1.0 g PVDF pellets, then heating at 60 ^oC with constant stirring for 45 minutes. This formed a gel-like solution. The solution was allowed to cool to room temperature before adding P25 TiO_2 (0.03 g, 3% solids) and stirring 30 minutes at 600 rpm. NH_4HCO_3 (0.2 g) was added to the PVDF solution and the solution stirred for another 30 minutes before coating. The mixture was coated on glass slides, then allowed to evaporate for 6 hours at room temperature, then baked at 80 °C in the oven for 48 hours.

2.2.9. Preparation of F_{64}PcZn-coated TiO_2-doped PVDF films, (F_{64}PcZn$\cup TiO_2$) $\in$PVDF.

The coating material was prepared by adding 10 ml of DMF to 1.0 g PVDF pellets, then heating at 60 °C with constant stirring for 45 minutes. This formed a gel-like solution. The solution was allowed to cool to room temperature before adding $F6_4PcZn \cup TiO_2$ (0.03 g, 3% solids) and stirring 30 minutes at 600 rpm. The mixture was coated on glass slides, was allowed to evaporate for 6 hours at room temperature and then baked at 80 °C in the oven for 48 hours.

2.2.10. Preparation of F_{64}PcZn-coated TiO_2 and NH_4HCO_3-doped PVDF films, (F_{64}PcZn$\cup TiO_2$ &NH_4HCO_3) PVDF.

The coating material was prepared by adding 10 ml of DMF to 1.0 g PVDF pellets, then heating at 60 °C with constant stirring for 45 minutes. This formed a gel-like solution. The solution was allowed to cool to room temperature before adding $F_{64}PcZn \cup TiO_2$, (0.03 g, 3% solids and stirring 30 minutes at 600 rpm. NH_4HCO_3 (0.2 g) was added to the PVDF solution and stirred for another 30 minutes before coating. The mixture was coated on glass slides, was allowed to evaporate for 6 hours at room temperature and then baked at 80 °C in the oven for 48 hours.

2.3. Results - Data Analysis.

2.3.1. NH_4HCO_3 particles sizes characterization.

NH_4HCO_3 particles were characterized to determine the desired size for achieving the research objective of superhydrophobic surfaces. From sequential sieving, less than 63 µm was the smallest particle size obtained, while the largest particle size was 707 µm and greater. The correlation of particle size to contact angle is shown in **Table 2.1**. As the particle size becomes smaller, the observed contact angle of the coated surfaces increases. **Equation 1** shows the decomposition reaction of NH_4HCO_3.

$$NH_4HCO_{3(s)} \rightarrow NH_{3(g)} + H_2O_{(g)} + CO_{2(g)} \quad 1$$

Table 2.1. Contact angle as a function of NH_4HCO_3 particle size.

NH_4HCO_3 particle size (µm)	**Contact Angle θ (°)**
As received (no grinding or sieving)	97
250-707	118
125-250	120
63-125	141
<63	159

2.3.2. Ethanol leaching of $F_{64}PcZn \cup TiO_2$ photocatalyst hybrid.

The hybrid catalyst prepared was greenish in color from the $F_{64}PcZn$ adsorbed on the surface of the TiO_2. Strong van der Waal interactions were formed after the heat treatment of the TiO_2 surface. Treatment for 24 hours at 200 °C removed adsorbed water from TiO_2 to enhance interaction/ adsorption. The brilliant greenish hybrid complex first formed is shown in **Figure 2.2**, after repeated washings a faint greenish colored hybrid complex remained. Vial #1, the first washing with ethanol showed a deep green color from excess $F_{64}PcZn$ washed from TiO_2. After 10 washes, vial #10 was colorless as no additional $F_{64}PcZn$ was removed. UV-Vis-NIR diffuse reflectance spectroscopy, shown in **Figure 2.3**, confirmed $F_{64}PcZn$ was attached to the TiO_2 particles forming a hybrid complex; a peak at 680 nm confirmed the $F_{64}PcZn$ Q-band.

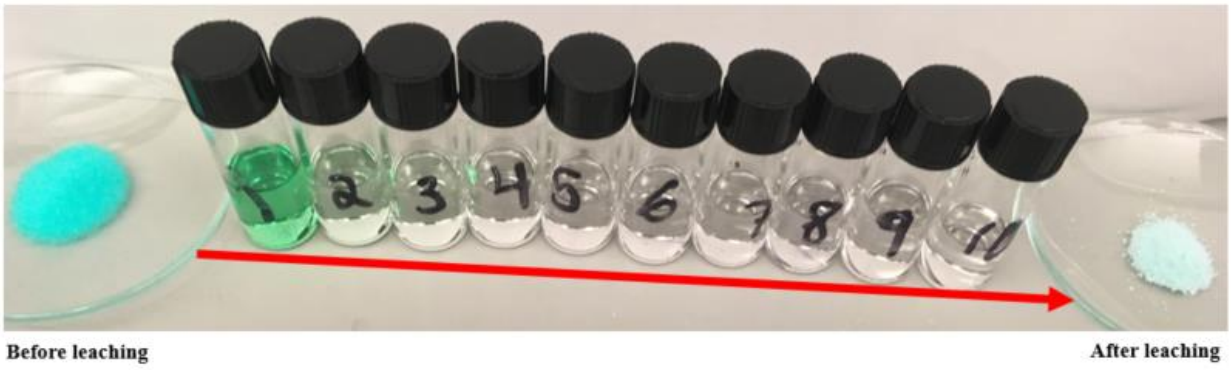

Figure 2.2. Leaching study of the $F_{64}PcZn \cup TiO_2$ hybrid catalyst. *"Image courtesy of Abdul Azeez"*.

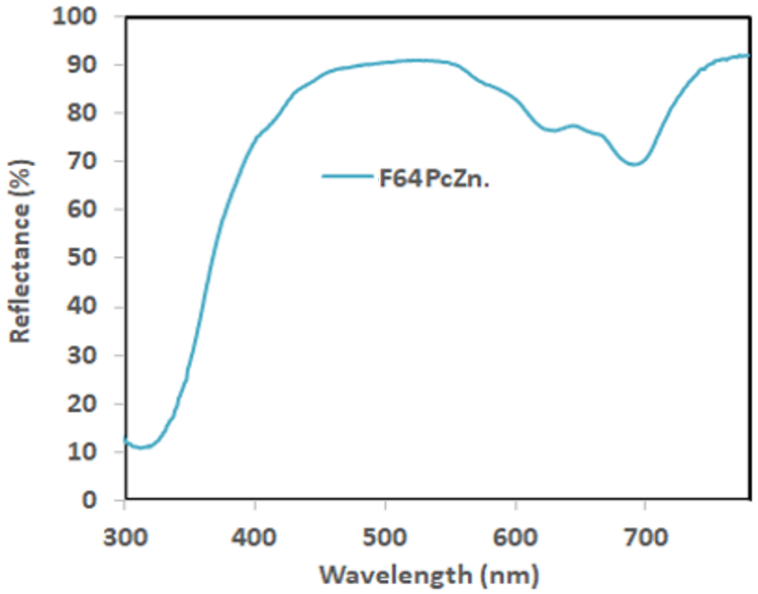

Figure 2.3. UV-Vis-NIR diffuse reflectance spectroscopy of solid $F_{64}PcZn \cup TiO_2$ hybrid catalyst complex.

2.3.3. Engineering surfaces.

Six types of coated surfaces are shown schematically in **Figure 2.4**: plain PVDF **1**), NH_4HCO_3&PVDF **2**), $TiO_2 \in$PVDF **3**), TiO_2&$NH_4HCO_3 \in$PVDF **4**), $F_{64}PcZn \cup TiO_2 \in$PVDF **5**), $F_{64}PcZn \cup TiO_2$&$NH_4HCO_3 \in$PVDF **6**). These coated surfaces were made of fluoro-organic polymer PVDF and additives: the volatile NH_4HCO_3 salt, and/or the photocatalysts TiO_2 and $F_{64}PcZn \cup TiO_2$. On characterizing the coated materials, roughened surfaces were revealed on all samples containing NH_4HCO_3 after thermal treatment and volatilization at 80 °C for 48 hrs. These surfaces revealed roughness, porous surfaces and channels on the matrix as seen in **Figure 2.4,** this surface roughness leads to superhydrophobicity upon characterization.

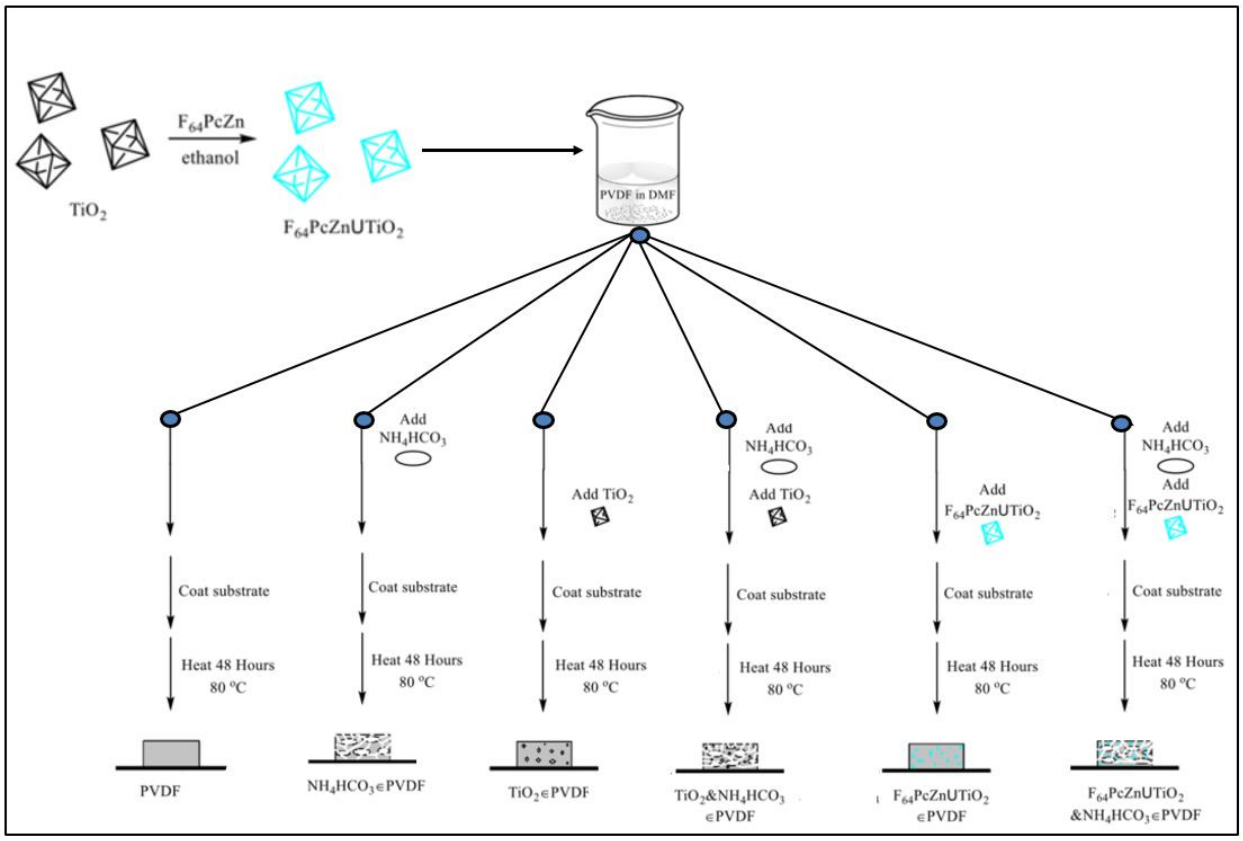

Figure 2.4. Engineering surfaces of six different types. *"Image courtesy of Abdul Azeez"*

.

2.3.4. Coating method replicated with TGA.

The coating method was replicated in the TGA to quantitatively determine the volatilization and decomposition rates of the solvent and the NH_4HCO_3 salt during the coating process. The first step was isothermal at a temperature at 25 °C for 10 hours, representing the time when the coatings were allowed to evaporate at room temperature. The second step was a ramp at 10 °C/min up to 80 °C then held isothermal at 80 °C for 48 hours, representing the oven bake time for the coatings. Most of the solvent evaporated rapidly at 25 °C: 77% of the DMF was evaporated within 180

minutes (3 hrs). The residual 23% of the DMF evaporated within 20 minutes after the temperature ramp to 80 °C.

More than half of the NH_4HCO_3 salt 60% was volatilized in the first 60 min at 80 °C, at a total time of 660 min. At 960 min (360 min at 80 °C), 98% of the salt was volatilized; leaving 2% that gradually decomposed in the next 240 minutes (360-600 min at 80 °C). The gradual volatilization of the last 2% may be associated with salt particles trapped within closed cells of the polymer, slowing volatilization. The total time it took for NH_4HCO_3 salt to decompose was approximately 1200 min (600 min at 25 °C, 600 min at 80 °C). The TGA experiment was run to a total of 3480 min (600 min at 25 °C, 2880 min at 80 °C) to replicate the coating process, however, the organic additives were fully volatilized at about 1200 minutes.

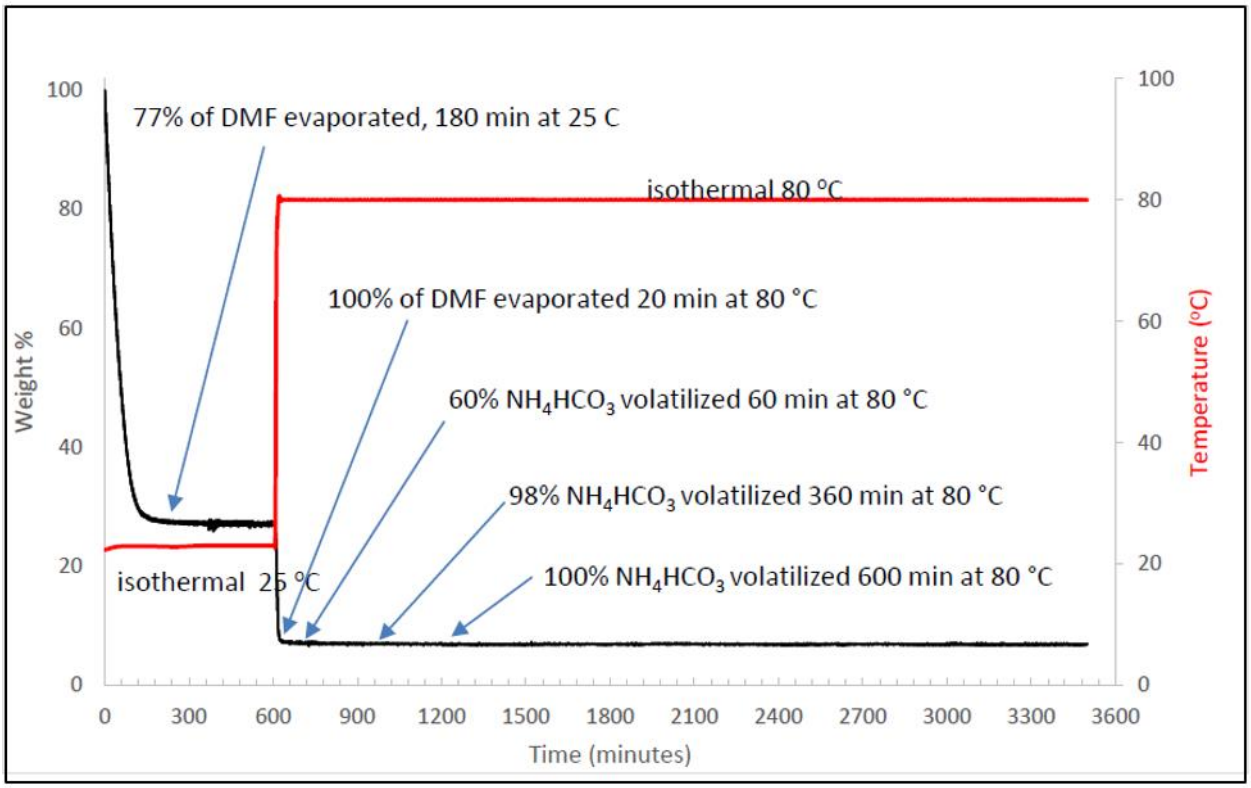

Figure 2.5. Isothermal thermogravimetric analysis of NH_4HCO_3∈PVDF film formation. The film forming suspension (DMF, PVDF, and NH_4HCO_3) was placed in the TGA pan and held at 25 °C for 10 hours (600 minutes). The temperature was then ramped to 80 °C at 10 °C/min and held at 80 °C for 48 hours (2880 minutes). The red line shows the temperature changes, the black line is the weight %. Key points in the evaporation and volatilization processes are shown with arrows. The procedure (6.5 hours to allow most DMF to evaporate, 10 hours to fully volatilize NH_4HCO_3) is shown to be effective.

2.3.5. Characterizations of coated surfaces with Differential Scanning Calorimeter (DSC).

2.3.5.1. Thermal determination of PVDF films stability.

DSC analysis was performed after complete thermolysis and volatilization at 80 °C for 48 hours. The 2-cycle analysis was performed by heating from -60 °C at 10 °C/min to 175 °C, then cooling to -40 °C, then another heating and cooling. The analysis revealed the stability of coated surfaces

with respect to changes in glass transition temperature (T_g), at which the polymer transitions from the rigid, glassy state to a more mobile state. Melting temperature (T_m) on the heating part of the cycle and crystallization temperature (T_c) on the cooling part of the cycle were also determined. Films with the added inorganic sensitizers were analyzed to see if there are any changes in the films' thermal transition temperatures.

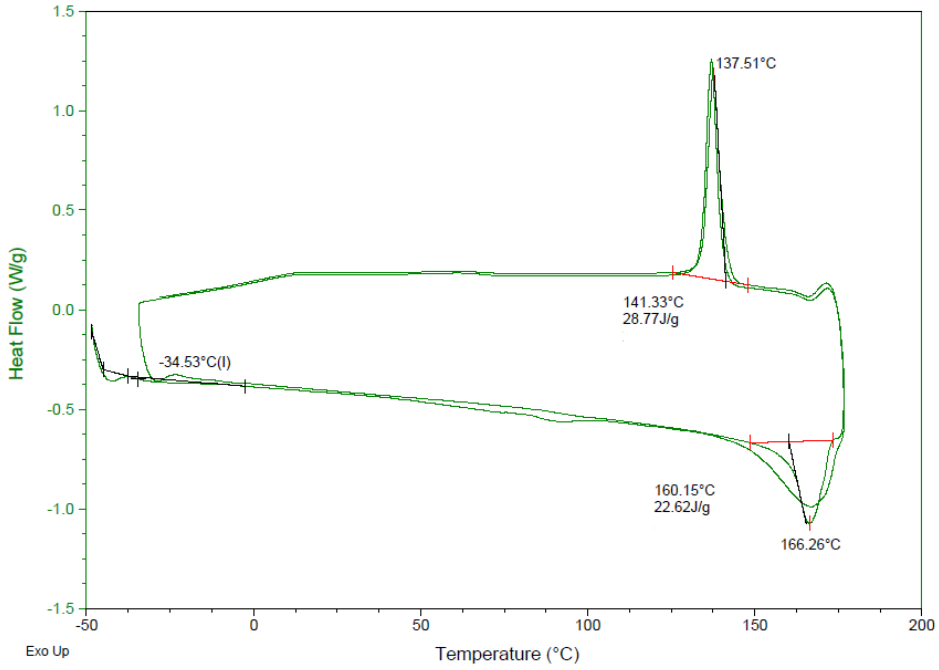

Figure 2.6. (**a**). DSC thermogram of PVDF film after curing for 48 hours.

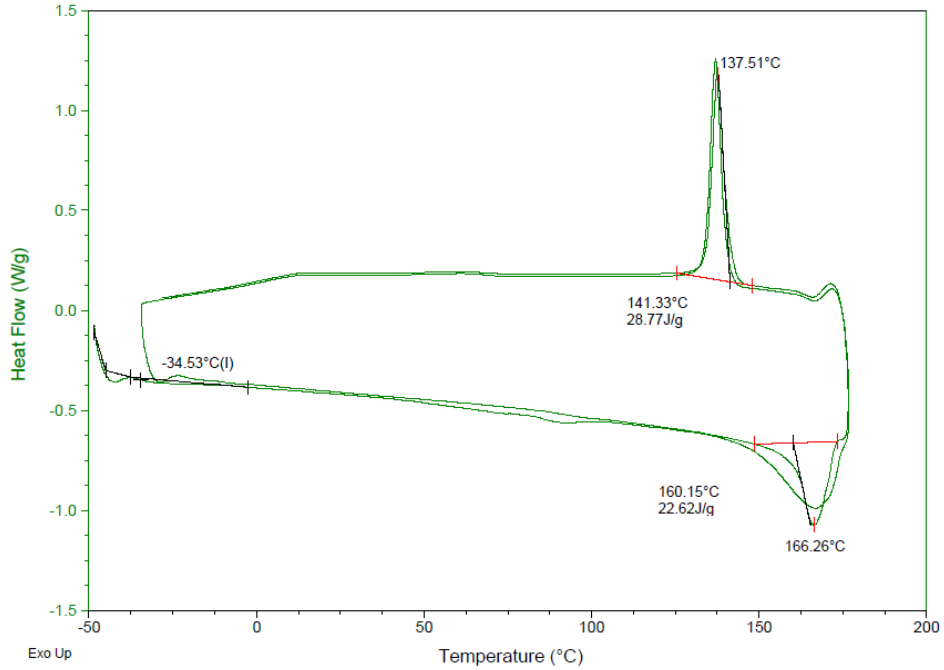

Figure 2.6. (**b**). DSC thermogram of PVDF∈TiO_2 film after curing for 48 hours.

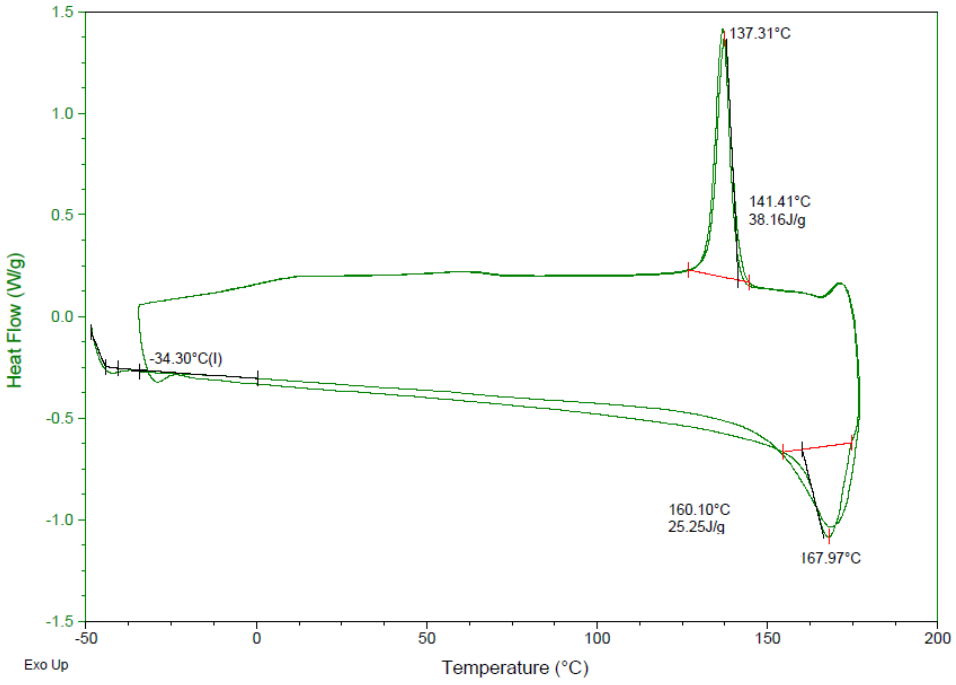

Figure 2.6. (**c**). DSC thermogram of PVDF∈TiO_2∪F_{64}PcZn film after curing for 48 hours.

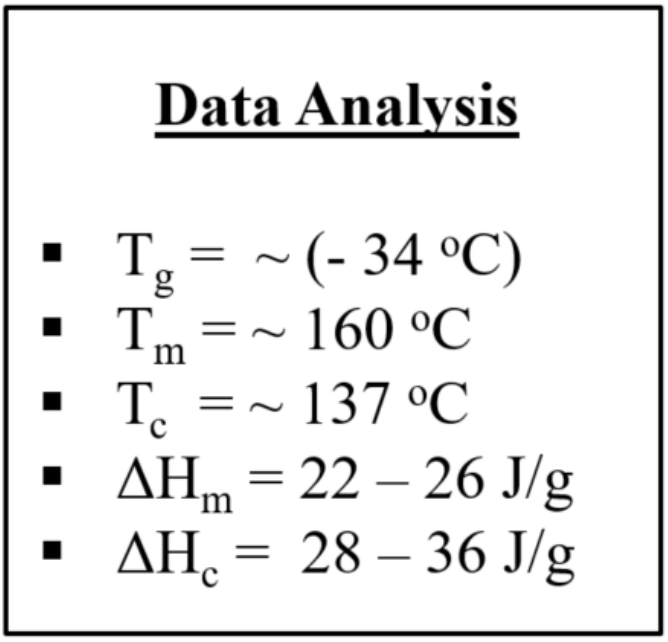

Figure 2.6. (**d**) DSC thermogram analysis of films: T_g, T_m, T_c, ΔH_m, and ΔH_c of all Films.

There were only minor changes in all films with regard to the various thermal transitions and energies (T_g, T_m, T_c, ΔH_m, and ΔH_c). The coated surfaces were stable up to their melting temperature at approximately 170 °C. The second cycle typically gave a sharper melting transition as seen in **Figure 2.6 (a-d).** The inorganic compound embedded in the PVDF matrix does not appreciably change the thermal properties.

2.3.5.2. Thermal determination of PVDF-NH_4HCO_3 films stability.

PVDF films embedded with the volatile were analyzed for thermal stability, the enthalpy and the crystallinity of the films were determined. **Figure 2.7(a-d)** and **Table 2.2**, revealed a melting temperature and crystallization temperature within 3 °C for all NH_4HCO_3 processed films. The changes in enthalpy of all films were examined. The ΔH_m of 38.5 J/g for PVDF∈NH_4HCO_3 was much lower than ΔH_m of the PVDF∈(NH_4HCO_3 & TiO_2) film and PVDF∈(NH_4HCO_3 &

$TiO_2 \cup F_{64}PcZn$) film as shown from **Table 2.3**. The % crystallinity was determined with the formulas given below from **Table 2.3,** where $\Delta H_m°$ PVDF reference value for the heat of melting at 100% crystalline (104 J/g).

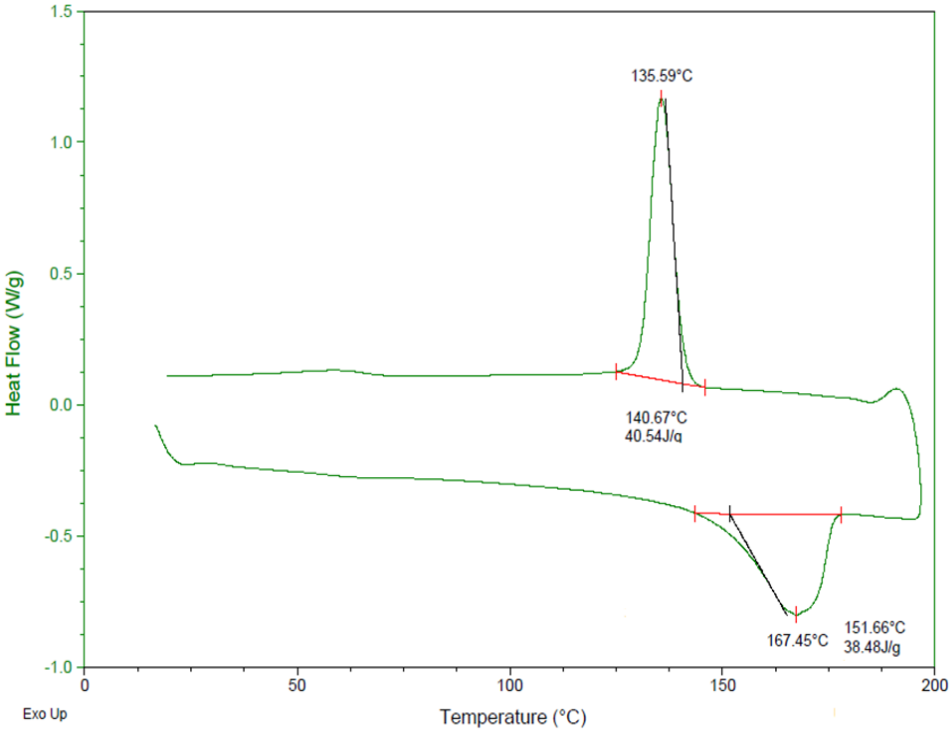

Figure 2.7 (a). DSC analysis of PVDF∈NH_4HCO_3 film after curing for 48 hours.

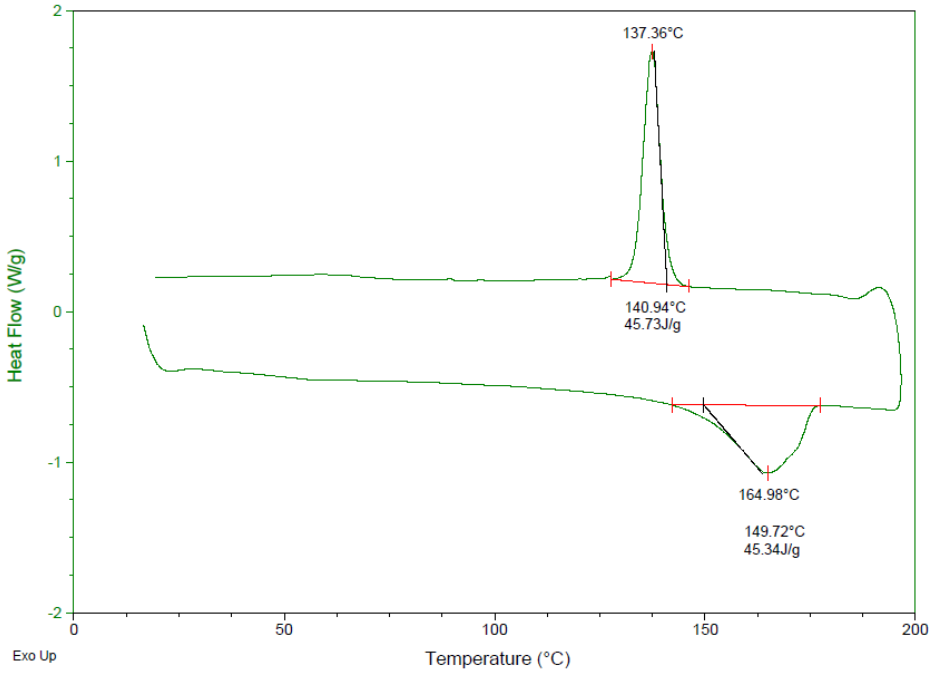

Figure 2.7 (b). DSC analysis of PVDF∈ (NH_4HCO_3 & TiO_2) film after curing for 48 hours.

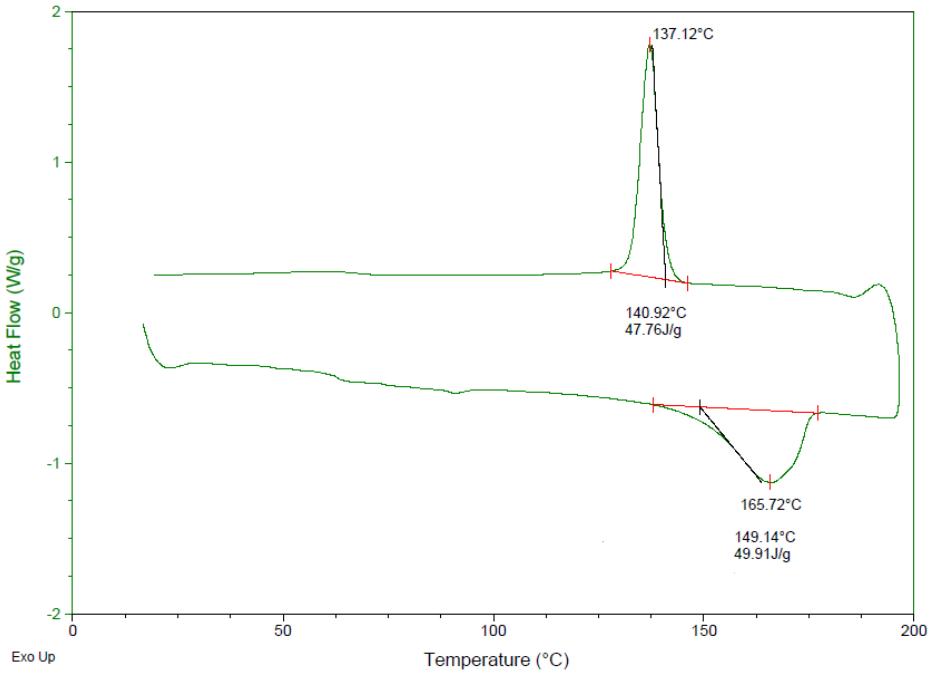

Figure 2.7 (c). DSC analysis of PVDF∈ (NH_4HCO_3&TiO_2∪F_{64}PcZn) film after curing for 48 hours.

Table 2.2. DSC analysis of the T_m and T_c three films containing NH_4HCO_3.

Films	T_m (°C)	T_c (°C)
PVDF	167	135
PVDF-TiO_2	164	137
PVDF-TiO_2-F_{64}PcZn	165	137

T_m represents the temperature of melting and T_c represents the temperature of crystallization.

Table 2.3. DSC analysis of change in enthalpy (ΔH) and % crystallinity of all three films containing NH_4HCO_3.

Films	ΔH_m (J/g)	% Crystallinity H_m	ΔH_c (J/g)	% Crystallinity H_m
PVDF	38.5	38	40.6	39
PVDF-TiO_2	45.3	43	45.7	43
PVDF-TiO_2-F_{64}PcZn	49.9	47	47.7	45

Percent crystallinity of all films was determined by using the crystallinity equation: % Crystallinity = $[(\Delta H_{observed})/ \Delta H_m^o] \times 100\%$
ΔH_m = heat of melting enthalpy
ΔH_c = heat of crystallization enthalpy
ΔH_m^o = PVDF reference value for the heat of melting at 100% crystalline (104 J/g)

2.3.6. Characterizations of coated surfaces with Thermogravimetric Analysis (TGA).

TGA analysis of all films was performed after complete thermolysis and volatilization at 80 °C for 48 hours. Samples were heated at the rate of 10 °C/min up to 900 °C. The data shown in **Figure 2.8 (a-c)** clearly reveals that all films were stable above 300 °C before degradation starts. As is also known in literature, F_{64}PcZn is stable to above 300 °C, when volatilization starts to occur. The only losses at this point are organic solvent, moisture, and volatiles, which represented less than 2.5% total weight percentage of the films. The weight loss from PVDF from 40 to 342 °C (defined as **Phase 1**) is slightly higher than the weight loss from the other films - this can be

attributed to the additional mass of the refractory inorganic composite catalyst, in the other films**.** From 342 to 468 °C (defined as **Phase 2**) PVDF alone had a higher onset temperature, followed by a rapid loss of mass. This pattern of degradation is consistent with literature. [41, 42] The PVDF with the added catalysts revealed a stepwise degradation pattern in **Phase 2**, with a lower onset temperature and changes in decomposition rate throughout the temperature range. This is attributed to the presence of the catalysts. **Phase 3** is defined as the temperature range from 468 to 879 °C. In this temperature range, all three films showed a slow loss of mass. For total mass loss after heating, the PVDF film degraded the most, as is expected because of the absence of the refractory inorganic catalysts found in PVDF$\in TiO_2$ and PVDF$\in TiO_2 \cup F_{64}$PcZn. The films were thermally stable to 300 °C, well beyond the temperature range for the proposed photocatalytic application.

Table 2.4. TGA data analysis of weight loss in percentage of films.

Films	**$W_{loss(phase\ 1)\ (\%)}$**	**$W_{loss(phase\ 2)\ (\%)}$**	**$W_{loss(phase\ 3)\ (\%)}$**
PVDF	2.3	64.4	16.8
PVDF-TiO_2	1.8	54.8	15.5
PVDF-TiO_2-F_{64}PcZn	1.6	53.0	20.8

W_{loss} is weight loss (%) as a function of temperature increase (°C).

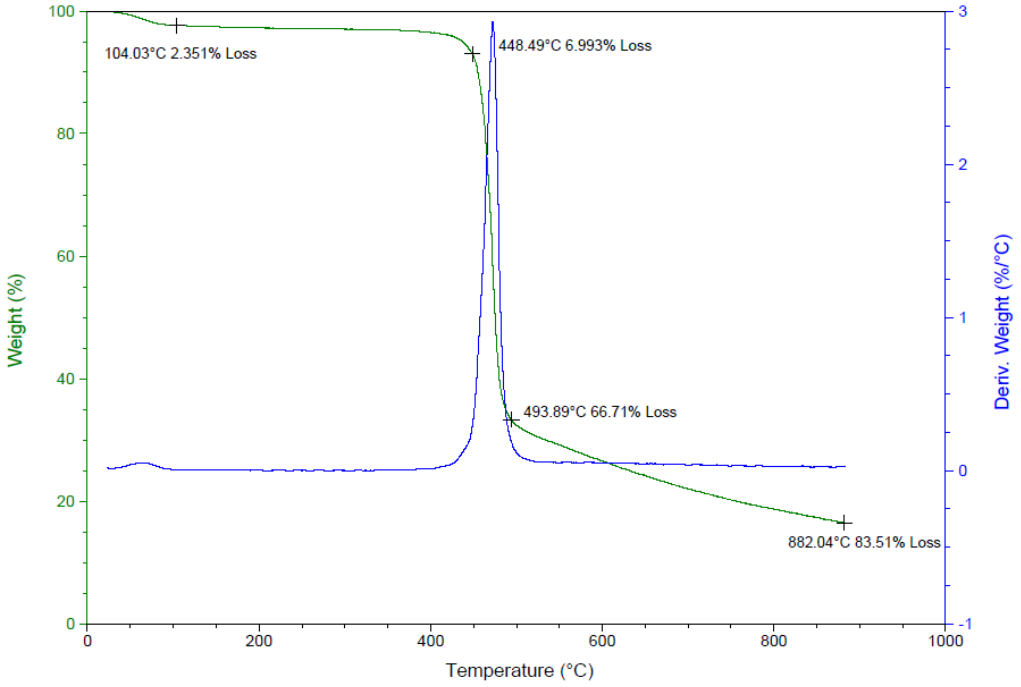

Figure 2.8 (a). TGA thermogram analysis of PVDF∈NH_4HCO_3 Film.

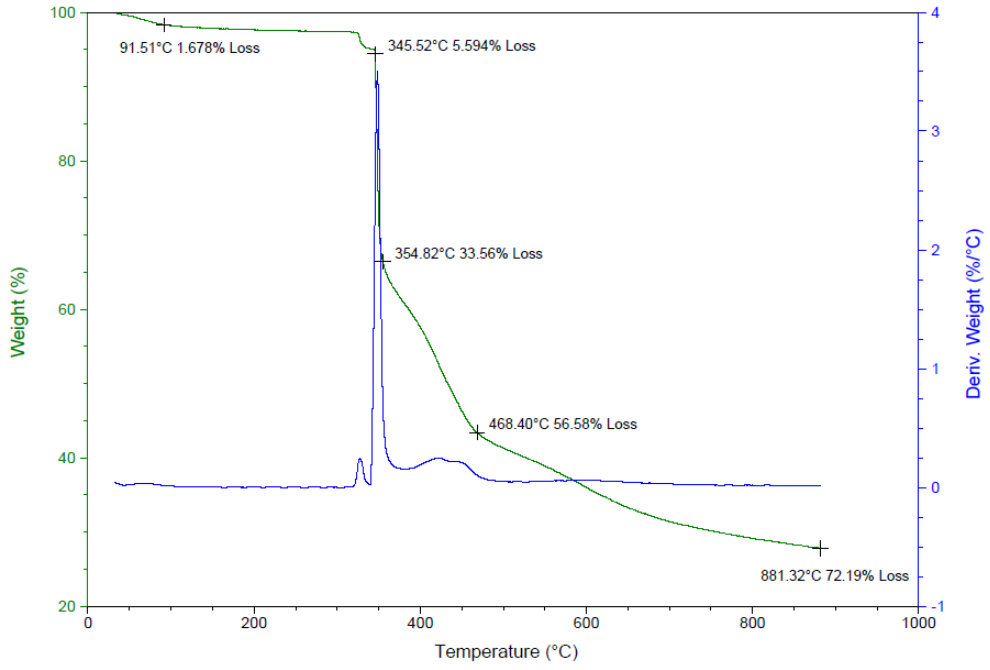

Figure 2.8 (b). TGA thermogram analysis of PVDF∈ (TiO_2 & NH_4HCO_3) film.

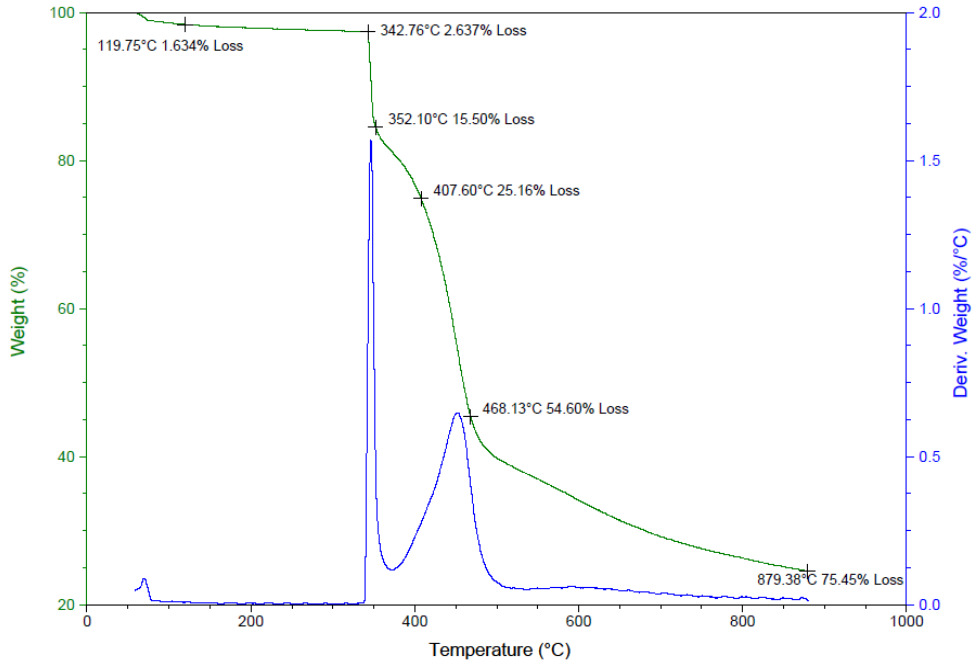

Figure 2.8 (c). TGA thermogram analysis of PVDF∈ (TiO_2∪F_{64}PcZn & NH_4HCO_3) Film.

2.3.7. Contact Angle Analysis of Coated Surfaces.

Contact angles (CA) of the films were measured with a Goniometer using the sessile water drop method, with a 5µL volume. The reported contact angle measurements were the average of five different droplets at different locations on the surface of each film. Glass slides were used as a control, they are hydrophilic with a low water contact angle of approximately $\theta = 23°$. The untreated PVDF surfaces displayed a slightly hydrophobic surface, average $\theta = 92 \pm 2°$ shown in **Figure 2.8 (a).** To generate roughened surfaces for enhanced hydrophobicity, NH_4HCO_3 was introduced into the PVDF coating to create roughness when volatilization occurred during thermolysis. The smallest NH_4HCO_3 particle size used, < 63 µm, gave the highest contact angle measured. The treated NH_4HCO_3∈PVDF film revealed the highest water CA, average θ =

159(0.8)°, shown in **Figure 2.9 (b).** This can be attributed to the roughness created by the decomposing salt within the surface. Optimal effectiveness of the decomposition was obtained after equilibrating the coated surfaces at room temperature for 10 hours prior to baking. Placing coated surfaces in the oven immediately after coating gave lower CA.

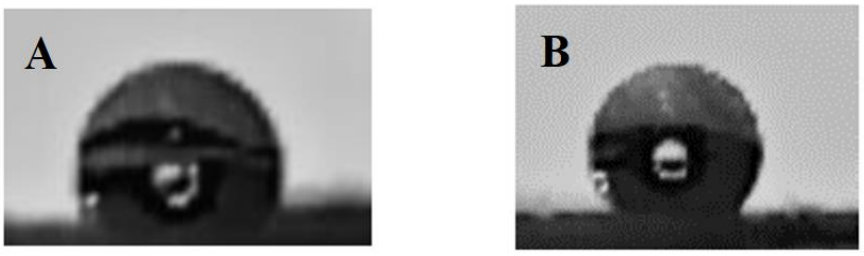

Figure 2.9. Images of CA on surfaces: **(a)** PVDF and **(b)** $NH_4HCO_3 \in$PVDF. *"Image courtesy of Abdul Azeez"*.

The coatings with NH_4HCO_3 and the photocatalysts also gave increased CA, as seen in **Figure 2.10.** The coating with PVDF$\in$ (NH_4HCO_3 & TiO_2) revealed a CA with average θ = 136(0.8)° (**Figure 2.10(a)**). TiO_2 is hydrophilic, the presence of this additional hydrophilic component may reduce the observed CA from that observed for the coating without the catalyst. The coating with PVDF$\in$ (NH_4HCO_3 & $F_{64}PcZn \cup TiO_2$) revealed a CA with average θ = 144(0.4)°, (**Figure 2.10(b)**). This is higher than the coating with only TiO_2 but not as high as the coating with no catalyst. Coating the TiO_2 with the fluorinated Pc will reduce the hydrophilicity of the added catalyst, which in turn increases the hydrophobicity of the final film.

Figure 2.10. Images of CA on surfaces: **(a)** $(TiO_2\&NH_4HCO_3)\in PVDF_2$ and **(b)** $F_{64}PcZn\cup TiO_2\&NH_4HCO_3)\in PVDF$. *"Image courtesy of Abdul Azeez"*.

As noted above, the particle size of the NH_4HCO_3 salt also played a role in increasing the hydrophobicity of these films in general. The CA values are collected in **Table 2.5**. The $PVDF\in NH_4HCO_3$ film contact angle revealed a superhydrophobic surface, while the films with added catalyst fell short of superhydrophobicity. After UV-Vis photolysis, all films were stable and maintained their CA value, except $PVDF\in(\ NH_4HCO_3\ \&\ TiO_2)$. This material shows a decrease in CA on photolysis: before post UV-Vis photolysis the CA was measured as θ = 136(0.8)°, but after photolysis, the CA fell to θ = 114°.

Table 2.5. Material Compositions and CA (θ) of Surfaces.

Surface	Composition (before) after 80°C bake	θ, post bake	θ, post UV-Vis photolysis
Glass slide	Glass slide	23±4	N/A
$F_{64}PcZn\cup TiO_2$	(0.003:1) 0.003:1	N/A	N/A
Untreated PVDF	PVDF	92±2	92±2
$TiO_2\in PVDF$	(0.03:1) 0.03:1	119(0.5)	Not determined
$NH_4HCO_3\in PVDF$	(0.2:1) <0.01:1	159(0.8)	159(0.8)
$(TiO_2\&NH_4HCO_3)\in PVDF$	(0.03:0.2:1) 0.03:<0.01:1	136(0.8)	114(0.4)
$(F_{64}PcZn\cup TiO2)\in PVDF$	(0.003:0.03:1) 0.003:0.03:1	128(0.7)	Not determined
$(F_{64}PcZn\cup TiO_2\&\ NH_4HCO_3)\in PVDF$	(0.003:0.03:0.2:1) 0.003:0.03:<0.01:1	144(0.4)	144(0.4)

The relationship between particle size and the cosine of the CA θ is given in **Figure 2.11.** The cos θ of PVDF∈NH_4HCO_3 film is inversely related to the radii of the NH_4HCO_3 particle size. As the particles sizes get smaller, cos θ goes toward 0 (θ = 180º). The finer particles provide the necessary nano/micrometer needed superhydrophobicity. As the sample is heated, NH_4HCO_3 starts to decompose from 48 °C, gases are formed, and the pressured gases lead to the creation of surface roughness, porosity, and channels on the surface and in the matrix of the polymer. The larger particles will produce larger features, creating void sizes as a function of the size of the particle. The larger-scale roughness on surfaces may result in water droplets behaving in a Wenzel state instead of the Cassie-Baxter state, water droplets on the surface of the polymer will spread all over the rough surface, called surface wetting, even though the surface is rough.

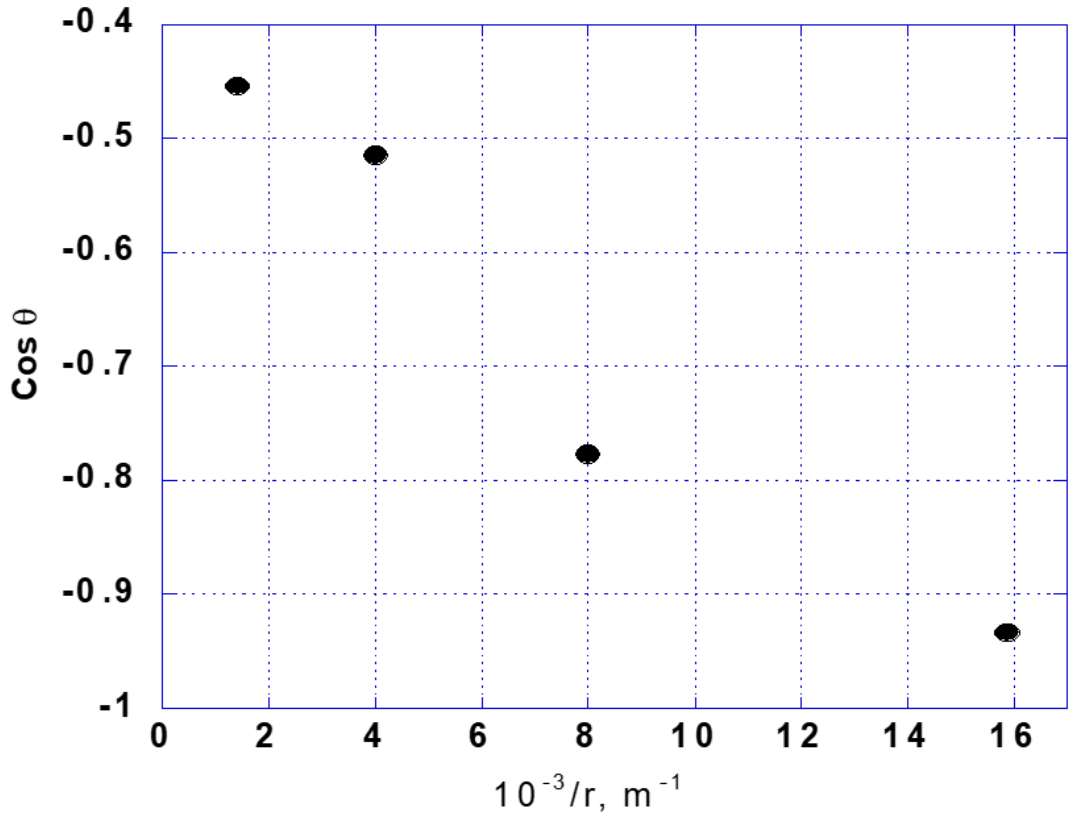

Figure 2.11. Cosine of observed θ of NH_4HCO_3 & PVDF films as a function of the inverse radii of NH_4HCO_3 particles.

2.3.8. Scanning Electron Microscopy (SEM) Surface Morphology of Coated Films.

Scanning electron microscopy was used to determine the surface morphology of the coated films. NH_4HCO_3∈PVDF film was examined at different magnification (800x, 8000x and 80000x magnification) to determine the low-end and high-end topography of the coated surface. **Figure 2.12 (a),** at 800x magnification with 100 µm scale revealed roughness as a result of the way the surface was tailored as specified previously.

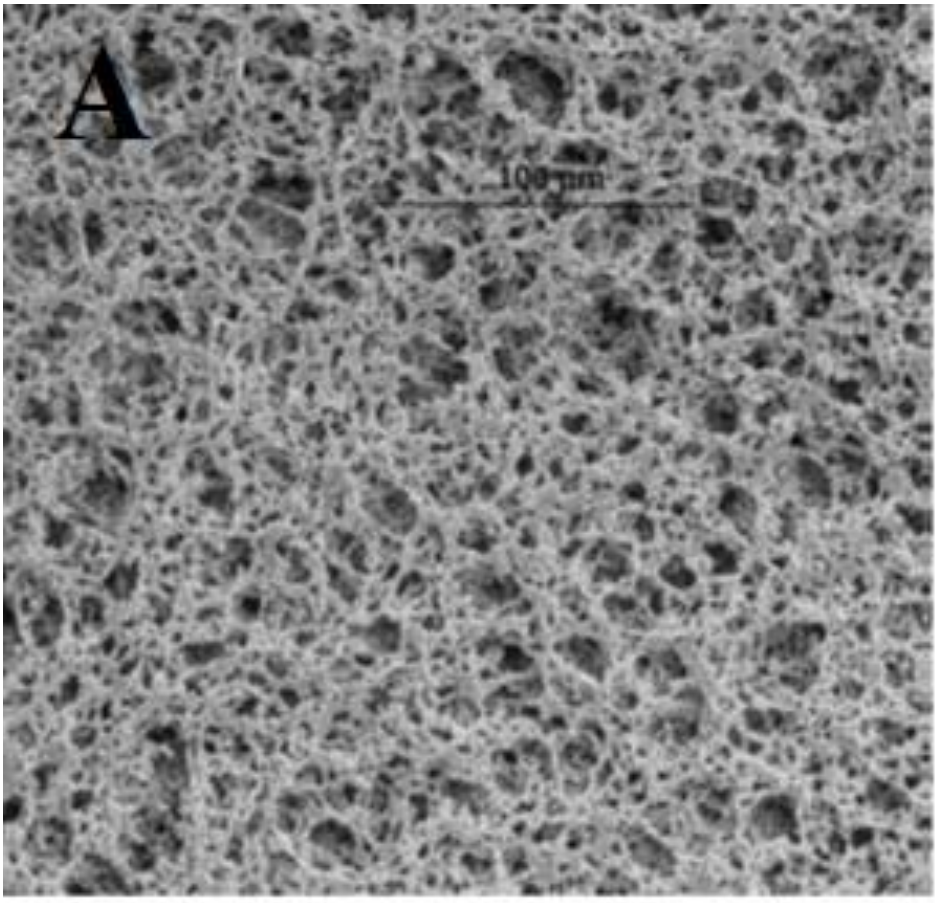

Figure 2.12. (**a**) SEM morphology of NH_4HCO_3∈PVDF film at 100 µm scale. *"Image courtesy of Abdul Azeez"*.

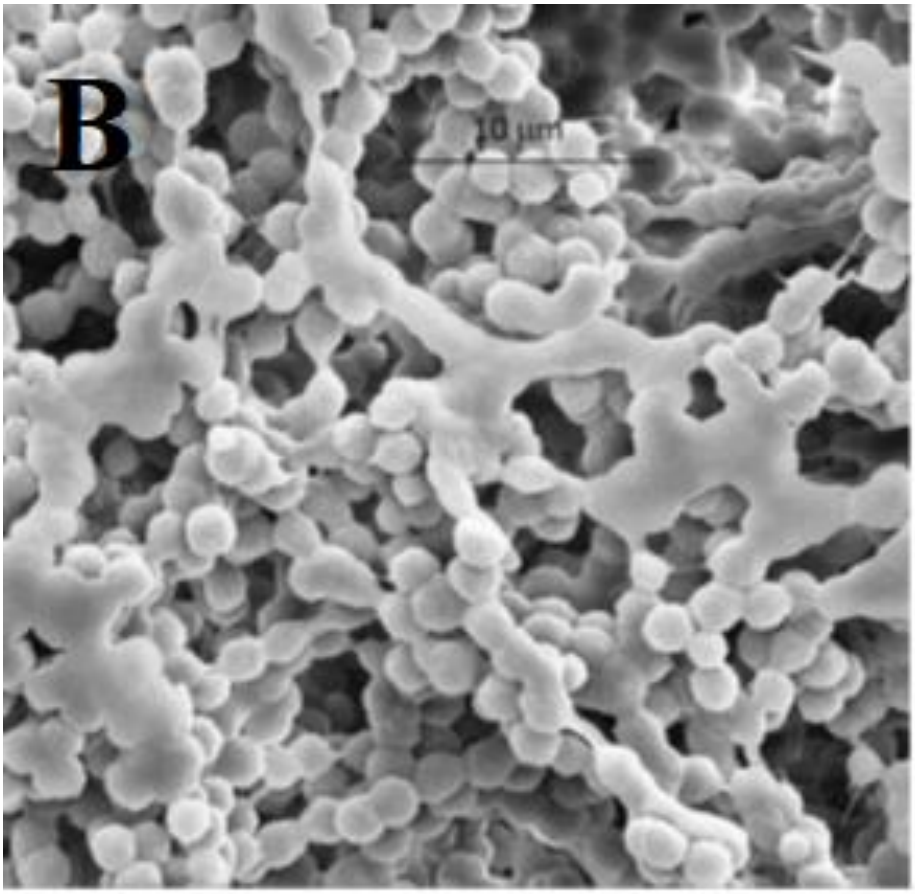

Figure 2.12. (**b**) SEM morphology of $NH_4HCO \in PVDF$ film at 10 µm scale. *"Image courtesy of Abdul Azeez"*.

The SEM micrograph from **Figure 2.12 (b),** revealed a phase that is clearly showing roughness and morphological arrangement as the decomposing salt creates voids while the polymer fragments rearrange stacking on top of one another. Porosity can obviously be noticed from this scale and as the gases expand inside the polymer matrix, surface roughness occurs as they escape. **Figure 2.13 (a),** shows a larger magnification at 80,000x, enough to view the details of the coated surface at close range.

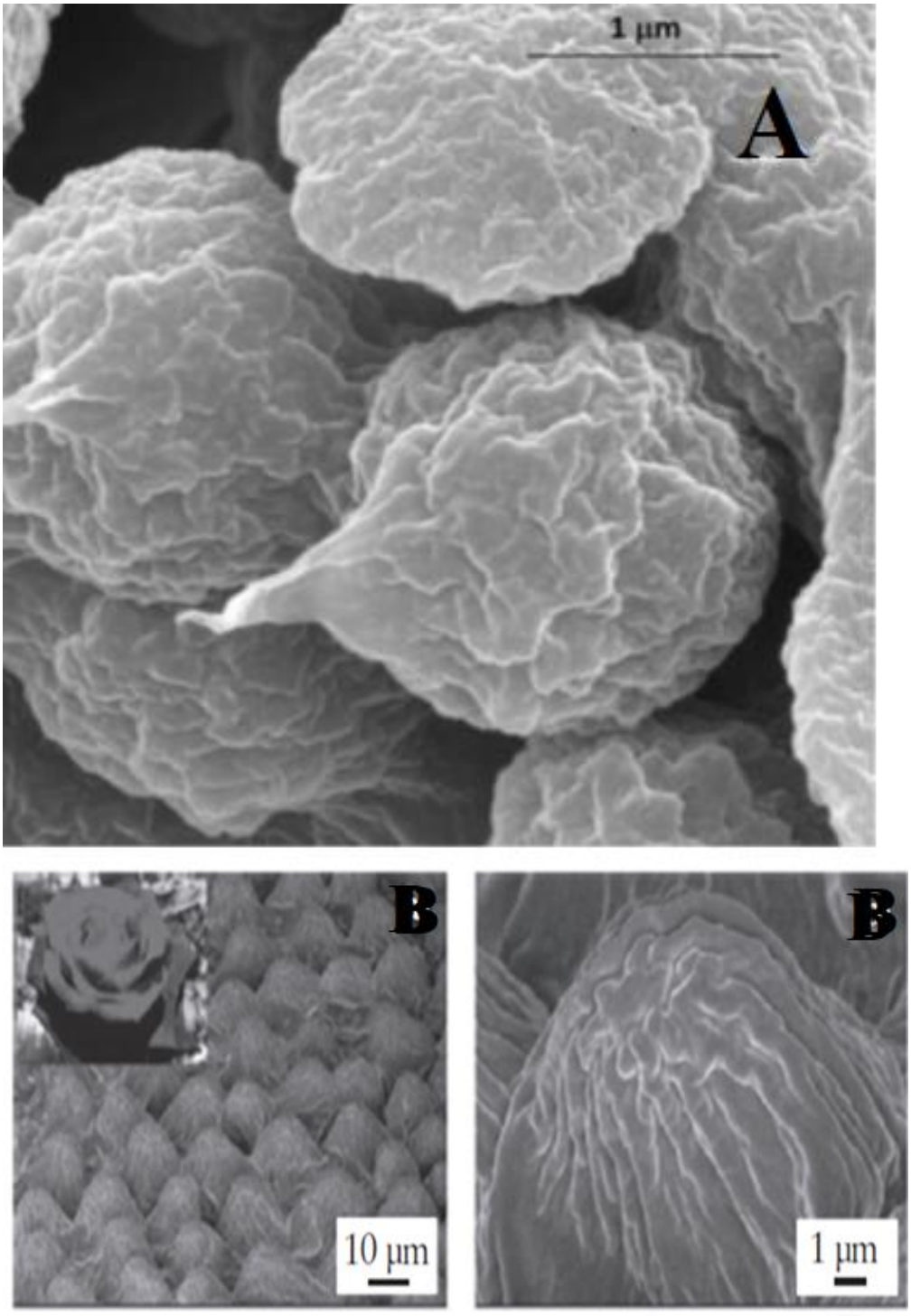

Figure 2.13. SEM morphologies of (**a**) 1 µm NH_4HCO_3∈PVDF film. *"Image courtesy of Abdul Azeez"* and (**b**) picture of rose petal, and SEM image of 1 µm and 10 µm respectively. *"Reproduced with permission from Springer Nature".* [36]

The topography revealed a well-tailored morphology arranged in a similar fashion to that of the rose flower petal shown in **Figure 2.12 (b)** with SEM images by Das *et al*. [36] The arrangement of the topography clearly dictate why the CA exceeds 150°. It will prevent water from completely wetting the surface by trapping air between the water suspended on top of the surface, forming a composite between the roughened coated surface and the sessile water. Based on the SEM image above and CA of $\theta = 159(0.8)°$, the surface is in a Cassie-Baxter state, a superhydrophobic surface.

2.3.9. SEM: Morphology of different PVDF films at 50 µm scale.

SEM imaging allowed the analysis of the morphology of the different surfaces: untreated PVDF film, $NH_4HCO_3 \in$PVDF film and $(NH_4HCO_3$ & $F_{64}PcZn \cup TiO_2) \in$PVDF film were analyzed to determine topographical changes on surfaces. **Figure 2.14 (a)** revealed the surface of PVDF film without NH_4HCO_3 treatment, the SEM analysis showed some roughness, but only at a very fine scale, the nearly planar surface gave $\theta = 92°$. **Figures 2.14 (b and c)** showed the surfaces of $NH_4HCO_3 \in$PVDF film and $(NH_4HCO_3$ & $F_{64}PcZn \cup TiO_2) \in$PVDF film. The surfaces show a comparable morphology based on the SEM images. There are no changes as a result of the inorganic catalyst added to $(NH_4HCO_3$ & $F_{64}PcZn \cup TiO_2) \in$PVDF film. Both surfaces represented the Cassie-Baxter model based on their CA with very high hydrophobicity shown in **Table 2.5.** The surface with treated $NH_4HCO_3 \in$PVDF film is superhydrophobic with $\theta = 159(0.8)°$ and the $(NH_4HCO_3$ & $F_{64}PcZn \cup TiO_2) \in$PVDF film is almost superhydrophobic with $\theta = 144(0.4)°$. Since the morphology is the same, the difference in CA must be due to the difference in film composition the addition of the catalyst reduces the innate hydrophobicity of the material.

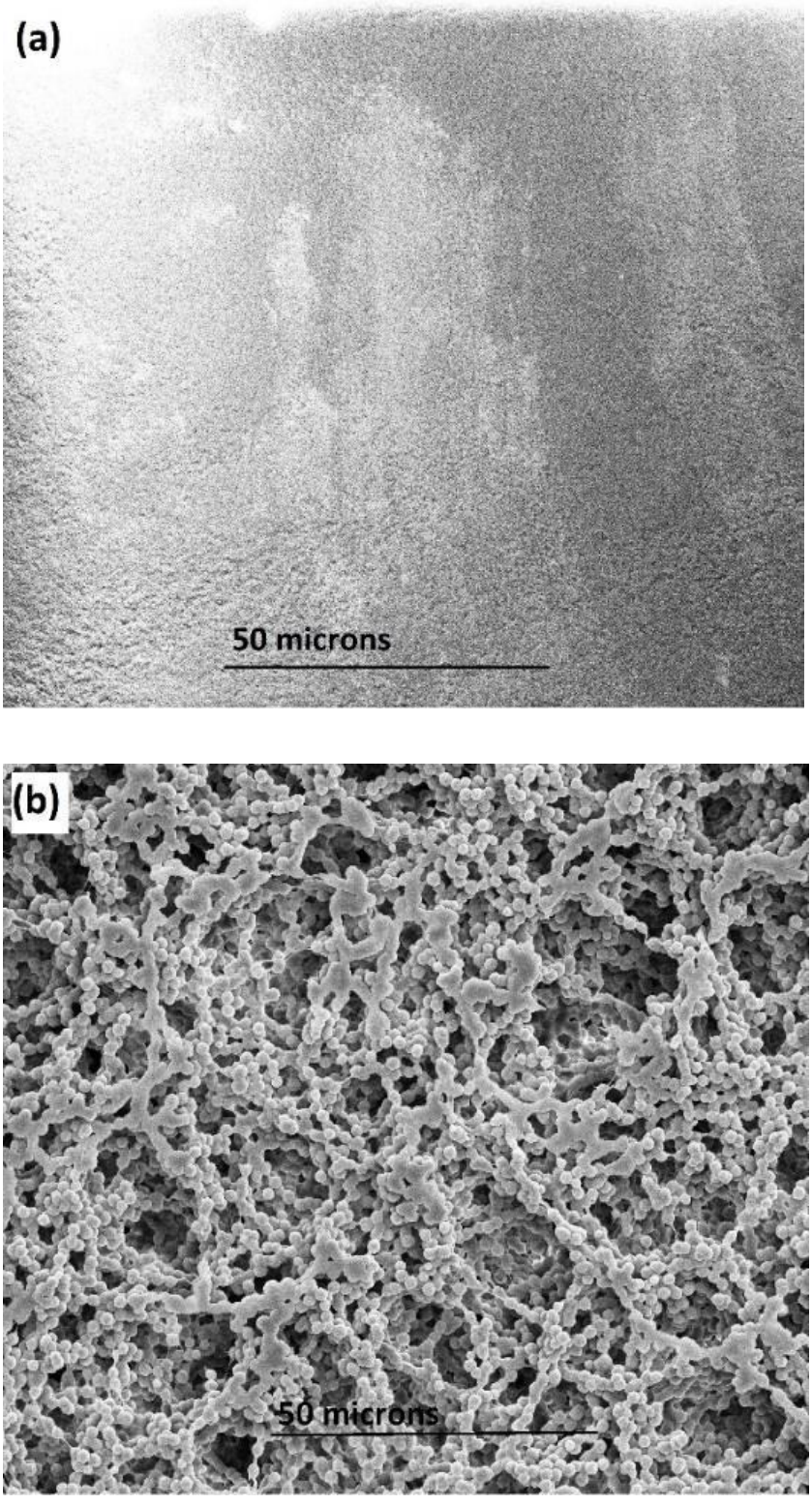

Figure 2.14. SEM morphology of (**a**) untreated PVDF film and (**b**) NH_4HCO_3&PVDF film. *"Image courtesy of Abdul Azeez"*.

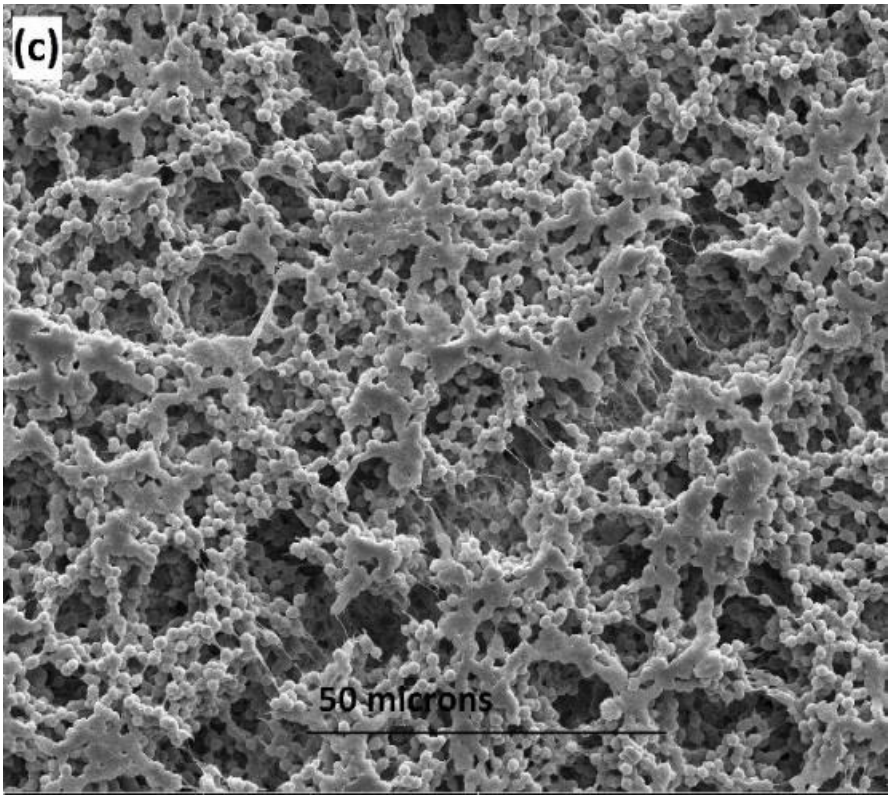

Figure 2.14. (**c**) SEM morphology of (NH_4HCO_3&$F_{64}PcZn$∪TiO_2) ∈ PVDF film. *"Image courtesy of Abdul Azeez"*.

2.3.10. SEM: Morphology of different PVDF films at 10 µm scale.

The morphology of five different films was analyzed at higher magnification (8000X) for better qualitative analysis of the surfaces. **Figure 2.15 (a, b and c),** are the same materials as in Figure **2.14 (a, b, and c)**. **Figure 2.15 (d and e)** are films containing TiO_2, before (**d**) and after (**e**) UV irradiation. The morphology of these films is the same as that of the NH_4HCO_3 ∈ PVDF and (NH_4HCO_3&$F_{64}PcZn$∪TiO_2) ∈ PVDF films. The lower CA of the (NH_4HCO_3& TiO_2) ∈ PVDF

film again must be assigned to the difference in composition of this material, with the hydrophilic TiO_2.

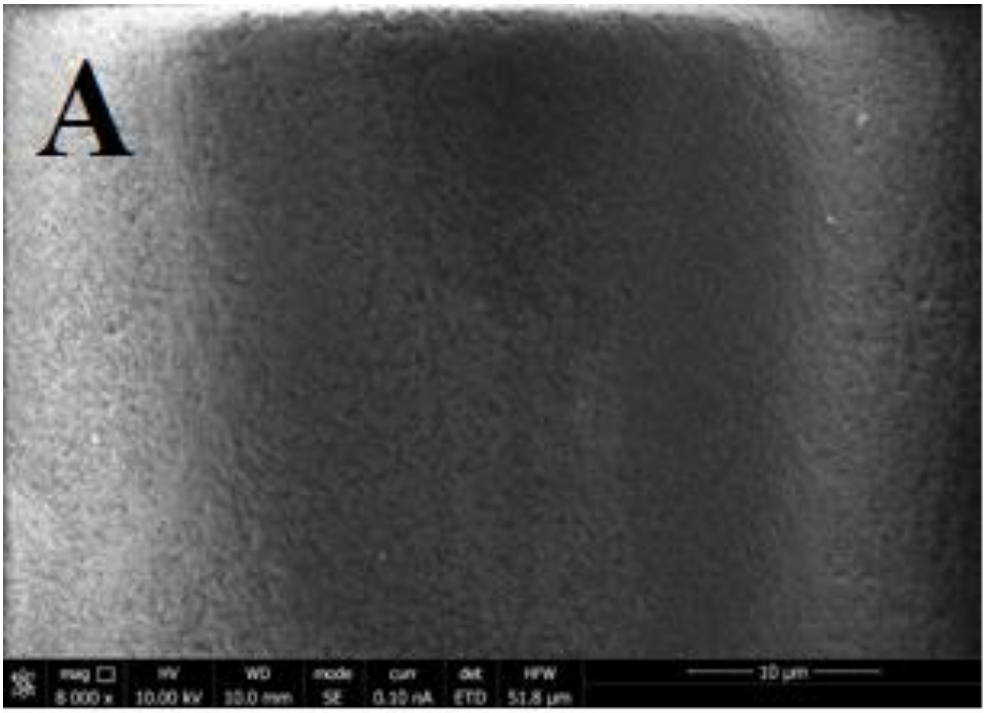

Figure 2.15. (**a**) SEM morphology of untreated PVDF film. *"Image courtesy of Abdul Azeez"*.

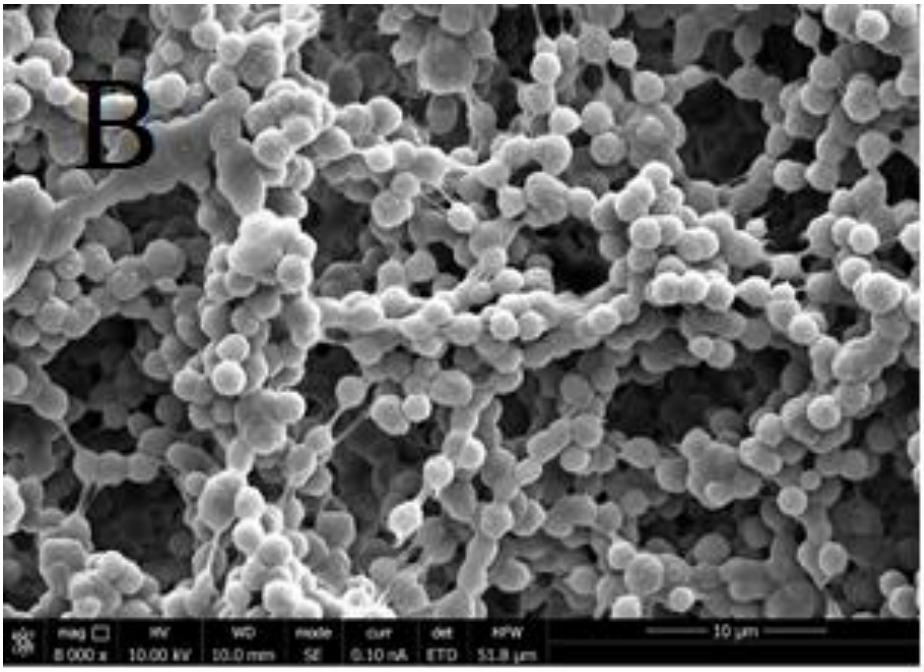

Figure 2.15. (**b**) SEM morphology of NH_4HCO_3&PVDF film. *"Image courtesy of Abdul Azeez"*.

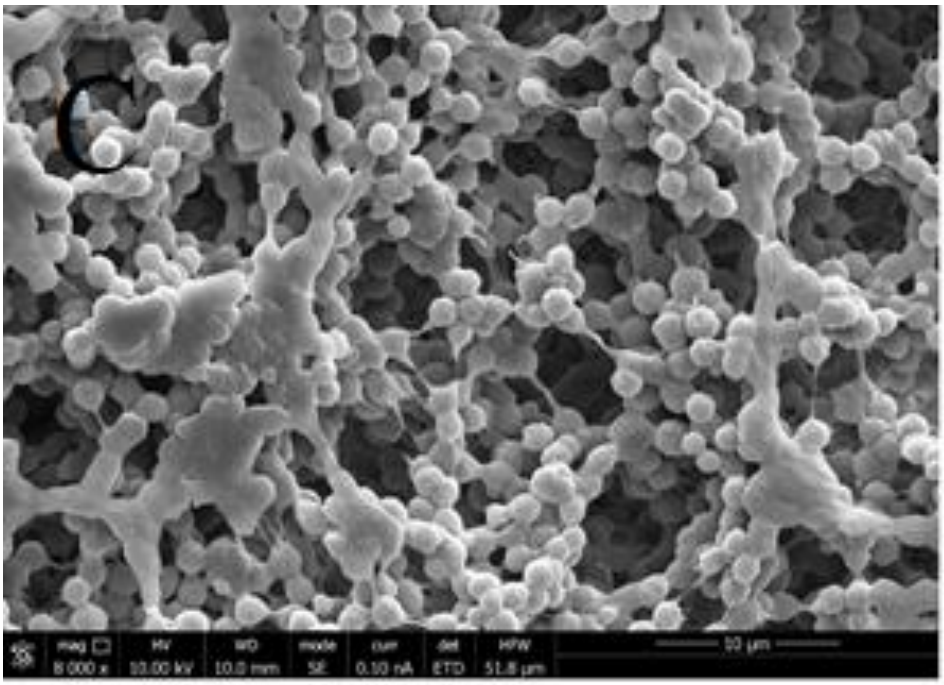

Figure 2.15. (**c**) SEM morphology of NH_4HCO_3&PVDF$\cup TiO_2 \in F_{64}PcZn$ film. *"Image courtesy of Abdul Azeez"*.

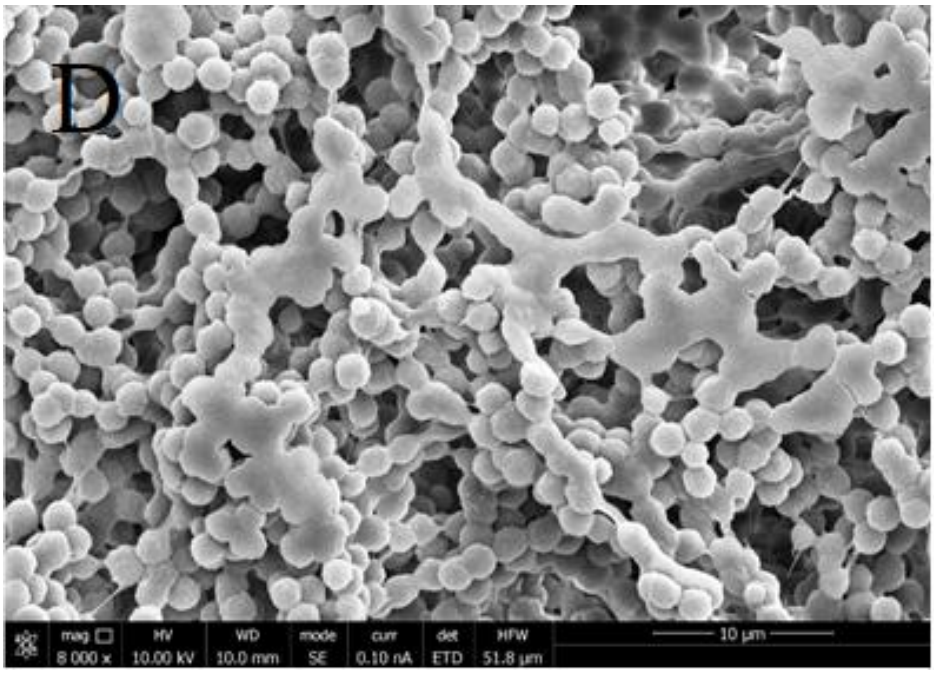

Figure 2.15. (**d**) SEM morphology of NH_4HCO_3&PVDF∪TiO_2 film before irradiated. *"Image courtesy of Abdul Azeez"*.

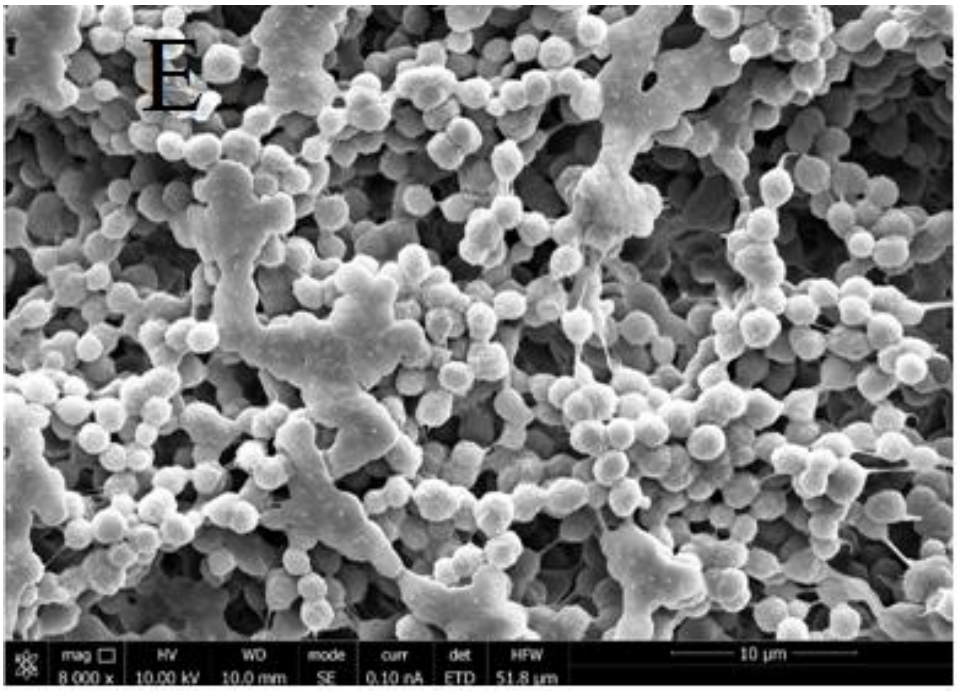

Figure 2.15. (**e**) SEM morphology of NH_4HCO_3&PVDF∪TiO_2 film after irradiated. *"Image courtesy of Abdul Azeez"*.

Figure 2.15 (d and e) were analyzed for the effects of reactive oxygen species (ROS) produced by TiO_2 during irradiation. The surfaces after irradiation reveal some noticeable white dots on the surface, although the overall morphology is unchanged. The surface before irradiation water contact angle was 136(0.8)°, while the contact angle after irradiation fell to 114^o. This suggests the ROS effect a change in the surface composition, either additional exposure of the TiO_2 or changes in the PVDF matrix.

2.4. Conclusions.

Surface modification was performed on PVDF films by incorporation of the volatile salt NH_4HCO_3. The hydrophobicity can be greatly enhanced to generate a superhydrophobic surface with CA θ = 159°. The method is considered a bottom-up surface modification approach. The surfaces that were embedded with photoreactive inorganic catalysts were highly hydrophobic, the optimal material (NH_4HCO_3& $F_{64}PcZn \cup TiO_2$) $\in$PVDF surface was θ = 144°. The films proved to have strong thermal resistance as shown through DSC and TGA analysis. The surfaces maintained the PVDF glass transition temperature, melting temperature and were stable above 300 °C as revealed by TGA analysis. The TGA isotherm analysis also gave a quantitative analysis of the surface preparation method from the start at 25 °C, where the coated films were allowed to equilibrate for 10 hours until the temperature was ramped to 80 °C at the rate of 10 °C/min for 48 hours. DMF was evaporated mostly at room temperature and 20 minutes at 80 °C, at about 600 minutes, while the NH_4HCO_3 was completely volatilized after 1200 minutes. The photoreactivity of the surfaces will be tested in the next chapter.

References.

1. Klee, D., Ademovic, Z., Bosserhoff, A., Hoecker, H., Maziolis, G., & Erli, H. (**2003**). Surface modification of poly(vinylidene fluoride) to improve the osteoblast adhesion. *Biomaterials*, *24*(21), 3663–3670.

2. Meng, J., Chen, C., Huang, L., Du, Q., & Zhang, Y. (**2011**). Surface modification of PVDF membrane via AGET ATRP directly from the membrane surface. *Applied Surface Science*, *257*(14), 6282–6290.

3. Park, Y., & Inagaki, N. (**2003**). Surface modification of poly(vinylidene fluoride) film by remote Ar, H_2, and O_2 plasmas. *Polymer*, *44*(5), 1569–1575.

4. Singh, N., Husson, S. M., Zdyrko, B., & Luzinov, I. (**2005**). Surface modification of microporous PVDF membranes by ATRP. *Journal of Membrane Science*, *262*(1-2), 81–90.

5. Zhu, L., Yu, J., Xu, Y., Xi, Z., & Zhu, B. (**2009**). Surface modification of PVDF porous membranes via poly(DOPA) coating and heparin immobilization. *Colloids and Surfaces B: Biointerfaces*, *69*(1), 152–155.

6. Buonomenna, M., Lopez, L., Favia, P., D'Agostino, R., Gordano, A., & Drioli, E. (**2007**). New PVDF membranes: The effect of plasma surface modification on retention in nanofiltration of aqueous solution containing organic compounds. *Water Research*, *41*(19), 4309–4316.

7. Crowe, R., & Badyal, J. P. S. (**1991**). Surface modification of poly(vinylidene difluoride)(PVDF) by LiOH. *Journal of the Chemical Society, Chemical Communications*, (14), 958.

8. Duca, M. D., Plosceanu, C. L., & Pop, T. (**1998**). Surface modifications of polyvinylidene fluoride (PVDF) under rf Ar plasma. *Polymer Degradation and Stability*, *61*(1), 65–72.

9. Peng, C., Xing, S., Yuan, Z., Xiao, J., Wang, C., & Zeng, J. (**2012**). Preparation and anti-icing of superhydrophobic PVDF coating on a wind turbine blade. *Applied Surface Science*, *259*, 764–768.

10. Salimi, A., & Yousefi, A. (**2003**). Analysis Method. *Polymer Testing*, *22*(6), 699–704.

11. Yan, L., Li, Y., Xiang, C., & Xianda, S. (**2006**). Effect of nano-sized Al_2O_3-particle addition on PVDF ultrafiltration membrane performance. *Journal of Membrane Science*, *276*(1-2), 162–167.

12. Abbrent, S., Plestil, J., Hlavata, D., Lindgren, J., Tegenfeldt, J., & Wendsjö, Å. (**2001**). Crystallinity and morphology of PVdF–HFP-based gel electrolytes. *Polymer*, *42*(4), 1407–1416.

13. Bormashenko, Y., Pogreb, R., Stanevsky, O., & Bormashenko, E. (**2004**). Vibrational spectrum of PVDF and its interpretation. *Polymer Testing*, *23*(7), 791–796.

14. Chen, N., & Hong, L. (**2002**). Surface phase morphology and composition of the casting films of PVDF–PVP blend. *Polymer*, *43*(4), 1429–1436.

15. Gregorio, Jr., R., & Cestari, M. (**1994**). Effect of crystallization temperature on the crystalline phase content and morphology of poly(vinylidene fluoride). *Journal of Polymer Science Part B: Polymer Physics*, *32*(5), 859–870.

16. Kabir, E., Khatun, M., Nasrin, L., Raihan, M. J., & Rahman, M. (**2017**). Pureβ-phase formation in polyvinylidene fluoride (PVDF)-carbon nanotube composites. *Journal of Physics D: Applied Physics*, *50*(16), 163002

17. Salimi, A., & Yousefi, A. (**2003**). Analysis Method. *Polymer Testing*, *22*(6), 699–704.

18. Zha, D., Mei, S., Wang, Z., Li, H., Shi, Z., & Jin, Z. (**2011**). Superhydrophobic polyvinylidene fluoride/graphene porous materials. *Carbon*, *49*(15), 5166–5172.

19. Salimi, A., & Yousefi, A. A. (**2004**). Conformational changes and phase transformation mechanisms in PVDF solution-cast films. *Journal of Polymer Science Part B: Polymer Physics*, *42*(18), 3487–3491.

20. Basu, B. B. J., & Paranthaman, A. K. (**2009**). A simple method for the preparation of superhydrophobic PVDF–HMFS hybrid composite coatings. *Applied Surface Science*, *255*(8), 4479–4483.

21. Chakradhar, R., Prasad, G., Bera, P., & Anandan, C. (**2014**). Stable superhydrophobic coatings using PVDF–MWCNT nanocomposite. *Applied Surface Science*, *301*, 208–215.

22. Ganesh, V. A., Nair, A. S., Raut, H. K., Yuan Tan, T. T., He, C., Ramakrishna, S., & Xu, J. (**2012**). Superhydrophobic fluorinated POSS–PVDF-HFP nanocomposite coating on glass by electrospinning. *Journal of Materials Chemistry*, *22*(35), 18479.

23. Satapathy, S., Pawar, S., Gupta, P. K., & Varma, K. B. R. (**2011**). Effect of annealing on phase transition in poly(vinylidene fluoride) films prepared using polar solvent. *Bulletin of Materials Science*, *34*(4), 727–733.

24. Razmjou, A., Arifin, E., Dong, G., Mansouri, J., & Chen, V. (**2012**). Superhydrophobic modification of TiO_2 nanocomposite PVDF membranes for applications in membrane distillation. *Journal of Membrane Science*, *415-416*, 850–863.

25. Shi, H., He, Y., Pan, Y., Di, H., Zeng, G., Zhang, L., & Zhang, C. (**2016**). A modified mussel-inspired method to fabricate TiO_2 decorated superhydrophilic PVDF membrane for oil/water separation. *Journal of Membrane Science*, *506*, 60–70.

26. (a) Choi, W., Tuteja, A., Mabry, J. M., Cohen, R. E., & McKinley, G. H. (**2009**). A modified Cassie–Baxter relationship to explain contact angle hysteresis and anisotropy on non-wetting textured surfaces. *Journal of Colloid and Interface Science*, *339*(1), 208–216. (b) Tao, M., Xue, L., Liu, F., & Jiang, L. (**2014**). An Intelligent Superwetting PVDF Membrane Showing Switchable Transport Performance for Oil/Water Separation. *Advanced Materials*, *26*(18), 2943–2948.

27. (a) Hamzah, N., & Leo, C. (**2016**). Fouling prevention in the membrane distillation of phenolic-rich solution using superhydrophobic PVDF membrane incorporated with TiO_2

nanoparticles. *Separation and Purification Technology*, *167*, 79–87. (b) Sahoo, B. N., & Balasubramanian, K. (**2014**). Facile synthesis of nano cauliflower and nano broccoli like hierarchical superhydrophobic composite coating using PVDF/carbon soot particles via gelation technique. *Journal of Colloid and Interface Science*, *436*, 111–121.

28. Li, Y., Li, L., & Sun, J. (**2010**). Bioinspired Self-Healing Superhydrophobic Coatings. *Angewandte Chemie International Edition*, *49*(35), 6129–6133.

29. Das, S., Kumar, S., Samal, S. K., Mohanty, S., & Nayak, S. K. (**2018)** A Review on Superhydrophobic Polymer Nanocoatings: Recent Development and Applications. *Industrial & Engineering Chemistry*, *Research*, *57*, 2727–2745.

30. Lissau, J. S., Gardner, J. M., & Morandeira, A. (**2011**). Photon Upconversion on Dye-Sensitized Nanostructured ZrO_2 Films. *The Journal of Physical Chemistry C*, *115*(46), 23226–23232.

31. (a) Feng, X., Zhang, S., Wu, H., & Lou, X. (**2015**). A novel folic acid-conjugated TiO2–SiO_2 photosensitizer for cancer targeting in photodynamic therapy. *Colloids and Surfaces B: Biointerfaces*, *125*, 197–205. (b) Xue, C., Li, X., Jia, S., Guo, X., & Li, M. (**2016**). Fabrication of robust superhydrophobic fabrics based on coating with PVDF/PDMS. *RSC Advances*, *6*(88), 84887–84892.

32. Vinodgopal, K., Hua, X., Dahlgren, R. L., Lappin, A. G., Patterson, L. K., & Kamat, P. V. (**1995**). Photochemistry of $Ru(bpy)_2(dcbpy)^{2+}$ on Al_2O_3 and TiO_2 Surfaces. An Insight into the Mechanism of Photosensitization. *The Journal of Physical Chemistry*, *99*(27), 10883–10889.

33. Yan, L., Wang, K., & Ye, L. (**2003**). Superhydrophobic property of PVDF/$CaCO_3$ nanocomposite coatings. *Journal of Materials Science Letters*, *22*(23), 1713–1717.

34. Meng, S., Mansouri, J., Ye, Y., & Chen, V. (**2014**). Effect of templating agents on the properties and membrane distillation performance of TiO_2-coated PVDF membranes. *Journal of Membrane Science*, *450*, 48–59.

35. Li, F., Li, Q., & Kim, H. (**2013**). Spray deposition of electro-spun TiO_2 nanoparticles with self-cleaning and transparent properties onto glass. *Applied Surface Science*, *276*, 390–396.

36. Qing, Y., Yang, C., Yu, N., Shang, Y., Sun, Y., Wang, L., & Liu, C. (**2016**). Superhydrophobic TiO_2 /polyvinylidene fluoride composite surface with reversible wettability switching and corrosion resistance. *Chemical Engineering Journal*, *290*, 37–44.

37. Zhang, Z., Zhang, W., Wang, F., Tolbert, L. M., & Blalock, B. J. (**2012**). Analysis of the switching speed limitation of wide band-gap devices in a phase-leg configuration. *2012 IEEE Energy Conversion Congress and Exposition (ECCE)*.

38. Walsh, A., Buckeridge, J., Catlow, C. R. A., Jackson, A. J., Keal, T. W., Miskufova, M., . . . Sokol, A. A. (**2013**). Limits to Doping of Wide Band Gap Semiconductors. *Chemistry of Materials*, *25*(15), 2924–2926.

39. Gorun, S. M.; Bench, B. A.; Carpenter, G.; Beggs, M. W.; Mague, J. T.; Ensley, H. E. (**1998**). Synthesis and structural characterization of non-planar perfluoro phthalonitriles. J. *Fluorine Chem*. 91, 37-40.

40. Bench, B. A.; Beveridge, A.; Sharman, W. M.; Diebold, G. J.; van Lier, J. E.; Gorun, S. M. (**2002**). Introduction of bulky perfluoroalkyl groups at the periphery of zinc perfluorophthalocyanine: chemical, structural, electronic, and preliminary photophysical and biological effects. *Angew. Chem. Int. Ed*, 41, 747-750.

41. Malmonge, L. (**2000**). Thermal analysis of conductive blends of PVDF and poly(o-methoxyaniline). *Polymer*, *41*(23), 8387–8391.

42. Jaleh, B., & Jabbari, A. (**2014**). Evaluation of reduced graphene oxide/ZnO effect on properties of PVDF nanocomposite films. *Applied Surface Science, 320*, 339–347.

Chapter 3

Superhydrophobic and Photoreactive Hybrid Composite Surfaces.

3.1. Introduction.

The removal of discharged organic dyes from wastewaters around the globe have proven challenging, these have contributed to environmental pollution and are potentially lethal to marine life. Dyes from wastewater are known to be very persistent and resistive to environmental biodegradation because of their chemical characteristics. Numerous attempts have been made to mitigate organic dyes in industrial wastes, chemical decomposition methods have been generally effective for the purpose of wastewater remediation. Organic photosensitizers, such as phthalocyanines, are effective for photooxidation against organic dyes. To maximize their photoreactivity, aggregation must be reduced, as this reduces photoactivity. This can be overcome by coating phthalocyanines onto a high surface area material, solid supports such as TiO_2, SiO_2, and Al_2O_3 are commonly used to properly disperse the catalyst for maxima output. Other stable solid supports like resins, graphite, and zeolites have also been studied as supports.

It is known that inorganic photosensitizers, for example, tungsten oxide (WO_3) and TiO_2 can resist oxidation,[1] but TiO_2 is only active in a small region of the electromagnetic spectrum and exhibits a wide band-gap requiring UV light for the creation of reactive electron-hole pairs.[2] TiO_2 also has the drawback of exhibiting an unfavorably fast recombination rate of the charge carriers, reducing photoreactivity.[3] It is of great interest to improve this performance, but efforts to narrow the TiO_2 band gap through doping have been ineffective[2,4] the absorption has not been shifted significantly toward the Visible-NIR region of the solar spectrum, where most of the energy of solar radiation is concentrated.[5]

A number of organic photosensitizers have also been explored, such as Rose Bengal, which can generate singlet molecular delta oxygen, $^1\Delta_g$ $^1O_2$ from its triplet ground-state by contact with the

triplet ground state, $^3\Sigma_g$ $^3O_2$. Rose Bengal is susceptible to attack and degradation by the reactive oxygen species it produces, a major difficulty for this photosensitizer.[6] The need for more robust photosensitizers with optimal absorption energies that can withstand the photo-oxidative conditions is of great importance, therefore, a class of bioinspired organic photosensitizers that can survive electrophilic, nucleophilic and radical attacks has been reported in literature. They are robust with refractory properties being imparted by the presence of C-F bonds.[7]

The prototypical molecule is zinc 1,4,8,11,15,18,22,25-octakisfluoro-2,3,9,10,16,17,23,24-octakis-perfluoro(isopropyl) phthalocyanine, F_{64}PcZn. One of the great advantages of this class of molecules is the presence of frontier orbital energy gaps that remain relatively unchanged with modification of the ligands or fluorinated substituents, thus allowing structural variations without significant shifts in the Q-band light absorption energies in the 600 - 800 nm visible/NIR region.[7,8] The enhanced chemical robustness can be attributed to the bulky aliphatic perfluoroalkyl groups, not present in either the all-aromatic, planar F_{16}Pc scaffold[9] or the parent H_{16}Pc molecule.

It has been demonstrated that the incorporation of fluoro-perfluoroalkyl Pc's in polysiloxane polymers has resulted in robust materials that can be used to form coatings capable of bleaching a model pollutant (methyl orange) deposited as films on the coating surface. The efficiency of the photosensitizer is lowered as a result of aggregation and uneven disbursement, prompting the use of solid support to greater efficiency.[10] These photocatalytic Pc's can be used to the same effect when supported on porous materials used as water filters.[11]

A further increase in the efficiency of surface protection by coatings in aqueous environments could be achieved by enhancing their hydrophobicity. Therefore, modifications of surface morphology are of interest, especially if contact angles (CA) increase from less than 90° (hydrophilic) to over 150 ° (hydrophobic to superhydrophobic) and water hysteresis is lesser than

10°.[12] A polymer that has been shown to be susceptible to modification of surface morphology is polyvinylidene fluoride (PVDF).[13] PVDF has good thermal stability with melting temperature (T_m) of approximately 175 °C and glass transition temperature (T_g) of approximately – 35 °C. The high T_m and the low T_g gives PVDF a broad temperature working range of – 20 °C to + 130 °C, this excellent combination of properties has contributed to its wide application. PVDF has an excellent track record and great interest in the areas of energy collection, sensors, biomaterials, etc. PVDF has been explored as part of a nano-composite, this interest is attributed to the thermal, dielectric, optical, mechanical and electrical properties comparable to other smart materials.

Methyl orange (MO), an anionic dye, is a model for common azo dyes found in the paper, textile and chemical industries; it was therefore used for this study as a model to determine the pattern of degradation by the hybrid catalyst. MO has a single azo bond and with a sulfonate group, these give the dye its principal characteristic of bright orange color and solubility in water. MO may be destroyed by coming in contact with the reactive oxygen species produced by the hybrid catalyst. By the process of oxidation, the dye will start to lose its color as the azo linkage is destroyed. Further degradation of MO and the primary oxidative byproducts continues by the process of photooxidation to complete mineralization.

Our research studies have demonstrated the production of PVDF-based hybrid organic-inorganic coatings that can generate reactive oxygen species while retaining increases in hydrophobicity from surface modification. Such coatings promise to combine the self-cleaning effects derived from high hydrophobicity, which prevents adherence of aqueous contaminants, and photoactivity, which destroys any contaminants which do adhere to the surface.

3.2. Materials and Methods.

3.2.1. General.

All chemicals and solvents were obtained commercially and used as received unless stated otherwise. Methyl orange, (MO), (4-[[(4-dimethylamino) phenyl]-azo] benzene sulfonic acid, sodium salt), **Figure 3.1. (a)**, was obtained from Alfa-Aesar. Ammonium hydrogen carbonate (NH_4HCO_3) and polyvinylidene fluoride (PVDF, M_w = 180,000) were purchased from Sigma-Aldrich. NH_4HCO_3 was treated as described below. Fumed TiO_2 was purchased from Evonik (P25 Aeroxide®, surface area (BET) 50 m^2/g). Deionized H_2O (Milli-Q, resistivity15 $M\Omega$-cm) was used to prepare all solutions. MO solutions were filtered through 0.45 μm cellulose filters. Fluorinated phthalocyanine, $F_{64}PcZn$, was prepared from zinc acetate and perfluoro-(4,5-di-isopropyl) phthalonitrile as previously described.[7]

3.2.2. Instruments.

Contact angles (θ) were measured with a RAMA-HART goniometer using the sessile water drop method, 5 μL volume. The reported θ values are averages of measurements at five different points on the surface of each film. Uncoated glass slides, θ = 45° were used as a control. Scanning electron micrographs were obtained on a Verios 460 Extreme High-Resolution Scanning Electron Microscope (XHR SEM) at the Princeton University PRISM Institute. Differential scanning calorimetry (DSC) experiments were performed aerobically with a TA model 2920 instrument. Thermogravimetric analyses (TGA) were performed with a TA model Q500 instrument. Experiments were conducted under a blanket of N_2. A 10 °C/min heating gradient was used for both DSC and TGA unless noted otherwise. Photochemical experiments were carried out using a

300 W OSRAM halogen lamp placed 14 cm from the sample, average illuminance of 109,000 lux measured with an Extech EasyView 33 light meter, **Figure 3.1b**, was obtained by excluding wavelengths below 300 nm with a 60 mm glass filter (S-83605, Sargent Laboratory). Solution and solid-state electronic spectra were obtained with a Cary 500 UV-Vis-NIR spectrophotometer. For time-dependent MO concentration measurements, the absorbance at 465 nm was converted to concentrations using the Beer-Lambert equation with ε_{465} = 24,600 mol^{-1} cm^{-1}. Glass slides, 75 x 25 x 1 mm (VistaVision) were washed with acetone and deionized water and dried in the oven at 80 °C.

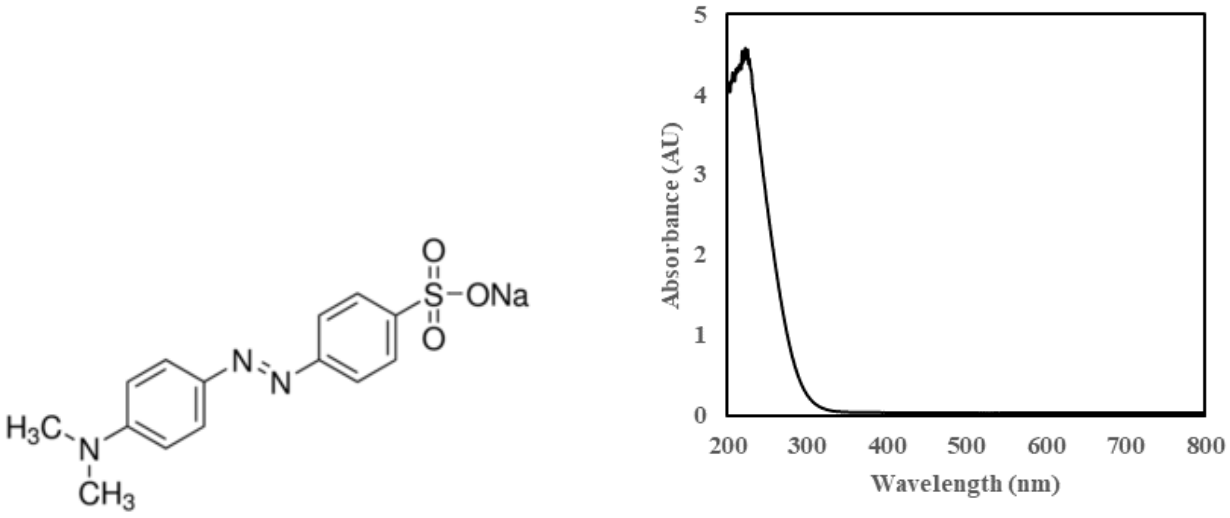

Figure 3.1. (a) The structure of methyl orange (MO); **(b)** The UV-vis spectrum of the glass filter used to remove radiation of wavelengths below 400 nm.

3.2.3. Sample Preparation.

The description of the composition of materials uses the union and inclusion symbols "∪" and "∈", which mean "deposited on" and "embedded in", respectively.

3.2.3.1. Preparation of NH_4HCO_3 of controlled particle size.

Described in detail in **chapter 2.**

3.2.3.2. Preparation of $F_{64}PcZn$ coated TiO_2, $F_{64}PcZn \cup TiO_2$.

Described in detail in **chapter 2.**

3.2.3.3. Preparation of NH_4HCO_3-doped PVDF films, $NH_4HCO_3 \in PVDF$.

Described in detail in **chapter 2.**

3.2.3.4. Preparation of TiO_2-doped PVDF films, $TiO_2 \in PVDF$.

Described in detail in **chapter 2.**

3.2.3.5. Preparation of TiO_2 and NH_4HCO_3-doped PVDF films, $(NH_4HCO_3 \& TiO_2) \in PVDF$.

Described in detail in **chapter 2**.

3.2.3.6. Preparation of $F_{64}PcZn$-coated TiO_2-doped PVDF films, $(F_{64}PcZn \cup TiO_2) \in PVDF$.

Described in detail in **chapter 2**.

3.2.3.7. Preparation of $F_{64}PcZn$-coated TiO_2 and NH_4HCO_3-doped PVDF films, $(F_{64}PcZn \cup TiO_2 \& NH_4HCO_3) \in PVDF$. $F_{64}PcZn \cup TiO_2$.

Described in detail in **chapter 2.**

3.2.4. Preparation of TiO_2-doped PVDF films, $TiO_2 \in PVDF$.

The coating material was prepared by adding 10 ml of DMF to 1.0 g PVDF pellets, then heating at 60 °C with constant stirring for 45 minutes. This formed a gel-like solution. The solution was allowed to cool to room temperature before adding P25 TiO_2 (0.03 g, 3% solids) and stirring 30 minutes at 600 rpm. The resulting mixture was coated on glass slides, the coated surface was allowed to evaporate for 6 hours at room temperature, then baked at 80 °C in an oven for 48 hours.

3.2.5. Photodegradation of solutions of model contaminant Methyl Orange (MO).

Doped PVDF-coated glass slides were laid flat and immersed in 3 ml aqueous 2.5 x 10^{-5} M MO solutions and the solution was illuminated with109,000 lux (~1 Sun) along the axis perpendicular to the center of the solution surface for 30 minutes at a time. Following irradiation, the films were washed with 2 ml of DI water and the washings combined with the solution from the irradiation. The combined liquids were filtered through a 0.45 μm pore-size cellulose membrane prior to UV-Vis-NIR analysis. A total of 210 minutes irradiation was done with samples taken every 30 minutes for kinetic studies.

3.2.6. Self-cleaning Efficacy.

Coated slides were held at 0, 45 or 90 ° relative to horizontal, and were then treated with 1.0 mL of a 2.5 x 10^{-5} M solution of MO sprayed onto their surfaces. The solutions were allowed to evaporate in the air, and their optical densities measured by reflectance spectroscopy. The samples were then irradiated perpendicular to the surface with 27,250 lux and their optical densities again measured by reflectance spectroscopy.

3.3. Results.

3.3.1. Results and Observations.

The composition of the materials described herein is a coating made of an organic polymer (here PVDF) with an inorganic additive (here TiO_2) coated with a photosensitizer (here $F_{64}PcZn$, **Figure 3.2**) and a second additive composed of particles of a volatile solid (NH_4HCO_3). After thermolysis

and volatilization of the second, volatile additive, the final coating has a roughened morphology that leads to increased hydrophobicity as measured by the contact angle θ of the coating. A prior report had shown that the incorporation of the volatile salt ammonium hydrogen carbonate (NH_4HCO_3) into PVDF films increases the value of θ to over 150° after thermolysis and volatilization.[13] The photoactivity of TiO_2 and of $F_{64}PcZn$ have also been demonstrated repeatedly in the literature.[14]

a) b)

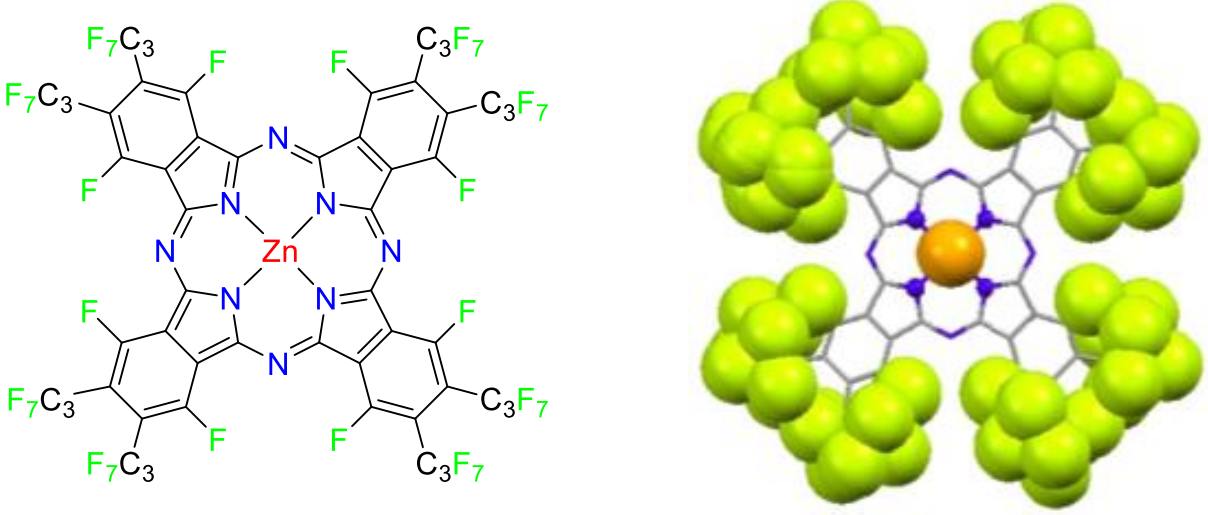

Figure 3.2. The perfluorinated phthalocyanine $F_{64}PcZn$. Chemical structure and the Single-crystal X-Ray structure depicting Zn and F as van der Waals spheres. Color code: Zn, orange; F, green; N, blue; C, gray.

A schematic representation of how the coated surfaces were prepared in **Chapter 2**. A solution of PVDF in DMF is the starting point for each type of coating. The control coating is untreated PVDF. Other coatings may then include either TiO_2 or $F_{64}PcZn$ coated onto TiO_2 support ($F_{64}PcZn \cup TiO_2$) as a photosensitizer or photocatalyst and may also include the volatile salt NH_4HCO_3. Thermolysis and volatilization of NH_4HCO_3 within the PVDF generates a roughened surface as voids and channels are created by the decomposition of the salt and the subsequent outgassing as shown in **Chapter 2**. The ultimate coating prepared as the goal of this work (($F_{64}PcZn \cup TiO_2 \& NH_4HCO_3) \in PVDF$) contains both the TiO_2 supported phthalocyanine photocatalyst and the volatile salt to generate increased hydrophobicity. The temperature-dependent changes in the composition and contact angles of the materials were summarized previously in **Table 2.5.**

3.3.2. Photochemical Studies.

One of the major advantages of the bulky, *iso* C_3F_7 substituents of $F_{64}PcZn$ as shown in **Figure 3.2. (b),** clearly displayed van der Waals spheres impeded deactivating stacking in solution, and for this study, in solid-state where $F_{64}PcZn$ is impregnated onto solid supports.[7] The coated surfaces for this study were described in chapter 2 and images were shown and analyzed in **section 2.3.7**.

The UV-Vis traces of MO solutions from the photolysis with broad-spectrum light using the coated surface slides ($F_{64}PcZn \cup TiO_2 \& NH_4HCO_3) \in PVDF$ and ($TiO_2 \& NH_4HCO_3) \in PVDF$ are shown in **Figure 3.7 (a)** and **(b)**. The figure revealed a steady decrease in MO concentration with photolysis time for films incorporating these catalysts. The decrease in MO concentration in solution is greater for the ($F_{64}PcZn \cup TiO_2 \& NH_4HCO_3) \in PVDF$ surface than for the ($TiO_2 \& NH_4HCO_3) \in PVDF$ surface. Plots of the ln[MO] vs. time for the photocatalyzed decomposition of MO by ($F_{64}PcZn \cup TiO_2 \& NH_4HCO_3) \in PVDF$ and ($TiO_2 \& NH_4HCO_3) \in PVDF$ films are shown below in **Figure 3.3 (d)**. Contact angles following UV-

visible light irradiation were previously listed in **Table 2.5**. Each value is the average of 5 independent determinations. The standard errors of the means are given in parentheses

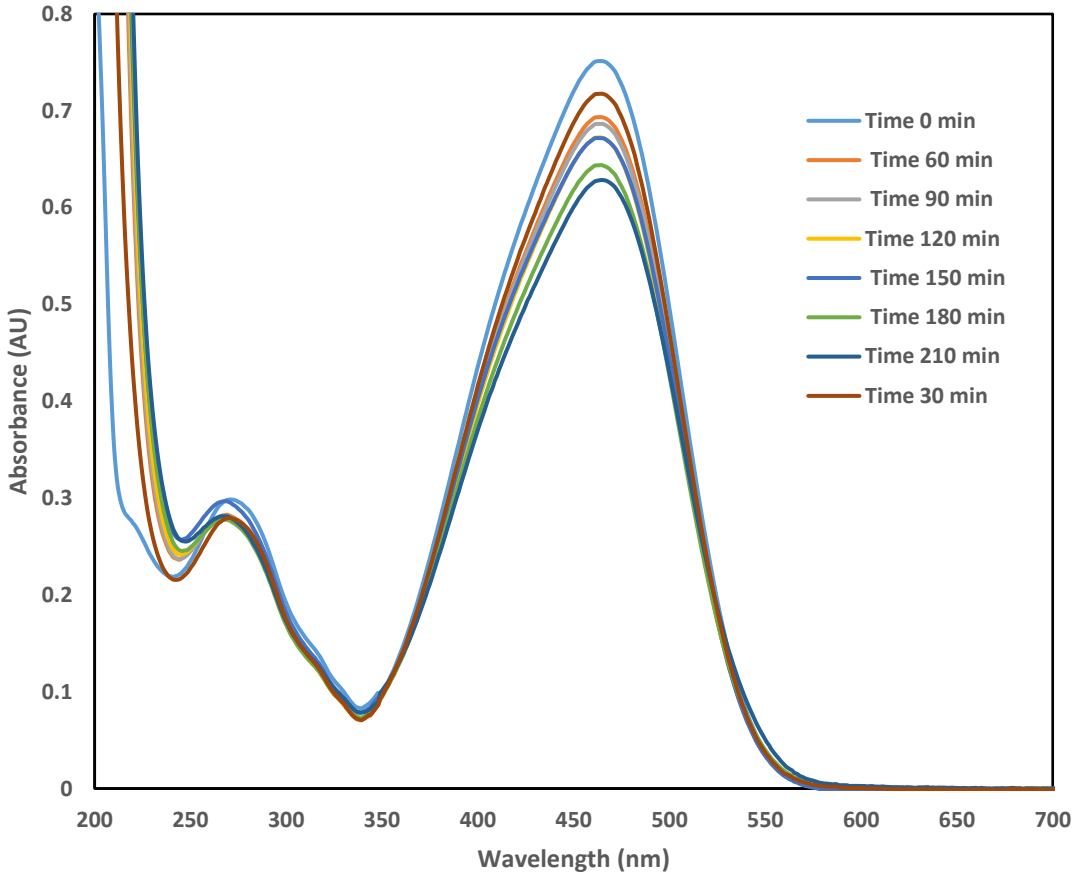

Figure 3.3. (a) Time-dependent *broad spectrum light* photodegradation of 0.025 mM MO by $TiO_2 \in$PVDF.

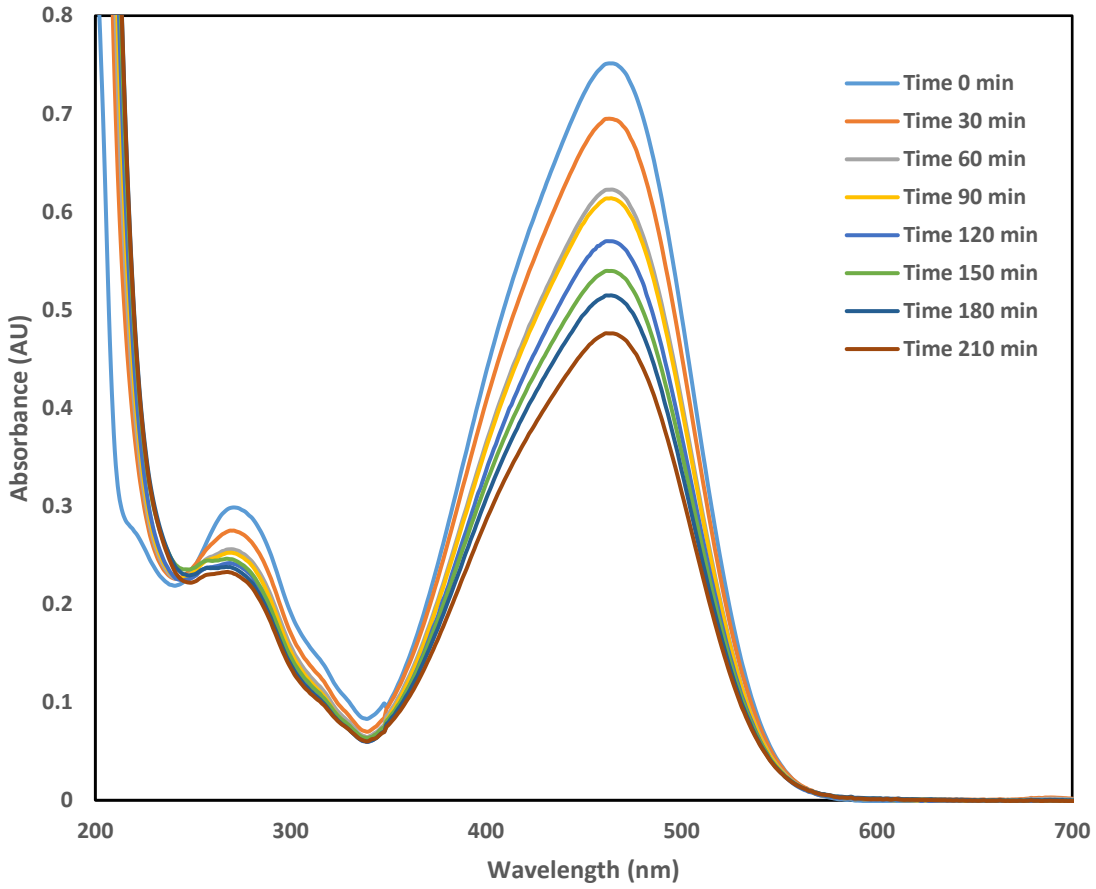

Figure 3.3. (b) Time-dependent *broad-spectrum light* photodegradation of 0.025 mM MO by (F_{64}PcZn $\cup TiO_2) \in$PVDF films.

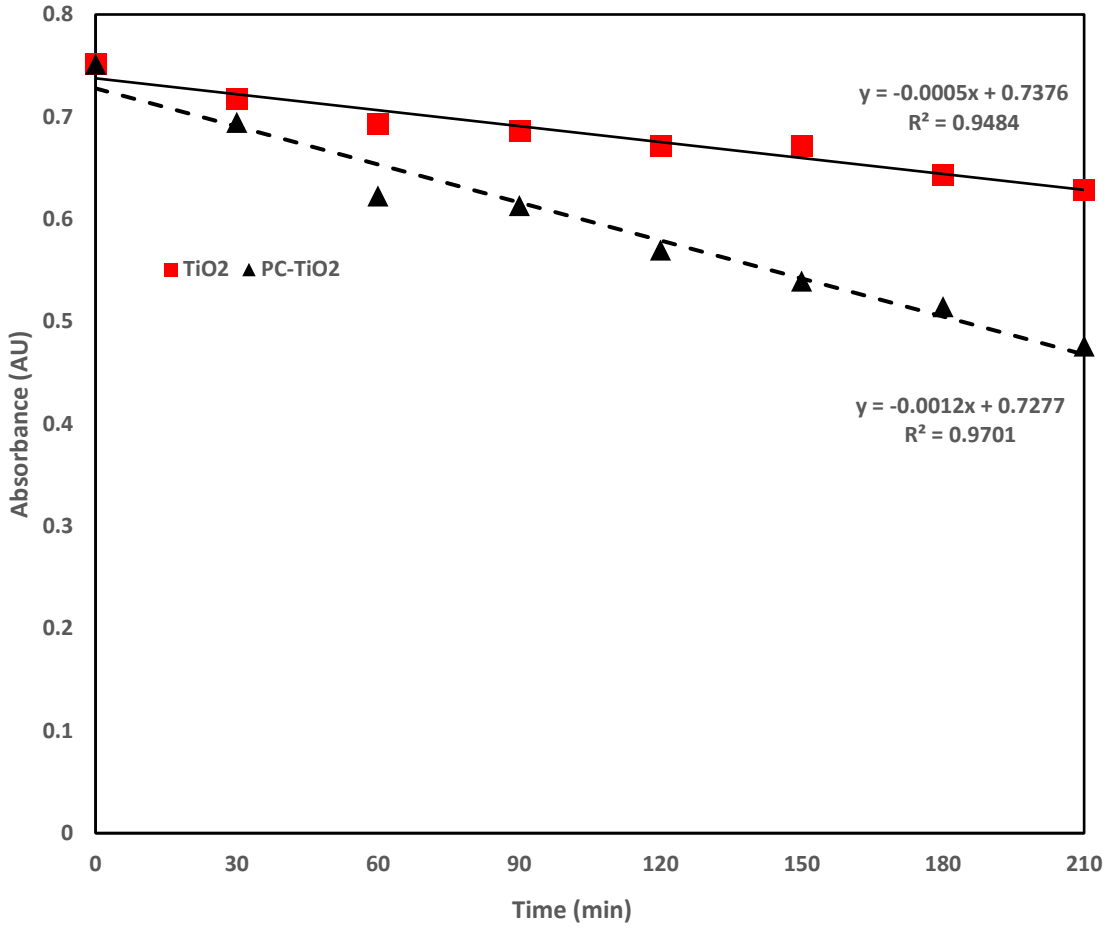

Figure 3.3. (c) Time-dependent *broad-spectrum light* photodegradation of 0.025 mM MO by Plot of the absorbance vs. time. The $TiO_2 \in PVDF$ and $(F_{64}PcZn \cup TiO_2) \in PVDF$ films are abbreviated TiO_2 and $Pc \cup TiO_2$, respectively.

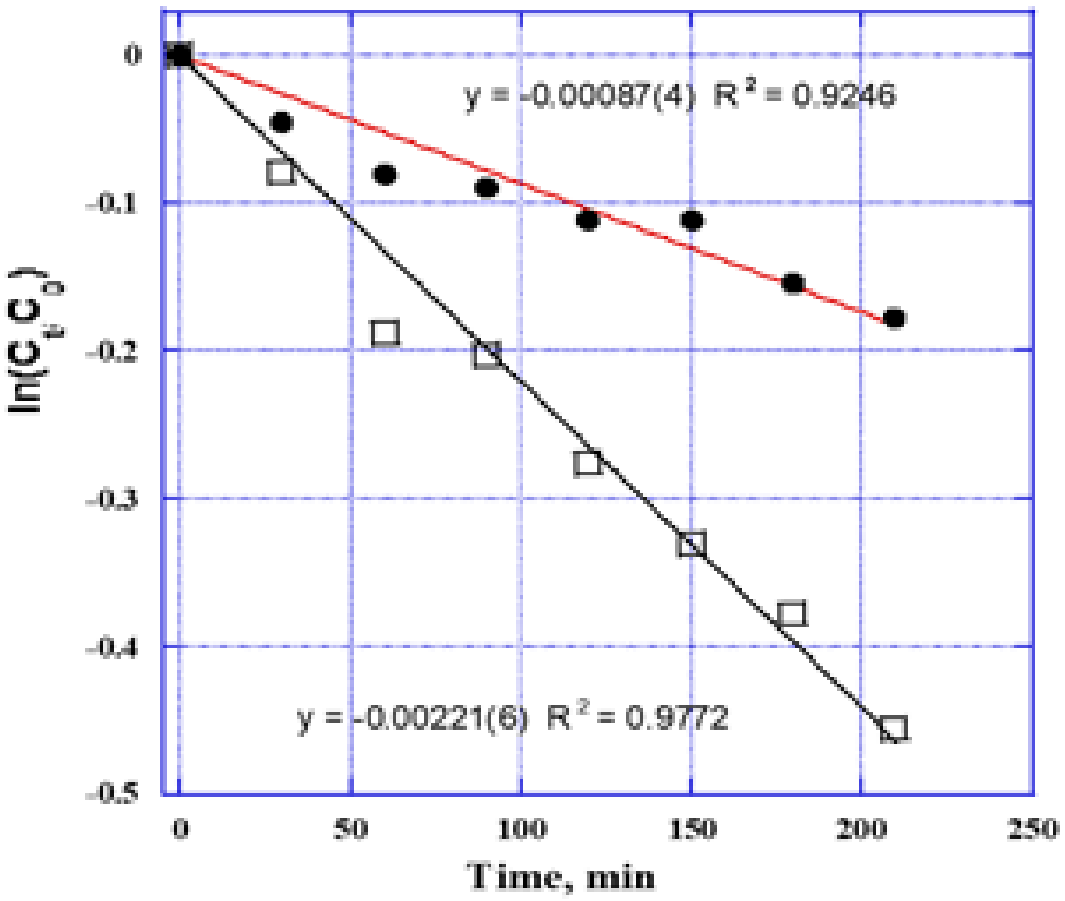

Figure 3.3 (d) Time-dependent *broad-spectrum light* photodegradation of 0.025 mM MO by Plot of the ln(C_t/C) vs. time. The TiO_2∈PVDF and (F_{64}PcZn∪TiO_2)∈PVDF films are abbreviated TiO_2 and Pc∪TiO_2, respectively.

The electronic spectra for the degradation of MO over the same surfaces using only visible radiation, λ > 300 nm are shown in **Figure 3.4 (a)** and **(b)**. Plots of the ln[MO] vs. time for the photocatalyzed decomposition of MO by (F_{64}PcZn∪TiO_2& NH_4HCO_3) ∈PVDF and (TiO_2&NH_4HCO_3)∈ PVDF films are shown below in **Figure 3.4 (c)**. Only minimal photolysis is seen with the TiO_2 catalyst using visible light, as these wavelengths are not absorbed by TiO_2. The small amount of degradation observed is

attributed to stray ambient UV light. The MO degradation results in the absence of light are shown in **Figure 3.5.**

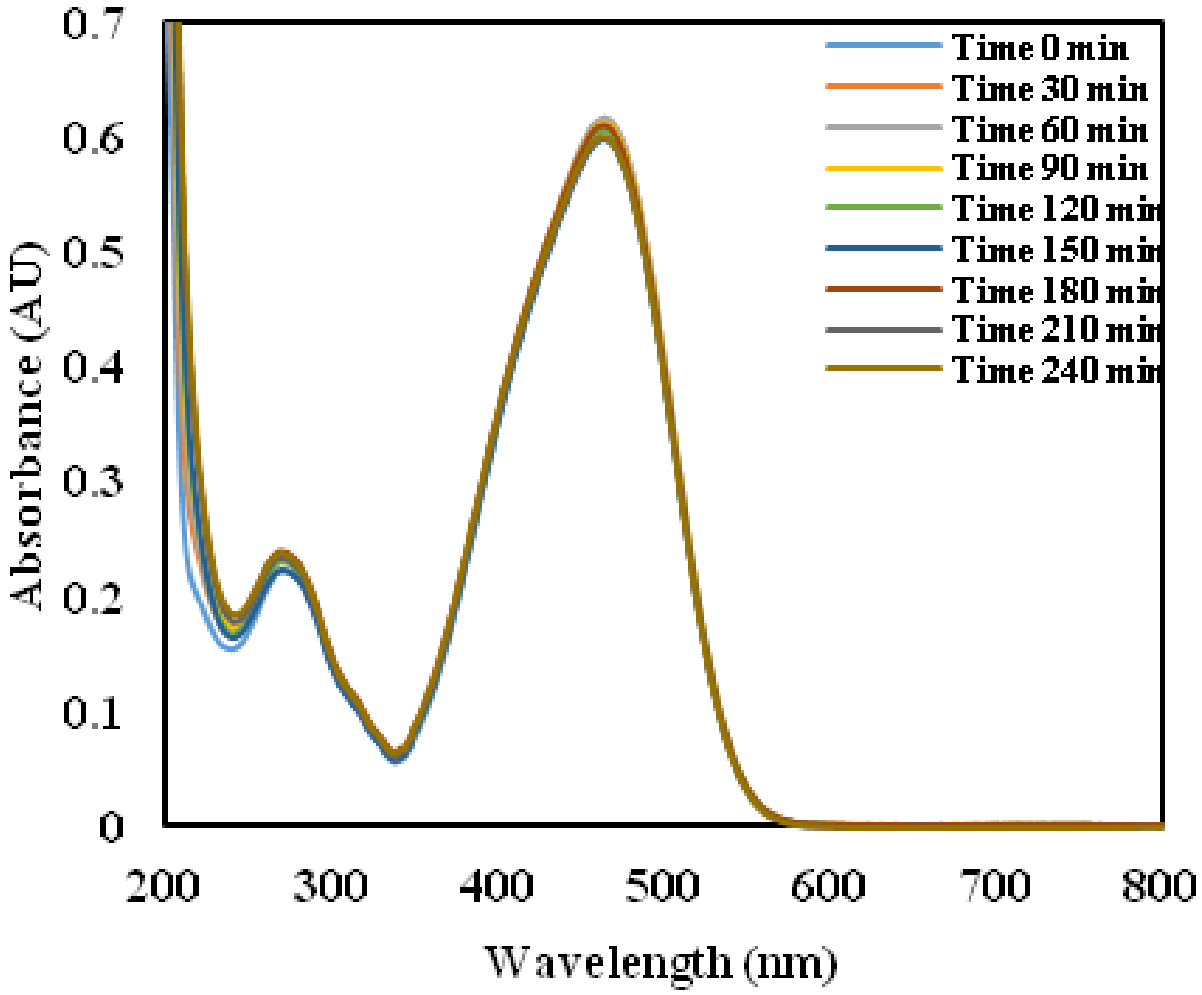

Figure 3.4 (a) Time-dependent *visible light* photodegradation of 0.025 mM MO by $TiO_2 \in$PVDF film.

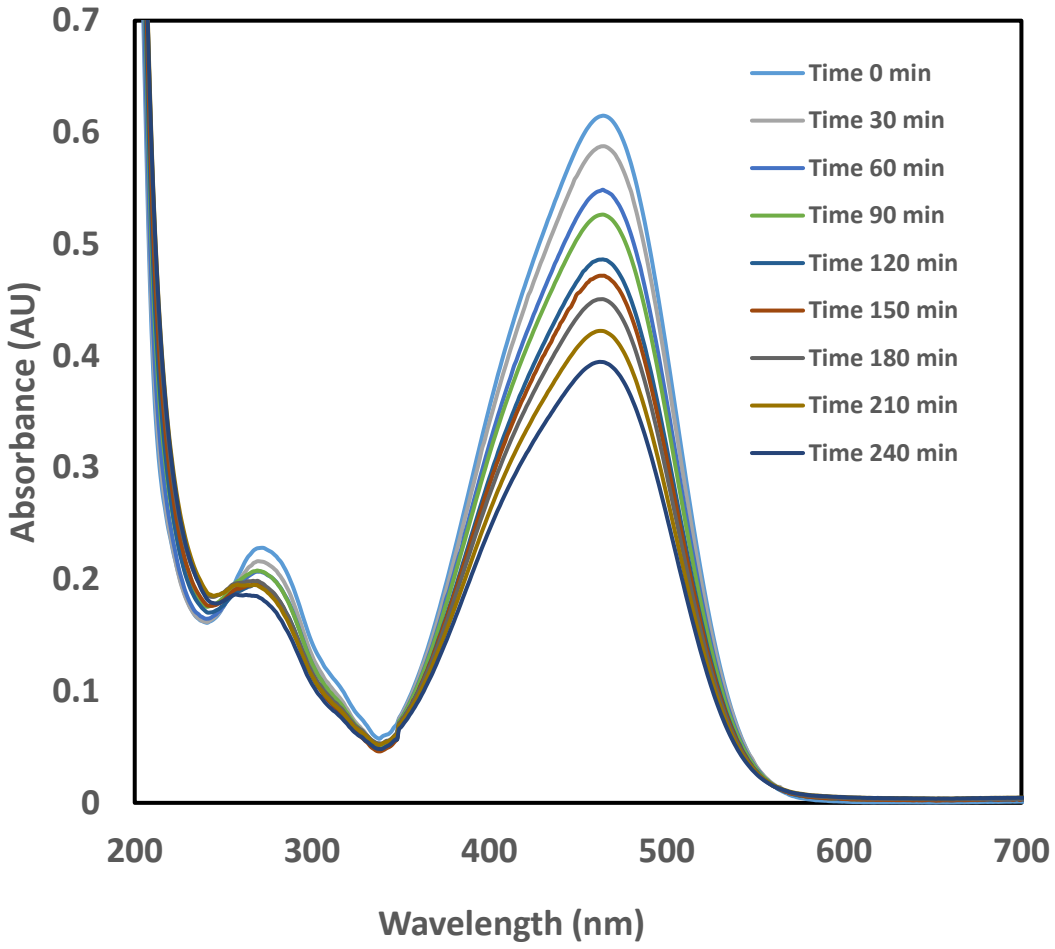

Figure 3.4. (b) Time-dependent *visible light* photodegradation of 0.025 mM MO by $(F_{64}PcZn \cup TiO_2) \in PVDF$ films.

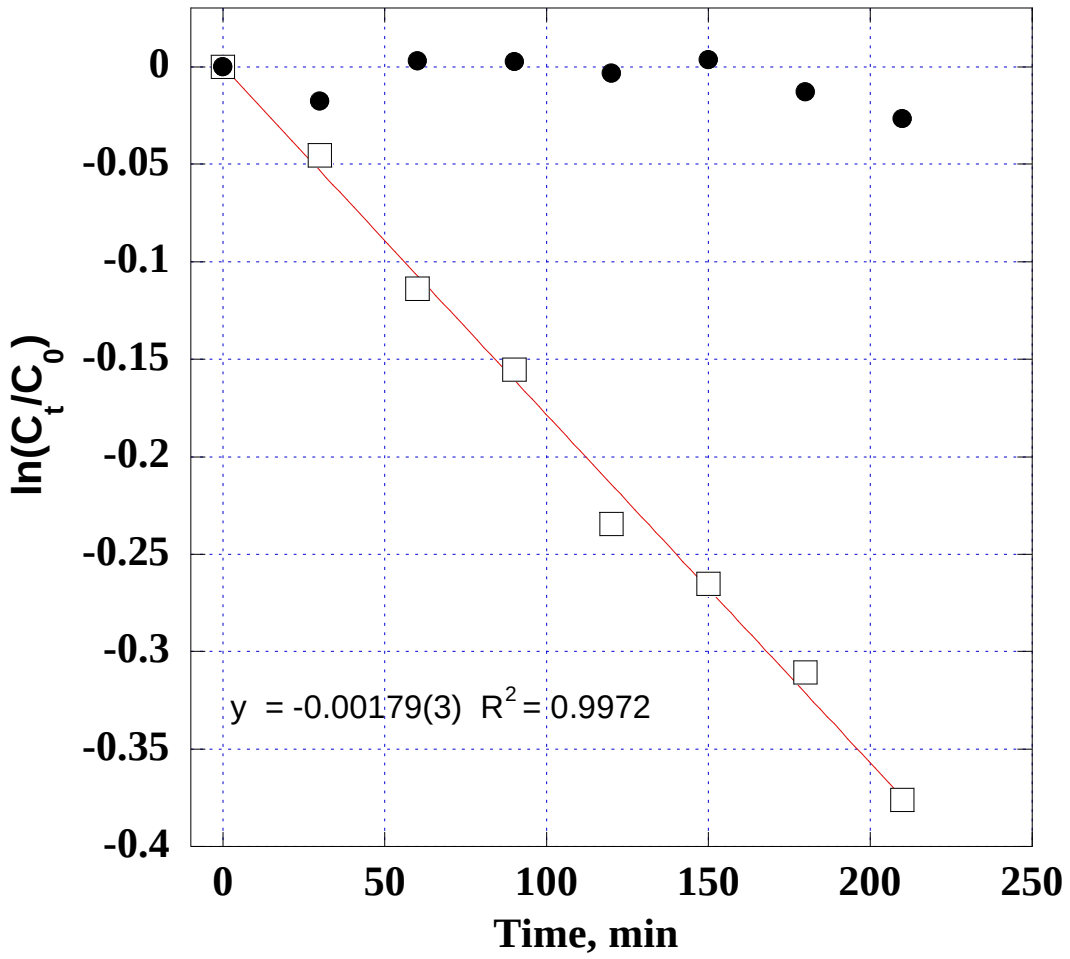

Figure 3.4 (c) Photodegradation of MO by (TiO_2&NH_4HCO_3) ∈PVDF (•) and ($F_{64}PcZn$∪TiO_2& NH_4HCO_3)∈PVDF (□) films using *visible light*.

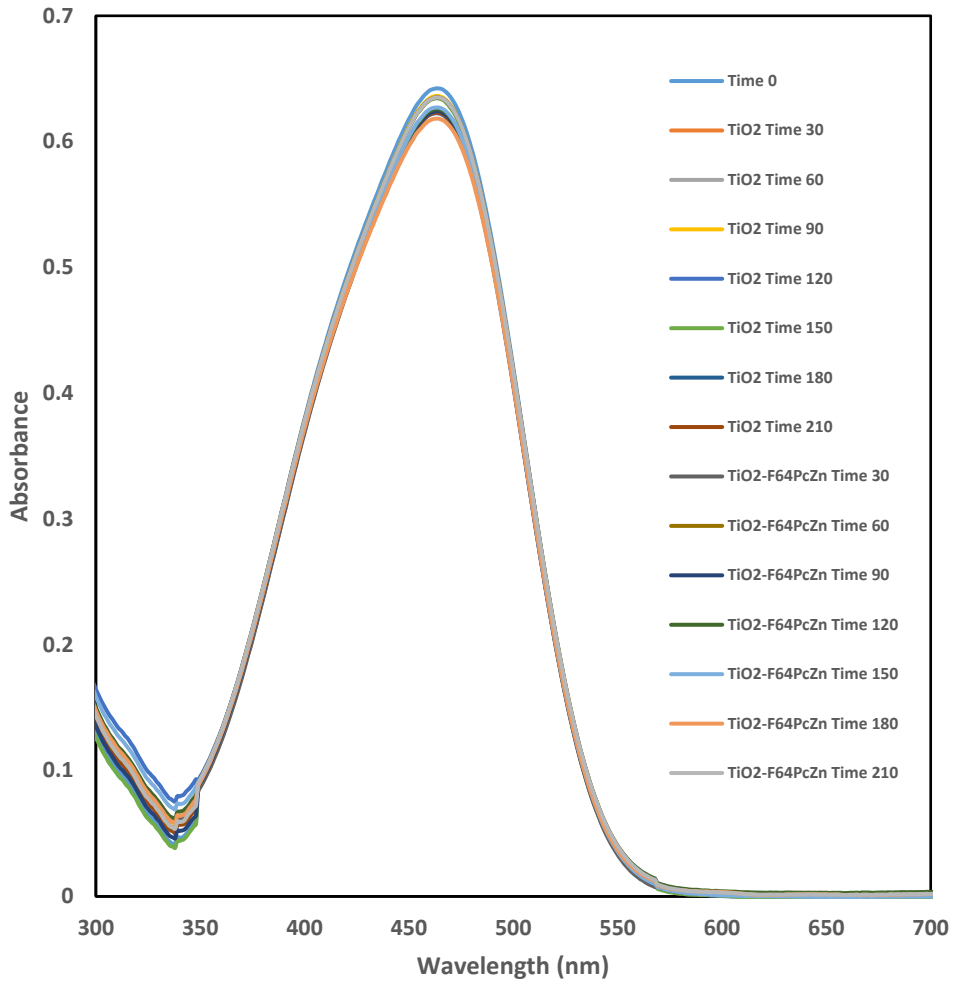

Figure 3.5 (a) Time-dependent MO degradation in the absence of light, but in the presence of $TiO_2 \in PVDF$ and $(F_{64}PcZn \cup TiO_2) \in PVDF$ films.

The electronic spectra for the degradation of MO in the absence of light on the surface of $TiO_2 \in PVDF$ and $(F_{64}PcZn \cup TiO_2) \in PVDF$ films shown in **Figure 3.5 (a)** revealed no activities compared to the degradation of MO in the presence of broadband light. This phenomenal revealed that both catalysts are only active in the presence of light. The time-dependent MO degradation

graph in the absence of light, but in the presence of both $TiO_2 \in PVDF$ and $(F_{64}PcZn \cup TiO_2) \in PVDF$ films, maintained a constant straight-line suggesting no activities as shown in **Figure 3.5 (b).**

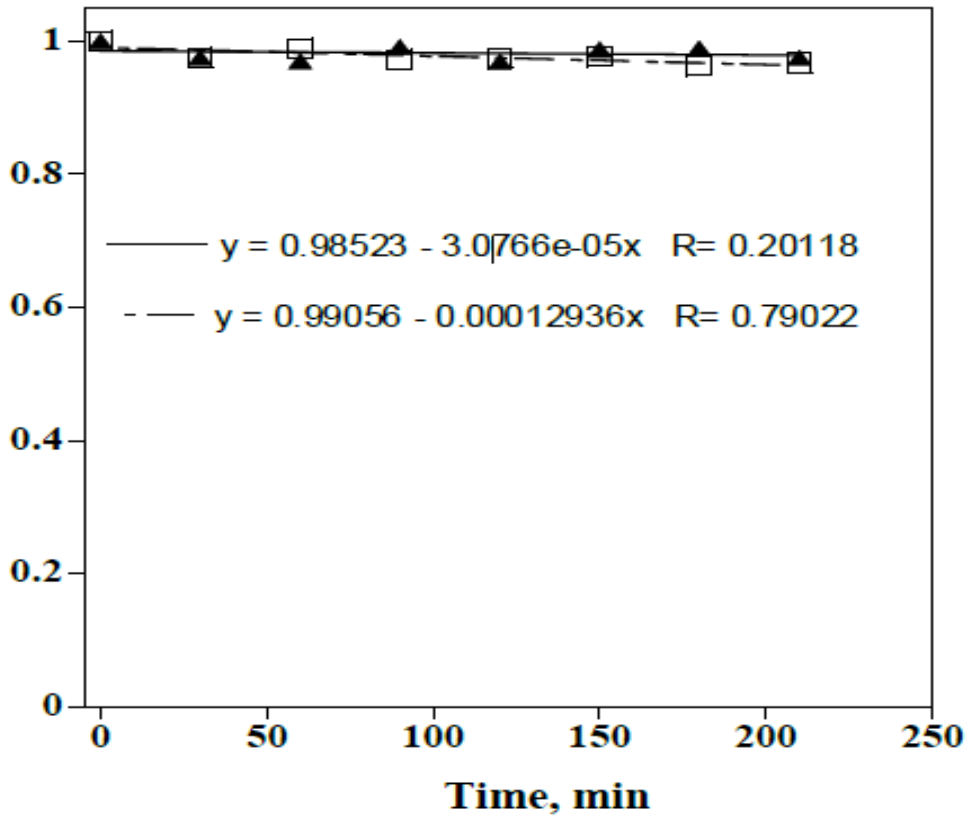

Figure 3.5 (b) Time-dependent MO degradation in the absence of light, but in the presence of $TiO_2 \in PVDF$ and $(F_{64}PcZn \cup TiO_2) \in PVDF$ films.

The reusability of the catalyst was tested, a daily preparation of a fresh batch of MO was photodegraded on the surface of the same $(F_{64}PcZn \cup TiO_2 \& NH_4HCO_3) \in PVDF$ film was repeated for 7 consecutive days. The effectiveness and durability data are shown in **Figure 3.6**. The photoreactive surface proved efficient without loss of activities as a result of MO photodegradation

by the photocatalyst. A supplementary graph of daily rate of MO degradation is shown embedded inside the main figure.

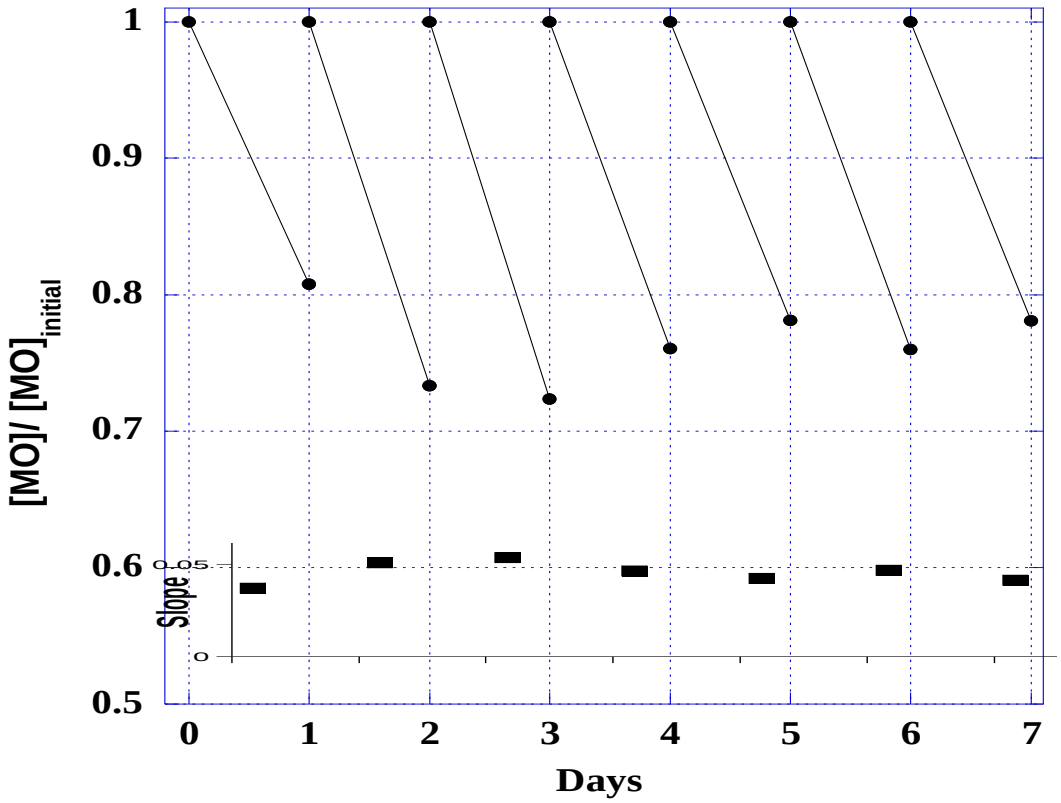

Figure 3.6. Photodegradation of daily prepared MO batches by the same (F_{64}PcZn∪TiO_2 &NH_4HCO_3)∈PVDF film repeated for 7 consecutive days. Inset: daily rates of MO degradation.

3.3.3. Testing for Self-cleaning Effectiveness.

An extensive test was carried out in order to determine if there were an improvement in the self-cleaning capability of coated surfaces with the combination of superhydrophobic and photooxidative properties. The degradation of MO solutions as a function of the surfaces as they

were oriented in certain positions. The substrates were: untreated PVDF (no enhanced hydrophobicity, no photocatalysis), $NH_4HCO_3 \in$PVDF after thermolysis and volatilization (enhanced hydrophobicity but no photocatalysis), and (F_{64}PcZn$\cup TiO_2$& NH_4HCO_3)$\in$PVDF after thermolysis and volatilization (enhanced hydrophobicity and photocatalysis). The substrates were held in different positions: vertical (90°), inclined (45°), and horizontal (0°), then sprayed with a representative aliquot of measured aqueous solution of MO (one standard spray of 1.0 mL representing 8 micrograms MO), allowed to air-dry, and either irradiated for 1 hr. or not irradiated. The MO optical density was evaluated by UV-Vis reflectance spectroscopy. This allowed evaluation of the self-cleaning characteristics of the coated surfaces: the determination of whether the MO solution was readily rejected by the low energy surface, represented by the superhydrophobicity of surfaces; and whether the MO solution is degraded due to photoreactive characteristics of the coated surfaces. The normalized observed values are represented below in **Table 3.1.**

Table 3.1. Optical Density at 460 nm of MO Solutions Applied to Surfaces Function of Surface Position.

Surface	Vertical (90 °)		Inclined (45 °)		Horizontal (0 °)	
	Not Irradiated O.D. x 10^3	Irradiated O.D. x 10^3	Not Irradiated O.D. x 10^3	Irradiated O.D. x 10^3	Not Irradiated O.D. x 10^3	Irradiated O.D. x 10^3
PVDF	**5.5**	**5.5**	**13.1**	**13.1**	**17.4**	**17.4**
$NH_4HCO_3 \in$PVDF	**0.15**	**0.15**	**2.6**	**2.6**	**9.7**	**9.7**
(F_{64}PcZn$\cup TiO_2$& NH_4HCO_3)$\in$PVDF	**1.3**	**~0**	**4.4**	**~0**	**5.5**	**~0**

3.4. Discussion.

3.4.1. Discussions and Analysis.

The photocatalyst used for this study is a fluoroalkyl-substituted fluoro-phthalocyanine, R_FPc, very robust and resistive to oxidation. These are the building blocks for the recent construction of self-oxidation-resistant catalytic materials based on organic molecules.[7,8] The Zinc(II) complexes, with a d^{10} transition, closed-shell metal, anchored in the macrocenter of the phthalocyanine, photogenerated singlet oxygen, $^1O_2$, which affords the oxidation of dyes and other organic compounds.[6]

Phthalocyanines have been explored for the purpose of photoreactivity. The integration of metal-R_FPc into Si-based polymers has proven results as hybrid coating materials, they have been used for decolorizing surface-bonded dyes, such as methyl orange (MO) and rhodamine b (Rb) in the presence of broad-spectrum light.[10,11] Surfaces can be self-cleaning if they are both photoreactive and superhydrophobic. The addition of a modified surface to a coating to improve its hydrophobicity, without hampering the photooxidative or bleaching capacity, could have important applications as the coating may both repel hydrophilic, water-borne contaminants while deactivating any adsorbing, hydrophobic contaminants by photogenerated singlet oxygen and other ROS. Therefore, the addition of sensitizers that can produce singlet oxygen or other reactive oxygen species can result in a self-cleaning surface: superhydrophobic photo-oxidative coated surface.

3.4.2. Catalytic Photo-oxidation.

Fluorinated phthalocyanines such as $F_{64}PcZn$, when incorporated into polysiloxane, photocatalytically bleach MO applied as a solid-layer on the polymer surface,[10] or, when supported on membranes, degrade aqueous dye solutions.[11] The effectiveness in degrading MO solutions by PVDF coated films containing fluorinated phthalocyanines that are morphologically modified to enhance surface hydrophobicity was determined following the protocols as described in the Experimental section. The MO solutions revealed two known peaks with UV-visible absorption spectra: λ_{maxima} at 464 and 270 nm, shown in **Figure 3.3.** The intensity of the MO spectrum decreases over time as the MO solution is degraded by catalytic photooxidation. As expected, control coatings prepared from PVDF or $NH_4HCO_3 \in$PVDF were not photoreactive upon irradiation with light. On the other hand, $(TiO_2\&NH_4HCO_3)\in$PVDF coated surfaces irradiated with broad-spectrum (λ = 200 - 900 nm) exhibited photoactivity and degradation of MO solution as shown in **Figure 3.3 (a)**. The MO solution degradation was fitted with a linear ln (C_0/C_t) vs. time equation shown in **Figure 3.3 (d),** following pseudo-first-order kinetics.

Notably, the PVDF matrix is also degraded after irradiation, as evidenced by a decrease in θ from 136(0.8) to 114(0.4)° for the $(TiO_2\&NH_4HCO_3)\in$PVDF coated surfaces upon irradiation with light, **Table 2.5**. The degradation pattern of the matrix can be observed by FTIR spectroscopic interpretation. **Figure 3.7** shows the changes observed in the FTIR spectra of $(TiO_2\&NH_4HCO_3)\in$PVDF films before and after 4 hours of broadband irradiation.

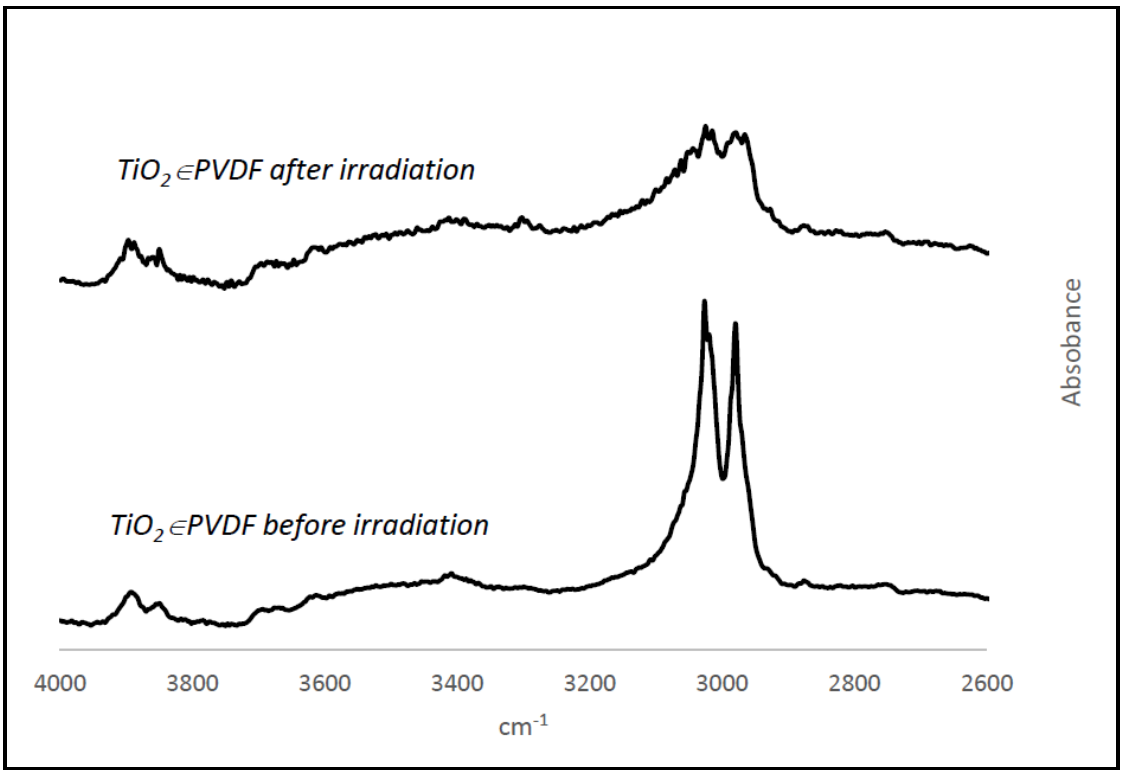

Figure 3.7. FTIR spectra of $TiO_2 \in$PVDF before and after broadband (UV-Vis) irradiation. Only the C-H stretching region is displayed: there is a reduction in the intensity of the C-H stretching absorptions after irradiation.

The intensities of the C-H stretching modes are significantly diminished as seen in **Figure 3.7**, pointing to changes in the chemical composition of the film as a result of the irradiation. **Figure 3.8,** shows morphological changes observed in the SEM with $(TiO_2 \& NH_4HCO_3) \in$PVDF coated surfaces before and after broad-spectrum irradiation. After irradiation, it is noted that the TiO_2 particles embedded in the polymer matrix became visible as small white dots, an indication of the polymer surface erosion due to degradation of the polymer that previously covered the TiO_2 particles. This degradation leading to surface erosion of the polymer can result in the weakening of the polymer and potentially causing erosion of the protected substrate, allowing oxidation and corrosion of metal substrates.

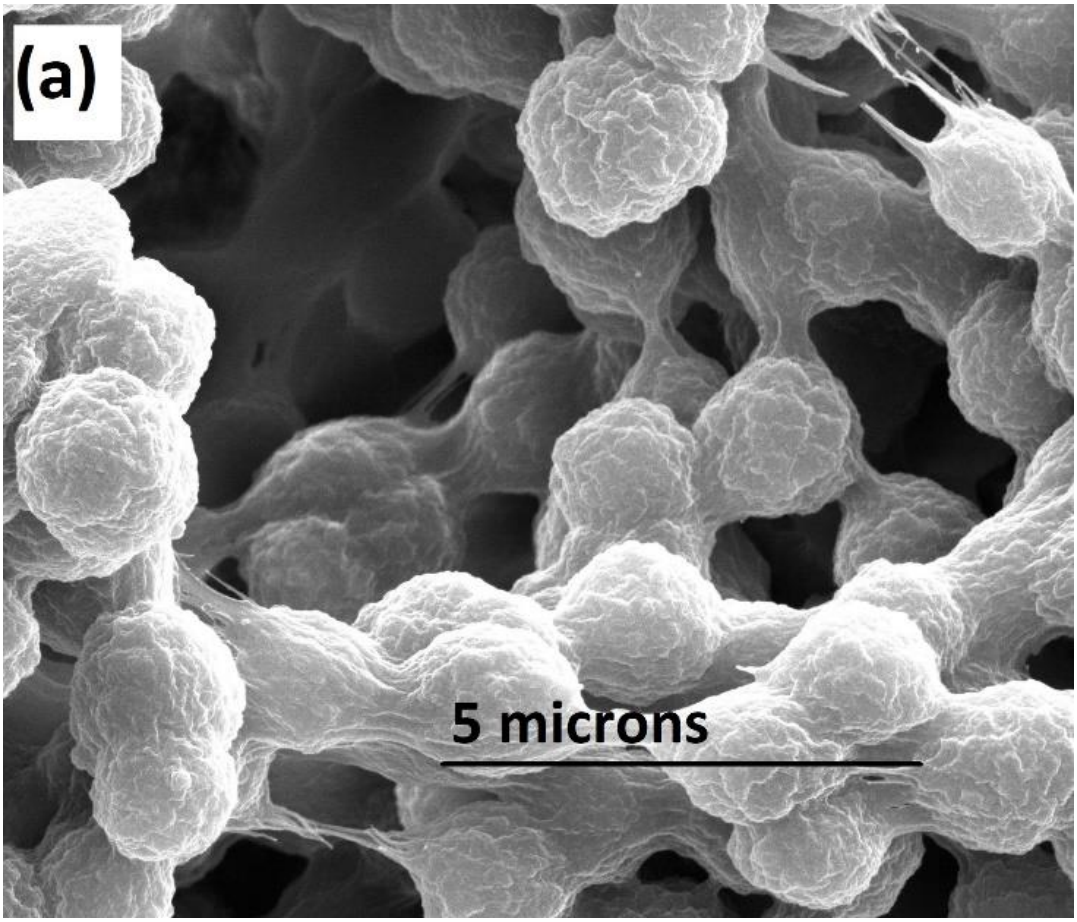

Figure 3.8. (a) SEM micrographs of $TiO_2 \in$PVDF films before broad spectrum irradiation. *"Image courtesy of Abdul Azeez"*.

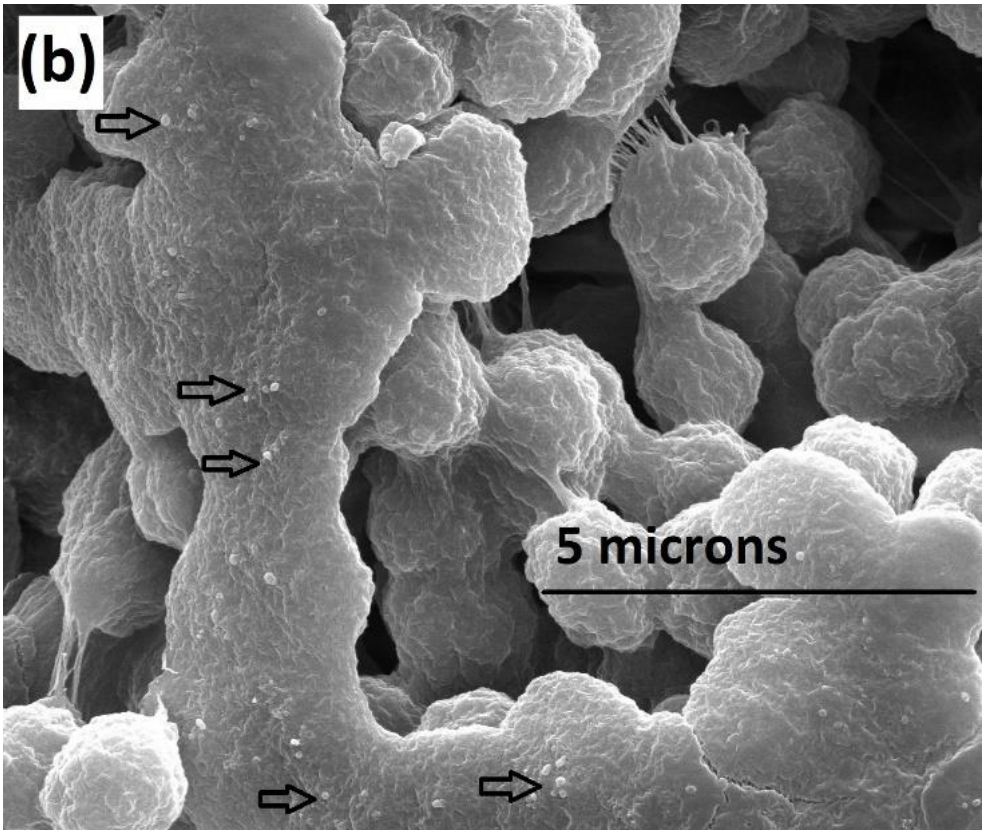

Figure 3.8. (b) SEM micrographs of $TiO_2 \in$PVDF films after (b) broad-spectrum irradiation. Photodegradation of the PVDF film can be observed around the TiO_2 particles, which appear as white dots. Several of the TiO_2 particles are marked with arrows. *"Image courtesy of Abdul Azeez".*

Photodegradation of PVDF embedded with TiO_2 photosensitizer is a known phenomenon and is usually ascribed to dehydrofluorination or depolymerization.[25 a-c] Either of these two processes would be supported by the observed changes in FTIR and SEM analysis.

According to the mechanism outlined by Zulfiqar, *et al,* [25 c] the scission of the C-H bond as a result of thermal instability at elevated temp (350 °C) under vacuum gives rise to the cleaving of the C-H bond, which causes the weakening of the C-F bond resulting in an overall loss of HF. As a result, the C-C backbone rearranged, forming the C=C bond [25]. FTIR spectroscopy **Figure 3.9 (a)** also revealed and the formation of the C=C bond after irradiation, as observed at about 1610 cm^{-1} after irradiation.

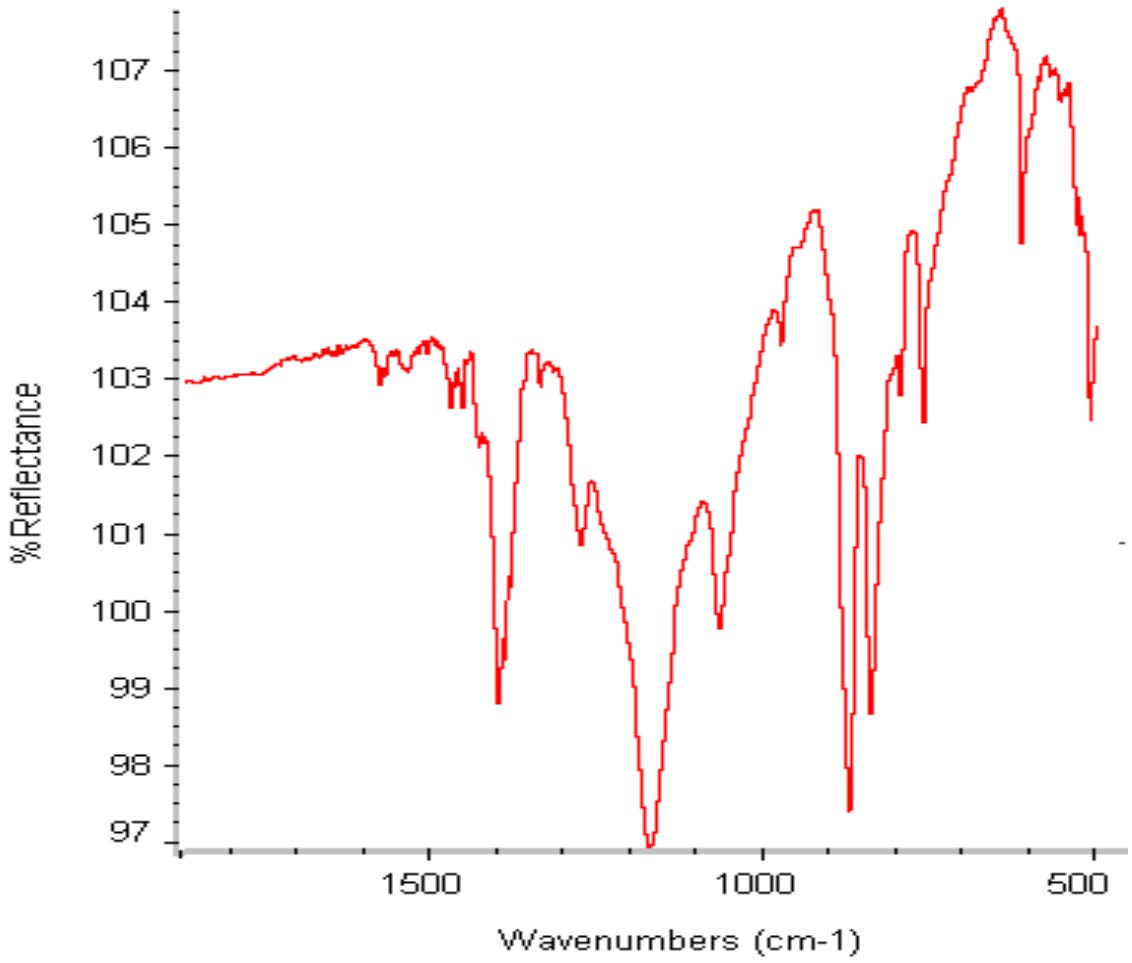

Figure 3.9. (a) FTIR spectra of TiO_2)∈PVDF film formation of new C=C due to the release of C-H and C-F bond.

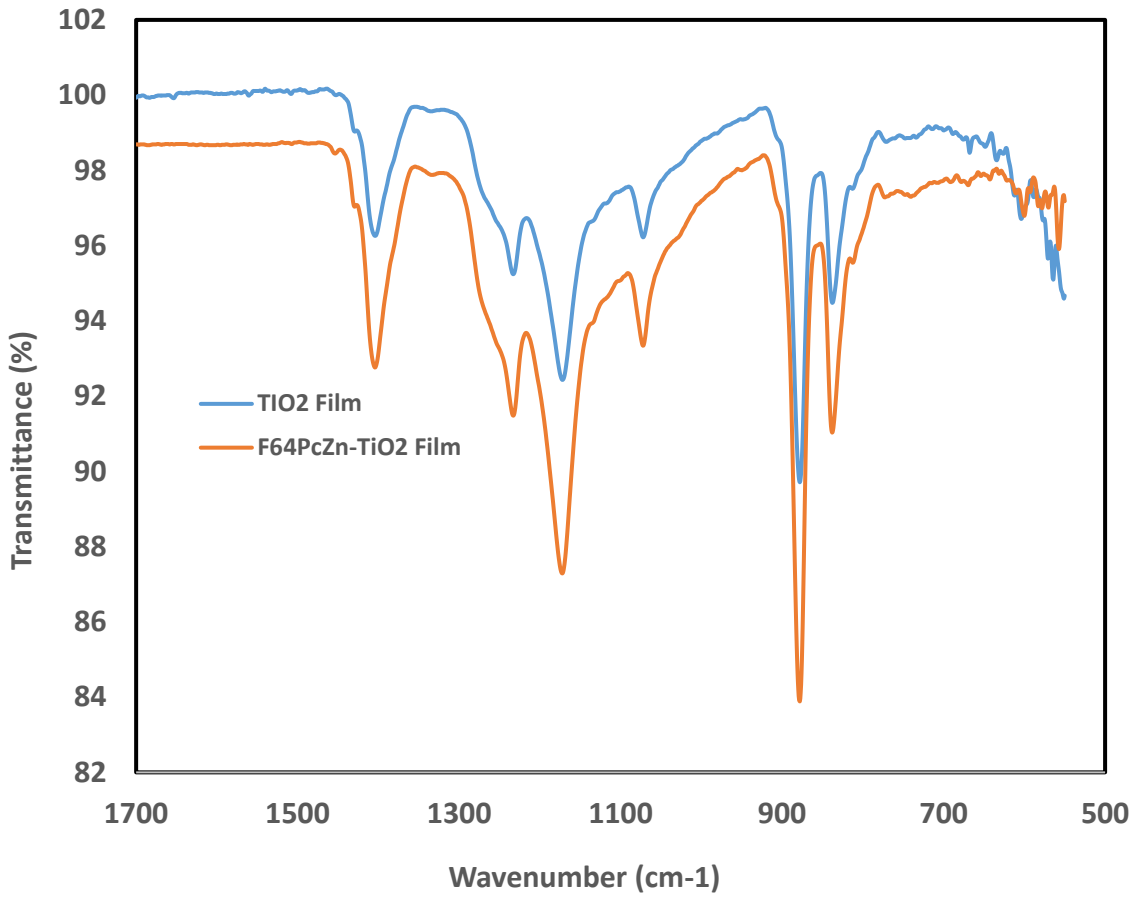

Figure 3.9. (b) FTIR spectra of PVDF film and F64PcZn∪TiO_2)∈PVDF film after irradiation, films remain stable and no changes noticed.

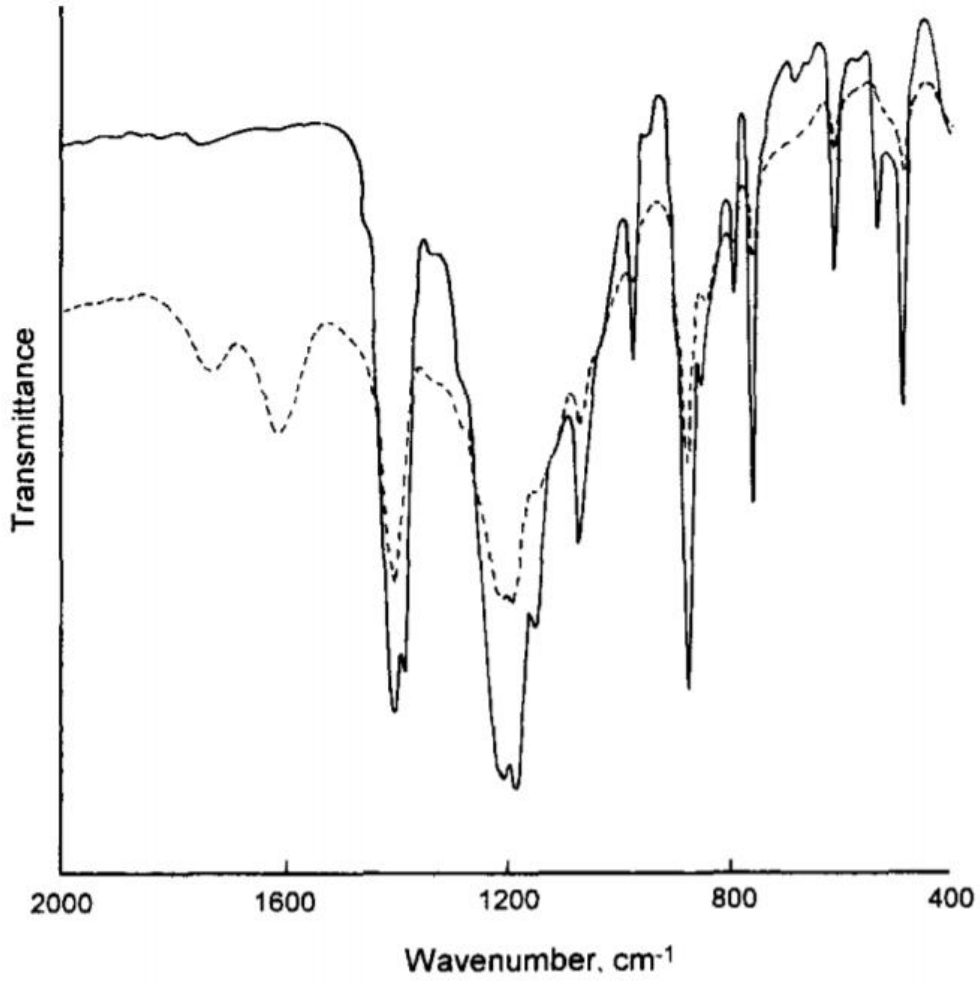

Figure 3.10. Thermal degradation of PVDF at 350 °C, the formation of new C=C due to the release of C-H and C-F bond. *"Reproduced with permission from Elsevier".* [25c]

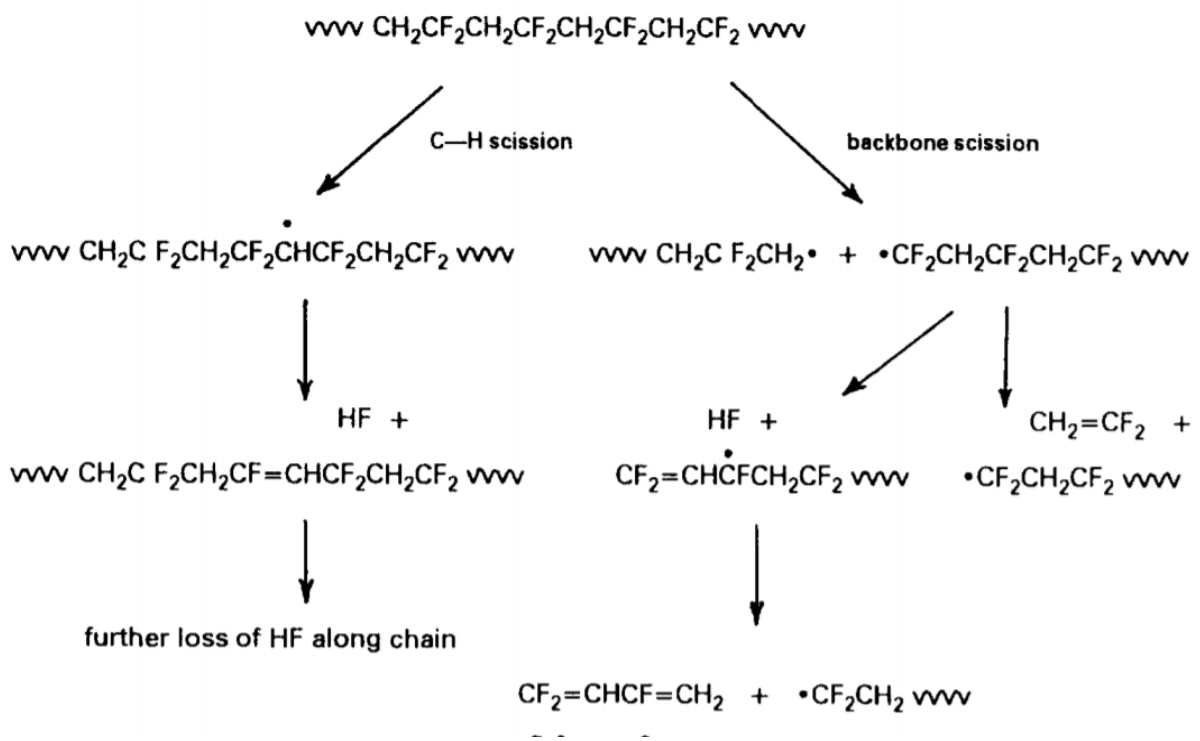

Figure 3.11. Degradation pathways of PVDF, with scission of C-H bond leading to C=C bond formation. *"Reproduced with permission from Elsevier".* [25c]

Although PVDF with TiO_2 is degraded under UV illumination, degradation of the PVDF matrix is not expected when the included catalyst is $F_{64}PcZn \cup TiO_2$. Whether by IR, SEM, or CA, no photodegradation was observed with the supported phthalocyanine catalyst on TiO_2 coated films. The incorporation of $F_{64}PcZn$ photosensitizer supported onto TiO_2, ($F_{64}PcZn \cup TiO_2$ &NH_4HCO_3) $\in$ PVDF material, results in increased photoreactivity. As shown in **Figure 3.3 (d)**, the MO degradation proceeds about 2.5 times faster (0.00221/0.00087) for ($F_{64}PcZn \cup TiO_2$ &NH_4HCO_3)$\in$PVDF than for (TiO_2&NH_4HCO_3)$\in$PVDF. The faster degradation rate can be attributed to the combined effects of TiO_2 and $F_{64}PcZn$, both excited by the broadband spectrum light, and both causing MO decomposition. The degradation of PVDF caused by TiO_2 is not noticed when TiO_2 is coated with $F_{64}PcZn$ photosensitizer. The coating appears to diminish the

deleterious effect of TiO_2 on the PVDF film as seen on our SEM images. The contact angle θ of the coated films remain constant following irradiation at 144(0.4)°.

The photoreactive coated films were studied in order to separate the two photosensitizer effects on MO degradation. An optical filter was used to cut-off wavelengths below 300 nm. The photon energy in the UV region is required to excite P25 TiO_2,[26] so any effects are from $F_{64}PcZn$ photosensitizer alone, supported on a material photochemically inert at these wavelengths. As is shown in F**igure 3.4 (a)**. MO solution is not degraded in the presence of $(TiO_2\&NH_4HCO_3)\in$PVDF with visible irradiation alone.

The two photocatalysts (TiO_2 and $F_{64}PcZn$) appear to work independently, degrading MO in solutions. The degradation of MO in solutions catalyzed by $(F_{64}PcZn\cup TiO_2\&NH_4HCO_3)\in$PVDF using broad-spectrum light will comprise both TiO_2 catalysis from the UV component and $F_{64}PcZn$ catalysis from the visible component, which are relatively different in energy production during irradiation. The determined value, 0.00221, is close to the sum of the values while using $(F_{64}PcZn \cup TiO_2\&NH_4HCO_3) \in$PVDF with visible light, 0.00179 (only $F_{64}PcZn$ is active) and $(TiO_2\&NH_4HCO_3)\in$PVDF with broad-spectrum light ($TiO_2\in$PVDF is active), 0.00087: 0.00179 + 0.00087 = 0.00266 > 0.00221. It is noted that the rate of the combined catalyst ($F_{64}PcZn \cup TiO_2$ with broad-spectrum light) is approximately 17% lower than the sum of independently-acting catalyst determined rates (TiO_2 with broad-spectrum light + $F_{64}PcZn\cup TiO_2$ with visible light). When catalysts $F_{64}PcZn$ and TiO_2 independently catalyze the degradation of MO solution separately, they proved to be slightly more efficient than when they coupled together as one catalyst on the same MO solution sample. Thus, the catalytic effects are nearly additive, as noted previously when aqueous suspensions of the same catalysts were used to degrade MO solution.[11]

The degradation process of these two photosensitizers are known to generate different reactive species, at least during the initial stages of photoreaction: TiO_2 reacts through a hole and electron ($h^+ + e^-$) process, forming oxidizing, cationic holes upon the photo-promotion of a valence electron into a conduction band, while the $F_{64}PcZn$ forms $^1O_2$ by excitation transfer from the triplet state of the photosensitizer. For the reaction of TiO_2, the electron can reduce dioxygen to superoxide anion, this anion moves on to generate other reactive oxygen species (ROS) for the purpose of degrading MO in solution. The cationic hole, on the other hand, will carry out different chemistry. The cationic hole can react with water to generate very reactive hydroxyl radical species. These ROS act on MO in solution by first destroying the azo (N=N) moiety and eventually continues to degrade and mineralize the dye to the elemental oxides. The degradation process of MO in solution has been extensively researched, although, the complexity of the degradation routes pose a problem: the exact mechanism of the dye degradation is not firmly established.[28] There are proposed mechanisms, one of the accepted mechanism is provided by Li *et al* [28], shown below.

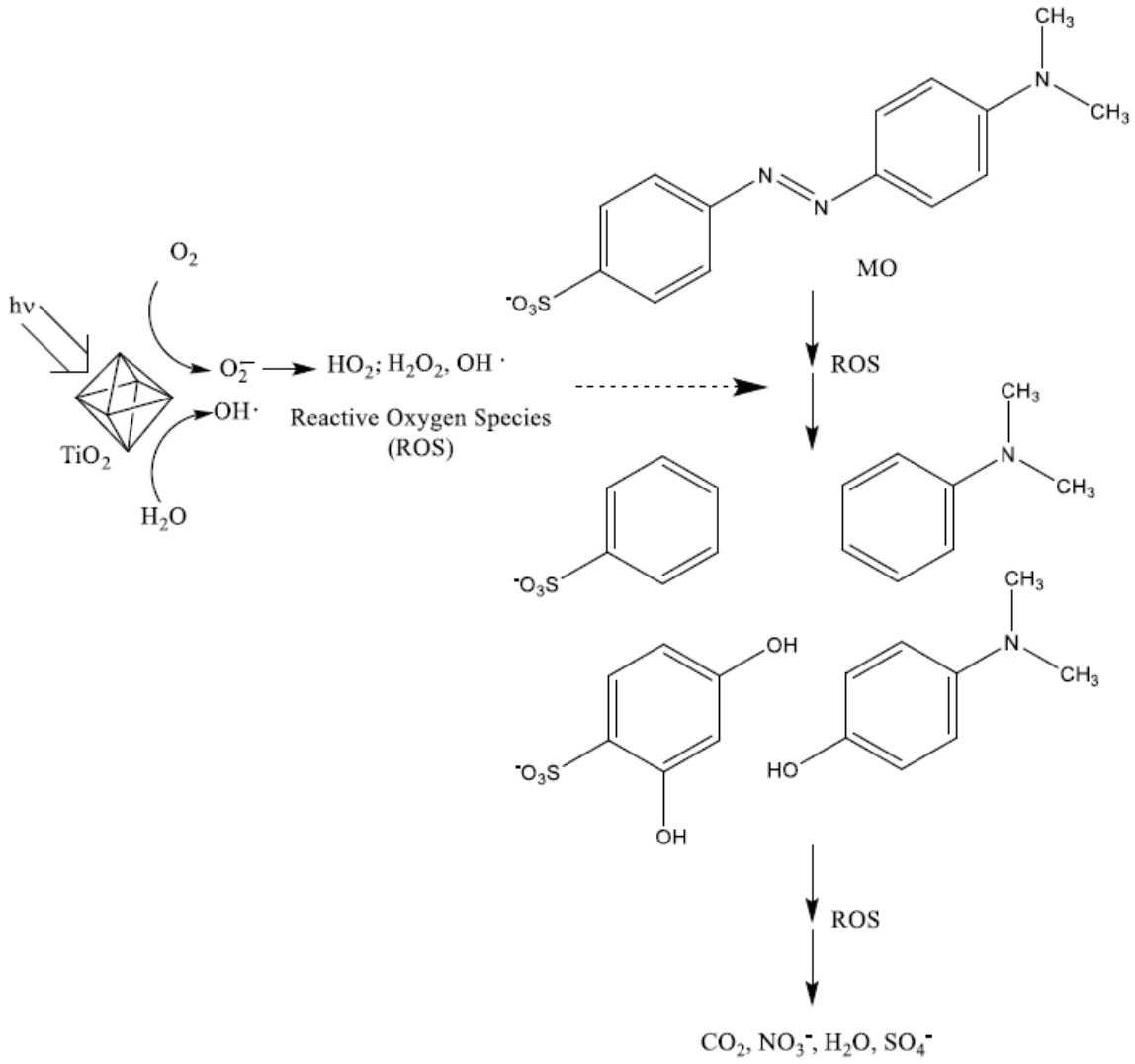

Figure 3.12. The accepted mechanism for the degradation of methyl orange (MO) and other azo dyes by reactive oxygen species (ROS) generated by TiO_2. Absorption of light by TiO_2 generates holes and electrons; holes can react with water to form hydroxyl radicals; electrons reduce dioxygen to superoxide anions, which in turn can react with water to form hydroperoxyl radicals, hydrogen peroxide, and hydroxyl radicals. These reactive oxygen species oxidize MO. Early intermediates are mostly from loss of N_2 and include benzenesulfonate, N,N-dimethylaniline and phenolic variants of each. Ultimate oxidation products are the oxides of the atomic components of MO ($C_{14}H_{14}N_3O_3S$). This mechanism is based on the literature cited in the reference. *"Reproduced with permission from American Chemical Society".* [28]

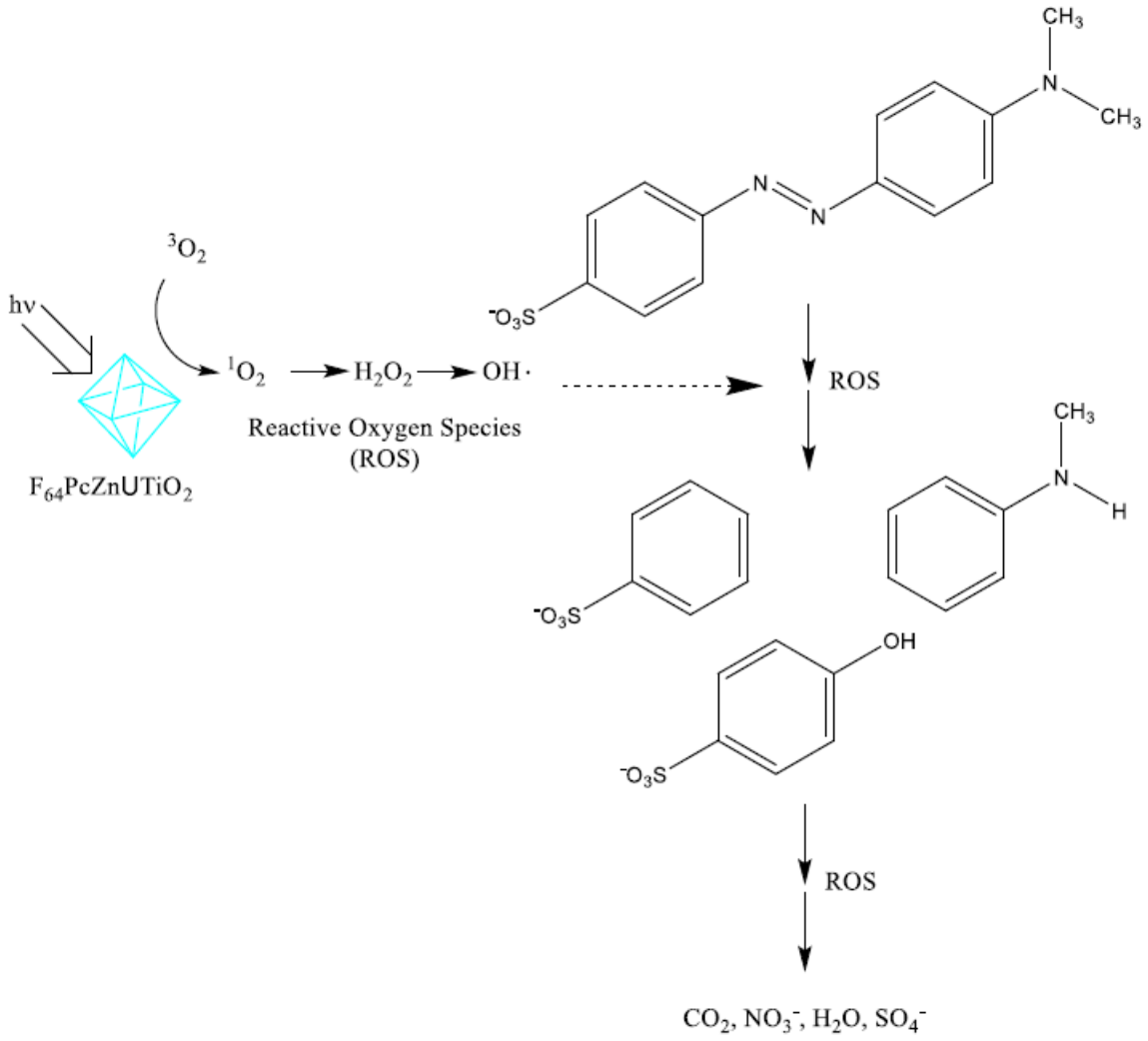

Figure 3.13. The accepted mechanism for degradation of methyl orange (MO) and other azo dyes by $^1O_2$. Absorption of light by $F_{64}PcZn \cup TiO_2$ generates $^1O_2$ by energy transfer; $^1O_2$ can react with water to form hydrogen peroxide and hydroxyl radicals. These reactive oxygen species oxidize MO as indicated by the mechanism above. The mechanism is based on the literature cited in the reference. *"Reproduced with permission from American Chemical Society".* [29]

The photodegradation process by $F_{64}PcZn$ can be classified into primary and secondary processes, the primarily $^1O_2$ produced can generate other secondary ROS. $^1O_2$ and these ROS then degrade MO by the destruction of the azo moiety and further mineralization, this process is similar because of the attack on the azo moiety but not identical to that of TiO_2 because of the hole and electron process in the valence and conduction band. Although the singlet oxygen mechanism has been

researched, the real process of the decomposition of the MO is not known.[8b, 29] The accepted mechanism is shown above starting from the cleavage of the (N=N) to produce benzyl sulfate ($C_7H_8O_4S$) anion and aromatic amine and to further smaller molecules. We demonstrated a significant difference in the photo-oxidation processes observed in the time-dependent MO spectra in **Figures 3.3 (a, b) and 3.5 (a)**. While both TiO_2 and $F_{64}PcZn \cup TiO_2$ show loss of the azo moiety of MO that absorbs at 450 nm, only the $F_{64}PcZn \cup TiO_2$ shows loss of the aromatic absorbance at 250 nm which is significant to the complete mineralization of MO dye. Our research finding suggested that $^1O_2$ mechanism by $F_{64}PcZn \cup TiO_2$ degrades MO more rapidly than TiO_2 catalyst.

For the combined catalytic action, it can be suggested that the competition for the same substrate may explain in part the lower efficiency of the binary catalyst, but other factors may also influence this lower efficiency. For example, both TiO_2 and $F_{64}PcZn$ absorb in the UV region, the photochemical screening of TiO_2 exerted by $F_{64}PcZn$, which has absorbing B bands in the UV region, may reduce the number of photons absorbed by TiO_2. The $F_{64}PcZn$ coating effects may also reduce the reactivity of the TiO_2 by simple distance and or barrier effects since the TiO_2 cannot as easily come into physical contact with MO in solution. It was also observed that no reactivity is shown for either material in the absence of light as shown in **Figure 3.5.**

One common deficiency of superhydrophobic surfaces is long-term durability, the long term catalytic viability of the $(F_{64}PcZn \cup TiO_2 \& NH_4HCO_3) \in$PVDF material was examined to determine both the catalytic reactivity and ability of the surface roughness to sustain long-time exposure to the ROS produced by the catalyst, the MO dye, and its degradation products. The results of a 7-day cycle are illustrated in **Figure 3.6** with 4-hours illumination period each day with fresh batches of MO solution. The catalyst remains stable and active over the seven day period, although there was some non-systematic variability in the amount of MO degraded each day. The reason for this

variability is not known, but it could be attributed to fluctuations in lamp intensity or slight variations in the geometry of the irradiation of light energy leading to the observed minor variability.

3.4.3. Simulated Application Test.

As the goal of this research was to combine the pollutant repelling activity of an enhanced hydrophobic surface with the self-cleaning activity of a photocatalytic coating, the effectiveness of decontamination in three geometries was determined. Films made up of untreated PVDF, superhydrophobic PVDF ($NH_4HCO_3 \in$PVDF), and superhydrophobic, photocatalytic PVDF ($F_{64}PcZn \cup TiO_2 \& NH_4HCO_3$) $\in$PVDF) were used as substrates. Substrates were held vertical (90 ^{o}), inclined at a 45 ^{o} angle, or horizontal (0 ^{o}), then sprayed with a standard quantity of MO solution, allowed to dry, then irradiated for 1 hour.

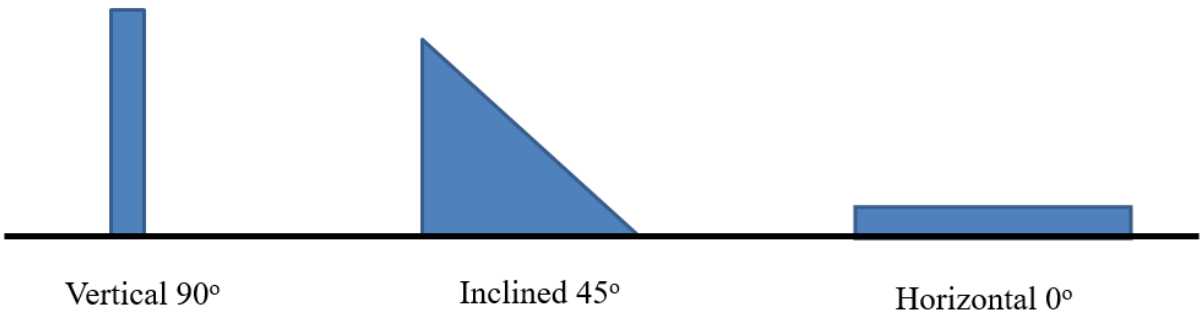

Figure 3.14. MO sprayed at different angles on surfaces before photo irradiation. *"Image courtesy of Abdul Azeez".*

It is expected that the superhydrophobic PVDF would be more effective at shedding the aqueous MO solution at 90º and 45º, but not at 0º, the different positions shown above in **Figure 3.14.** The dried films were either non-illuminated or illuminated for 60 minutes using broadband light. The results of these experiments, **Table 3.1**, indicate that in the absence of irradiation the superhydrophobic films are superior at vertical and inclined geometries, as expected. The superhydrophobic film with no photocatalyst shows a slightly lower O.D. than the superhydrophobic film that includes the photocatalyst, which correlates with their measured contact angles, 159º and 144º, respectively. The untreated, non-superhydrophobic film is noticeably less effective at shedding the MO solution at vertical and inclined geometries. Somewhat unexpectedly, the superhydrophobic films are also significantly better at shedding the MO solution in the horizontal geometry. Here the film with the photocatalyst is slightly better than the superhydrophobic film with no catalyst, perhaps as a result of stray light. With irradiation, the superhydrophobic film with the photocatalyst is superior in all geometries. The O.D. at 460 is essentially 0 with photocatalysis, demonstrating the degradation of MO in all geometries. The non-catalytic films give identical results with or without irradiation, as expected. These experiments demonstrate the potential utility and superiority of films incorporating both superhydrophobicity and photocatalysis for self-cleaning. In the absence or presence of light, the superhydrophobic surfaces will repel most waterborne contaminants. When light is present, the photocatalytic oxidation degrades any contaminants that are able to adhere despite the superhydrophobicity. By combining these two approaches to self-cleaning surfaces, a coating with significantly superior performance might be constructed.

3.5. Conclusions.

PVDF with modified surface morphology and embedded photocatalyst was successfully demonstrated in this research study. PVDF films containing a perfluorinated phthalocyanine, a visible light photosensitizer, supported on TiO_2 were roughened by incorporation of the volatile salt NH_4HCO_3. The roughened morphology revealed carefully tailored topographical surfaces, with similarity to the surface of rose petals, leading to increased hydrophobicity for the PVDF, approaching the superhydrophobic threshold ($\theta = 150^o$). The combination of increased hydrophobicity from modified topographical surface morphology and photocatalytic oxidation from the photosensitizer provide the resulting films with improved self-cleaning capabilities demonstrated using the model dye methyl orange in solution. Comparing the perfluorinated phthalocyanine photosensitizer supported on TiO_2-containing films to the just the TiO_2-containing films, the perfluorinated phthalocyanine containing films proved 2.5 x faster-degrading methyl orange than the TiO_2-containing films. Most importantly, phthalocyanine photosensitizer supported on TiO_2-containing films showed no signs of polymer degradation as was noticed with TiO_2-containing films.

References.

1. a) Li, Y.; Aschauer, U.; Chen, J.; Selloni, A. "Adsorption and Reactions of O_2 on Anatase TiO_2" *Acc. Chem. Res.* **2014**, *47*, 3361-3368. b) Smida, H.; Jamoussi, B. "Degradation of Nitroaromatic Pollutant by Titanium dioxide/Zinc Phthalocyanine: Study of the Influencing Factors" *IOSR Journal of Applied Chemistry*. **2012**, *2*, 11-17.

2. Gesenhues, U. "Al-doped TiO_2 pigments: influence of doping on the photocatalytic degradation of alkyd resins". *J. Photochem. Photobiol. A.* **2001**, *139*, 243-251.

3. a) Allen, N. S.; McKellard, J. F.; Wood, D. G. M. "Photochemical processes involving TiO_2 pigments and TiO_2–light stabilizer combinations in commercial polyolefins" *Journal of Polymer Science: Polymer Chemistry Edition*, **1975,** *13*, 2319–2325. b) Peiró, A. M.; Colombo, C.; Doyle, G.; Nelson, J.; Mills, A.; Durrant, J. R. "Photochemical Reduction of Oxygen Adsorbed to Nanocrystalline TiO_2 Films: A Transient Absorption and Oxygen Scavenging Study of Different TiO_2 Preparations" *J. Phys. Chem. B.* **2006**, *110*, 23255–23263.

4. Banerjee, S.; Dionysiou, D. D.; Pillai, S. C. "Self-cleaning applications of TiO_2 by photo-induced hydrophilicity and photocatalysis" *Applied Catalysis B: Environmental* **2015**, *176-177*, 396–428.

5. Banerjee, S.; Pillai, S.; Falaras, P.; O'Shea, K.; Byrne, J.; Dionysiou, D. "New Insights into the Mechanism of Visible Light Photocatalysis" *J. Phys. Chem. Lett.* **2014**, *5*, 2543-2554.

6. a) DeRosa, M. "Photosensitized singlet oxygen and its applications" *Coord. Chem. Rev*. **2002,** *233-234*, 351–371. b) Carrion, E. N.; Loas, A.; Patel, H. H.; Pelmuş, M.; Ramji, K.; Gorun, S. M. Fluoroalkyl phthalocyanines: Bioinspired catalytic materials. *J. Porphyr. Phthalocyanines* **2018**, *22*, 371-397.

7. a) Bench, B. A.; Beveridge, A.; Sharman, W. M.; Diebold, G. J.; Van Lier, J. E.; Gorun, S. M. "Introduction of Bulky Perfluoroalkyl Groups at the Periphery of Zinc Perfluorophthalocyanine: Chemical, Structural, Electronic, and Preliminary Photophysical and Biological Effects" *Angew. Chem., Int. Ed.* **2002**, *41*, 747-750. b) Pelmuş, M.; Carrion, E. N.; Colomier, C.; Santiago, J.; Gorun, S. M. Group III Perfluoroalkyl Perfluoro Phthalocyanines, *J. Porphyr. Phthalocyanines* **2016**, *20*, 1401-1408.

8. a) Beveridge, A. C.; Bench, B. A.; Gorun, S. M.; Diebold, G. J. "Evaluation of photodynamic therapy agents through transient grating measurements" *J. Phys. Chem. A.* **2003**, *107*, 5138-5143. b) Drozd, D.; Szczubiałka, K.; Łapok, L.; Skiba, M.; Patel H.; Gorun, S. M.; Nowakowska, M. "Visible light induced photosensitized degradation of acid orange 7 in the suspension of bentonite intercalated with perfluoroalkyl perfluoro phthalocyanine zinc complex" *Applied Catalysis B: Environmental*, **2012**, 125, 35-40.

9. Schöllhorn, B.; Germain, J.; Pauly, A.; Maleysson, C.; Blanc, J. "Influence of peripheral electron-withdrawing substituents on the conductivity of zinc phthalocyanine in the presence of gases. Part 1: reducing gases" *Thin Solid Films*, **1998,** *326*, 245–250.

10. a) Gorun, S. M.; Sullivan, J.; Ramji, K. Self-Cleaning Protective Coating. *U.S. Patent*. 9,260,630 **2016**. b) Sullivan, J. MS Thesis, Seton Hall University, South Orange NJ: **2016**.

11. Ramji, K. PhD Dissertation, Seton Hall University, South Orange, NJ: **2018**.

12. a) Blossey, R. "Self-cleaning of superhydrophobic surfaces by self-propelled jumping condensate" *Nature Mater.* **2003**, 2, 301-306. b) Feng, L.; Li, S.; Li, Y.; Li, H.; Zhang, L.; Zhai, J.; Song, Y.; Liu,

B.; Jiang, L.; Zhu, D. "Super-Hydrophobic Surfaces: From Natural to Artificial" *Adv. Mater.* **2002**, 14, 1857-1860. c) Furstner, R.; Barthlott, W.; Neinhuis, C.; Walzel, P. "Wetting and Self-Cleaning Properties of Artificial Superhydrophobic Surfaces" *Langmuir* **2005**, 21, 956-961.

13. Peng, C., Xing, S., Yuan, Z., Xiao, J., Wang, C., & Zeng, J. Preparation and anti-icing of superhydrophobic PVDF coating on a wind turbine blade. *Applied Surface Science*. **2012**, *259*, 764–768.

14. Trashin, S.; Rahemi, V.; Ramji, K., Neven, L., Gorun, S. M., & De Wael, K. "Singlet oxygen-based electrosensing by molecular photosensitizers" *Nature Communications*. **2017**, *8*, 16108.

15. Steinmann, W.; Walter, S.; Beckers, M.; Seide, G.; Gries, T. "Thermal Analysis of Phase Transitions and Crystallization in Polymeric Fibers. (Applications of Calorimetry in a Wide Context - Differential Scanning Calorimetry, Isothermal Titration Calorimetry and Microcalorimetry), 1st Ed", *InTech*. **2013**.

16. Li, N.; Fu, Y.; Lu, Q.; Xiao, C. "Microstructure and Performance of a Porous Polymer Membrane with a Copper Nano-Layer Using Vapor-Induced Phase Separation Combined with Magnetron Sputtering" *Polymers*, **2017,** *9*, 524.

17. Law, K. "Definitions for Hydrophilicity, Hydrophobicity, and Superhydrophobicity: Getting the Basics Right" *J. Phys. Chem. Lett*. **2014,** *5*, 686–688.

18. Wang, D.; Li, K.; Teo, W. "Preparation and characterization of polyvinylidene fluoride (PVDF) hollow fiber membranes" *J. Membrane Sci.* **1999**, *163*, 211–220.

19. a) Qin, J.; Lay, W.C.L.; Kekre, K. A. "Recent developments and future challenges of forward osmosis for desalination: a review" *Desalination and Water Treatment*, **2012,** *39*, 123–136. b) Jiao, K.; Mandapati, S.; Skipper, P. L.; Tannenbaum, S. R.; Wishnok, J. S. "Site-Selective Nitration of Tyrosine in Human Serum Albumin by Peroxynitrite" **2001**, *Anal. Biochem. 293*, 43–52.

20. Zheng, Q.; Lü, C. "Size Effects of Surface Roughness to Superhydrophobicity" *Procedia IUTAM*. **2014**, *10*, 462–475.

21. Dubois, I.E.; Holgersson, S.; Allard, S.; Malmstrom, M.E. "Correlation between particle size and surface area for chlorite and K-feldspar", in "Water-Rock Interaction" Birkle and Torres-Alvarado eds., *Taylor and Francis*, **2010**, 717-720.

22. Li, M.; Katsouras, I.; Piliego, C.; Glasser, G.; Lieberwirth, I.; Blomb, P.W.M.; de Leeuw, D.M. "Controlling the microstructure of poly(vinylidenefluoride) (PVDF) thin films for microelectronics" *J. Mater. Chem. C.* **2013**, *1*, 7695-7702.

23. Damchan, J.; SIkong, L.; Kooptarnond, K.; Niyomwas, S. "Contact Angle of Glass Substrate Coated with TiO_2/SiO_2 Thin Film" *CMU J. Nat. Sci.* **2008**, *7*, 19-23.

24. Sahoo, B.N.; Kandasubramanian, B.; Thomas, A. "Effect of TiO_2 powder on the surface morphology of micro/nanoporous structured hydrophobic fluoropolymer based composite material" *Journal of Polymers*. **2013**, 615045.

25. a) Dzinun, H.; Othman, M.H.D.; Ismail, A.F.; Puteh, M.H.; Rahman, M.A.; Jaafar, J. "Stability Study of PVDF/TiO_2 dual layer hollow fibre membranes under long term UV irradiation exposure" *J. Water Process Eng.* **2017**, *15*, 78-82. b) Lee, M.J.; Ong, C.S.; Lau, W.J.; Ng, B.C.; Ismail, A.F.; Lai, S.O. "Degradation of PVDF-based composite membrane and its impacts on membrane intrinsic and separation properties" *J. Polym. Eng.* **2016**, *36*, 261-268. c) Zulfiqar, S., Zulfiqar, M., Rizvi, M., Munir, A., & McNeill, I. **1994**. Study of the thermal degradation of polychlorotrifluoroethylene, poly(vinylidene fluoride) and copolymers of chlorotrifluoroethylene and vinylidene fluoride. *Polymer Degradation and Stability*, *43*(3), 423–430.

26. Swetha, S.; Santhosh, S.M.; and Geetha Balakrishna, R. "Synthesis and Comparative Study of Nano-TiO_2 Over Degussa P-25 in Disinfection of Water" *Photochem. Photobiol.* **2010**, 86, 628-632.

27. Liao, M.S.; Watts, J.D.; Huang, J.M.; Gorun, S.M.; Kar, T.; Scheiner, S. "Effects of Peripheral Substituents on the Electronic Structure and Properties of Unligated and Ligated Metal Phthalocyanines, Metal = Fe, Co, Zn" *J. Chem. Theory Comput.* **2005**, *1*, 1201-1210.

28. a) Li, W.; Li, D.; Lin, Y.; Wang, P.; Chen, W.; Fu, X.; Shao, Y. "Evidence for the Active Species Involved in the Photodegradation Process of Methyl Orange on TiO_2" *J. Phys. Chem. C* **2012**, *116*, 3552-3560. b) Legumi, O.; Oliveras, E.; Braun, A.M. "Photochemical Processes for Wastewater Treatment" *Chem. Rev.* **1993**, *93*, 671-698. c) Ranjbar, P.Z.; Ayati, B.; Ganjdurst, H. "Kinetic Study on Photocatalytic Degradation of Acid Orange 52 in a Baffled Reactor Using TiO_2 Nanoparticles" *Journal of Environmental Sciences* **2019**, *79*, 213-224. d) Nguyen, C.H.; Fu, C.C.; Juang, R.S. "Degradation of methylene blue and methyl orange by palladium-doped TiO_2 photocatalysis for water reuse: efficiency and degradation pathways" *Journal of Cleaner Production*, **2018**, *202*, 413-427. e) Yu., L.; Xi, J.; Li, M.D.; Chan, H.T.; Su, T.; Phillips, D.L.; Chan, W.K. "The Degradation Mechanism of Methyl Orange under Photo-Catatlysis of TiO_2" *Phys. Chem. Chem. Phys.* **2012**, *14*, 3589-3595. f) Stylidi, M.; Kondarides, D.I.; Verykios, X.E. "Visible light induced photocatalytic degradation of Acid Orange 7 in aqueous TiO_2 suspensions" *Applied Catalysis B: Environmental* **2004**, *47*, 189-201. g) Han, J.; Zeng, H.Y.; Xu, S.; Chen, C.R. Liu, X.J. "Catalytic Properties of CuMgAlO Catalysts and Degradation Mechanism in CWPO of Methyl Orange" *Applied Catalysis A: General* **2016**, *527*, 72-80.

29. a) Bortolus, P.; Monti, S.; Albini, A.; Fasani, E.; Pietra, S. "Physical Quenching and Chemical Reaction of Singlet Molecular Oxygen with Azo Dyes" *J. Org. Chem.* **1989**, *54*, 534-540. b) DeRosa, M.C.; Crutchley, R.J. "Photosensitized Singlet Oxygen and its Applications" *Coord. Chem. Rev.* **2002**, *233/234*, 351-371. c) Xu, X.; Muller, R.P.; Goddard III, W.A. "The gas-phase reaction of singlet dioxygen with water: a water-catalyzed mechanism" *Proc. Nat. Acad. Sci.* **2002**, *99*, 3376-3381. d) Sousa, C.; Botelho do Rego, A.M.; Sa e Melo, T. "Singlet Oxygen Reactivity in Water-Rich Solvent Mixture" *Quim. Nova* **2008**, *31*, 1392-1399. e) Wang, C.; Zhang, M.; Fang, Y.; Chen, G.; Li, Q.; Sheng, X.; Xu, X.; Hui, J.; Lan, Y.; Fang, M.; Wang, X.; Wang, X.; Dai, Z.; Bao, J.; Wang, P. "SbSi Nanocrystals: An Excellent Visible Light Photocatalyst with Efficient Generation of Singlet Oxygen" *ACS Sustainable Chem. Eng.* **2018**, *6*, 12166-12175. f) Sreedhara, A.; Lau, K.; Li, C.; Hosken, B.; Macchi, F.; Zhan, D.; Shen, A. "Role of Surface-Exposed Tryptophan as Substrate Generators for the Antibody Catalyzed Water Oxidation Pathway" *Mol. Pharmaceutics* **2013**, *10*, 278-288. g) Yao, Y.; Huang, Z.; Zheng, B.; Zhu, S.; Lu, W.; Chen, W.; Chen, H. "Photocatalytic Degradation of Dyes Using Dioxygen Activated by Supported Metallophthalocyanine Under Visible Light Irradiation" *Curr. Appl. Phys.* **2013**, *13*, 1738-1742.

Chapter 4

Perfluorinated Phthalocyanines Embedded in Epoxy Modified Polysiloxane Hybrid Coated Surface.

4.1. Introduction.

Corrosion of components made of steel and iron have posed a challenge to the science and research community at large, with great expense required for protecting and repairing existing surface materials and structures. [1 - 6] Understanding, controlling and preventing corrosion is an enormous area of research. The durability and stability of coated surfaces are faced with challenges from a number of factors, including temperature, water vapor, [3] and contact with liquid water. [4] Water mediates electron transfer, facilitating redox processes that occur between a steel surface and the ubiquitous oxygen (O_2) reagent, a strong oxidizer. [6]

One way to combat the corrosion of surfaces [6, 7] is to reduce their wettability and thus surface moisture. The invention of water-repellent coating materials has allowed coated surfaces to better withstand atmospheric conditions, a technology that is currently very promising. Hydrophobicity is the ability for a coated surface to resist wetting, which can be assessed using the contact angle θ of water droplets on the surface. Hydrophobic surfaces are considered to have a contact angle that exceeds $\theta = 90°$. There have been tremendous improvements in the hydrophobicity of coatings for the protection of surfaces that are most vulnerable to oxidation, such as those exhibited by marine vessels, steel equipment, and other assets near marine and riverine environments.[5]

The coated surface of a protected substrate is characterized by determining the contact angle of a water droplet, if that exceeds $\theta > 90°$ the surface is deemed hydrophobic.[5] In particular, the ability of moisture to sit on the coated hydrophobic surface and eventually spread out onto the surface and penetrate is still challenging. [6 - 8] The ability to produce a non-wetting surface with a polymer can be challenging, but the great variation in properties has provided polymeric materials with

advantages relative to other surface modification materials. [6] There are effective ways to achieve non-wetting surfaces include using a polymer with a low surface energy which will repel water and the creation of a textured surface with micro- and nano-scale roughness. [5, 9] Surface roughness reduces the water contact with the surface by creating air pockets between the rough surface and the (beaded) water. Such a surface is classified as superhydrophobic [6] when the water contact angle exceeds 150° and hysteresis is less than 10°, examples of such surfaces can be found in nature (the lotus leaf). The advances in modern surface coating technology that result in coatings exhibiting hydrophobicity and superhydrophobicity can benefit from tough and resistant compounds. [10 -12]

Silicon-containing polymers have been widely explored for durable and long-lasting coatings due to their unique properties.[10] In the siloxanes, the silicon atom is fused between two electron-withdrawing oxygen atoms (O-Si-O), forming strong bonds with a wide bond angle of 143º. [12] The angle and a low rotational barrier impart mobility, making the polysiloxane network a flexible polymeric material. [13 -18] An advantage of siloxanes is that it is possible to introduce other functional groups as the silicon substituents, useful for a wide range of functions. [15] The side chains can be modified with groups that impart particular properties (methyl, phenyl, etc.) or reactive groups like epoxy, urethane, acrylate, vinyl, alkoxy, and others. The structure of a network of a reactive organosilicon resin is shown in **Figure 4.1**.

Epoxy resins are commonly used as coatings, sealants, and adhesives. They are materials of choice in many cases due to their rapid curing, combined with properties such as toughness, strength and thermal stability. These characteristic qualities can be combined with the qualities of polysiloxane to produce a durable coating surface that is strong yet flexible. These combined qualities can provide the basis for long-lasting applications. Mironova *et al,* [5] prepared novel silicone-epoxy binders for coatings with a contact angle $\theta > 90°$, thus classified as hydrophobic surfaces. The

combination of these resins to form a binder is important for coating applications. Moreover, the binder can withstand harsh conditions because of the durability and resistance to corrosion, along with the low glass transition temperature of the siloxane. The composite still maintains high elasticity even at low temperature. [5] Solvent-based application of polymers, such as PVDF in DMF in the previous chapters, has some advantages in mixing and preparation. Drawbacks of solvent-based processes include solvent evaporation which requires energy and pollution of the environment by the evaporated solvent during the coating process. [15 - 17] The need for polymers coatings that are solvent-free or waterborne is of great interest beyond environmental concerns. [15]

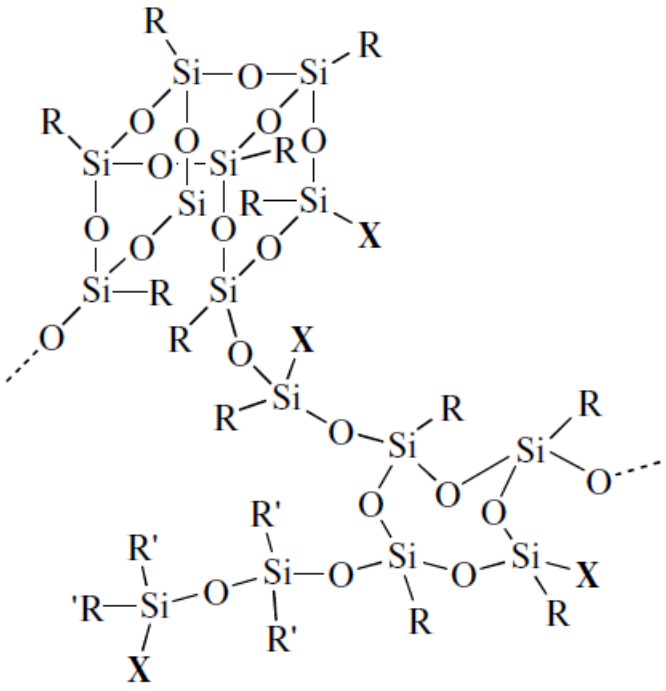

Figure 4.1. Structure of a reactive organosilicon resin. **X** represents a number of functional groups: amino, carbinol, vinyl, epoxy, alkoxy, etc. *"Reproduced with permission from Springer Nature"* [5]

In the case of siloxane epoxy resin, a crosslinking agent is necessary during the reaction process. This curing agent causes an epoxide ring-opening along with dual hydrolysis and condensation reactions to create the surface coating. Siloxane-epoxy can be modified with fluorinated compounds or long-chain hydrocarbon groups to decrease surface energy and increase hydrophobicity. [5] Decreasing the surface energy alone cannot shift the surface properties to superhydrophobicity. [6] Superhydrophobicity requires introducing roughness [18] onto the surface of the polymer coating through different techniques, such as micro and nano-structuring or selectively treating the surface. [19] These techniques, are designed to accomplish micro and nanoscale structured roughness and can be very efficient in combination with a low energy surface polymer, resulting in superhydrophobicity. [18, 22] Different methods have been applied to surface coatings, including the addition of carbon nanotubes, [19] the use of fillers such as silicon dioxide, [23] polystyrene latexes, [24] and fluoride latexes. [25 - 29]

Many methods of designing superhydrophobic surfaces are too tedious or expensive to employ at a large scale industrial level. [31 - 33] Achieving durability of surfaces and superhydrophobicity can be challenging, [34] since long-term thermal and oxidative stability and solar exposure of surfaces can ultimately damage the coated surfaces as a result of a variety of processes. [35] As shown previously, PVDF a widely used polymer [26] suffers from thermal and UV induced long-term degradation due to the (C-H) functional group resulting in scissioning of the backbone. [35] A study by Zulfiqar *et al*, [35] described the mechanism of PVDF thermal degradation at elevated temperature.

This chapter is designed to explore an alternative polymer system, a robust durable hybrid epoxy modified polysiloxane, to contrast with the observed degradation of PVDF embedded with TiO_2 photocatalyst under broadband irradiation. The alternative polymer will be embedded with

perfluorinated phthalocyanine photocatalyst coated on SiO_2. Photoreactive materials have been studied for the degradation of organic compounds, [37 - 39] A study by Natarajan *et al*, [37] used a doped Ag-TiO_2 semiconductor for the destruction of biological compounds: *Staphylococcus Aureus* and *Escherichia Coli*.

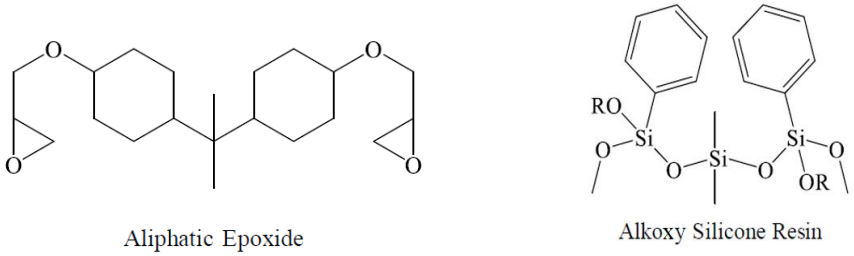

Scheme 4.2. Structures of aliphatic epoxy and alkoxy siloxane resin before cross-linking reaction leading to the polymerization.

Sullivan, [40] described the use of epoxy modified polysiloxane embedded with $F_{64}PcZn \cup TiO_2$ for photobleaching of methyl red dye in solid-state. He described how the methyl red was applied to the polymer surface containing the photooxidation catalyst, and the surface was irradiated with UV-Vis light. The degradation of the methyl red dye was recorded as a function of irradiation time.

Superhydrophobic surfaces are effective and economically efficient but fall short as self-cleaning surfaces. [41 – 46] One important aspect of a self-cleaning surface is the capability to degrade organic pollutant in contact with the surface, whether chemisorbed, physisorbed or in solution. Adsorption of an organic pollutant can also result in surface degradation from oxidation. [47] Studies have shown that the attachment of bioorganic compounds can reduce surface superhydrophobicity, making the surfaces more hydrophilic. Some common problems associated with bioorganic compounds attached to coated surfaces [47] are, drag-reduction, biofouling, and promoting surface. The combination of a superhydrophobic and photoreactive surface will be an improvement for self-

cleaning surfaces. Successful execution of this twofold approach to surface design will promote the longevity of the coated surface, saving money over time.

4.1.1. Research Objective.

In this chapter we address two main issues, designing a coated surface that is superhydrophobic and embedding a photoreactive organic-inorganic molecule in the superhydrophobic coated surface. A superhydrophobic coating prevents the substrate from coming directly in contact with water, and this reduces oxidation of the substrate surface. Water contact with the metal substrate promotes rust and often initiates physical damage to the metal substrate. The photooxidative coating can degrade bioorganic compounds that can otherwise be resistant to hydrophobicity. In the presence of visible light, the photoreactive compound will degrade these bioorganic compound, and the degradation products will be easily washed way in the presence of water on the superhydrophobic coated surface.

4.2. Materials and Methods.

4.2.1. General.

Chemicals and solvents used in these studies were obtained commercially and used as received, if not otherwise stated. The photoreactive coated films were used to study six (6) commercial dyes, to determine the photooxidative capability of the engineered surfaces, although, the dyes data will be found in the following chapter. All dyes were obtained from Alfa-Aesar:

- ***Crystal Violet***, (CV), (Tris(4-(dimethylamino)phenyl) methylium chloride, Cationic triphenylmethyl dye),
- ***Rhodamine b***, (Rb), (9-(2-carboxyphenyl)-6-diethylamino-3-xanthenylidene)-diethylammonium chloride, cationic fluorone dye),
- ***Methyl Orange***, (MO), (4-[[(4-dimethylamino) phenyl]-azo] benzene sulfonic acid, sodium salt),
- ***Evans Blue***, (EV), (6,6'-{(3,3'-dimethyl[1,1'-biphenyl]-4,4'-diyl) bis[diazene-2,1-diyl]} bis(4-amino-5-hydroxynaphthalene-1,3-disulfonate, organic tetra-sodium salt),
- ***Methylene Blue***, (MB), (3,7-bis(dimethylamino)phenothiazin-5-ium, organic chloride salt cationic phenothiazine dye),
- ***Rose Bengal***, *(RB),* (2,3,4,5-tetrachloro-6-(2,4,5,7-tetraiodo-3-oxido-6-oxoxanthen-9-yl) benzoate, disodium anionic fluorescein dye).

Ammonium hydrogen carbonate (NH_4HCO_3) was purchased from Sigma-Aldrich and characterized as described below. Fumed Silica (SiO_2) was purchased from Aerosil®, (P90 surface

area Brunauer-Emmett-Teller (BET) measured at 90 m^2/g, particle size determined at 20 nm, pH 3.7 - 4.7), and the fumed silica was calcined for surface modification as described below. Deionized H_2O (Milli-Q, resistivity15 $M\Omega$-cm) was used for all aqueous solution preparation. The crosslinker Dynasylan AMEO (3-aminopropyltriethoxysilane) was purchased from Evonik (density 0.95 g/cm^3). The resin material Silikopon EF (resin composition: Siloxane Epoxy hybrid) was purchased from Evonik. All studied dye solutions were filtered through 0.45 µm cellulose filters for purity. Fluorinated phthalocyanine, $F_{64}PcZn$, was prepared from zinc acetate and perfluoro-(4,5-di-isopropyl) phthalonitrile as previously described.[7]

4.2.2. Instruments.

Contact angles (θ) for all surfaces were measured with a RAMA-HART goniometer using approximately 5 µL volume, using the sessile water drop method. The θ values obtained were averages of measurements at five different points on each surface. Untreated glass slides, θ = 45 ° were used as the experimental control. The morphology of coated surfaces was determined with Scanning Electron Microscopy (SEM), Quanta 200 FEG Environmental SEM at the Princeton University PRISM Institute. Thermal analysis was performed with Differential Scanning Calorimetry (DSC), all experiments were performed aerobically with a TA model 2920 instrument. Coated film weight loss was determined with Thermogravimetric Analysis (TGA), a TA model Q500 instrument was used in all experiments. All experiments were conducted under a blanket of N_2 at 40 ml/min flow rate. A 10 °C/min heating and cooling rate was used for both DSC and TGA unless otherwise stated. A 300 W OSRAM halogen lamp was used for photochemical

experiments at a distance of 14 cm from the sample, average illuminance of 109,000 lux measured with an Extech EasyView 33 light meter. A 60 mm glass filter (S-83605, Sargent Laboratory) was used to exclude wavelengths below 300 nm for Visible light illumination. All glass slides were washed with acetone followed by deionized water before use, (Glass slides, 75 x 25 x 1 mm, purchased from VistaVision). A Cary 500 UV-Vis-NIR spectrophotometer was used to determine the concentration of photooxidized dyes in solution and for solid-state electronic spectra.

4.2.3. Sample Preparation Symbols.

The description of the composition of materials uses the union and inclusion symbols "$\cup$" and "$\in$", which mean "deposited on" and "embedded in" respectively.

4.2.4. Preparation of NH_4HCO_3 of controlled particle size.

NH_4HCO_3 was ground with a mortar and pestle, then sieved sequentially to separate particles of 707, 250, 125, and 63 μm maximum size, as described in **chapter 2.2.4.**

4.2.5. Preparation of $F_{64}PcZn$ coated SiO_2, $F_{64}PcZn \cup SiO_2$ Hybrid photocatalyst.

P90 SiO_2 (0.10 g) was calcined in a furnace at 600 ^oC for 1 hour, the particles were allowed to cool to room temperature. The calcined SiO_2 was added to 10 ml solution of ethanol in 3 mg ($1.45x10^{-5}$ moles) $F_{64}PcZn$, (3 wt% of SiO_2) (w/w %). The mixture was stirred on a stir plate at 600 rpm for 45 minutes to facilitate adsorption onto the silica surface. The mixture was then refluxed for 60 minutes, then allowed to equilibrate in the dark for 24 hours. The solvent was removed *in vacuo*

on a rotary evaporator and the resulting deep greenish solid baked at 170 °C for 24 hours, then washed with deionized H_2O to remove adsorbed particles, and finally washed with ethanol until the ethanol was colorless, as shown in **Figure 4.3**. UV-Vis quantification of the amount of $F_{64}PcZn$ removed in the sequential washings allowed determination of the amount of $F_{64}PcZn$ strongly bound to the P90 SiO_2 solid support. The $F_{64}PcZn \cup SiO_2$ hybrid complex, exhibiting light-greenish solid particles, was mechanically ground to break apart any adhering grains, and stored in the dark until further usage.

Figure 4.3. Leaching study of the $F_{64}PcZn \cup SiO_2$ hybrid catalyst to determine the binding ability of the catalyst to the solid support. *"Image courtesy of Abdul Azeez"*.

4.2.6. Preparation of Plain Siloxane-Epoxy coated films.

The AMEO crosslinker (1.0 mL) was added to 4.0 g of siloxane-epoxy resin under vigorous mixing at ambient temperature, mixing was continued with speed 700 RPM for 2 hours, at this point the mixture was a homogeneous, clear, viscous polymer gel. The mixture was coated on a clean, dry glass slide substrate by spreading. The coated sample was heated at 80 °C for 48 hours.

4.2.7. Preparation of Siloxane-Epoxy treated with NH_4HCO_3 coated films.

Step 1: (pre-coat cure). AMEO crosslinker (1.0 mL) was added to 4.0 g of siloxane-epoxy resin under vigorous stirring at ambient temperature, and stirring continued with mixing speed 700 RPM for 1hr, enough time to start the epoxy ring-opening, hydrolysis and condensation reaction. Different NH_4HCO_3 loadings were studied for surface roughness: 3%, 5%, 12%, 17% and 24% w/w were used for these experiments. Ultimately, 5% w/w (0.2 g) NH_4HCO_3 proved to be the best loading for surface roughness, therefore, it was used as shown in **Tables 4.1 and 4.2** respectively.

Step 2: (post-coat cure). A clear viscous gel-like solution formed. The solution was coated on clean dry glass-slide substrates by spreading and or brushing the solution on the substrate, the coating was left to cure for various times, see **Tables 4.1 and 4.2** respectively.

Step 3 (bake time). The coated samples were baked in an oven at 60 ºC then allow to air cool at room temperature. All implemented curing strategies are listed in **Tables 4.1 and 4.2** respectively.

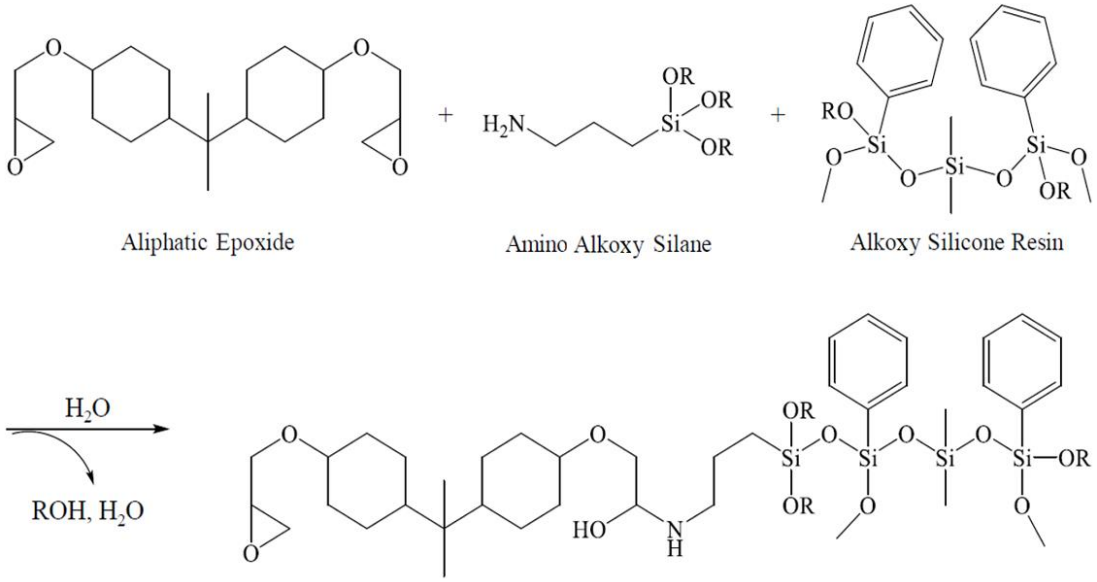

Figure 4.4. Two-step curing reaction-mechanism of hydrolysis and condensation of the siloxane-epoxy polymer.

A two-step reaction mechanism for the preparation of the coated surfaces is illustrated above shown in **Figure 4.4**. The reaction comprised of epoxidation, hydrolysis, and condensation reaction followed by different types of curing processes described below.

Table 4.1. Siloxane-Epoxy curing methods for coated films: 3-hour pre-coat cure.

Sample #	Pre-Coat Cure time (hrs) @ RT	Post-Coat Cure time (hrs) @ RT	Bake time (hrs) Temp @ 60 °C
1	3	3	48
2	3	3	72
3	3	3	96
4	3	6	48
5	3	6	72
6	3	6	96
7	3	9	48
8	3	9	72
9	3	9	96
10	3	12	48
11	3	12	72
12	3	12	96

Table 4.2. Siloxane-Epoxy curing methods for coated films: 6-hour pre-coat cure.

Sample #	Pre-Coat Cure Time (hrs) @ RT	Post-Coat Cure Time (hrs) @ RT	Bake Time (hrs) Temp @ 60 °C
13	6	3	48
14	6	3	72
15	6	3	96
16	6	6	48
17	6	6	72
18	6	6	96
19	6	9	48
20	6	9	72
21	6	9	96

4.2.8. Preparation of $F_{64}PcZn$-coated SiO_2-doped Siloxane-Epoxy with NH_4HCO_3, $(F_{64}PcZn \cup SiO_2 \& NH_4HCO_3) \in$ Siloxane-Epoxy film.

Three acceptable standard epoxy modified siloxane shown in **Tables 4.1 and 4.2** were mixed with an amount of photoreactive catalyst and an amount NH_4HCO_3 to provide films that were acceptable for photochemical studies. These are shown below in **Table 4.3,** for pre-cure, post-cure and bake-cure as implemented.

Step 1: (pre-coat cure). AMEO crosslinker (1.0 mL) was added to 4.0 g of siloxane-epoxy resin under vigorous stirring at ambient temperature and stirring continued with mixing speed 700 RPM

for 1hour. NH_4HCO_3 (0.2 g, 5% w/w) and $F_{64}PcZn \cup SiO_2$ (0.03 g, 3% solids) were added to the mixture and stirring continued under the same conditions for times shown below in **Table 4.3**.

Step 2: (post-coat cure). The greenish viscous gel-like solution was coated on clean dry glass slide substrates by spreading or brushing the solution on the substrate, the solution was left to equilibrate for times shown below in **Table 4.3**.

Step 3 (bake time). The coated samples were baked in the oven at 60 °C for 48 hours and allowed to air cool at room temperature (RT).

Table 4.3. Siloxane-Epoxy embedded $F_{64}PcZn \cup SiO_2$ strategies applied to coated film.

Sample #	Pre-Coat Cure Time (hrs) @ RT	Post-Coat Cure Time (hrs) @ RT	Bake Time (hrs) Temp @ 60 °C
4	3	6	48
7	3	9	48
16	6	6	48

The results from these coatings demonstrated that extended post-coat curing time before baking improved coating performance. The second set of Pc containing samples was prepared using these parameters as described in **Table 4.4**.

Table 4.4. Siloxane-Epoxy doped $F_{64}PcZn \cup SiO_2$ curing strategies for the film.

Sample #	Pre-Coat Cure Time (hrs) @ RT	Post-Coat Cure Time (hrs) @ RT	Bake Time (hrs) Temp @ 45 °C
A	1	24	72
B	3	24	72

4.3. Results.

4.3.1. Characterization of particle size on coated films.

Characterization of NH_4HCO_3 particle size was important to achieving desired surface roughness of $F_{64}PcZn \cup SiO_2 \& NH_4HCO_3) \in$Siloxane-Epoxy film. The largest particle size of 707 µm or greater was sieved to the least particle size 63 µm or lesser with highest CA = 97° as shown in **Table 4.5**, this NH_4HCO_3 particle size was used for the research study.

Table 4.5. NH_4HCO_3 particle size as a function contact angle analysis $F_{64}PcZn \cup SiO_2 \& NH_4HCO_3) \in$Siloxane-Epoxy film.

NH_4HCO_3 Particle Sizes (µm)	Contact Angle θ (°)
250 - 707	75
125 - 250	89
63 - 125	93
< 63	97

The size of the NH_4HCO_3 particles was analyzed to determine the influence of particle size as a function of contact angle on each coated film, as had been done previously for the PVDF films in **Chapter 2**. Again, it was revealed that the smallest particle size 63 µm gave the most improved contact angle, while the lowest contact angle 75° was associated with the largest particle size 707 µm. **Table 4.5** and **Figure 4.5** revealed an inverse relationship between the size of NH_4HCO_3 particles and the relative contact angle from the films.

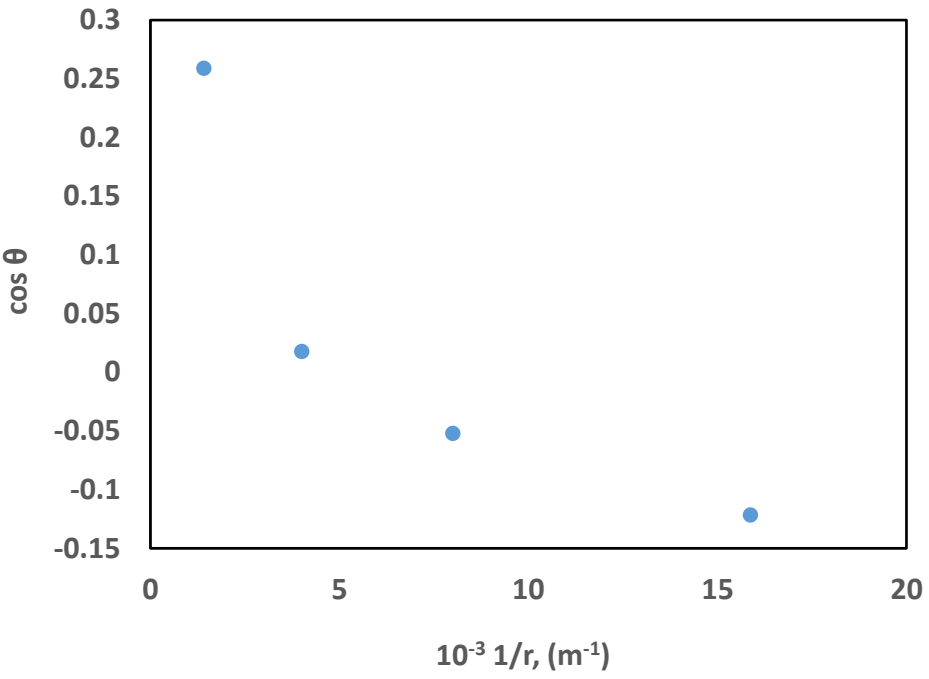

Figure 4.5. Contact angle as a function of NH_4HCO_3 particle size for $NH_4HCO_3 \in$Siloxane-Epoxy films.

It can be assumed that the finely divided NH_4HCO_3 must have disbursed uniformly throughout the matrix of the film, therefore resulting in uniform surface roughness during the decomposition process as the temperature increases. The NH_4HCO_3 influence on the surface improvement in hydrophobicity was realized, the 63 µm NH_4HCO_3 particle size was used from henceforth for the rest of the study.

4.3.2. Optimization of the curing process.

The first coated slides were baked at temperature 80 °C for 48 hrs following the protocol used previously for PVDF; this revealed a poor coating with noticeable foaming and slight discoloration, so the baking temperature was decreased to 60 °C with better results. The influence of % loading of NH_4HCO_3 on the morphology of the film surface was studied. NH_4HCO_3 loading parameters were established for 3%, 5%, 12%, 17% and 24%. The NH_4HCO_3 loading was optimized at 5% for creating micropores/channels as revealed by compound optical microscope imaging, shown in **Figures 4.6 and 4.7.**

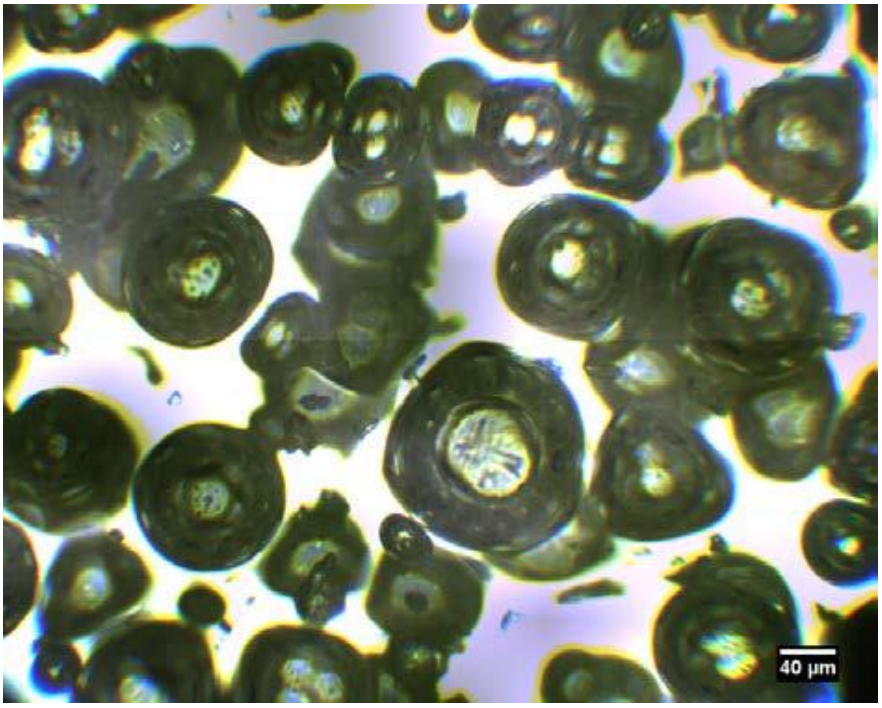

Figure 4.6. Compound microscope image from **Table 4.1,** [sample #4, 3.6.48]. *"Image courtesy of Abdul Azeez".*

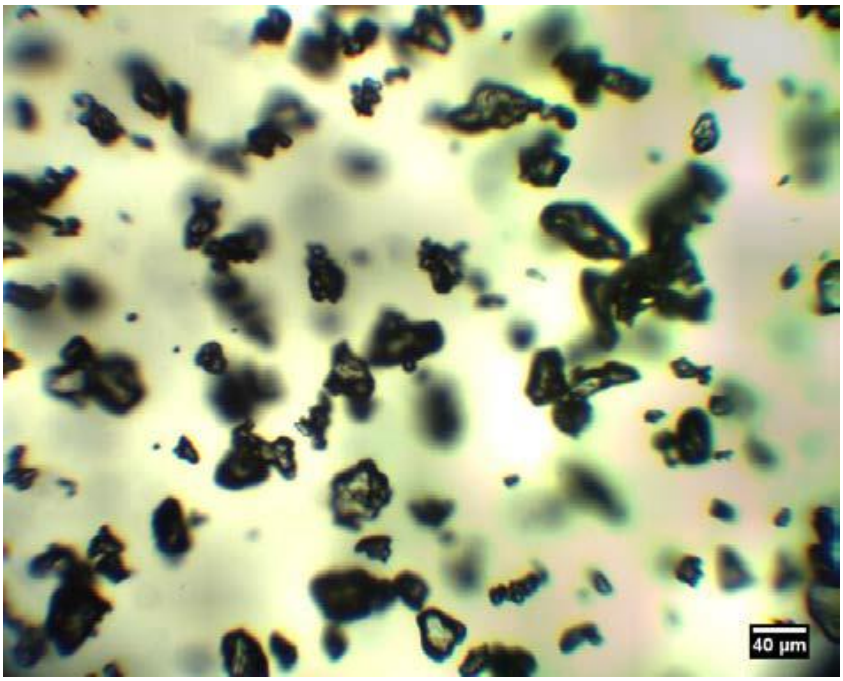

Figure 4.7. a. Compound microscope image from **Table 4.1**, [sample #7, 3.9.48]. *"Image courtesy of Abdul Azeez".*

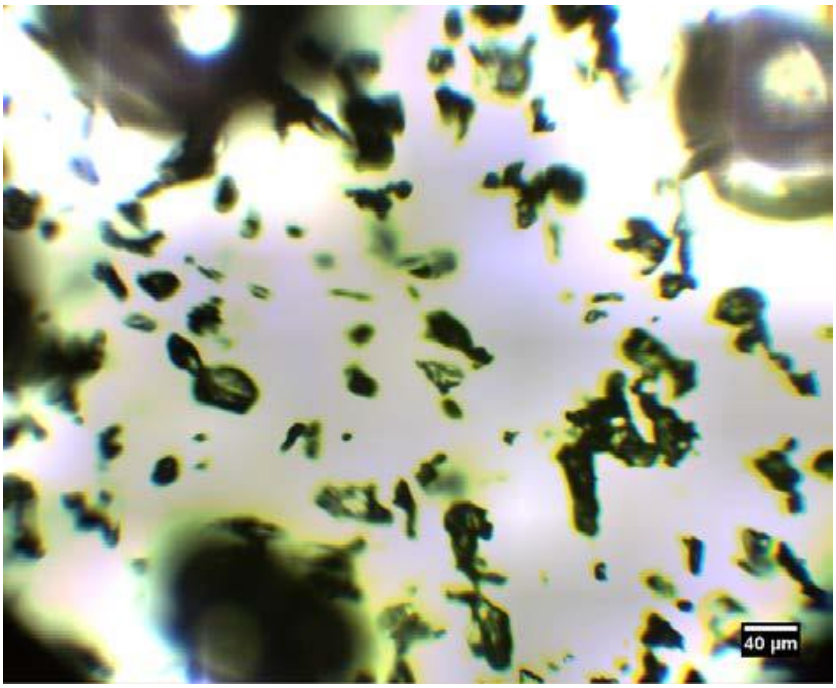

Figure 4.7. b. Compound microscope image from **Table 4.2**, [sample #16, 6.6.48]. *"Image courtesy of Abdul Azeez".*

The 5% NH_4HCO_3 loading resulted in a more defined path for achieving pores/channels in a coated film from Figures shown above. The coating procedure required three different processes: pre-coat curing, post-coat curing and finally baking at 60 °C. The time of each process was varied to optimize the procedure. Analysis of the films revealed foaming during the baking process of samples with total cure time less than 9 hours (3/3 and 3/6 and 6/3), which can be attributed to insufficient cure before baking while the coating is still fluid. Twelve hours total processes revealed good surfaces with the following combinations of pre and post-cure: 3 hours pre-cure followed by 9 hours post-cure, also 6 hours pre-cure followed by 6 hours post-cure, analysis of both processes gave similar characteristic, no foaming noticed, film surfaces have similar morphology as seen in **Figures 4.7 a, b.** The 15 hours processes also revealed good surfaces without foaming, although, the observation was longer cure times for the following samples (3/12 and 6/9) total of 15 hours of pre/post-cure promising surface, the improved processes revealed better morphology overall. For the post-cure baking at 60 °C, with 5% loading of NH_4HCO_3, 48 hours was sufficient to volatilize all the salt into water vapor and CO_2 and NH_3 gases. When post-cure baking was extended to 72 and 96 hours respectively, no noticeable improvement in the coated film was observed.

Using contact angle analysis, the untreated film revealed an average contact angle 75°. The treated film contact angle revealed an average of 97°, an increase over untreated films 75°. However, these results are far from achieving superhydrophobicity (150°), although micropores/channels were clearly created on the coated films.

Figure 4.8. The contact angle of the ***untreated surfaces*** with an average θ = 75°. *"Image courtesy of Abdul Azeez".*

Figure 4.9. a. The contact angle of the ***treated surfa***ces with an average θ = 97°. [Sample #16, 6.6.48]. *"Image courtesy of Abdul Azeez".*

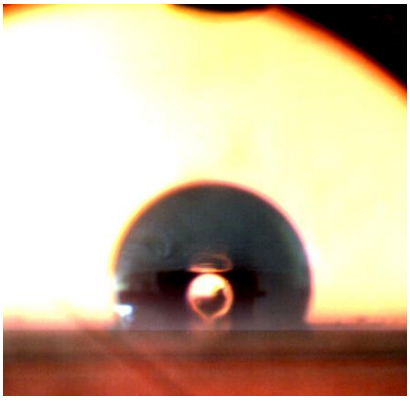

Figure 4.9, b. The contact angle of the ***treated surfaces*** with an average θ = 127° [Sample #B, 3.24.48]. *"Image courtesy of Abdul Azeez".*

Initial assessment of the films was visual, the results and observation are shown in (**Tables 4.6**. **a, b)** The effects of NH_4HCO_3 on the siloxane epoxy films during pre-coated cure, post-coated cure and baking time were observed. The combined cure time (pre and post coating) was more important than either of the individual times. As noted above, bake times longer than 48 hours did not change the film characteristics. Films with combined cure times less than 12 hours were observed to be foamy the material had not cured to sufficient rigidity to resist the expanding gases for the volatile salt. Films with 12 or 15 hours total cure time gave good films by visual inspection.

Table 4.6. a) Visual and CA evaluation of films, **3-hour** pre-coat cure.

Sample #	Process Times (hrs)	Results and Observations	Contact Angle θ
1	3.3.48	Foamy, no residual NH_4HCO_3	78
2	3.3.72	Foamy, no residual NH_4HCO_3	78
3	3.3.96	Foamy, no residual NH_4HCO_3	78
4	3.6.48	Foamy, no residual NH_4HCO_3	87
5	3.6.72	Foamy, no residual NH_4HCO_3	87
6	3.6.96	Foamy, no residual NH_4HCO_3	87
7	3.9.48	Good Film, no residual NH_4HCO_3	95
8	3.9.72	Good Film, no residual NH_4HCO_3	95
9	3.9.96	Good Film, no residual NH_4HCO_3	95
10	3.12.48	Good Film, no residual NH_4HCO_3	98
11	3.12.72	Good Film, no residual NH_4HCO_3	98
12	3.12.96	Good Film, no residual NH_4HCO_3	98

Table 4.6. b) Visual and CA evaluation of films, **6-hour** pre-coat cure.

Sample #	Process Times (hrs)	Results and Observations	Contact Angle (θ)
13	6.3.48	Foamy, no residual NH_4HCO_3	92
14	6.3.72	Foamy, no residual NH_4HCO_3	92
15	6.3.96	Foamy, no residual NH_4HCO_3	92
16	6.6.48	Good Film, no residual NH_4HCO_3	94
17	6.6.72	Good Film, no residual NH_4HCO_3	94
18	6.6.96	Good Film, no residual NH_4HCO_3	94
19	6.9.48	Good Film, no residual NH_4HCO_3	100
20	6.9.72	Good Film, no residual NH_4HCO_3	100
21	6.9.96	Good Film, no residual NH_4HCO_3	100

The contact angles observed, revealed longer total cure time gave higher contact angles than short total cure times. Films cured for 6 - 9 hours total produced surfaces that were hydrophilic or very weakly hydrophobic, with contact angles either below or slightly above 90^o. As the total cure time increased, the contact angle also increased, with the highest contact angle of 100^o for the 6-hour pre-coating cure, 9-hour post-coating cure sample, shown in **Figure 4.10**.

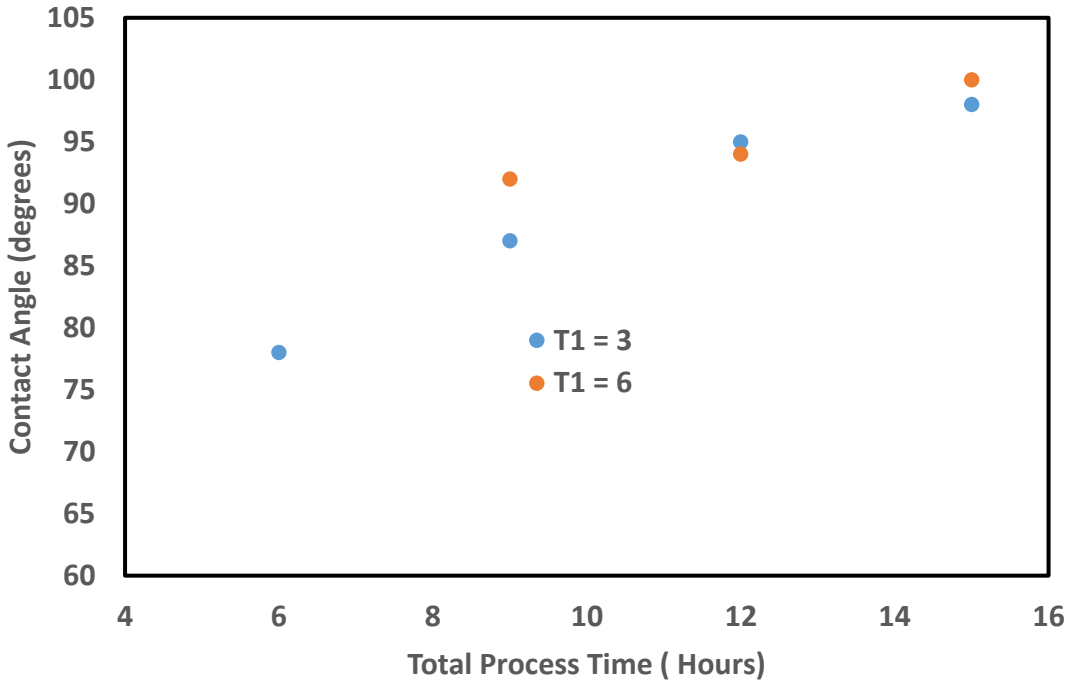

Figure 4.10. Contact Angle as a function of process time. **Blue dots** represent a 3-hour pre-coating cure, **orange dots** represent a 6-hour pre-coating cure.

The addition of photoreactive sensitizer $F_{64}PcZn$ was studied using the procedure optimized above. Film compositions were made from organic the siloxane-epoxy resin with the addition of aminopropyltriethoxysilane cross-linker, in a 4:1 ratio. The volatile organic salt NH_4NCO_3 was added at 5% to the composite to create roughness on the surface and pores/channels on the surface and matrix of the polymer. The Pc photosensitizer was coated on SiO_2 and dispersed in the polymer as described in the methods.

4.3.3. FTIR Data Analysis of Films after Curing.

Fourier-transform infrared (FTIR) spectra were obtained for the films for confirmation. As seen in **Figure 4.11**, the spectrum was nearly identical to those published in the literature.

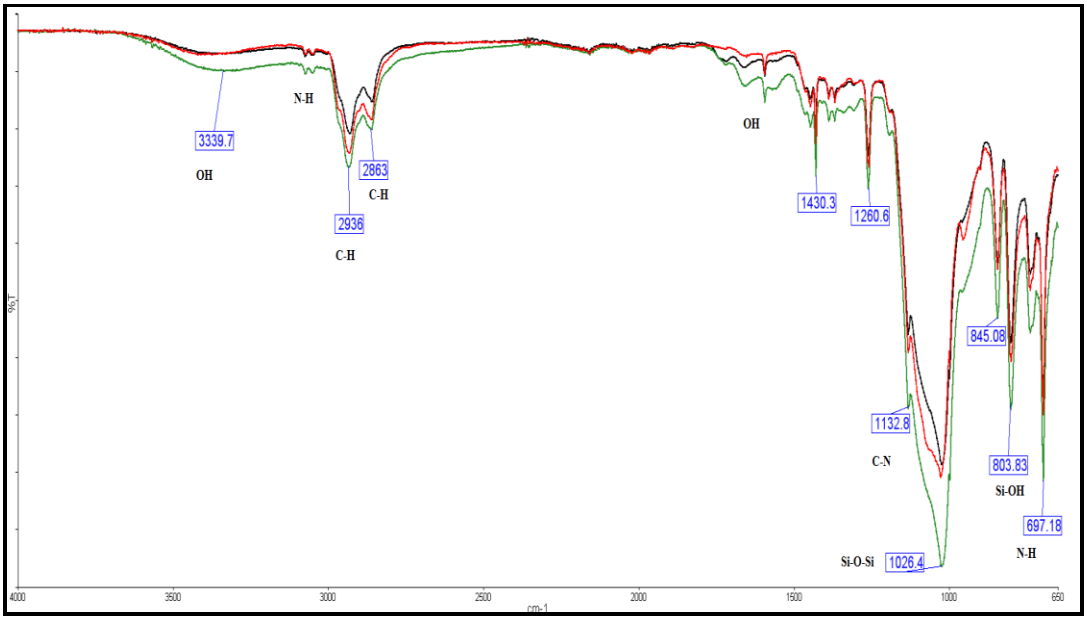

Figure 4.11. FTIR spectrum of coated plain siloxane-epoxy polymer (**Green**), siloxane-epoxy polymer with NH_4HCO_3 (**Red**), and siloxane-epoxy polymer embedded with $F_{64}PcZn \cup TiO_2$ (**Black**) baked at 60 °C for 48 hours.

4.3.4. DSC Thermal Analysis of Films.

Differential Scanning Calorimetry (DSC) of the epoxy modified siloxane polymer with NH_4HCO_3 films were analyzed across a broad temperature range, from -50 °C up to 500 °C to determine the thermal stability and transitions of the organic-inorganic hybrid film. A representative DSC is shown in **Figure 4.12.** The minor transition at 50 °C has been identified as a glass transition in the literature, however, the endothermic nature of the transition is more representative of a curing reaction. The change in heat flow after 200 °C correlates with the start of decomposition of the material, as demonstrated by TGA (see below).

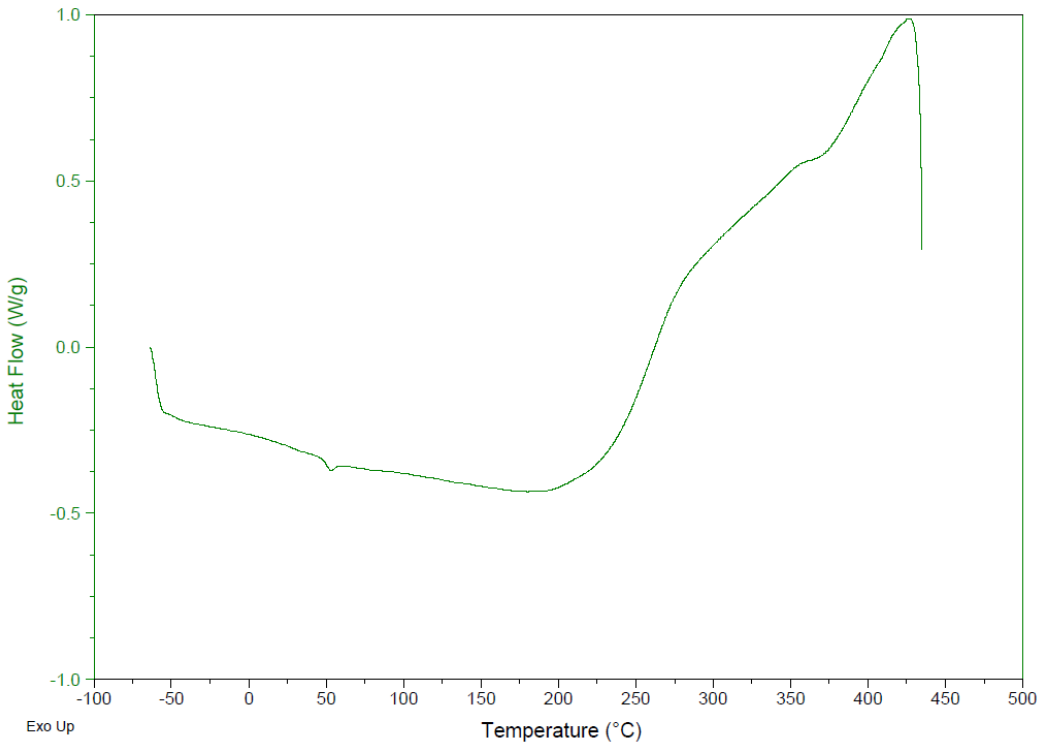

Figure 4.12. DSC analysis of pure siloxane-epoxy polymer with NH_4HCO_3 films with the heating rate at 10 °C/min from -50 °C until 500 °C to determine the thermal stability of the film.

The films were further studied for thermal stability under cycling conditions. Three cycles from 0°C up to 200 °C were run for the siloxane-epoxy polymer with NH_4HCO_3 and siloxane-epoxy polymer embedded with $F_{64}PcZn \cup TiO_2$ cured at 60 °C for 48 hours. The embedded catalyst is not expected to change the thermal stability of the films below 200 °C as shown in TGA (see below). As before, on the first cycle, a T_g or curing transition is seen at about 50 °C; a much weaker transition is seen in the same temperature range on the second and third cycles this might be assigned to a glass transition, although it continues to weaken from the second to third cycle, and glass transitions are expected to be reversible.

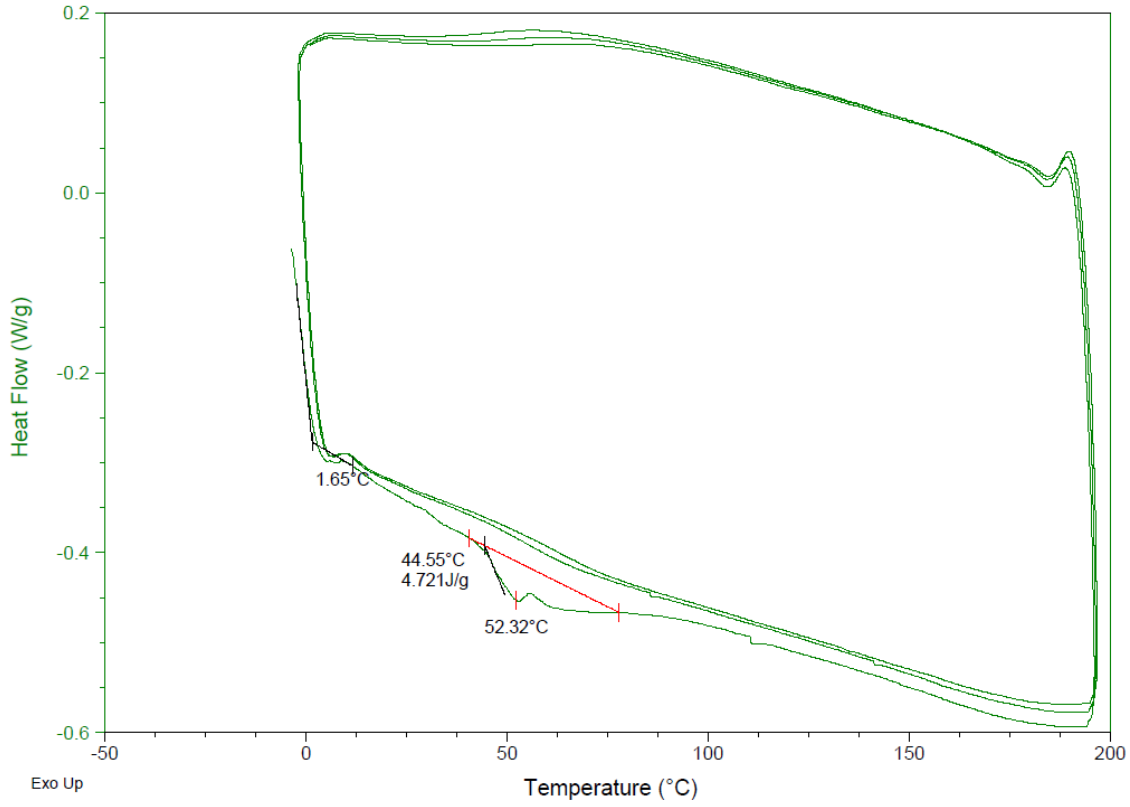

Figure 4.13. DSC Thermogram of pure siloxane-epoxy polymer & NH_4HCO_3 films with a three-cycle heating and cooling rate at 10 °C /min from 0 °C until 200 °C to determine the continuous thermal stability of the coated film.

The cycling DSC thermogram of siloxane-epoxy polymer & NH_4HCO_3 embedded $F_{64}PcZn \cup SiO_2$ is shown in **Figure 4.14.** The curves are very similar to the films without the embedded catalyst. There is a slight difference in the T_g/curing transition at ~50 °C on the first cycle: the film without catalyst shows a broader transition with two endothermic peaks, whereas the transition with the catalyst is sharper and has only one peak. The second and third cycles are essentially identical to the film without the catalyst.

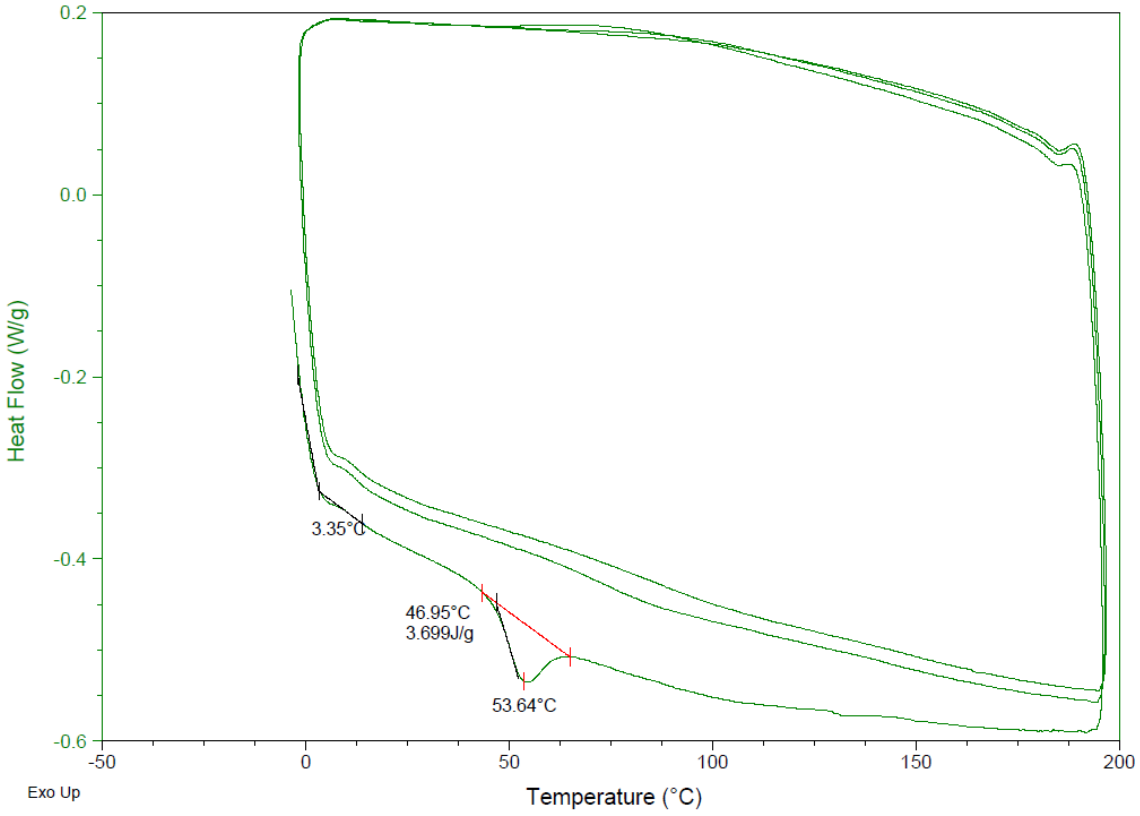

Figure 4.14. DSC Thermogram of siloxane-epoxy polymer & NH_4HCO_3 embedded $F_{64}PcZn \cup SiO_2$ film with a three-cycle heating and cooling rate at 10 °C /min from 0 °C until 200 °C to determine the continuous thermal stability of the coated film.

4.3.5. TGA Thermal Analysis of Films.

TGA was used to determine the thermal stability of the organic-inorganic hybrid coated film both with and without the perfluorinated phthalocyanine photooxidative catalyst. The two thermograms were compared as shown in **Figures 4.15, 4.16, and 4.17**. Pure siloxane epoxy-NH_4HCO_3, as shown in **Figure 4.15**, revealed a stable film until about 200 °C, in agreement with the DSC thermogram in **Figure 4.13**. **Figure 4.16 a**, further illustrates the pattern of weight loss, starting from 200 °C and reaching a maximum at 428 °C, reflecting a derivative weight 0.37 %/°C leading to 34.61% weight loss (4.173 mg of the total 12.057 mg of the original film). Heating was

continued to higher temperatures, and a second minor maximum was observed at 591.2 °C, with derivative 0.05 %/°C.

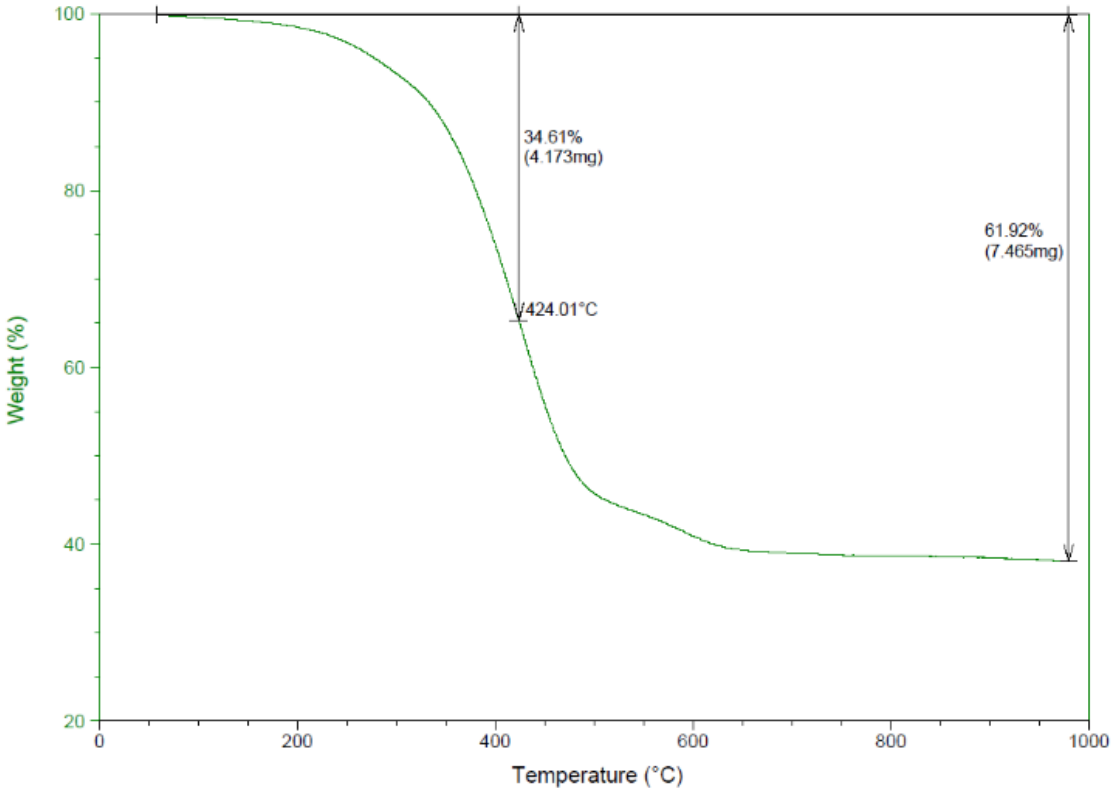

Figure 4.15. TGA thermogram analysis of weight (%) as a function increasing temperature of siloxane epoxy polymer after pre, post and baked cured.

The weight loss ceased at about 700 °C, with a net loss of 61.92% (7.465 mg of 12.057 mg). A total of 38.08% of the siloxane epoxy film was left as a residue at ~1000 °C (4.592 mg. of 12.057 mg).

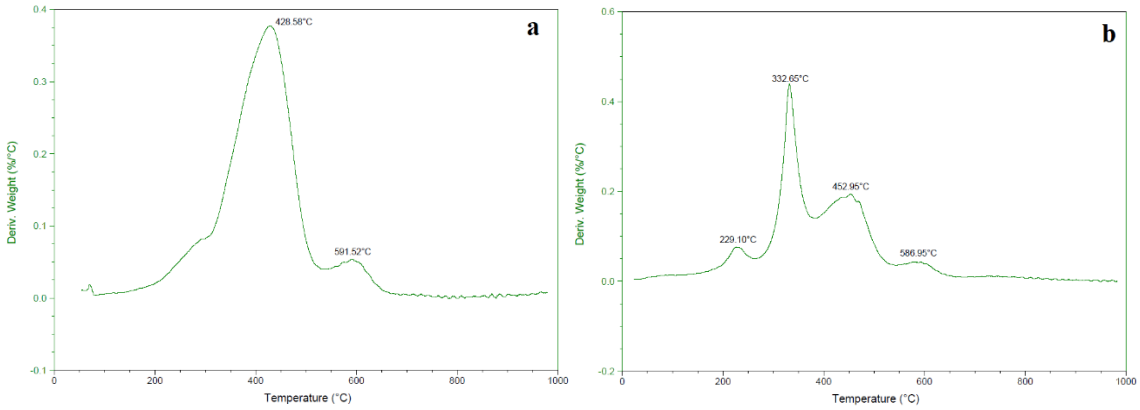

Figure 4.16. Thermogram of Derivative weight as a function of the temperature of (**a**) pure siloxane epoxy polymer and (**b**) siloxane epoxy polymer embedded $F_{64}PcZn \cup SiO_2$.

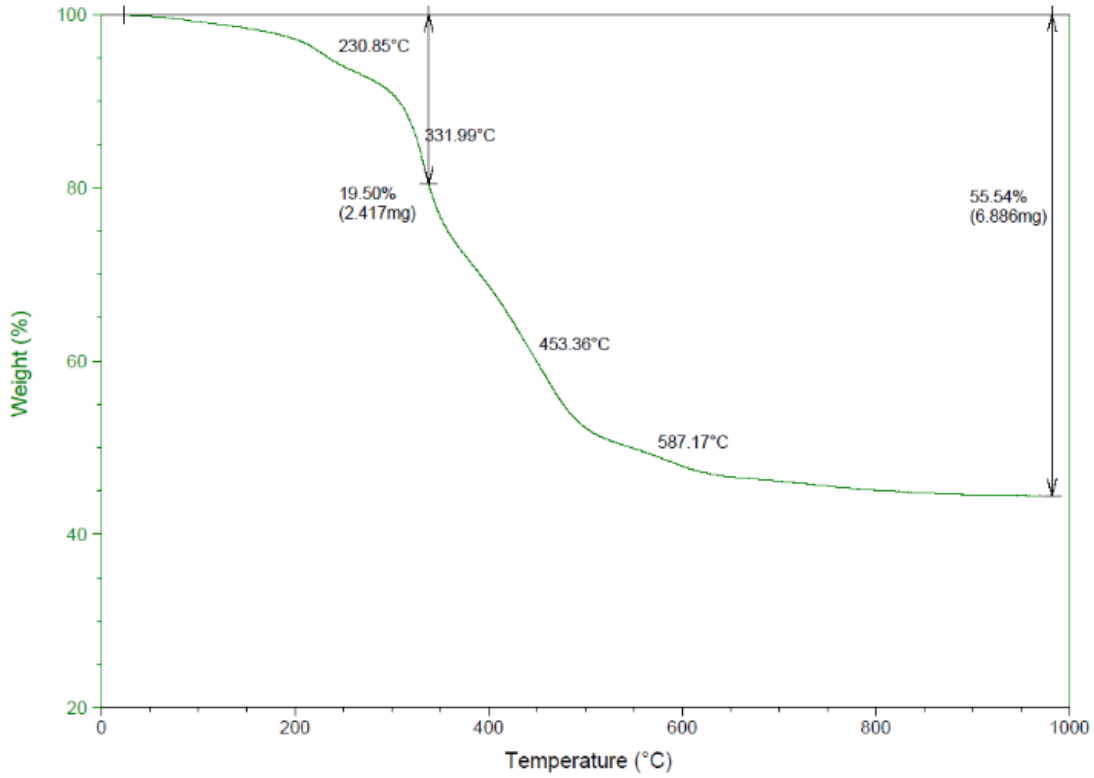

Figure 4.17. TGA thermogram analysis of weigh (%) as a function increasing temperature of siloxane epoxy polymer embedded $F_{64}PcZn \cup SiO_2$ after pre, post and baked cured.

Siloxane epoxy-containing $F_{64}PcZn \cup SiO_2$ was studied for comparison to determine any substantial differences due to the presence of the embedded catalyst complex. Thermogram derivative analysis is shown in **Figure 4.16b**, revealed four stages of weight loss in siloxane epoxy with embedded $F_{64}PcZn \cup SiO_2$. The film with an embedded catalyst was comparably stable to the pure siloxane epoxy film with no significant weight loss below 200 °C. A weight-loss event peaks at 230 °C for the catalyst embedded film, where the pure material only has a shoulder. Another minor weight-loss event was noted at 332 °C this is part of the broad maximum at 428 °C in the pure film. The third and fourth weight loss maxima, as seen from **Figure 4.17,** corresponded to the major weight loss maxima of the pure film in **Figure 4.15.** These two higher temperature events are most likely due to the decomposition of the organic components of the siloxane epoxy material. The lower temperature maxima seen with the embedded catalyst are at temperatures where the pure material decomposes but does not show a maximum in the derivative – the presence of the catalyst and support may be augmenting or changing the processes at these temperatures. The amount of weight loss is too high to be the catalyst itself, and the support (SiO_2) would not show weight loss at these low temperatures. The film with the embedded catalyst has a higher residual weight at 1000 °C, the addition of the refractory support accounts for most of this residue.

An overlay of the two TGA curves is shown in **Figure 4.18**. As seen in the derivative curves, the addition of the catalyst results in more defined low-temperature weight loss and higher residual weight. The greatest weight loss for both films occurred between 300 and 500 °C, well above the expected working temperature of the photocatalytic surface.

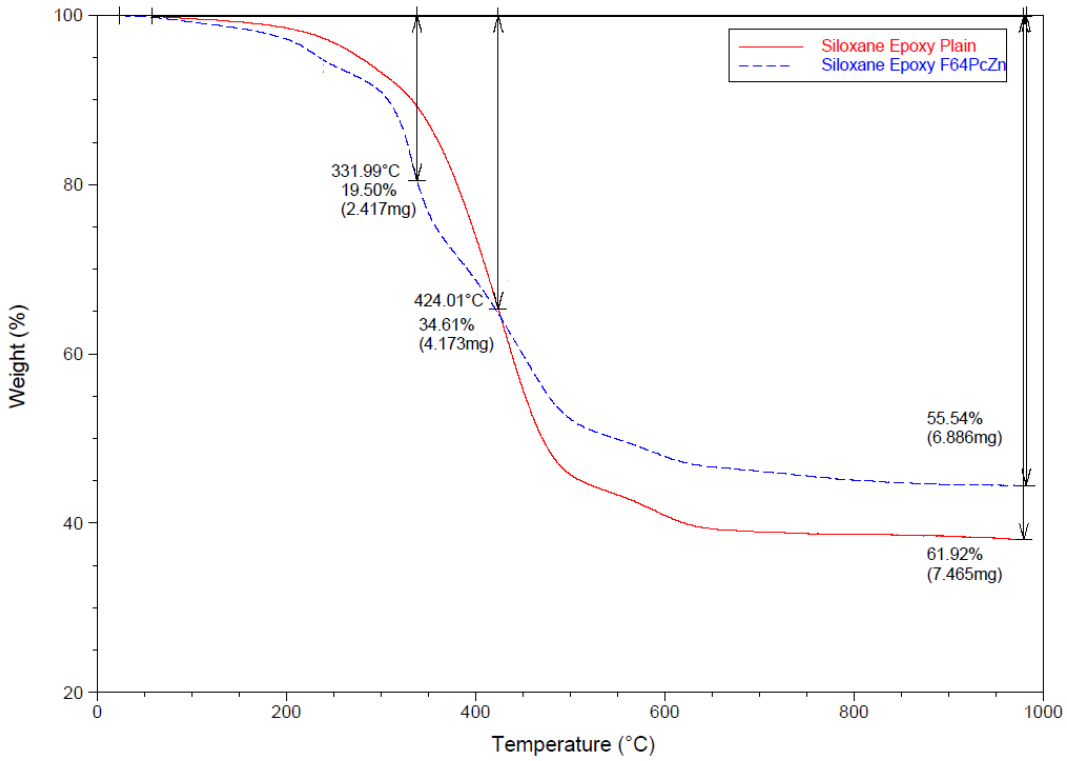

Figure 4.18. TGA thermogram analysis of weight (%) as a function of increasing temperature of pure siloxane epoxy and siloxane epoxy polymer embedded $F_{64}PcZn \cup SiO_2$ after pre, post and baked cured.

4.3.6. Optical properties of the coated films.

Optical properties of the coated films were measured by diffuse reflectance with a plain glass slide as control. As can be seen in **Figure 4.19**, the plain glass slide gave a percent reflectance of 89.6% from 400 - 800 nm, while the pure siloxane-epoxy coated film gave a percent reflectance of 87.2%, only ~2% below the plain glass side. Siloxane epoxy polymer with embedded $F_{64}PcZn \cup SiO_2$ coated film gave maximum reflectance at 500 nm of 82.1%. The absorbance of the catalyst can be seen in this reflectance curve, with a reflectance minimum of 63.4% at 691 nm. This is slightly shifted from the absorbance λ_{max} at 684 nm.

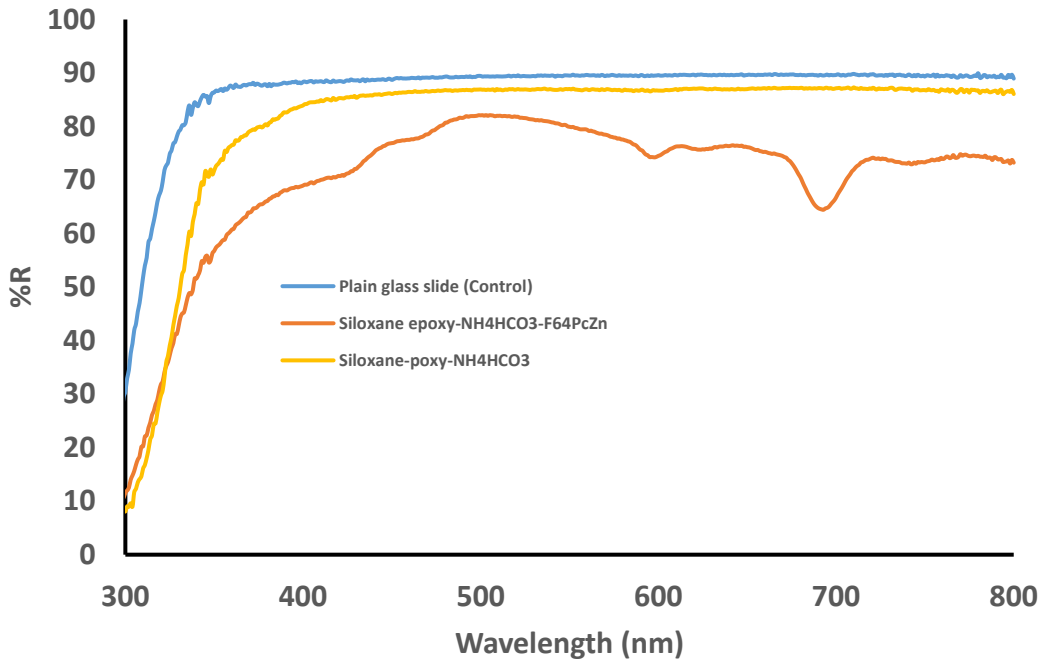

Figure 4.19. a. UV-Vis-NIR diffused reflectance of the plain glass slide, siloxane epoxy& NH_4HCO_3 and siloxane epoxy polymer embedded NH_4HCO_3&$F_{64}PcZn \cup SiO_2$ after pre, post and baked cured.

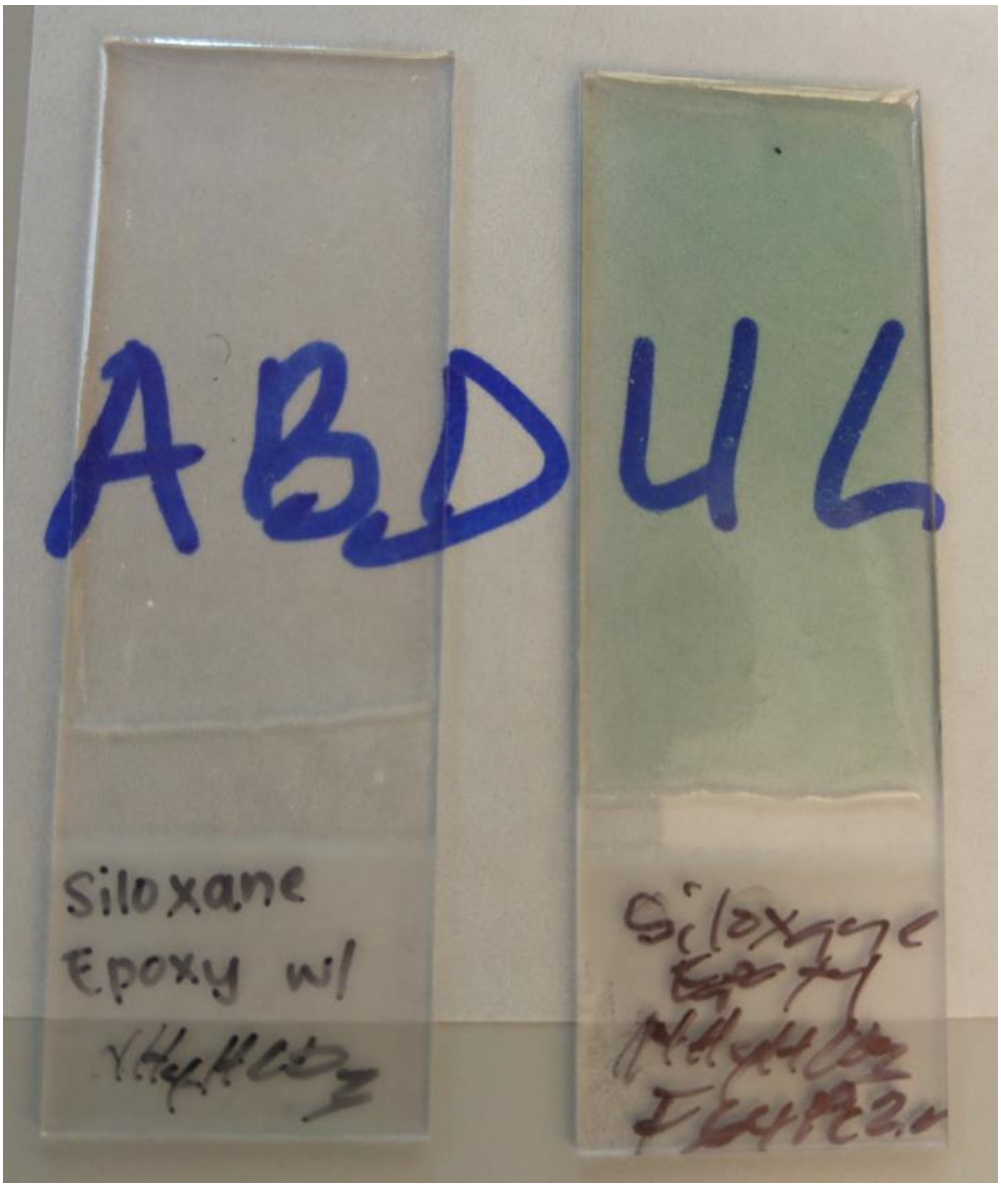

Figure 4.19. b. Picture of siloxane epoxy NH_4HCO_3 and siloxane epoxy polymer embedded NH_4HCO_3&$F_{64}PcZn\cup SiO_2$ after pre, post and baked cured. *"Image courtesy of Abdul Azeez"*.

The optical properties of the siloxane-epoxy films without an embedded catalyst are good very minimally absorbing. Some small visible light absorption is noted with the addition of the catalyst. These transparent, nearly colorless coatings are therefore appropriate for the coating of window materials and other transparent surfaces, such as fish tanks.

Figure 4.19b provides images of the siloxane epoxy-NH_4HCO_3 and siloxane epoxy polymer embedded NH_4HCO_3-$F_{64}PcZn \cup SiO_2$ after the coated films were pre, post and baked cured. The siloxane epoxy-NH_4HCO_3 without the $F_{64}PcZn \cup SiO_2$ photocatalyst shows a slightly off-white color, the siloxane epoxy polymer embedded NH_4HCO_3-$F_{64}PcZn \cup SiO_2$ shows a pale greenish color revealing the presence of phthalocyanine. A clear distinction in color can be made between these two coated films, but both films show a high degree of transparency, as can be clearly seen in **Figure 4.19b**.

4.3.7. SEM-EDX: Morphology and Imaging Analysis of Films.

Scanning electron microscopy and Energy Dispersal X-ray Spectroscopy (SEM-EDX) analysis were performed on films to understand the morphological and topographical of the films. Analytical specifications were held uniform for all films for easy comparison. All magnifications were set from low to high 2,000 - 60,000x range, sample distance to the nozzle; width distance 10.1 mm, sample analysis mode was set at secondary electron (SE). The instrument was set at high voltage (HV) 5.00 kV, the instrument chamber pressure was set at 5.39 x 10^{-1} Torr and sample scale bars were set from 1 - 50 µm.

The surface of the siloxane-epoxy$\in NH_4HCO_3$ film appeared to be uniformly rough at close magnification (**Figures 4.20, 4.21**). There is a noticeable microstructure without any surface deformation. Some surface charging can be noticed in the micrograph images, these charging effects on the surface do not contribute to the surface morphology. The roughness was tailored for improved hydrophobicity as a result of the decomposing NH_4HCO_3, although a true superhydrophobic condition (CA > 150°) was not achieved. Compared to the PVDF films

described in **Chapters 2 & 3**, the siloxane-epoxy film reveals roughness only on a very fine scale (< 1 μm). The varying levels of surface roughness from tens of microns down to the submicron level are not apparent. This accounts, to some extent, for the lower contact angles achieved with the siloxane-epoxy coating. The reason for the different morphology is found in the different character of the two polymeric coatings. PVDF is a semicrystalline polymer, and the films are prepared by solvent casting. The siloxane-epoxy is an amorphous, cross-linked network polymer, and the films are prepared by a solvent-less process that requires a cross-linking or curing agent. As seen previously, the appearance to the naked eye or optical microscope of siloxane-epoxy∈NH_4HCO_3 films depend strongly on curing time at low cure times the films were observed to be foamy, with readily observed gas bubbles from the decomposing salt, giving roughness on too large of a length scale for superhydrophobicity. If allowed to cure to a nearly rigid condition, the roughness is limited to a very fine scale. Future studies to further optimize the curing conditions with regard to the amount of curing agent and length of cure prior to baking are recommended.

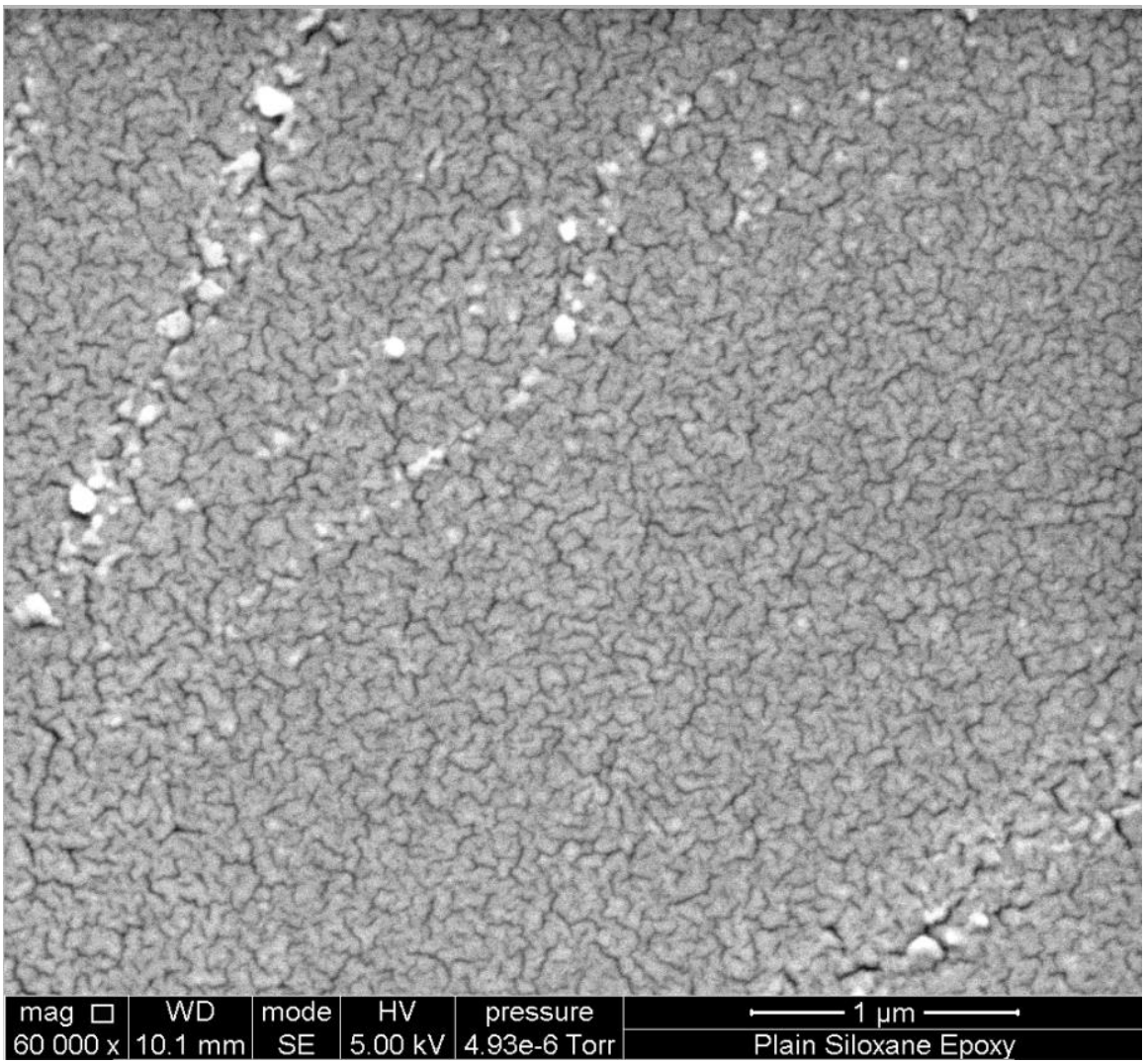

Figure 4.20. SEM micrograph of plain $NH_4HCO_3 \in$Siloxane epoxy film at 1 µm scale. *"Image courtesy of Abdul Azeez"*.

At lower magnifications shown in **Figure 4.21**, the siloxane-epoxy$\in NH_4HCO_3$ surfaces appear to be very smooth. Some charging effects are noticed, and a few large scale structures, possibly from the coating process (spreading/brushing) can be seen.

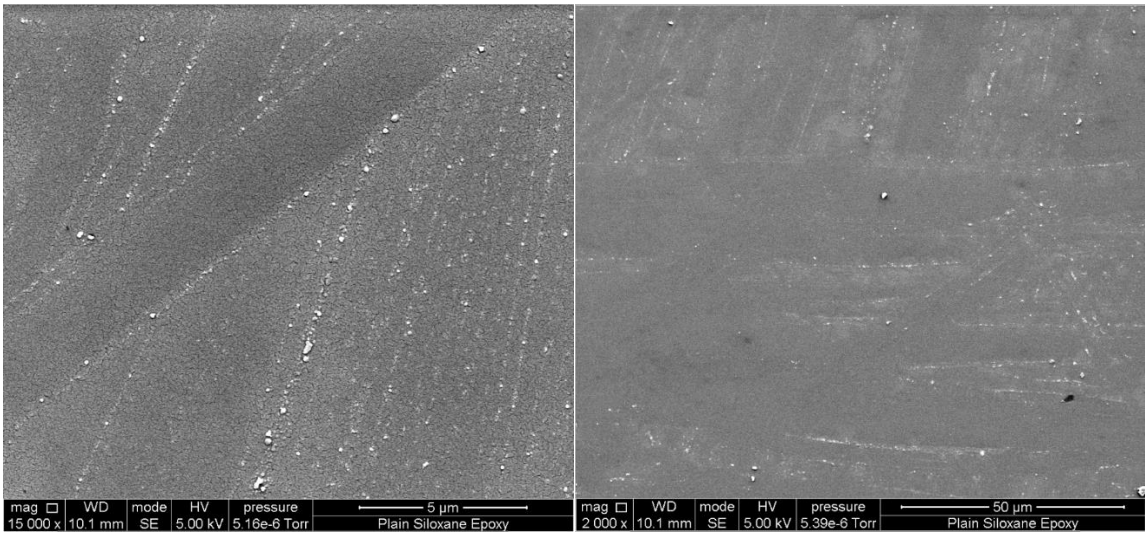

Figure 4.21. SEM micrograph of plain NH_4HCO_3∈Siloxane epoxy film set at 5 µm and 50 µm scale. *"Image courtesy of Abdul Azeez"*.

The surface morphology of a siloxane-epoxy∈**(**NH_4HCO_3 & TiO_2) film is shown in **Figure 4.22**. (*TiO_2 was used for these studies in place of SiO_2 because the EDX option on the instrument will allow us to observe the distribution of the particles from the titanium (Ti) element. If SiO_2 was used, the silicon in the siloxane-epoxy resin would interfere with observation of the silicon in the SiO_2.*) The image reveals a surface roughness similar to the surface roughness from **Figure 4.20**, for films without the added particles.

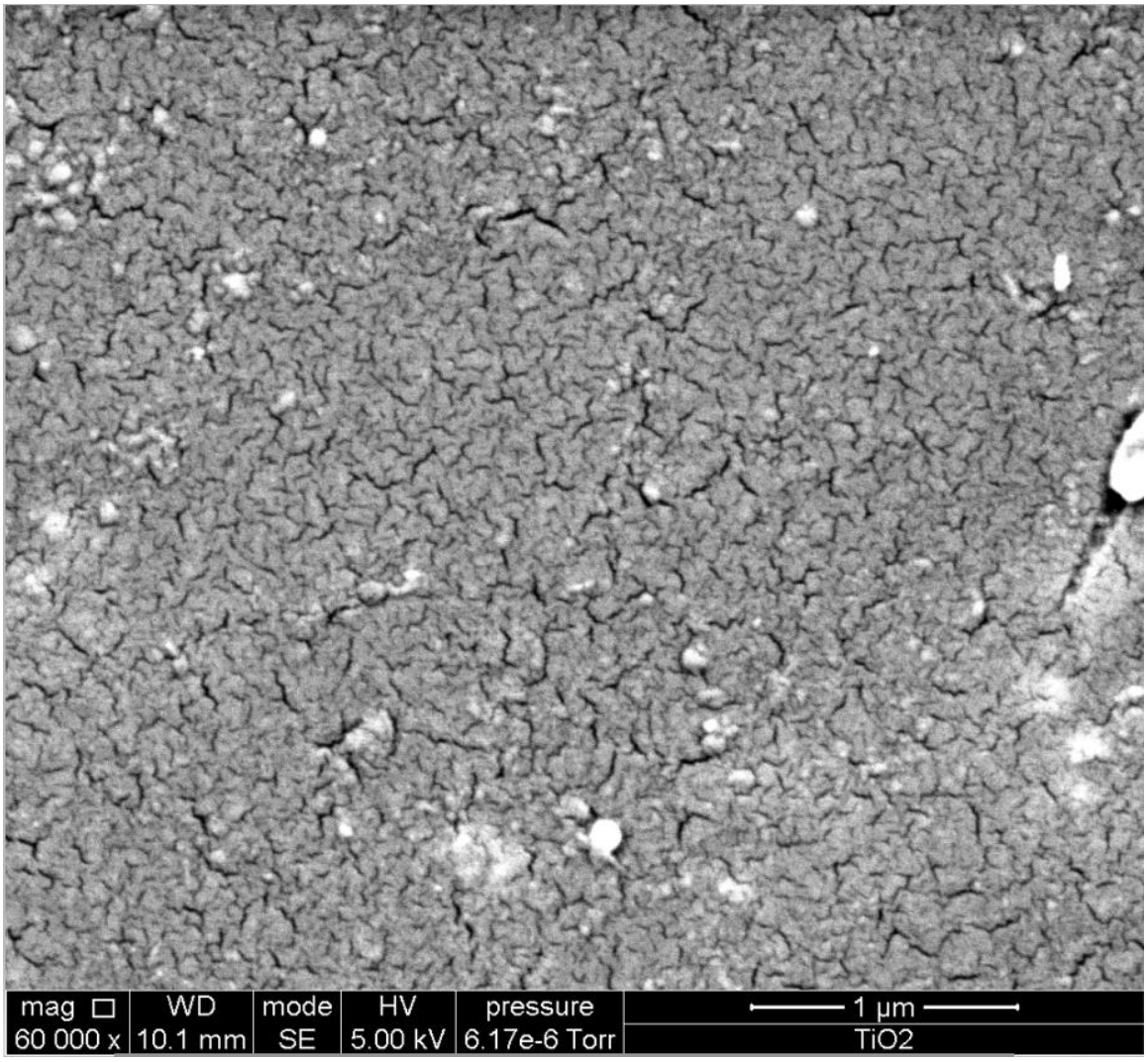

Figure 4.22. SEM micrograph of $NH_4HCO_3 \in$Siloxane epoxy$\in TiO_2$ film at 1 µm scale. *"Image courtesy of Abdul Azeez"*.

At lower magnification, the one difference to the earlier images are some roughness observed as lumps/bumps, believed to be from the TiO_2 catalyst, possibly as aggregates (see below). The hydroxyl groups on the surface of TiO_2 can form hydrogen bonding at close proximity during the mixing process complex. A study by Hugenschmidt *et al*, [50] revealed hydrogen bonding in the presence of water molecules within the TiO_2 proximity can result in hydrogen bonding with a free Ti^{+4} location.

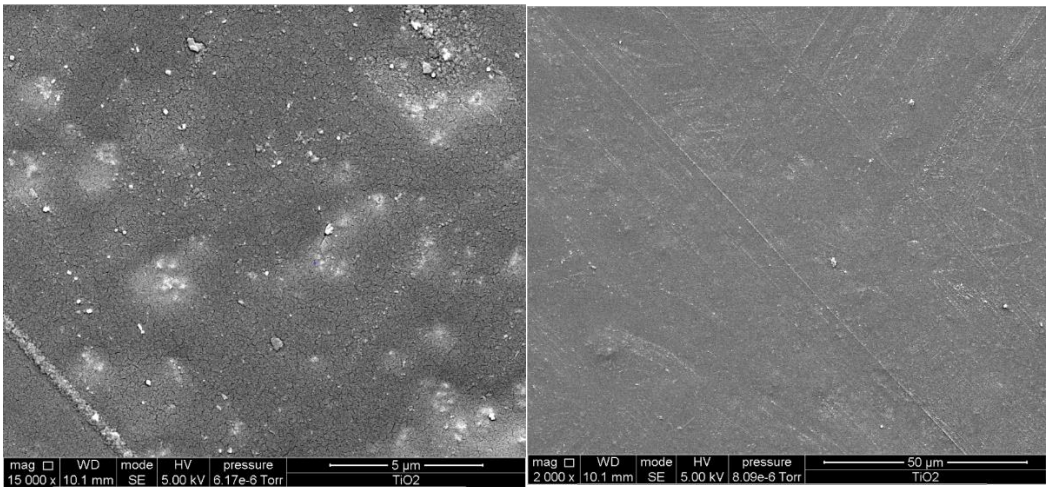

Figure 4.23. SEM micrograph of $NH_4HCO_3 \in$Siloxane epoxy$\in TiO_2$ film set at 5 µm and 50 µm scale. *"Image courtesy of Abdul Azeez"*.

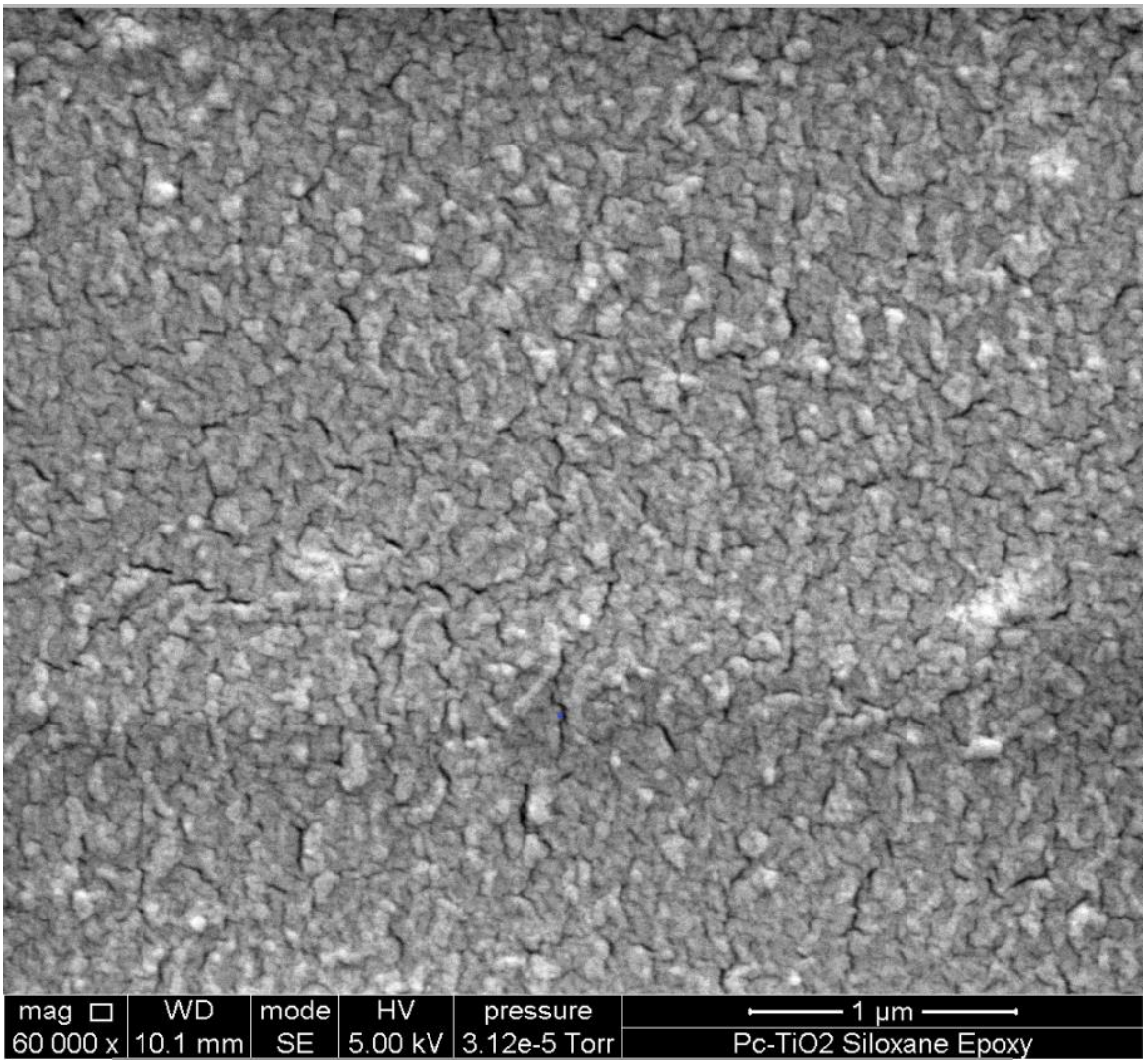

Figure 4.24. SEM micrograph of $NH_4HCO_3 \in$ Siloxane epoxy $\in TiO_2 \cup F_{64}$Pc Zn film at 1 µm scale. *"Image courtesy of Abdul Azeez"*.

The surface morphology of Siloxane-epoxy $\in NH_4HCO_3$ & $TiO_2 \cup F_{64}$Pc Zn photocatalyst is shown in **Figure 4.24,** shows similarity to the siloxane-epoxy $\in NH_4HCO_3$ film without photocatalyst from **Figure 4.20**, furthermore, the added catalyst does not change the morphology or topography of the film.

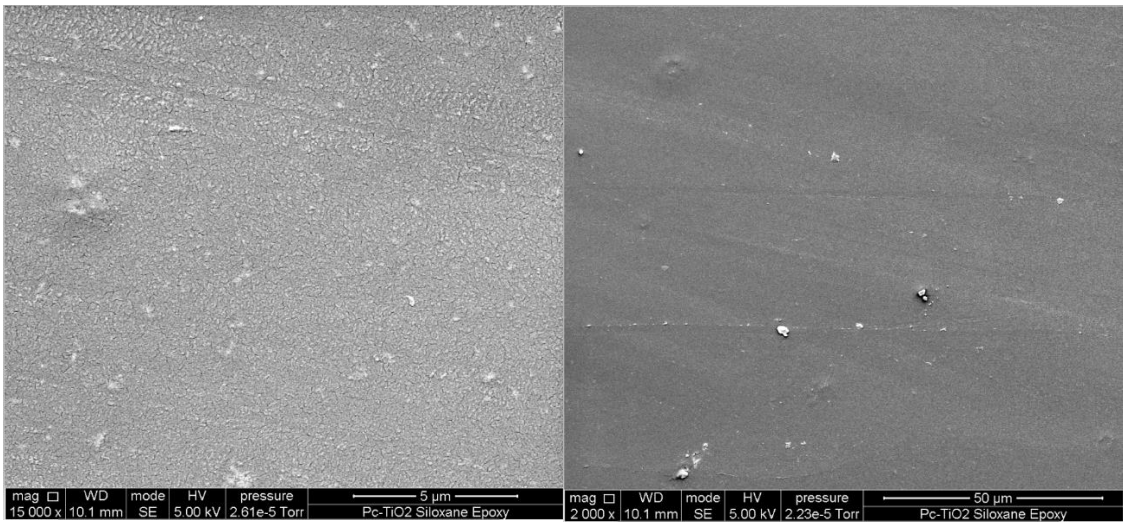

Figure 4.25. SEM micrograph of $NH_4HCO_3 \in$ Siloxane epoxy $\in TiO_2 \cup F_{64}PcZn$ film set at 5 µm and 50 µm scale. *"Image courtesy of Abdul Azeez"*.

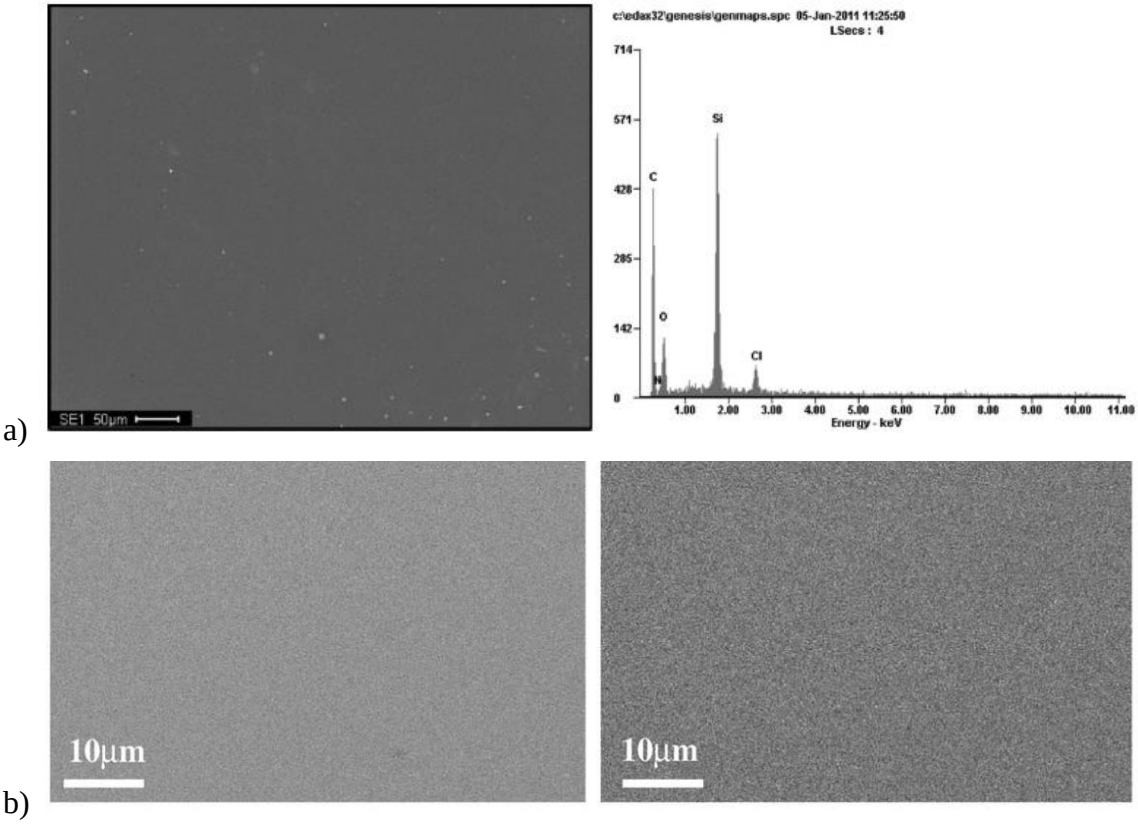

Figure 4.26. SEM micrograph of epoxy resin modified silicone surfaces. **a**) Surface image and EDX analysis from Wang *et al*. [26,] **b**) Surface images of films from MEK and toluene from *"Reproduced with permission from Elsevier"*. [26]

The lower magnification micrographs shown in **Figure 4.25**, revealed a uniform coating, without the lumps/bumps observed with TiO_2 alone. The coating of the TiO_2 particles with the fluorinated Pc catalyst prevents the hydrogen bond mediated aggregation of the TiO_2. The surfaces shown above from **Figure 4.26**, are from literature studies on siloxane-epoxy surfaces.

4.3.8. Energy Dispersion X-ray Spectroscopy (EDX).

EDX revealed the elemental composition mapping of the film surface; the distribution of the catalyst in the top layer of the polymer matrix can be determined to analyze the distribution pattern and observe any agglomeration of photocatalyst particles.

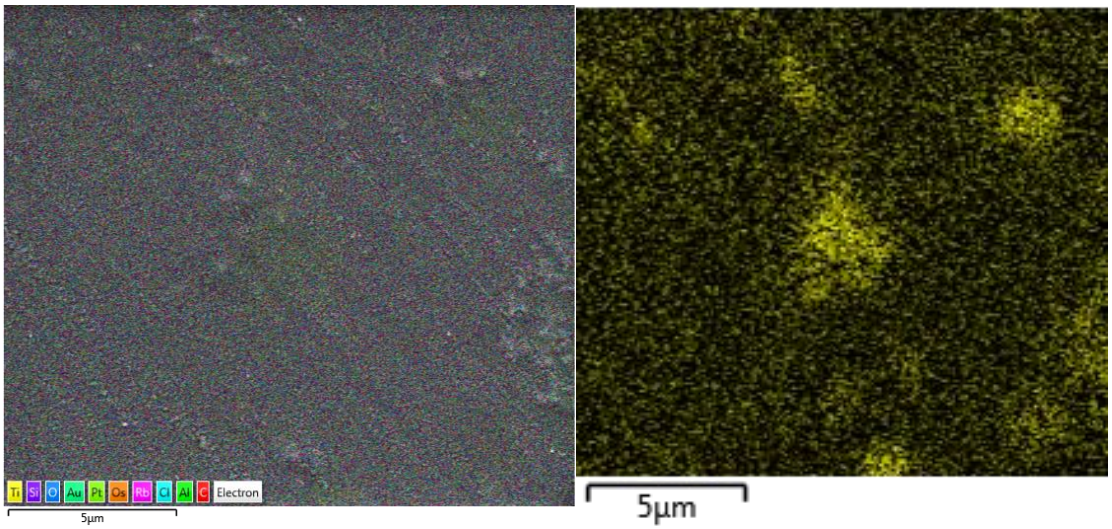

Figure 4.27. EDX micrograph and elemental mapping of siloxane-epoxy∈ (NH_4HCO_3 & TiO_2) film, revealing [TiO_2 catalyst (Ti element)] positions near the surface. *"Image courtesy of Abdul Azeez"*.

An EDX micrograph of the surface of a siloxane-epoxy∈ (NH_4HCO_3 & TiO_2) film is shown in **Figure 4.27**. Tracking the elemental mapping of Ti as a means to determine the photocatalyst particles positioned on or near the surface of the film, the image revealed an uneven distribution

of the TiO_2 photocatalyst, with agglomerations or clusters of the photocatalyst particles. The spectrum of the mapped elements is shown in **Figure 4.28** for carbon (C), oxygen (O), silicon (Si), titanium (Ti), chlorine (Cl), platinum(Pt) and gold (Au): the materials used in coating the samples for SEM-EDX analysis (Au, Pt) also find their way into the spectrum shown in **Figure 4.28**.

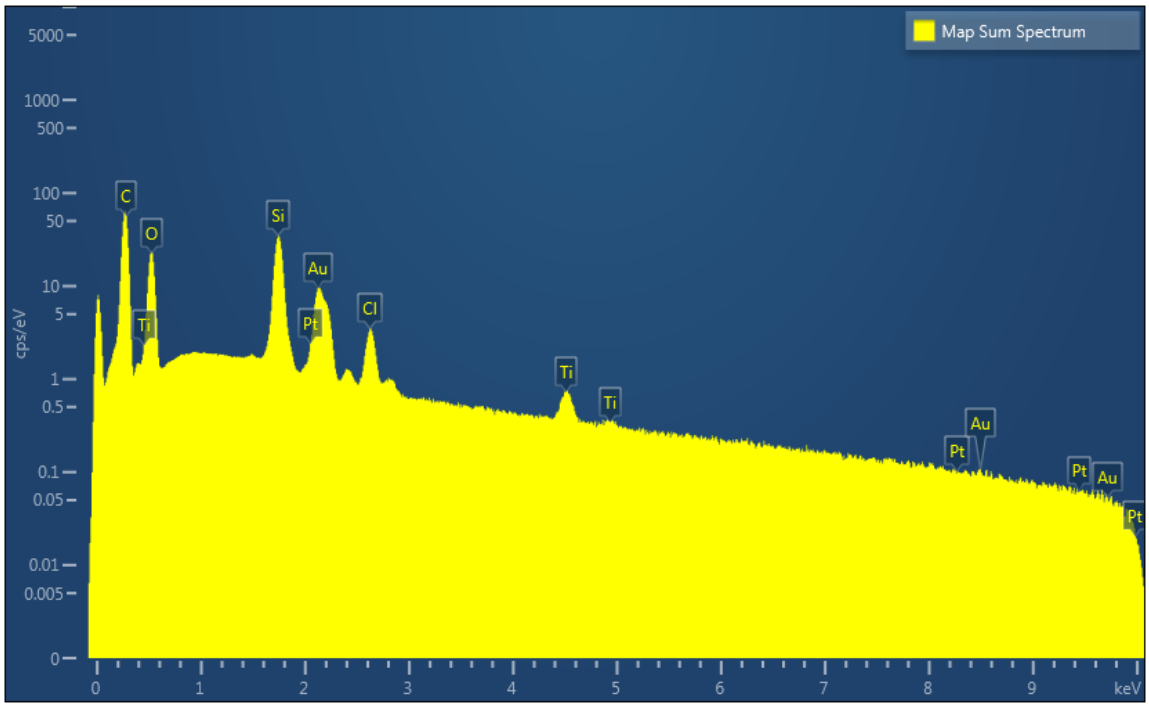

Figure 4.28. EDX elemental mapping of Siloxane epoxy∈ (NH_4HCO_3 & TiO_2) film, showing cps/eV as a function of keV. *"Image courtesy of Abdul Azeez"*.

AN EDX micrograph of the surface of a siloxane-epoxy∈ (NH_4HCO_3 & TiO_2∪$F_{64}PcZn$) film is shown in **Figure 4.29**. The Ti-based image revealed a uniform distribution of the TiO_2∪$F_{64}PcZn$ photocatalyst across the film, with no agglomeration or uneven distribution shown on the micrograph. The coated TiO_2∪$F_{64}PcZn$ photocatalyst distributed much more evenly through the film compared to the TiO_2 film without $F_{64}PcZn$ photosensitizer shown in **Figures 4.27** and **4.28**.

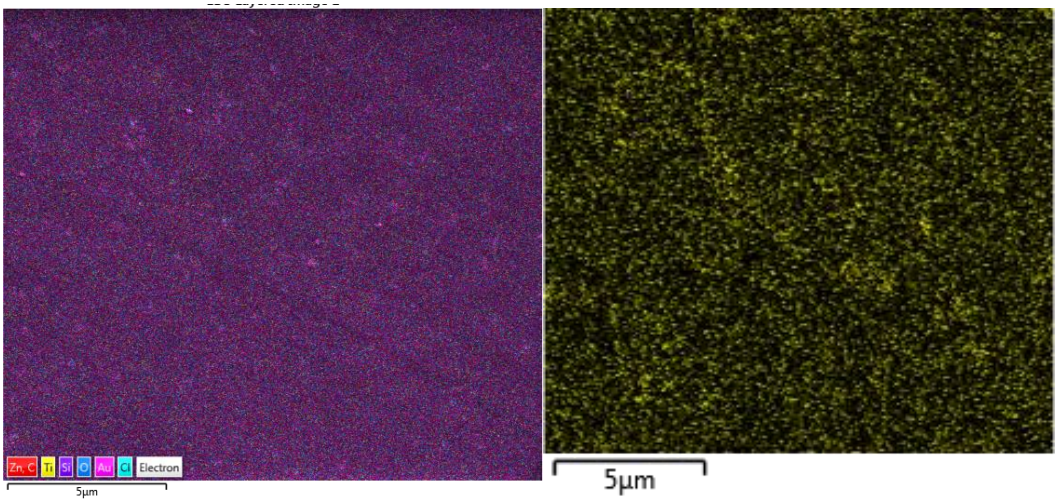

Figure 4.29. EDX elemental mapping of Siloxane epoxy∈ (NH_4HCO_3 & TiO_2∪F_{64}PcZn) film, revealed the positions of [TiO_2∪F_{64}PcZn (Ti element)] on the film. *"Image courtesy of Abdul Azeez"*.

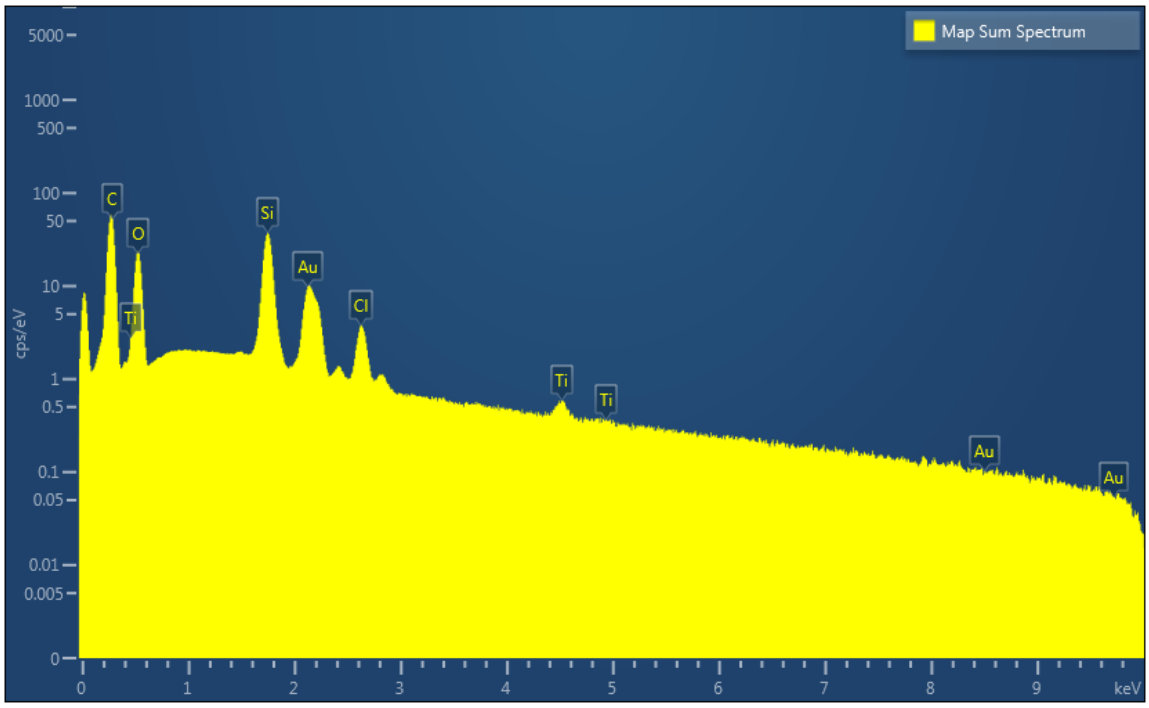

Figure 4.30. EDX elemental mapping of Siloxane epoxy∈ (NH_4HCO_3 & TiO_2∪F_{64}PcZn) film, showing cps/eV as a function of keV. *"Image courtesy of Abdul Azeez"*.

Titanium, fluorine, and zinc represented the photosensitizer catalyst and the solid support catalyst, although, the element of fluorine and zinc were not seen in the EDX spectrum shown in **Figure 4.31.** The amount of $F_{64}PcZn$ used for the preparation of the catalyst complex $TiO_2 \cup F_{64}PcZn$ was less than 1%, and futher 25% of $F_{64}PcZn$ was adsorbed onto TiO_2, 3% $TiO_2 \cup F_{64}PcZn$ complex was added to siloxane epoxy (%w/%w). This smallness might be responsible for the lack of fluorine and zinc elements in the EDX spectrum. On the other hand, 3% TiO_2 account for the amount shown in the EDX spectrum.

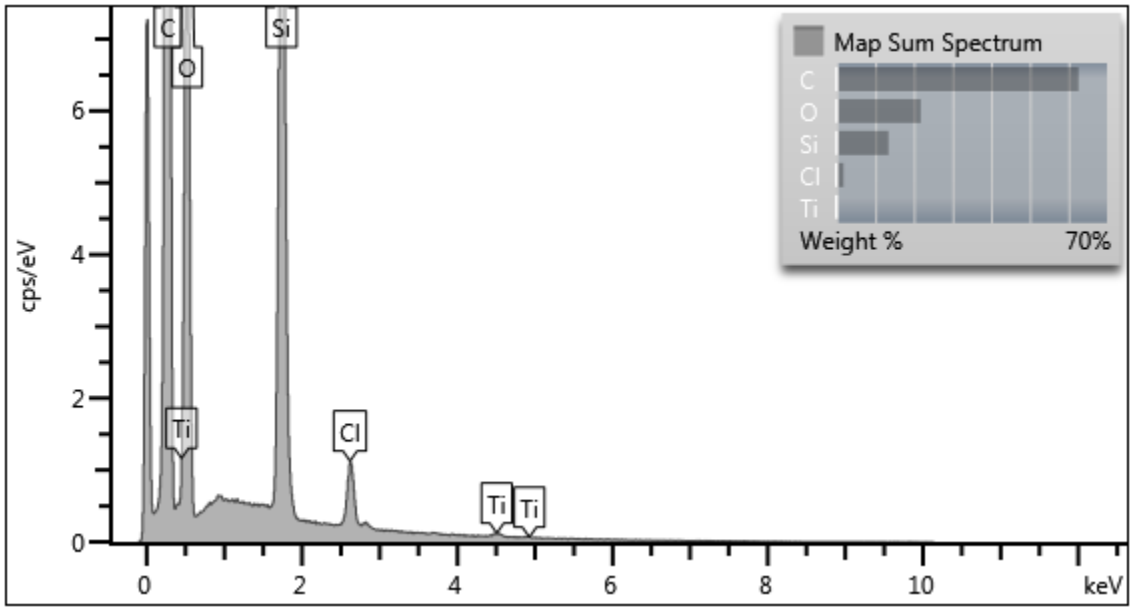

Figure 4.31. EDX elemental mapping of Siloxane epoxy∈ (NH_4HCO_3 & $TiO_2 \cup F_{64}PcZn$) film, revealed the weight % of each element, represented by cps/eV as a function of keV. *"Image courtesy of Abdul Azeez"*.

4.4. Conclusions.

This chapter demonstrated the preparation of siloxane modified epoxy resin cross-linked with aminopropyltriethoxysilane with NH_4HCO_3 to form a microstructure rough surface. Two separate surfaces containing $NH_4HCO_3 \in$ Siloxane epoxy film and $NH_4HCO_3 \in$ Siloxane epoxy $\in SiO_2 \cup F_{64}$Pc Zn film were characterized to determine and compare their thermal stability. The prepared films were thermally stable at temperature until 300 ^oC, the embedded catalyst on the matrix of siloxane modified epoxy did not change regardless of the thermal treatment at this elevated compared to the original siloxane modified epoxy film. These characteristics of the studied polymer show a film with an excellent working application range regarding thermal sensitivity. Infra-red spectroscopy characterization revealed the formation of two sharp peaks at 2863 cm^{-1} also represent the secondary amine (N-H bond), which clearly illustrates the epoxy reaction, and the absence of one hydrogen bond form the ($N\text{-}H_2$ bond) from the aminopropyltriethoxysilane crosslinker. The surface roughness was achieved as reveal by SEM morphology and confirmed by CA measurement and the optimization clearly played a role in achieving the surface roughness that leads to increasing CA, although, superhydrophobicity was not achieved the surface became more hydrophobic after the optimization process. The EDX micrograph mapping and elemental analysis clearly revealed the difference between Siloxane-epoxy&$NH_4HCO_3 \in TiO_2$ surface and Siloxane-epoxy&$NH_4HCO_3 \in TiO_2 \cup F_{64}$PcZn surface. The elemental mapping of Ti Siloxane-epoxy&$NH_4HCO_3 \in TiO_2$ surface revealed agglomeration due to hydrogen bonding and the same thing was not noticed with Siloxane-epoxy&$NH_4HCO_3 \in TiO_2 \cup F_{64}$PcZn surface because of the protective coating provided by F_{64}PcZn.

References.

1. Hosking, N., Ström, M., Shipway, P., & Rudd, C. (**2007**). Corrosion resistance of zinc–magnesium coated steel. *Corrosion Science*, *49*(9), 3669–3695.
2. Huang, C., Tsai, W., & Lee, J. (**1996**). Surface modification of carbon steel with laser treated nitrogen-containing stainless steel layers. *Surface and Coatings Technology*, *79*(1-3), 67–70.
3. Peyre, P., Scherpereel, X., Berthe, L., Carboni, C., Fabbro, R., Béranger, G., & Lemaitre, C. (**2000**). Surface modifications induced in 316L steel by laser peening and shot-peening. Influence on pitting corrosion resistance. *Materials Science and Engineering: A*, *280*(2), 294–302.
4. Song, H., & Saraswathy, V. (**2006**). Studies on the corrosion resistance of reinforced steel in concrete with ground granulated blast-furnace slag An overview. *Journal of Hazardous Materials*, *138*(2), 226–233.
5. Il'darkhanova, F. I., Mironova, G. A., Bogoslovsky, K. G., Men'shikov, V. V., & Bykov, E. D. (**2012**). Development of paint coatings with superhydrophobic properties. *Protection of Metals and Physical Chemistry of Surfaces*, 48(7), 796–802.
6. Lee, W., Lewandowski, Z., Nielsen, P. H., & Hamilton, W. A. (**1995**). Role of sulfate-reducing bacteria in corrosion of mild steel: A review. *Biofouling*, *8*(3), 165–194.
7. Deqing, W., Ziyuan, S., & Longjiang, Z. (**2003**). A liquid aluminum corrosion resistance surface on steel substrate. *Applied Surface Science*, *214*(1-4), 304–311.
8. Hong, I., & Koo, C. (**2005**). Antibacterial properties, corrosion resistance and mechanical properties of Cu-modified SUS 304 stainless steel. *Materials Science and Engineering: A*, *393*(1-2), 213–222.
9. Li, Y., Huang, X. J., Heo, S. H., Li, C. C., Choi, Y. K., Cai, W. P., & Cho, S. O. (**2007**). Superhydrophobic Bionic Surfaces with Hierarchical Microsphere/SWCNT Composite Arrays. *Langmuir*, *23*(4), 2169–2174.
10. Vasconcelos, D., Carvalho, J., Mantel, M., & Vasconcelos, W. (**2000**). Corrosion resistance of stainless steel coated with sol-gel silica. *Journal of Non-Crystalline Solids*, *273*(1-3), 135–139.
11. Bravo, J., Zhai, L., Wu, Z., Cohen, R. E., & Rubner, M. F. (**2007**). Transparent Superhydrophobic Films Based on Silica Nanoparticles. *Langmuir*, *23*(13), 7293–7298.
12. Wang, G., Guo, Z., & Liu, W. (**2014**). Interfacial effects of superhydrophobic plant surfaces: A review. *Journal of Bionic Engineering*, *11*(3), 325–345.
13. Wang, M., Xue, J., Gao, R., Gao, H., Zhou, Y., Zhao, Y., Wang, J. (**2019**). Interface morphology and corrosion behavior of bulk Fe_2B in liquid Al. *Materials Characterization*, *152*, 1–11.

14. Bell, W. T., Chalian, V. A., & Moore, B. (**1985**). Polydimethyl siloxane materials in maxillofacial prosthetics: Evaluation and comparison of physical properties. *The Journal of Prosthetic Dentistry*, *54*(3), 404–410.

15. Bott, R. H., Summers, J. D., Arnold, C. A., Taylor, L. T., Ward, T. C., & McGrath, J. E. (**1987**). Synthesis and Characteristics of Novel Poly(Imide Siloxane) Segmented Copolymers. *The Journal of Adhesion*, *23*(2), 67–82.

16. Furukawa, N., Yuasa, M., Omori, F., & Yamada, Y. (**1996**). Adhesive Properties of Siloxane Modified Polyimides and Application for Multi-Layer Printed Circuit Boards. *The Journal of Adhesion*, *59*(1-4), 281–294.

17. Ibrahim, M., Al-Gahtani, A. S., Maslehuddin, M., & Dakhil, F. H. (**1999**). Use of Surface Treatment Materials to Improve Concrete Durability. *Journal of Materials in Civil Engineering*, *11*(1), 36–40.

18. Scardino, A. J., Zhang, H., Cookson, D. J., Lamb, R. N., & Nys, R. (**2009**). The role of nano-roughness in antifouling. *Biofouling*, *25*(8), 757–767.

19. Kaempgen, M., Duesberg, G., & Roth, S. (**2005**). Transparent carbon nanotube coatings. *Applied Surface Science*, *252*(2), 425–429.

20. Flores-Vivian, I., Hejazi, V., Kozhukhova, M. I., Nosonovsky, M., & Sobolev, K. (**2013**). Self-Assembling Particle-Siloxane Coatings for Superhydrophobic Concrete. *ACS Applied Materials & Interfaces*, *5*(24), 13284–13294.

21. Gonçalves, G., Marques, P. A., Trindade, T., Neto, C. P., & Gandini, A. (**2008**). Superhydrophobic cellulose nanocomposites. *Journal of Colloid and Interface Science*, *324*(1-2), 42–46.

22. Fang, X., Huang, X., Lu, Z., Chen, L., & Chen, S. (**2010**). Synthesis of new superhydrophobic nanosilica and investigation of their performance in reinforcement of polysiloxane. *Polymer Composites*, *31*(9), 1628–1636.

23. Shiu, J., Kuo, C., Chen, P., & Mou, C. (**2004**). Fabrication of Tunable Superhydrophobic Surfaces by Nanosphere Lithography. *Chemistry of Materials*, *16*(4), 561–564.

24. Hikita, M., Tanaka, K., Nakamura, T., Kajiyama, T., & Takahara, A. (**2005**). Super-Liquid-Repellent Surfaces Prepared by Colloidal Silica Nanoparticles Covered with Fluoroalkyl Groups. *Langmuir*, *21*(16), 7299–7302.

25. Zhu, L., & Jin, Y. (**2007**). A novel method to fabricate water-soluble hydrophobic agent and super-hydrophobic film on pretreated metals. *Applied Surface Science*, *253*(7), 3432–3439.

26. (a) Wang, S., Li, Y., Fei, X., Sun, M., Zhang, C., Li, Y., Hong, X. (**2011**). Preparation of a durable superhydrophobic membrane by electrospinning poly (vinylidene fluoride) (PVDF) mixed with epoxy–siloxane modified SiO_2 nanoparticles: A possible route to superhydrophobic surfaces with low water sliding angle and high water contact angle. *Journal of Colloid and Interface Science*, *359*(2), 380–388. (b) Qian, M., Mcintosh Soutar, A., Tan, X. H., Zeng, X. T., & Wijesinghe, S. L. (**2009**). Two-part epoxy-siloxane

hybrid corrosion protection coatings for carbon steel. *Thin Solid Films*, *517*(17), 5237–5242.

27. Zhang, H., & Lamb, R. N. (**2009**). Superhydrophobic treatment for textiles via engineering nanotextured silica/polysiloxane hybrid material onto fibers. *Surface Engineering*, *25*(1), 21–24.

28. Falchi, L., Varin, C., Toscano, G., & Zendri, E. (**2015**). Statistical analysis of the physical properties and durability of water-repellent mortars made with limestone cement, natural hydraulic lime and pozzolana-lime. *Construction and Building Materials*, *78*, 260–270.

29. Zhang, S., Li, H., Jiang, Z., Zhang, B., Li, Z., Wu, J., Zhu, H. (**2019**). Effects of Cr and Mo on precipitation behavior and associated intergranular corrosion susceptibility of superaustenitic stainless steel S32654. *Materials Characterization*, *152*, 141–150.

30. Lee, W., Lewandowski, Z., Nielsen, P. H., & Hamilton, W. A. (**1995**). Role of sulfate-reducing bacteria in corrosion of mild steel: A review. *Biofouling*, *8*(3), 165–194.

31. Bravo, J., Zhai, L., Wu, Z., Cohen, R. E., & Rubner, M. F. (**2007**). Transparent Superhydrophobic Films Based on Silica Nanoparticles. *Langmuir*, *23*(13), 7293–7298.

32. Ming, W., Wu, D., Van Benthem, R., & De With, G. (**2005**). Superhydrophobic Films from Raspberry-like Particles. *Nano Letters*, *5*(11), 2298–2301.

33. Hikita, M., Tanaka, K., Nakamura, T., Kajiyama, T., & Takahara, A. (**2005**). Super-Liquid-Repellent Surfaces Prepared by Colloidal Silica Nanoparticles Covered with Fluoroalkyl Groups. *Langmuir*, *21*(16), 7299–7302.

34. Zhu, L., & Jin, Y. (**2007**). A novel method to fabricate water-soluble hydrophobic agent and super-hydrophobic film on pretreated metals. *Applied Surface Science*, *253*(7), 3432–3439.

35. Zulfiqar, S., Zulfiqar, M., Rizvi, M., Munir, A., & McNeill, I. (**1994)**. Study of the thermal degradation of polychlorotrifluoroethylene, poly(vinylidene fluoride) and copolymers of chlorotrifluoroethylene and vinylidene fluoride. *Polymer Degradation and Stability*, *43*(3), 423–430.

36. Lau, K. K. S., Bico, J., Teo, K. B. K., Chhowalla, M., Amaratunga, G. A. J., Milne, W. I., Gleason, K. K. (**2003**). Superhydrophobic Carbon Nanotube Forests. *Nano Letters*, *3*(12), 1701–1705.

37. M., S., & Natarajan, K. (**2015**). Antibiofilm Activity of Epoxy/Ag-TiO_2 Polymer Nanocomposite Coatings against Staphylococcus Aureus and Escherichia Coli. *Coatings*, *5*(2), 95–114.

38. Daniels, G. C., Iezzi, E. B., Fulmer, P. A., & Wynne, J. H. (**2016**). Synergistic antimicrobial and surface free energy of sol-gel coatings containing fluorosilanes and quaternary ammonium salts. *Progress in Organic Coatings*, *95*, 91–99.

39. Simoncic, B., & Tomsic, B. (**2010**). Structures of Novel Antimicrobial Agents for Textiles - A Review. *Textile Research Journal*, *80*(16), 1721–1737.

40. Sullivan, James F., "Epoxy Siloxane Self-Cleaning Coating using $F_{64}PcZn/TiO_2$ Photocatalyst Composite" (**2016**). *Seton Hall University Dissertations and Theses (ETDs).* 2171.

41. Wynne, J. H., Fulmer, P. A., McCluskey, D. M., Mackey, N. M., & Buchanan, J. P. (**2011**). Synthesis and Development of a Multifunctional Self-Decontaminating Polyurethane Coating. *ACS Applied Materials & Interfaces*, *3*(6), 2005–2011.

42. Sangermano, M., Palmero, P., & Montanaro, L. (**2009**). UV-Cured Polysiloxane Epoxy Coatings Containing Titanium Dioxide as Photosensitive Semiconductor. *Macromolecular Materials and Engineering*, 294(5), 323–329.

43. Gupta, P., & Bajpai, M. (**2011**). Development of Siliconized Epoxy Resins and Their Application as Anticorrosive Coatings. *Advances in Chemical Engineering and Science*, *01*(03), 133–139.

44. Sangermano, M., Palmero, P., & Montanaro, L. (**2009**). UV-Cured Polysiloxane Epoxy Coatings Containing Titanium Dioxide as Photosensitive Semiconductor. *Macromolecular Materials and Engineering*, *294*(5), 323–329.

45. Ge, H., Zhang, J., Yuan, Y., Liu, J., Liu, R., & Liu, X. (**2017**). Preparation of organic–inorganic hybrid silica nanoparticles with contact antibacterial properties and their application in UV-curable coatings. *Progress in Organic Coatings*, *106*, 20–26.

46. Zhou, L., Dong, X., Lv, G., Chen, J., & Shen, S. (**2015**). Fabrication of concave microlens array diffuser films with a soft transparent mold of UV-curable polymer. *Optics Communications*, *342*, 167–172.

47. Paluvai, N. R., Mohanty, S., & Nayak, S. K. (**2014**). Synthesis and Modifications of Epoxy Resins and Their Composites: A Review. *Polymer-Plastics Technology and Engineering*, *53*(16), 1723–1758.

48. Mowrer, N. R.; Foscante, R. E.; Rojas, J. L. Epoxy Polysiloxane coating and flooring compositions. *US*5618860A, April 8, (**1997**).

49. Vandeberg, J. T Infrared Spectroscopy Atlas for the Coatings Industry. *Federa-tion of Societies for;* (**1980**).

50. Chen, Y., Zhou, C., Chang, J., Zou, H., & Liang, M. (**2014**). The effect of epoxy–silicone copolymer content on the thermal and mechanical properties of cured epoxy resin modified with siloxane. RSC Adv., 4(105), 60685–60693.

51. Hugenschmidt, M. B., Gamble, L., & Campbell, C. T. (**1994**). The interaction of H_2O with a TiO_2(110) surface. Surface Science, 302(3), 329–340.

Chapter 5

Epoxy Modified Polysiloxane Hybrid Coated Surfaces for the Photooxidation of Organic Dyes with Visible Light.

5.1. Introduction.

Waste generated from modern industry sectors have resulted in severe environmental pollution.[1, 2] Organic waste generated by industrial processes is, in many cases toxic and cannot easily be degraded by biological organisms.[3] The numerous organic compounds in industrial use can be classified into various classes, including fertilizers, pharmaceuticals, organic dyes, detergents, pesticides, hydrocarbons, phenols, etc.[4 5] They are compositionally diverse and thus may be subjected to different forms of degradation, for example photodegradation, biological degradation , hydrolysis, oxidations, etc.[6 - 8] If chemically stable and resistant to environmental degradation, pollutants are harmful to the environment and its inhabitants.[9] Amongst organic pollutants organic dyes absorb and reflect light in the UV-Visible region of the solar spectrum, enhancing their harmful effects on ecosystems,[10] including negative effects on marine life.[11, 12, 13] Currently, some methods for remediating pollution by commercial dyes relay on adsorption and coagulation, but do not result in their *in-situ* transformation less harmful and non-toxic molecules, such as CO_2 and H_2O.[14, 15] Incomplete mineralization may produce secondary pollutants.[16] For example, chlorine, used as a disinfectant (destruction of biological and organic pollutants) can produce carcinogens.[17, 18]

Advanced oxidation processes (AOPs) have long been an effective way to degrade organic pollutants, as a result of the simplicity and the reproducibility of the oxidation process. AOP generally produce very effective reagents as they are generated *in situ* and are non-selective being able to degrade organic compounds, including organic dyes.[19] The nonselective oxidants such as $O_2^{\bullet}$, H_2O_2, $^{\bullet}OH$, and O_3 degrade organic compounds to CO_2, H_2O and other harmless organic compounds, although one major drawback is photo-induced corrosion.[20] Photocorrosion occurs during the irradiation of photocatalyst semiconductors. The photo-instability of some

photocatalysts results from the migration of metal ions into aqueous solution leading to their deactivation.[21] For example, transition metal sulfides are unstable and dissociate under irradiation, although, they exhibit narrow band gaps, tailored for the production of reactive oxygen species (ROS). A study by Lee *et al*, [21] represented in **Figure 5.1**, revealed a scheme of photocorrosion suppression through the addition of poly(ethylene oxide) to a polysulfide liquid electrolyte, thereby forming a thin layer around the quantum dot film through coordination bonding.

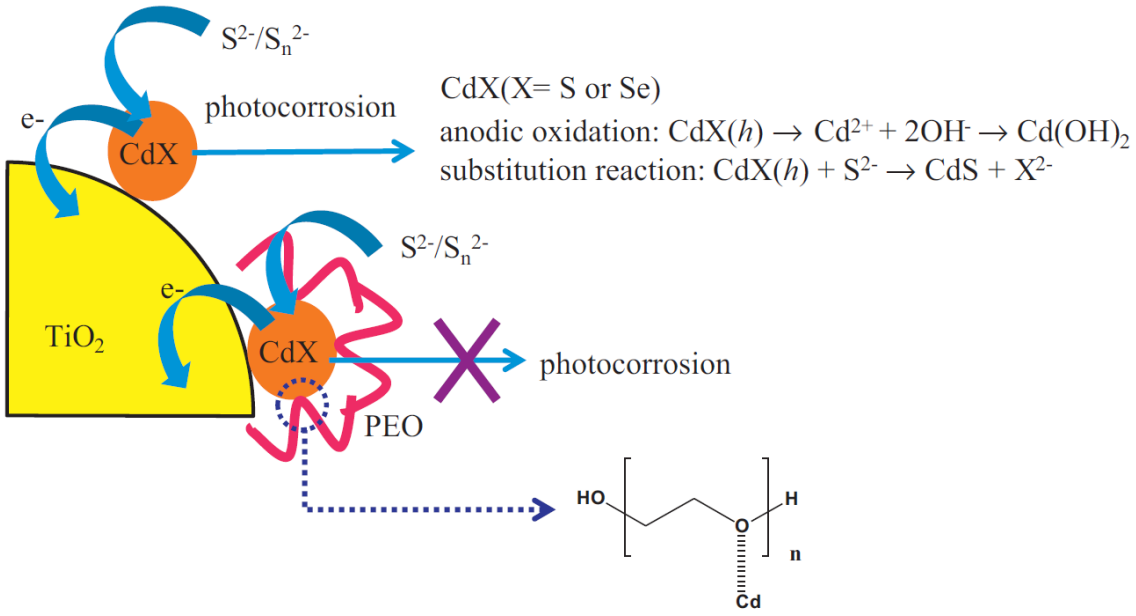

Figure 5.1. Representation of photocorrosion in quantum-dot-sensitized solar cells and poly(ethylene oxide) with polysulfide electrolyte. *"Reproduced with permission from Elsevier"* [21]

A number of transition metal oxides are also known to be susceptible to photocorrosion, including iron oxides, copper oxides, and silver oxides.[22]

As mentioned above, AOP reactivity processes always involve *in situ* generations of ROS that are very reactive toward organic dyes and other organic contaminants.[23] This process converts harmful and toxic organic contaminants into lesser, or non-toxic compounds.

The development of an active, robust photocatalyst, having the capacity to act as an effective photocatalyst without photocorrosion is of great importance. In this case, perfluorinated phthalocyanines have demonstrated their photocatalytic ability in the presence of a number of model organic dyes. Ramji *et al* demonstrated the use of $F_{64}PcZn$, $F_{64}PcCu$ and $F_{64}PcNi$ coated on semiconductors TiO_2 as well as SiO_2 and Al_2O_3 for the photodegradation of Methyl orange and Rhodamine B in aqueous media.[24] Sullivan *et al* demonstrated the photodegradation of a model organic dye in the solid-state: Methyl red was applied to and degraded on a solid surface, the photoactive surface had a composition of $F_{64}PcZn$ coated on TiO_2 ($F_{64}PcZn \cup TiO_2$) embedded in an organic-inorganic epoxy modified siloxane polymer.[25] The robustness of the photosensitizer cannot be overemphasized, as it is capable of withstanding ROS and radicals produced during the photoreactive process without self-destruction. One advantage of this class of photosensitizers vs. others, such as semiconductors based on transition metals, is the fast recombination of the electron and hole due to the wide band gap, rendering them less photoactive. Another advantage of the perfluorinated phthalocyanines is that their Q-band is positioned on the visible to NIR region of the electromagnetic spectrum, in the 600 - 800nm range giving them access to this region of the electromagnetic spectrum accounting for more than 50% of solar radiation. **Figure 5.2**, represents the chemical structure of the prototypical compound: zinc 1,4,8,11,15,18,22,25-octakisfluoro-2,3,9,10,16,17,23,24-octakis-perfluoro(isopropyl)phthalocyanine ($F_{64}PcZn$). It is important to mention that this class of molecule is more robust than its predecessors, $H_{16}PcZn$ and $F_{16}PcZn$,

and it is worth noting that the molecule remains relatively stable with modification without loss of its Q-band position in the visible light region.

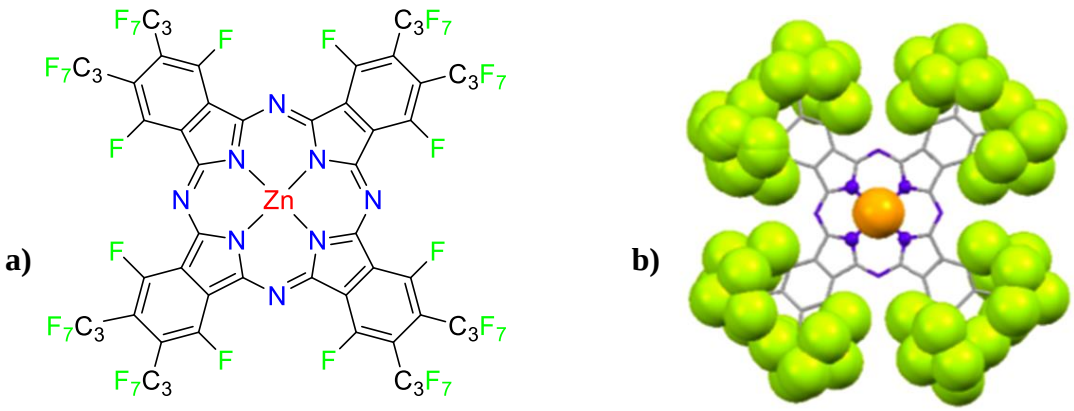

Figure 5.2. a) Chemical structure of $F_{64}PcZn$. **b)** Single-crystal structure of $F_{64}PcZn$, showing the Zn and the fluorinated groups as van der Waals spheres.

The emphasis of this chapter is the incorporation of this perfluorinated phthalocyanine photosensitizer into a durable polymer matrix. The robust hybrid organic-inorganic polymer can withstand the ROS and other radicals produced by the photosensitizer. The photoreactive organic-inorganic polymer used as a coated surface demonstrated the ability to degrade a wide range of organic dyes into much simpler, biodegradable molecules. Degradation of the model organic dye methyl orange was reported in Chapter 3 of this thesis. These organic dyes are degraded and the photocatalyst studied and the effect of the ROS produced by the photocatalyst completely documented and reported.

TiO_2 is photoreactive in the presence of UV producing ROS such as •OH and other radicals capable of oxidizing hydrocarbons and degrading hydrofluorocarbons.[26] Azeez *et al* observed the degradation of PVDF by TiO_2 in the presence of ultraviolet radiation in air.[26, 27] The degradation of hydrocarbon-based polymers can result in weakening of the surface and eventually corrosion of the metal.[26, 27] As a result to this defect, a new class of polymeric material durable, resistive to photo and thermal degradation is needed. Organic-inorganic hybrid polymers are of interest. A non-photoreactive, inorganic solid support may solve the problem of sensitivity to •OH and other radicals produced by TiO_2. **Figure 5.3**, represents a modified acidic silica surface, subjected to thermal treatment before its reaction with fluorinated phthalocyanine.

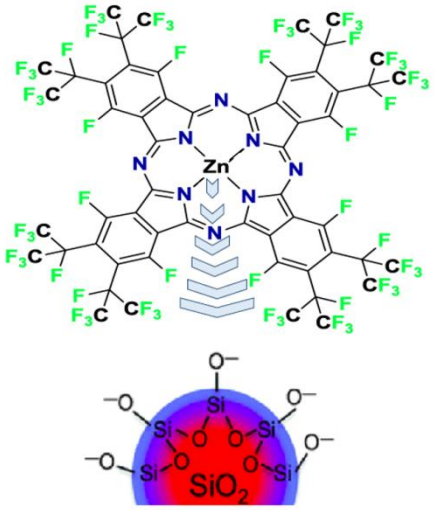

Figure 5.3. Representation of perfluoro (isopropyl) phthalocyanine grafted and/or adsorbed to the surface of modified silica: the silica surface becomes basic after its thermal modification at elevated temperature, before its reaction with the phthalocyanine.

This thermal treatment is performed to convert to Si-O-Si the surface silanol, Si-OH, functional groups that form a reactive network of the hydroxyl group on a silica surface. It is assumed that the perfluorinated phthalocyanine zinc metal center, extremely Lewis acidic due to the fluoro groups will coordinate with the oxygen of the surface metasilicate.[24] Furthermore, silica nanoparticles are not photoreactive, and so the production of ROS will not be an issue for the support.

The polymer of interest, which incorporates the silica-bearing phthalocyanine, is a durable organic-inorganic polymer, polysiloxane, which will not interfere with the reported phthalocyanine chemistry.[28]

In this chapter the formation of reactive polysiloxane/phthalocyanine films will the reported as, well as pattern and kinetics of their degradation of organic dyes. Their reactivity in solid-state will be compared with the films studied in Chapter 3.

5.2. Materials and Methods.

5.2.1. General.

Chemicals and solvents used in these studies were commercially obtained and were used as received, otherwise stated. Six (6) commercial dyes were obtained from Alfa-Aesar:

- ***Crystal Violet***, (**CV**), (Tris(4-(dimethylamino)phenyl)methylium chloride, Cationic triphenylmethyl dye),
- ***Rhodamine B***, (**Rb**), (9-(2-carboxyphenyl)-6-diethylamino-3-xanthenylidene)-diethylammonium chloride, cationic fluorone dye),
- ***Methyl Orange***, (**MO**), (4-[[(4-dimethylamino) phenyl]-azo] benzenesulfonic acid, sodium salt),
- ***Evans Blue***, (**EB**), (6,6'-{(3,3'-dimethyl[1,1'-biphenyl]-4,4'-diyl)bis[diazene-2,1-diyl]}bis(4-amino-5-hydroxynaphthalene-1,3-disulfonate, organic tetra-sodium salt),
- ***Methylene Blue***, (**MB**), (3,7-bis(dimethylamino)phenothiazin-5-ium, organic chloride salt cationic phenothiazine dye),
- ***Rose Bengal***, (**RB**), (2,3,4,5-tetrachloro-6-(2,4,5,7-tetraiodo-3-oxido-6-oxoxanthen-9-yl)benzoate, disodium anionic fluorescein dye).

Ammonium hydrogen carbonate (NH_4HCO_3) was purchased from Sigma-Aldrich and characterized as described below. Fumed Silica (SiO_2) was purchased from Aerosil®, (P90 surface area Brunauer-Emmett-Teller (BET): 90 m^2/g, particle size: 20 nm, pH 3.7-4.7). The fumed silica was calcined for surface modification as described below. Deionized H_2O (Milli-Q, resistivity15 *MΩ*-cm) was used for all solution preparations. The crosslinker Dynasylan AMEO (3-aminopropyltriethoxysilane), density 0.95 g/cm^3 was purchased from Evonik. The resin material was purchased from Silikopon EF (resin composition: Siloxane Epoxy hybrid). Dye solutions were filtered through 0.45 µm cellulose filters. Fluorinated phthalocyanine, $F_{64}PcZn$, was prepared from zinc acetate and perfluoro-(4,5-di-isopropyl) phthalonitrile as previously described.[7]

5.2.2. Instruments.

Contact angles (θ) were measured with a RAMA-HART goniometer using 5µL volume, sessile water drop method. The θ values obtained were averaged by measuring five different points on each surface of the coated film. Plain glass slides untreated, θ = 45° was used as the experimental control. The morphology of coated surfaces was determined with a Verios 460 Extreme High-Resolution Scanning Electron Microscope (XHR SEM) at the Princeton University PRISM Institute. A 300 W OSRAM halogen lamp was used for photochemical experiments, kept at a distance of 14 cm from the sample, average illuminance of 109,000 lux measured with an Extech EasyView 33 light meter. A 60 mm glass filter (S-83605, Sargent Laboratory) was used to exclude wavelengths below 300 nm. All glass slides were washed with acetone followed by deionized water before use. The Glass slides, 75 x 25 x 1 mm were purchased from VistaVision. A Cary 500 UV-Vis-NIR spectrophotometer was used to determine the photooxidized dyes in solution and

obtain solid-state electronic spectra for solid samples. Time-dependent concentrations for all six dyes concentration were measured, the lambda max absorbance values were converted to concentrations using the Beer-Lambert equations: **MO** ε_{466} = 25100 $cm^{-1}M^{-1}$, **Rb** ε_{543} = 106,000 $cm^{-1}M^{-1}$, **CV** ε_{590} = 87,000 cm^{-1} M^{-1}, **EB** ε_{626} = 7810 $cm^{-1}M^{-1}$, **MB** ε_{644} = 95000 $cm^{-1}M^{-1}$, **RB** ε_{599} = 90400 $cm^{-1}M^{-1}$.

a) ***Methyl orange*** (MO)

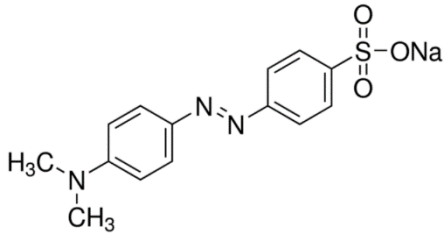

b) ***Rhodamine B*** (Rb)

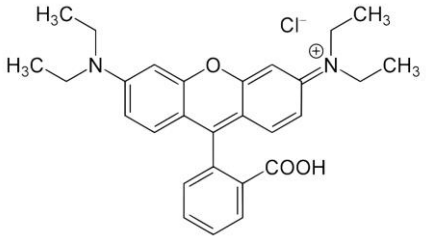

c) ***Crystal Violet*** (CV)

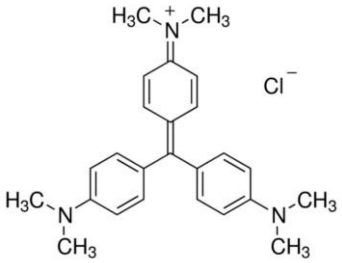

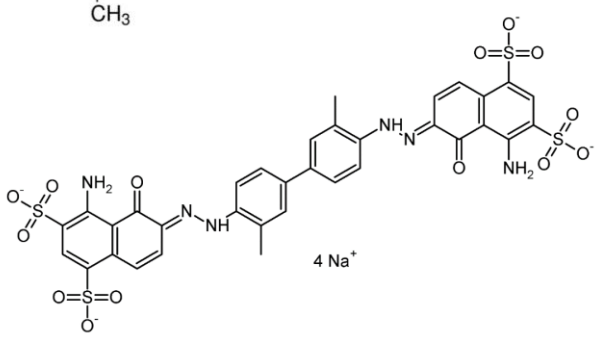

d) ***Evans Blue*** (EB)

e) *Methylene Blue* (MB)

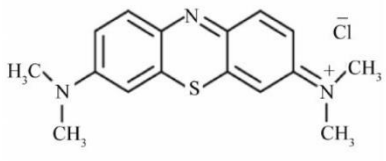

f) *Rose Bengal* (RB)

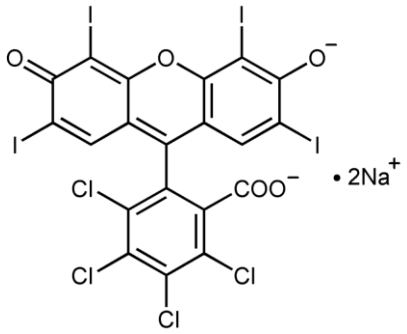

Figure 5.4. The structures of studied organic dyes.

5.2.3. Sample Preparation. The description of the composition of materials uses the union and inclusion symbols "∪" and "∈", which mean "deposited on" and "embedded in", respectively.

5.2.4. Preparation of NH_4HCO_3 of controlled particle size.

The procedure was reported previously in **section 3.2.4.**

5.2.5. Preparation of $F_{64}PcZn$ coated SiO_2, $F_{64}PcZn \cup SiO_2$ Hybrid photocatalyst.

The procedure was reported previously in **section 4.2.5.**

Phase 1.

5.2.6. Preparation of Plain Siloxane-Epoxy coated film.

The procedure was reported previously in **section 4.2.6.**

5.2.7. Preparation of Siloxane-Epoxy with NH_4HCO_3 coated film:

Step 1: (pre-coat cure).

Step 2: (post-coat cure).

Step 3: (bake time).

All procedures were reported previously in **section 4.2.7**.

5.2.8. Preparation of $F_{64}PcZn$-coated SiO_2-doped Siloxane-Epoxy with NH_4HCO_3, $(F_{64}PcZn \cup SiO_2 \& NH_4HCO_3) \in$ Siloxane-Epoxy film.

Step 1: (pre-coat cure

Step 2: (post-coat cure).

Step 3: (bake time).

All procedures were reported previously as in **section 4.2.8**.

The results from **Phase 1,** modified pre, post and bake time led to improved films morphology.

5.2.9. Preparation of $F_{64}PcZn$-coated SiO_2-doped Siloxane-Epoxy with NH_4HCO_3, $(F_{64}PcZn \cup SiO_2 \& NH_4HCO_3) \in$ Siloxane-Epoxy film.

The procedure was reported previously in **section 4.2.9**.

5.2.10. Photodegradation of dyes in solution: MO, Rb, CV, MB, RB, and EB.

Photoreactive siloxane-epoxy-coated glass slides were immersed in 3 ml aqueous solutions of various concentration listed above and were illuminated with109,000 lux (~1 Sun) along the axis perpendicular to the center of the solution surface; the intensity of illumination varies depending on the position of the solution. After irradiation/photooxidation of the solutions, the films were washed with deionized water and the washings were combined. A 0.45 μm pore-size cellulose membrane filter was used to filter the combined liquids prior to their UV-Vis-NIR analysis.

5.3. Results and Discussion.

5.3.1. Leaching study of $F_{64}PcZn \cup SiO_2$ hybrid photocatalyst.

The surface of SiO_2, generally an acidic surface was modified to a basic surface via calcination at 600 °C for 1 hour. This material produced a greenish colored hybrid prepared from the $F_{64}PcZn$ adsorbed onto this modified surface of SiO_2. The hybrid was treated for 24 hours at 200 °C yielding a bright-greenish hybrid complex, which was loaded with $F_{64}PcZn$ beyond monolayer level. Repeated washings with ethanol, shown in **Figure 5.5** yielded greenish colored hybrid complex. The color did not fade further. Vial #1, the first washing with ethanol showed a greenish color from the leached adventitious $F_{64}PcZn$. After 10 washes, vial #10 was colorless as no additional $F_{64}PcZn$ was removed. This observation was previously discussed in **Chapter 4**.

Figure 5.5. Leaching study of the $F_{64}PcZn \cup SiO_2$ hybrid catalyst before and after SiO_2 calcination to determine the binding ability of the catalyst to the solid support. *"Image courtesy of Abdul Azeez"*.

5.3.2. Photochemical Decomposition of Organic Dyes.

The photooxidative ability of the as-prepared surfaces was probed using six organic dyes: ***Methyl orange***, ***Rhodamine B***, ***Crystal Violet***, ***Evans Blue***, ***Methylene Blue***, and ***Rose Bengal***. The dyes solutions were kept in the dark before studies were conducted to ensure their minimal to zero degradation, as some dyes are susceptible to white light decomposition. The dyes were divided into two categories: (i) two azo dyes with (N=N) bond which exhibit the characteristic of nitrogen-nitrogen double bond both attached to aromatic groups and (ii) the non-azo dyes, fused together in a conjugated pattern, exhibiting its chromophore characteristic. As expected, the photodegradation pattern of the two categories is different. The azo dyes are oxidized by the reactive oxygen species via the direct attack of their N=N bond, while the non-azo dyes are photodegraded starting from the functional groups attached to the conjugated rings. All dyes solutions exhibit a decrease in light absorbance with increasing irradiation time, but the dyes have different degradation rates under broad UV-Vis light irradiation. The dyes that can self-produce singlet oxygen, for example, ***Rose Bengal*** have a higher rate of degradation. This pattern of photodegradation was expected because

of their own singlet oxygen production. The rapid decrease revealed in our study with these self-produced singlet oxygen dyes was not noticed in several other studies in which the mechanism of degradation might be different. For example TiO_2 photodegraded ***Rose Bengal*** very slowly; the photodegradation process is discussed extensively below.

The decrease in absorbance of all the dyes in solution was studied using the time dependency **equation 1**.

$$\ln(C_t/C_0) = -kt \qquad 1$$

This equation was used to determine if the degradation of the dyes was consistent with a pseudo-first-order kinetics approximation. C_t represents concentration at time t, t is the period of degradation, k is the rate constant and C_0 represents the initial concentration.

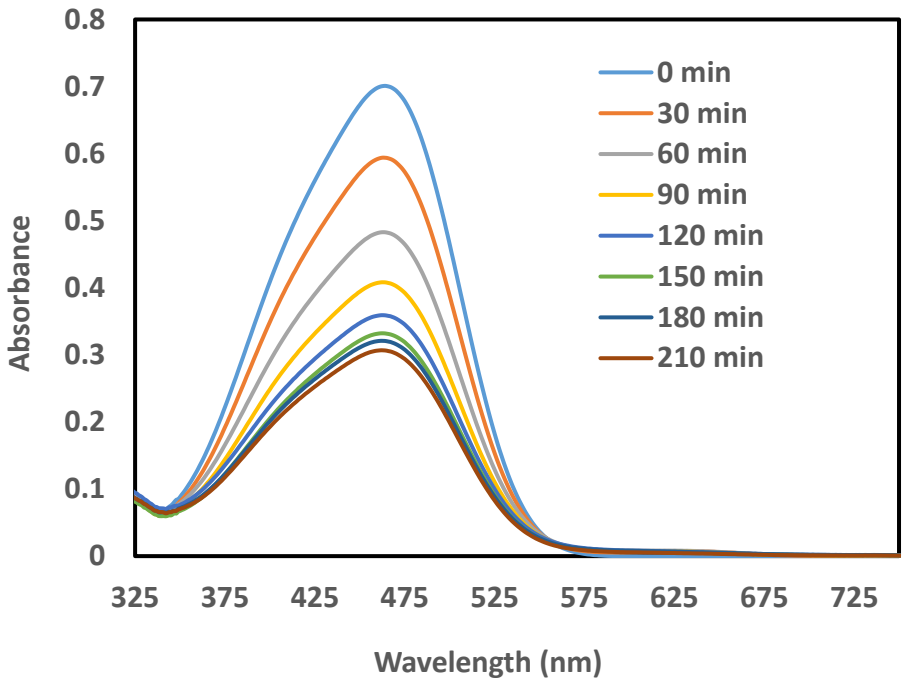

Figure 5.6. Time-dependent photodegradation of ***Methyl Orange*** deposited on the surface of $(F_{64}PcZn \cup SiO_2) \in$ Siloxane Epoxy films.

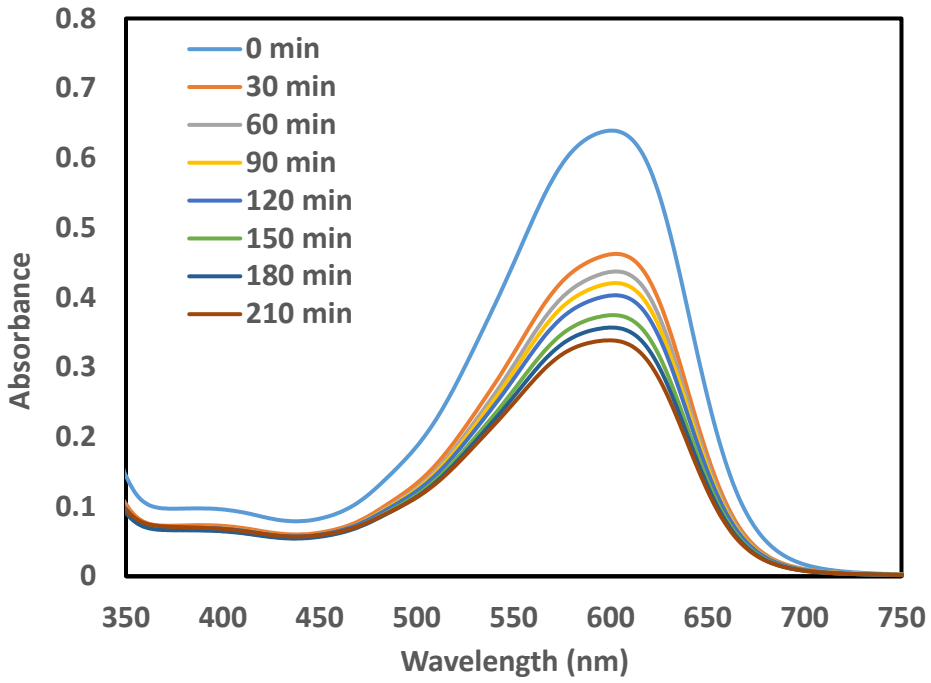

Figure 5.7. Time-dependent photodegradation of ***Evans Blue*** deposited on the surface of $(F_{64}PcZn \cup SiO_2) \in$ Siloxane Epoxy films.

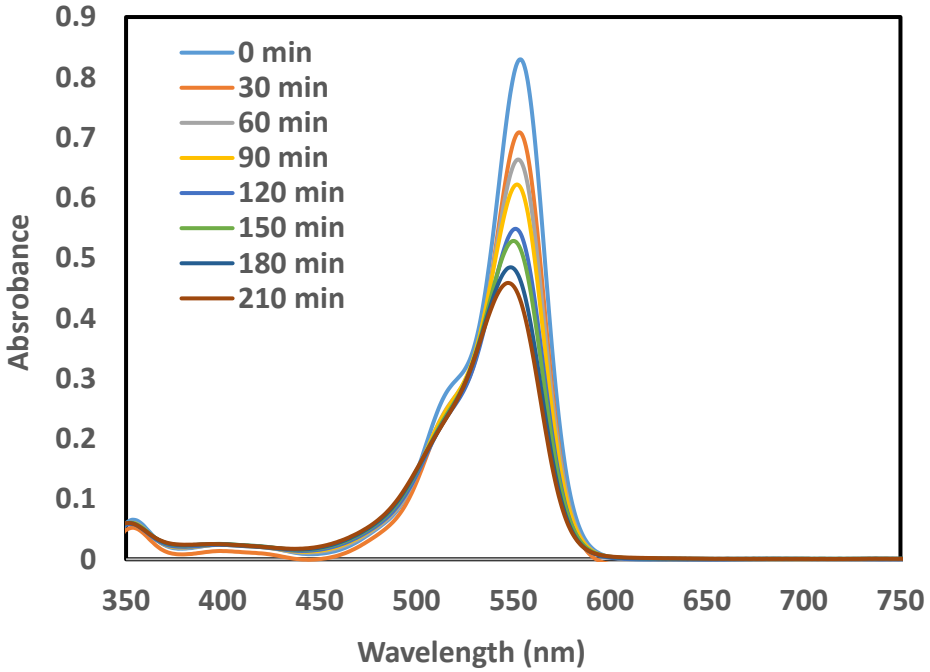

Figure 5.8. Time-dependent photodegradation of ***Rhodamine B*** deposited on the surface of $(F_{64}PcZn \cup SiO_2) \in$ Siloxane Epoxy films.

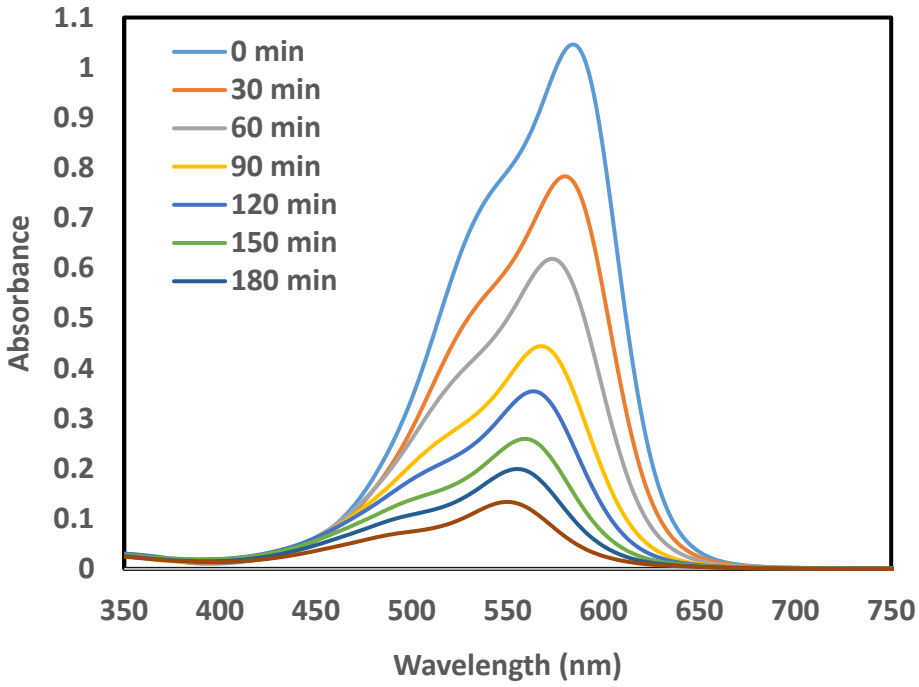

Figure 5.9. Time-dependent photodegradation of ***Crystal Violet*** deposited on the surface of $(F_{64}PcZn \cup SiO_2) \in$Siloxane Epoxy films.

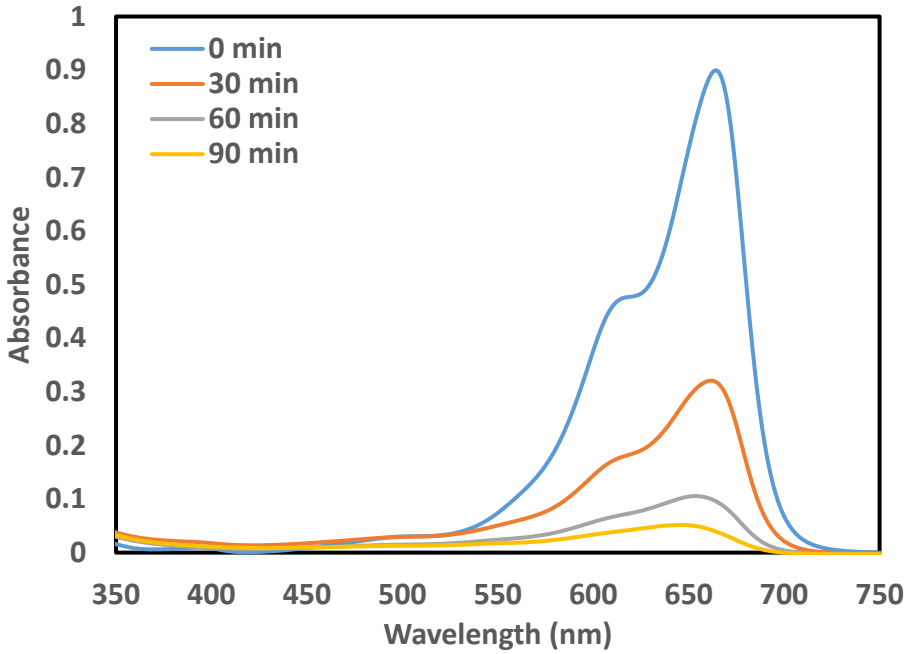

Figure 5.10. Time-dependent photodegradation of ***Methylene Blue*** deposited on the surface of $(F_{64}PcZn \cup SiO_2) \in$Siloxane Epoxy films.

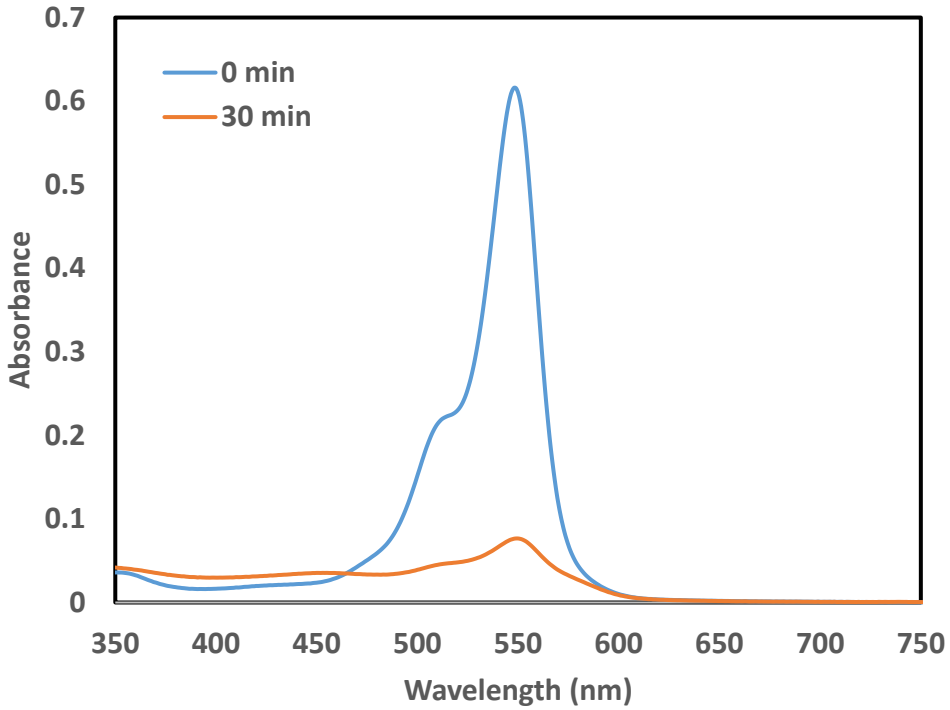

Figure 5.11. Time-dependent photodegradation of ***Rose Bengal*** deposited on the surface of $(F_{64}PcZn \cup SiO_2) \in$ Siloxane Epoxy films.

5.3.3. Kinetic Studies.

The plots of the time-dependent concentrations for all dyes, **Equation 1**, is shown in **Figure 5.12.**

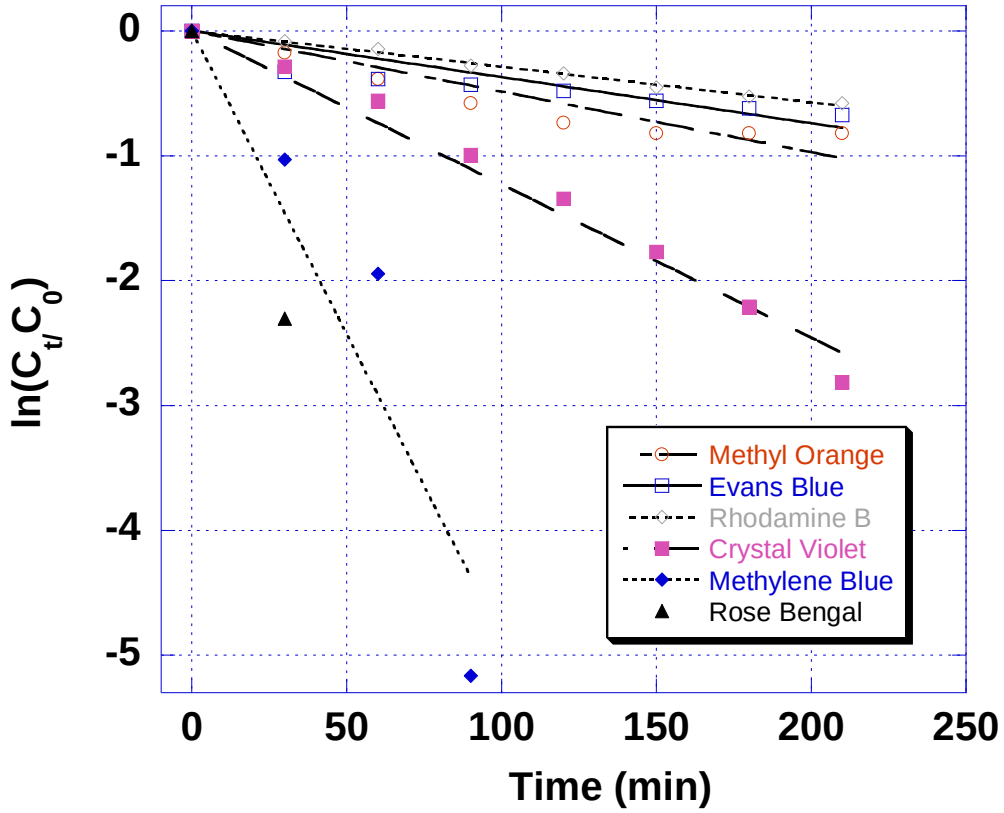

Figure 5.12. Kinetics of dyes degradation. The k x 10^3 and R (correlation coefficient) values are: -4.9(3) and 0.92560; -3.7(3) and 0.82720; -2.86(5) and 0.99647; -12.3(4) and 0.99056; -49(7) and 0.93968 for MO, EB, Rb, CV and MB, respectively. The estimated standard deviations of k values are in parentheses.

Methyl Orange was photooxidized as shown in **Figure 5.6;** a steady decline as the rate was recorded as the change in intensity of the absorption peak is recorded as a function of time, 30 minutes intervals. The slowdown of the decrease in absorbance peak intensity rate was noticed after 150 minutes. This can be attributed to the difficulty it takes to degrade phenyl fragments in

solution, the result of the photo-bleaching and fragmentation of the MO. The constant decrease of the λ_{max} at 465 nm confirmed the destruction of the azo bond and the discoloration associated with this process. The photooxidation of MO can be described by the first-order kinetic model $\ln(C_0/C_t) = kt$, $k = 0.0049$ min^{-1}. The semi-logarithmic determination of the concentration of MO as a function of time gave a straight line, confirming a pseudo-first-order reaction, the data points were fitted to a straight line to yield a correlation constant R = 0.92560, shown in **Figure 5.12**.

Kinetic analysis of ***Evans Blue*** was based on its λ_{max} 602 nm absorbance. Its intensity, measured every 30 minutes decreases as a function of time irradiation with UV-Vis light. There is an assumption to be made here which can be related to the molecular structure and arrangement pattern. Evans blue is a bis-azo molecule; the mechanism of singlet oxygen attack is the strong oxidation of the azo bond and subsequent destruction of the fragment through the production of daughter radical and/or combination of both reactive species. [29a] The photo-bleaching during the first 30 minutes can cause the accumulation of bulky fragments on the surface of the film, or block the active site from receiving the necessary illumination and therefore reducing the illumination which, in turn, will reduce the production of singlet oxygen necessary. The surface roughness contributes to the overall surface area of the film.

The photodegradation of ***Rhodamine B*** was studied in the presence of UV-Vis broadband light. The cationic tetraethylated ***Rhodamine B*** absorbance at λ_{max} at 554 nm decreases intensity; readings were taken every 30 minutes for a total of 210 minutes. The maximum absorbance decreasing during the irradiation period, λ_{max} at 554 nm was observed to shift slightly to 547 nm. The shift toward lower wavelengths (hypsochromic shift) of λ_{max} was shown by Ma *et al*, [29b] to be the result of a stepwise de-ethylation. As reported by Wu *et al*, [30] for a fully de-ethylated RhB, λ_{max} shifts to 506 nm. In their report, TiO_2, active in the UV region and Bi_2WO_6 active in the visible

region were used. A comparison of the photocatalysts indicated that the de-ethylation catalyzed by Bi_2WO_6 was more rapid than that catalyzed by TiO_2.[31, 32]

The photooxidation for 210 minutes using UV-Vis broadband light of cationic triphenylmethyl ***Crystal Violet*** deposited on the surface of $(F_{64}PcZn \cup SiO2) \in$Siloxane-epoxy films revealed a constant decrease of the intensity of the λ_{max} at 584 nm. The irradiation results were monitored every 30 minutes and the concentration of the dye was determined as a function of irradiation time. The deep purple color disappeared after 210 minutes; this clearly shows the degradation of the organic dye.

Hu *et al*, [31] studied the transformation of nitrogen-containing molecules during photodegradation. Although •OH, generated by TiO_2 reacts with nitrogen-containing compounds, the mineralization process produces NH_4^+ and/or NO^{3-} as the direct result of the oxidation of nitrogen. The adsorption of the dye onto the surface of TiO_2 contributes to the initial photomineralization of the organic dye, including crystal violet.[31] The decrease in the intensity of λ_{max} 584 nm occurs gradually but rapidly. Note that crystal violet has the same functional groups as the ***Rhodamine B*** and thus its de-methylation may contribute to its degradation the same way de-ethylation does for ***Rhodamine B***.

The photodegradation of ***Methylene Blue*** was followed at the λ_{max} 667 nm. A rapid loss of color occurs in the first 30 minutes, the brilliant blue color fading completely after 90 minutes. The disappearance of the λ_{max} at 667 nm suggests mineralization perhaps via de-methylation, the -$N(CH_3)_2$ group having been transformed in NO_3^-, NH_3, and N_2, see Zhao *et al*. [33] ***Methylene Blue*** is photoactive in the visible region and can produce singlet oxygen, but its self-degradation is very slow. According to a study by Zhang *et al*, [34] the ***Methylene Blue*** self-photo-degradation is slow compared with the photocatalytic activity of piezoelectric $ZnSnO_3$ nanowires, under both UV and stress, **Figure 5.13**. The slow self-degradation rate alone proves the point

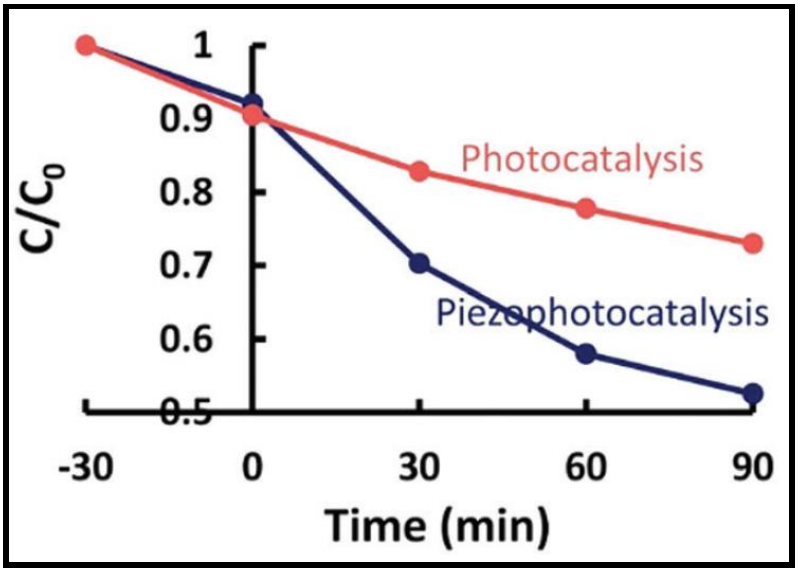

Figure 5.13. Comparison of ***Methylene Blue*** self-photodegradation and photocatalytic activity of $ZnSnO_3$ with and without applied stress and UV irradiation. *"Open Access Article"* [34]

Bhati *et al*, [35] revealed the photodegradation of ***Methylene Blue*** occurred, at least in part due to the adsorption of ***Methylene Blue*** on graphitic hollow carbon nano-rods (wsCNRs). Ion-pair interaction leading to photochemical degradation of adsorbed ***Methylene Blue*** is important.

Although ***Methylene Blue*** has been photodegraded via the above pathways, our approach to its photodegradation and that of other organic dye is much simpler and straightforward by simple irradiating ***Methylene Blue*** solution in contact with the surface of $(F_{64}PcZn \cup SiO_2) \in$Siloxane-epoxy films. No semiconductor, electrode or other materials is necessary. In our case, ***Methylene Blue*** deposited on the surface of $(F_{64}PcZn \cup SiO_2) \in$Siloxane-epoxy photodegradation is complete in approximately 90 minutes.

The time-dependent degradation of anionic fluorescein, ***Rose Bengal*** deposited on the surface of $(F_{64}PcZn \cup SiO_2) \in$Siloxane Epoxy in the presence of broadband light was investigated. The

photodegradation was complete in 30 minutes. Although ***Rose Bengal*** is visible-light photoactive and can self-produce singlet oxygen, it should be noted that this process of self-degradation is a very slow process, not comparable with the photodegradation by a photocatalyst. The rate of degradation of ***Rose Bengal*** by a photosensitizer compares unfavorably with that observed for semiconductors. Kumar *et al* [36] studied the reactivity of various compounds, nanocomposites of oxidized TiO_2, polyaniline/TiO_2 and polyaniline /TiO_2/Graphene oxide.[37] Their study shows TiO_2 to be very inefficient for the photodegradation of ***Rose Bengal***; the polyaniline /TiO_2/Graphene oxide composite was the best, completing the degradation in 150 minutes. In our study, we recorded only 30 minutes of degradation time for ***Rose Bengal***. A study by Kaur *et al* [38] revealed that the photodegradation of 0.01 mM ***Rose Bengal*** with ZnO by UV irradiation was completed within 90 minutes. We have used the same concentration, 0.10 mM and recorded 90% degradation of the dye in 30 minutes. Our rate data revealed three times faster degradation rate than the study conducted by Kaur *et al* [38] and, to the best of our knowledge, the highest rate reported to-date.

5.3.4. Proposed Mechanism of Sensitized Photocatalysis.

The mechanism was studied to determine the ways at which the photocatalyst degrades more effective than semiconductor photocatalysts. Although, the photodegradation routes are different, the effectiveness of ($F_{64}PcZn \cup SiO_2$)$\in$Siloxane-epoxy for the degradation of organic dyes regardless of their chemical composition is worth discussing in this chapter. Representation: photosensitizer **(P)**, singlet ground state **(S_0)**, singlet excited state **(S_1)** excited triplet state **(T_1)**, rate constant of electron transfer **(k_{et})**, rate constant of energy transfer **(k_{en})**, rate constant of intersystem crossing **(k_{ISC})**, singlet oxygen **($^1O_2$)** and ground state triplet oxygen **($^3O_2$)**.

The mechanism presented below, starting with the ground state absorption of photon energy by a photosensitizer **P(S_0),** to an excited singlet state **(S_1)** and an excited triplet state **(T_1)** and transferring its energy to triplet ground-state oxygen before returning back to the P(S_0), and **(k)** is the rate constant the processes are explained below, **equations 2 - 7**.

$$P(S_0) + h\nu \longrightarrow P(S_1) \longrightarrow k_{ISC} \longrightarrow P(T_1) \quad (2)$$

$$P(T_1) + {}^3O_2 \longrightarrow k_{en} \longrightarrow P(S_0) + {}^1O_2 \quad (3)$$

$$P(T_1) \longrightarrow k_r \longrightarrow P(S_0) + h\nu'' \quad (4)$$

$$P(T_1) \longrightarrow k_{nr} \longrightarrow P(S_0) \quad (5)$$

$$P(T_1) + O_2 \longrightarrow k_{dO2} \longrightarrow P(S_0) + O_2 \quad (6)$$

$$P(T_1) + O_2 \longrightarrow k_{et} \longrightarrow P(S_0) + O_2^{\bullet -} \quad (7)$$

5.3.5. Kinetic Interpretation Model in Liquid-State.

The Langmuir-Hinshelwood kinetic model clearly describes the rate of degradation with respect to the concentration of the organic dye solution from **equations 8 – 9** below explain the model.

$$R = dC/dt = kKC/1+KC \quad (8)$$

$$\ln(C_t/C_0) = -kt \quad (9)$$

Where **R** represents the rate of degradation (mM/min), $\mathbf{C_t}$ represents the concentration of the organic dye (mM), $\mathbf{C_0}$ represents the initial concentration of the organic dye (mM), **k** represents the reaction rate constant (min^{-1}), **K** represents the adsorption coefficient of the dye onto the surface of the photocatalyst, and t represents irradiation time (min). The reaction rate constants are tabulated in **Table 5.1.** Reaction rate constants were derived from **Figures 5.6 b – 5.10 b**, using line equation **y = mx**, where the plot of $\ln C_t/C_0$ vs time is represented by a straight line. The linear regression slope represents **k**, half-life ($t_{1/2}$) was determined using **equation 10**.

$$t_{1/2} = 0.693/k. \quad (10)$$

The values of all kinetic parameters for the photooxidative activity are shown in **Table 5.1.**

Table 5.1. Reaction Rates and half-lives of all degraded Dyes at Wavelength Maximum.

Organic Dye	R^2	Reaction Rate (min^{-1})	Half Live (min)
Methyl Orange	0.92560	0.0049	14.429
Evans Blue	0.82720	0.0037	187.297
Rhodamine B	0.99647	0.00286	242.308
Crystal Violet	0.99056	0.0123	56.341
Methylene Blue	0.93968	0.049	14.143
Rose Bengal	-	-	-

5.3.6. Percentage Degradation of Organic Dyes.

The percent degradation of the dyes was studied to evaluate the amount of each dye that was destroyed in the first 30 minutes of the reaction. The percent degradation ratio (D%) of each dye was calculated by the maximum strength of the absorbance wavelength intensity before irradiation process (A_0) and maximum absorbance after the irradiation process (A) respectively. Absorbance intensities were converted to concentrations, before and after absorbance intensities of the dyes were converted following the beer-lambda law, initial concentration (C_0) and final concentration (C_t) shown below in **equation 11**.

$$D\% = [(C_0 - C_t)/C0]* 100\% \qquad 11$$

Figure 5.14, shown below revealed results of six dyes belonging to different categories. It was noted that the cationic phenothiazine ***Methylene Blue*** and anionic fluorescein ***Rose Bengal*** were mostly degraded in the first 30 minutes.

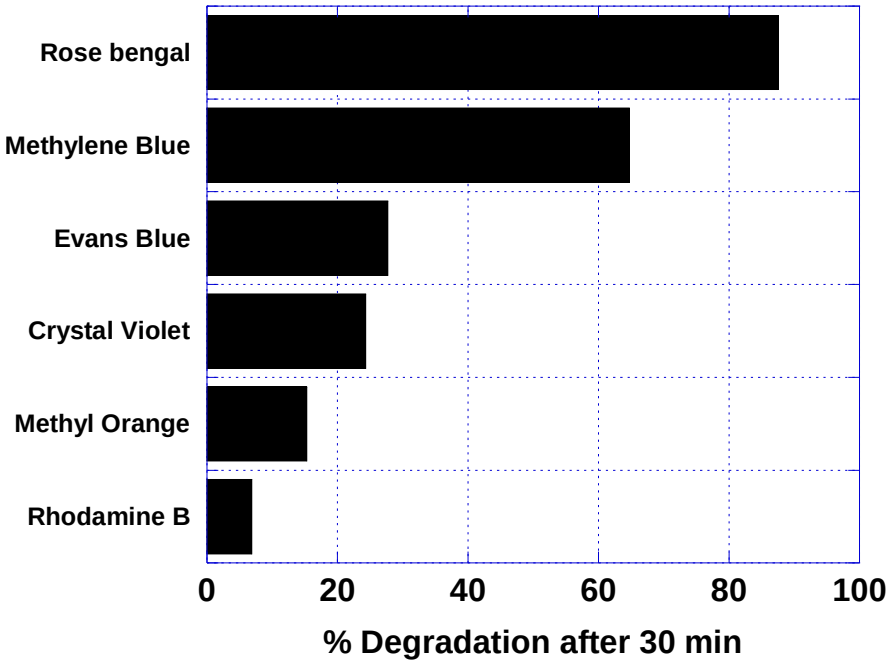

Figure 5.14. Percentage degradation of all dyes after 30 minutes of UV-Vis irradiation.

Table 5.2. Percentage Degradation of all Dyes after 30 minutes UV-Vis irradiation.

Organic Dye	**Degradation (%)**
Methyl Orange (**Mono-azo bond**)	16
Evans Blue (**Bis-azo bond**)	20
Rhodamine B (**Cationic fluorone**)	8
Crystal Violet (**Cationic triphenylmethyl**)	25
Methylene Blue (**Cationic phenothiazine)**	65
Rose Bengal (**Anionic fluorescein**)	90

The results tabulated in **Table 5.2** correlate with the kinetic data previously analyzed in **Table 5.1**, some of the organic dyes were degraded faster than the others and some with degradation relatively rapid compared to what is reported in the literature. Furthermore, ***Rose Bengal*** anionic fluorescein dye was the most degraded to 90% in 30 minutes, while ***Rhodamine B***, a cationic fluorone was the least degraded, results shown in **Table 5.2**.

5.3.7. FTIR Broadband Irradiation Studies of the Coated Films.

Fourier-transform infrared spectroscopy (FTIR) analysis was conducted on the epoxy modified siloxane coated films to determine the photooxidative stability of the surface. Siloxane epoxy is known to be polymerized both by thermally-induced or photo-induced polymerization. [39] The commonly photoinitiated cationic polymerization [40, 41] of monomers comes with a drawback: catalysts, at high concentrations, can lead to discoloration, observed by Rosas-Barrera *et al*. [42] The organic-inorganic hybrid polymer is very stable thermally and under UV illumination.

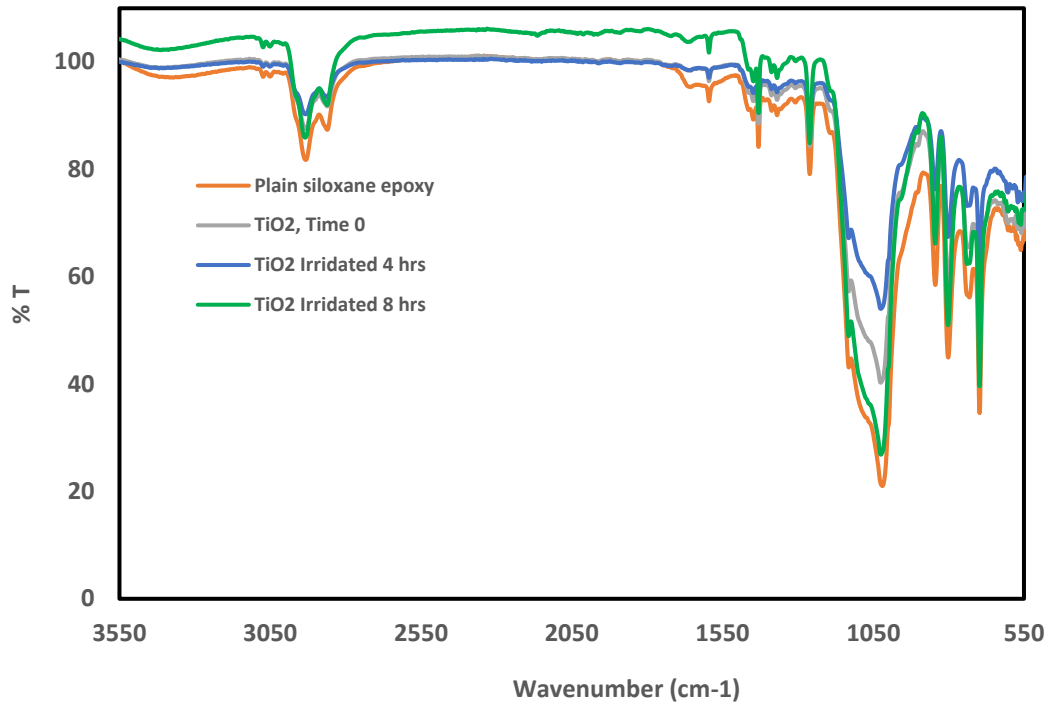

Figure 5.15 a. FTIR of siloxane epoxy embedded TiO_2 photocatalyst, $TiO_2 \in$Siloxane-epoxy films before and after broadband irradiation for 4 and 8 hours.

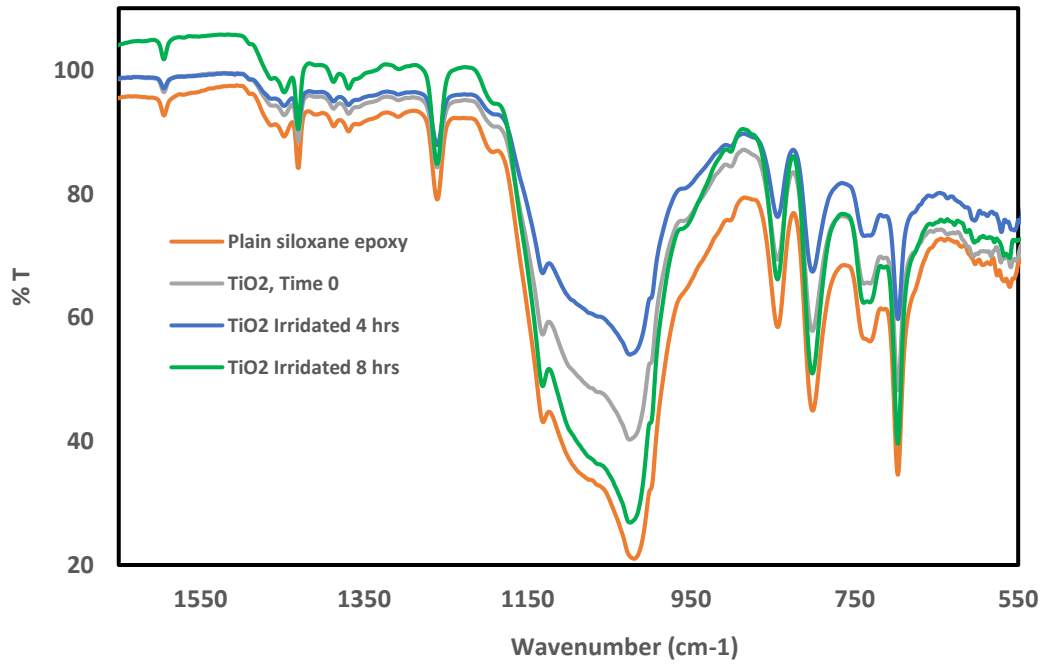

Figure 5.15 b. FTIR of siloxane-epoxy embedded TiO_2 photocatalyst $TiO_2 \in$Siloxane-epoxy films before and after broadband irradiation for 4 and 8 hours, 550 - 1600 cm^{-1} enlarged region.

Firstly, the IR spectrum of plain siloxane epoxy without additive was analyzed as a control, followed by epoxy modified siloxane embedded TiO_2, $(TiO_2)\in$Siloxane-epoxy. Irradiation times were 0, 4 and 8 hours. The spectra shown above in **Figures 5.15**, revealed no new peaks formation, or the disappearance of peaks after the irradiation. Thus, the coated film with embedded photo-generating ROS materials did not show a modification of the polymer.

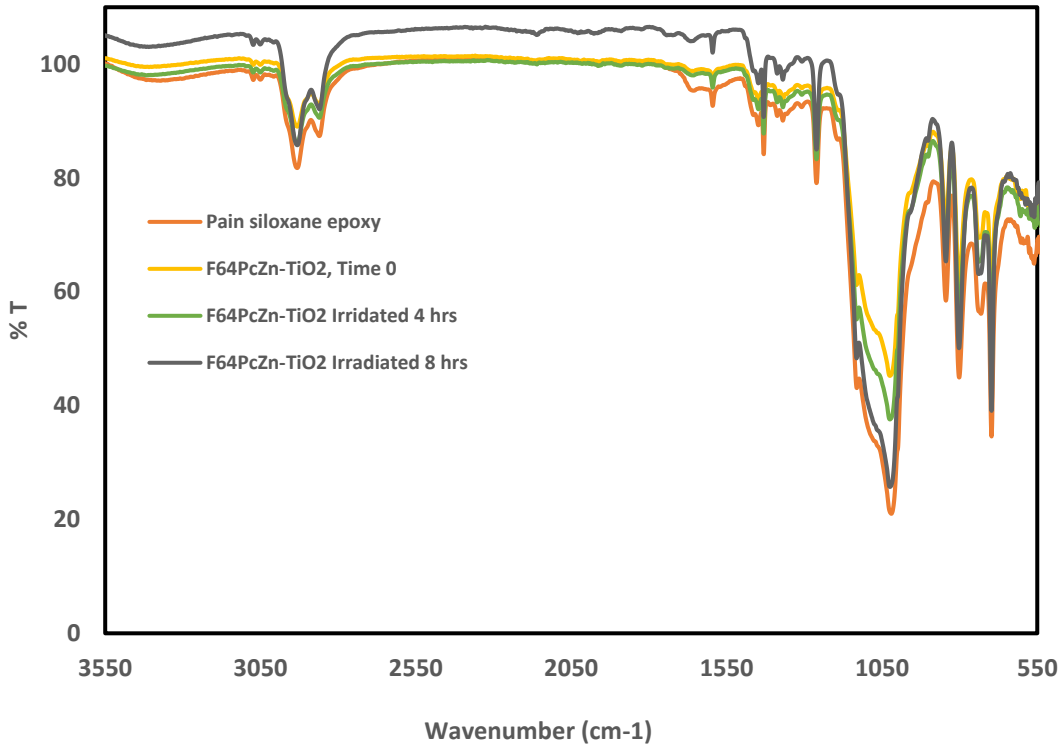

Figure 5.16 a. FTIR of siloxane epoxy embedded $F_{64}PcZn\cup TiO_2$ photocatalyst, $(F_{64}PcZn\cup TiO_2)\in$Siloxane-epoxy films before and after broadband irradiation for 4 and 8 hours.

Siloxane-epoxy embedded $F_{64}PcZn\cup TiO_2$ film was also studied with FTIR spectroscopy, before and after irradiation times set at 0, 4 and 8 hours can be seen in the spectrum shown in **Figures 5.16**. No new peaks were formed or peak disappearance at the end of the 8 hours study. Although

modification of the film was not expected, the coating of $F_{64}PcZn$ photocatalyst onto TiO_2 semiconductor solid support reduces or prevents the generation of ROS from TiO_2 during the irradiation process. In a previous Chapter 3, we demonstrated the irradiation effects on polyvinylidene fluoride by TiO_2. The PVDF embedded with TiO_2 was photodegraded during the same irradiation period the $F_{64}PcZn$ photocatalyst coated on TiO_2 embedded on PVDF did not show photodegradation as a result of the protection provided by $F_{64}PcZn$ over the TiO_2.

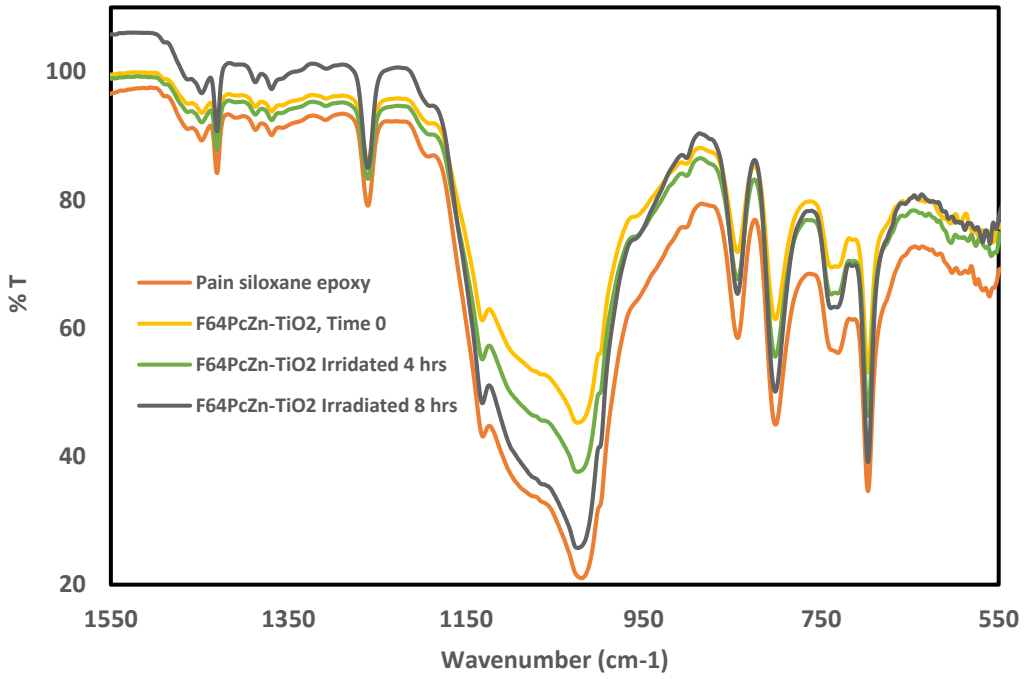

Figure 5.16 b. FTIR of siloxane-epoxy embedded $F_{64}PcZn \cup TiO_2$ photocatalyst, $(F_{64}PcZn \cup TiO_2) \in$ Siloxane-epoxy films before and after broadband irradiation for 4 and 8 hours, 550 - 1550 cm^{-1} enlarged region.

5.3.8. SEM-EDX Spectroscopy Studies of UV Irradiation Effects on Films.

Siloxane epoxy-based materials have been studied for their ability to resist thermal and ultraviolet (UV) irradiation degradation. [43] Epoxy resins are commonly used as a structural material, but their

UV resistant properties are not well studied according to a report by Peng *et al*. [43] Polyhedral oligomeric silsesquioxanes POSS, a relatively new class of SiO_2-based organic-inorganic polymer combined with TiO_2, was incorporated in an epoxy resin (EP), **Figure 5.17**. The study concluded that the POSS-TiO_2 nano-hybrid material proved a stable polymeric material, even under UV irradiation, subsequently producing ROS. [43]

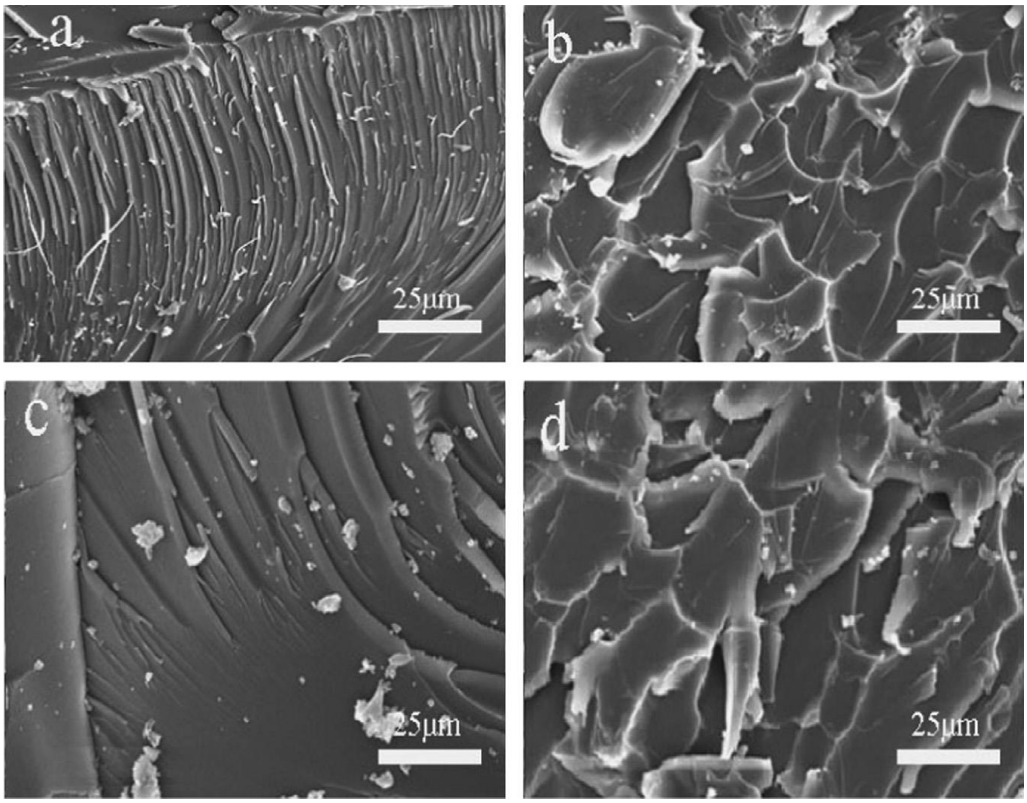

Figure 5.17. SEM micrograph of POSS–TiO_2/EP nano-composites: (**a**) pure EP (**b**) POSS–TiO_2/EP before UV irradiation, (**c**) neat EP and (**d**) POSS–TiO_2/EP after UV irradiation. *"Reproduced with permission from Elsevier"*[43]

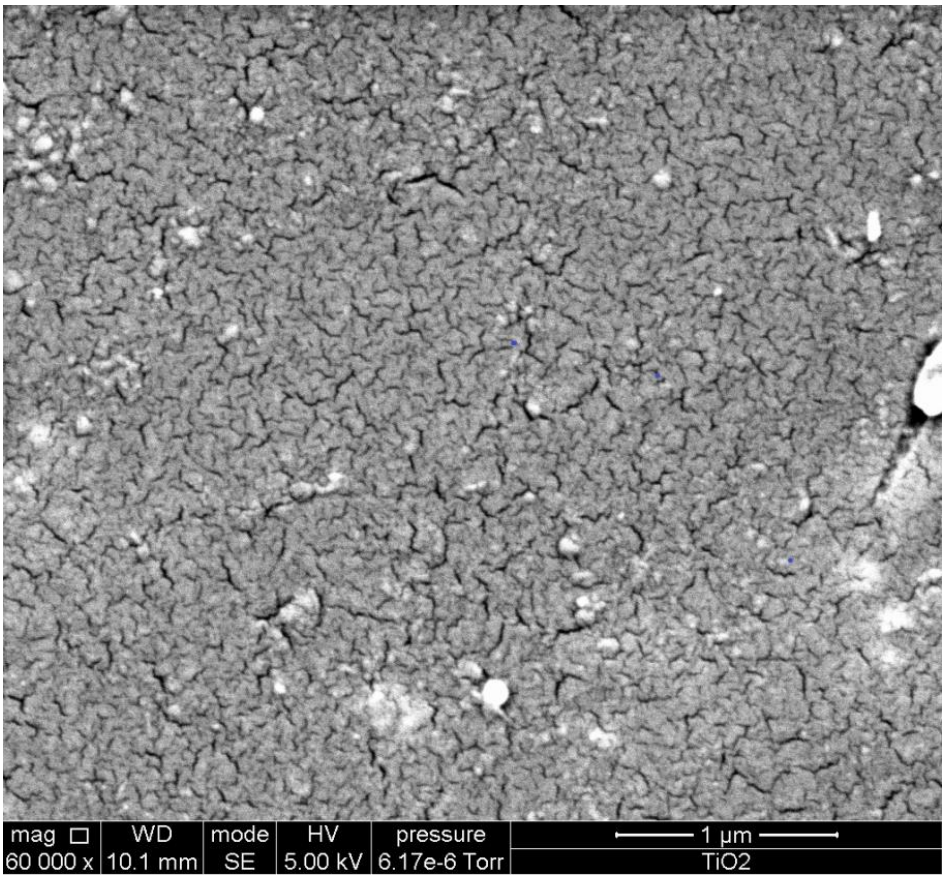

Figure 5.18. SEM micrograph of epoxy modified siloxane coated surface embedded with TiO_2, ($TiO_2 \in$ Siloxane-epoxy films) before irradiation. *"Image courtesy of Abdul Azeez"*.

In our study, the strength and durability of epoxy modified siloxane under continuous ultraviolet irradiation for 4 and 8 hours were investigated. **Figure 5.18** shows the micrograph of TiO_2 embedded in epoxy modified siloxane before irradiation, the charging, and roughness on the surface were previously discussed in **Chapter 4**. The film was irradiated for a total of 8 hours. The film surface that was irradiated for a total of 8 hours, shown in **Figure 5.19**, did not reveal any difference or changes as a result of the irradiation. Although TiO_2 produces ROS when excited under UV condition, the surface of the film retained its texture and character. This was not what was noticed when PVDF was studied under the same conditions, where surface degradation and partial exposure of the photocatalyst were noticed, as noticed in **Chapter 3** and reported recently.[27]

Epoxy modified siloxane coated surface embedded with TiO_2 revealed a robustness film, as indicated by SEM microscopy, and correlated with FTIR spectroscopy.

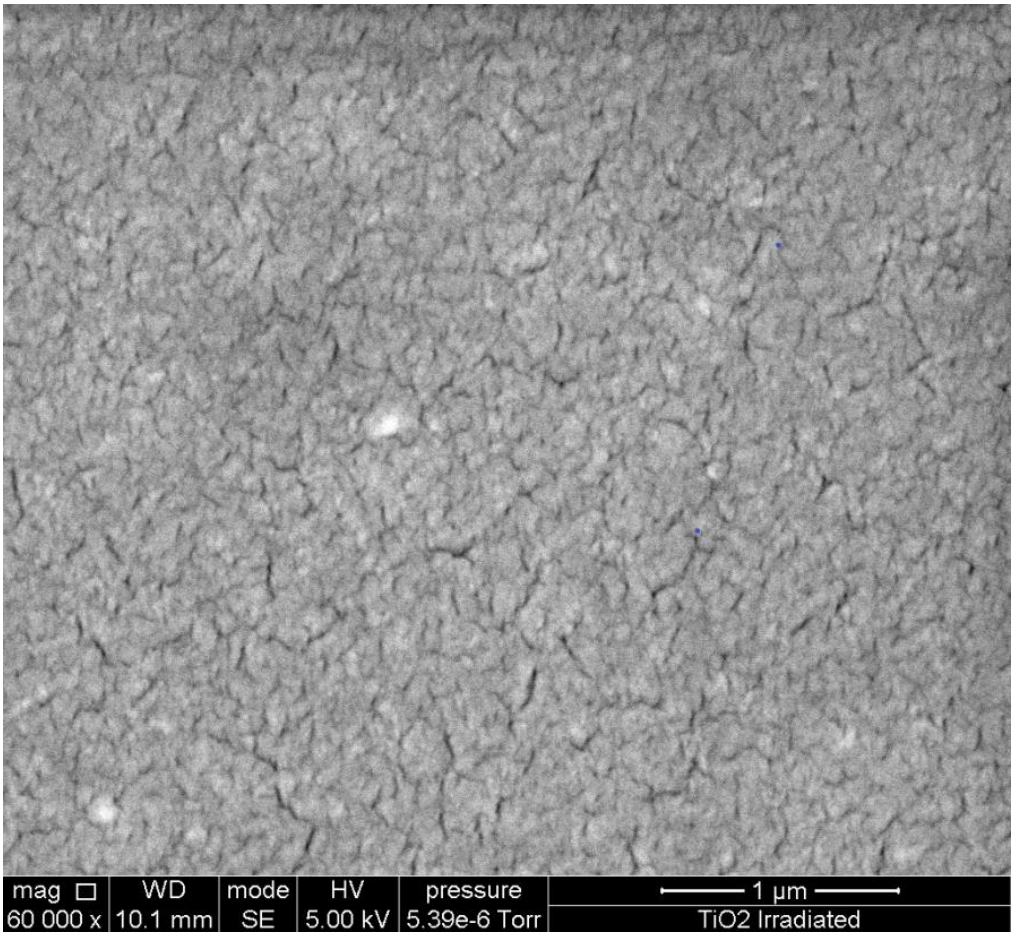

Figure 5.19. SEM micrograph of epoxy modified siloxane coated surface embedded with TiO_2, ($TiO_2 \in$ Siloxane-epoxy films) after irradiation. *"Image courtesy of Abdul Azeez".*

Epoxy modified siloxane films embedded with $F_{64}PcZn \cup TiO_2$ photocatalyst was also studied for robustness and the capability to withstand singlet oxygen and subsequently ROS. The micrograph from **Figure 5.20**, before irradiation, when compared with micrograph from **Figure 5.21,** after irradiated with the broadband illumination for a total of 8 hours did not show any difference in

surface morphology and topography. These results are consistence with the PVDF irradiation studies from **Chapter 3**, although epoxy modified siloxane is more durable polymer due to its organic-inorganic hybrid qualities.

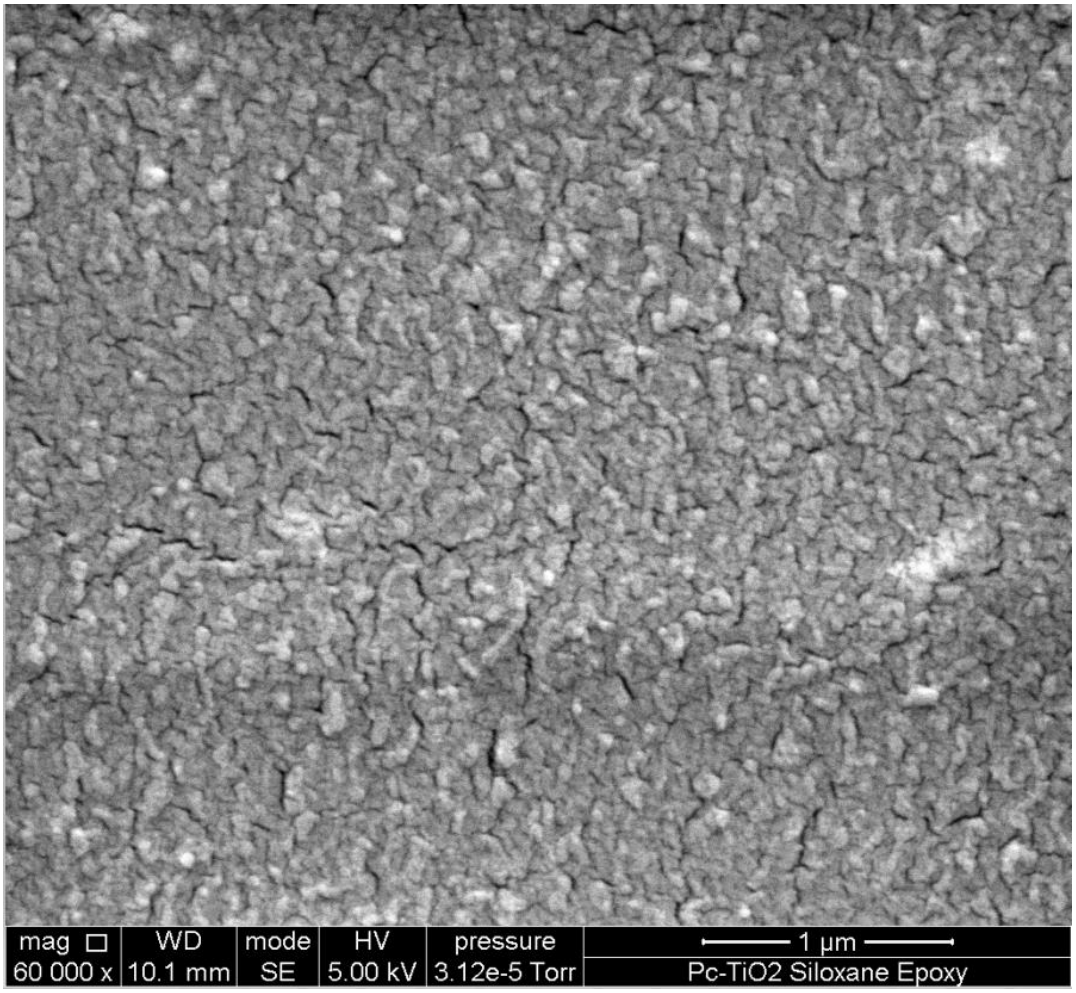

Figure 5.20. SEM micrograph of epoxy modified siloxane coated surface embedded with $F_{64}PcZn \cup TiO_2$ photocatalyst, $(F_{64}PcZn \cup TiO_2) \in$ Siloxane-epoxy films before irradiation. *"Image courtesy of Abdul Azeez"*.

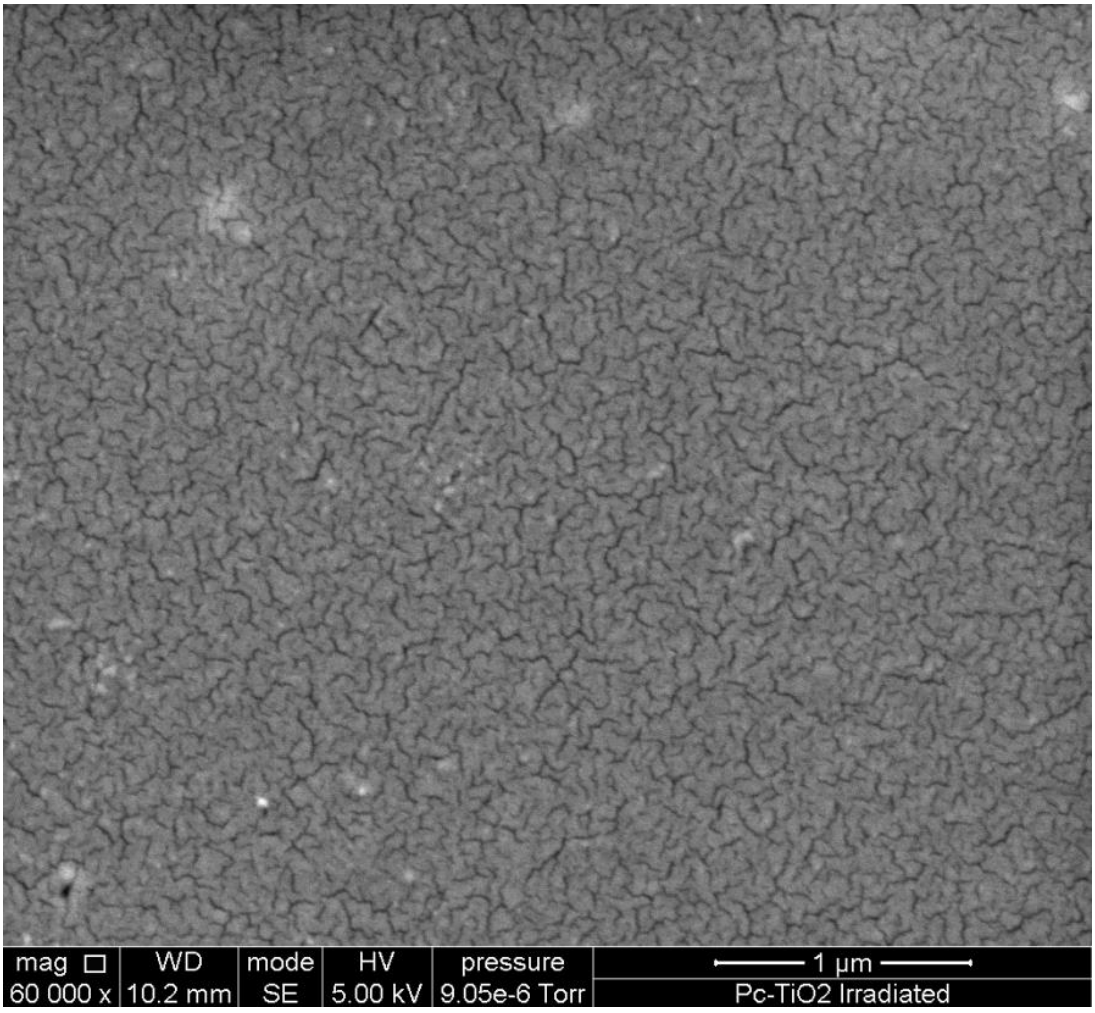

Figure 5.21. SEM micrograph of epoxy modified siloxane coated surface embedded with $F_{64}PcZn \cup TiO_2$ photocatalyst, $(F_{64}PcZn \cup TiO_2) \in$ Siloxane-epoxy films after irradiation. *"Image courtesy of Abdul Azeez".*

The resistance to UV degradation by these two epoxy modified siloxanes embedded with different catalysts is important because of applicability to daily usage. The above-mentioned surfaces do not only promote durability but also the longevity of polymeric material under harsh UV conditions while the polymeric surfaces are producing ROS for degradation of organic compounds but also resisting the ROS produced is an added advantage, overall.

5.4. Conclusions and future work.

This chapter initially focused on the ability of an epoxy modified siloxane film with embedded perfluoro phthalocyanine photocatalyst to degrade a wide range of organic dyes in solution. **Chapter 5**, clearly established the superiority the photoreactive qualities of the surfaces engineered in **Chapter 4** from the quantitative data produced from the photooxidative degradation of the organic dyes, such as kinetic studies of the degraded dyes, percentage degradation, and determination of half-life of the organic dyes. In comparison with our previous studies in chapters 2 and 3, with PVDF polymer, the results from epoxy modified siloxane coated proved to be better under UV-Vis illumination condition. The degradation of two dyes are worth further studies: ***Methylene Blue***, a cationic phenothiazine dye is degraded approximately 90% in 90 minutes, while ***Rose Bengal***, an anionic fluorescein dye was degraded approximately 90% in 30 minutes. Numerous research studies conducted to determine the degradation rate of ***Rose Bengal*** revealed that this organic dye is more resistive to photodegradation by the model semiconductor TiO_2. To understand the robustness of this superior organic-inorganic hybrid coated films embedded with a reactive photocatalyst, SEM and FTIR analysis was conducted to study PVDF and epoxy modified siloxane coated films under broadband light irradiation and subsequently the effects of the production of ROS and singlet oxygen.

Organic dyes are also degraded when deposited as solid on the same material suited here. A comparison of the efficiency of degradation of dyes in solution vs. the solid-state should be performed. The need for further exploration of these engineered surfaces is of great importance for large scale application because of the simplicity and easiness of the process.

References:

1. Bai, R., & Sutanto, M. (**2002**). The practice and challenges of solid waste management in Singapore. *Waste Management*, *22*(5), 557–567.
2. Duan, H., Huang, Q., Wang, Q., Zhou, B., & Li, J. (**2008**). Hazardous waste generation and management in China: A review. *Journal of Hazardous Materials*, *158*(2-3), 221–227.
3. Chen, J. L., Ortiz, R., Steele, T. W., & Stuckey, D. C. (**2014**). Toxicants inhibiting anaerobic digestion: A review. *Biotechnology Advances*, *32*(8), 1523–1534.
4. Ali, I., Asim, M., & Khan, T. A. (**2012**). Low cost adsorbents for the removal of organic pollutants from wastewater. *Journal of Environmental Management*, *113*, 170–183.
5. Adeyemo, A. A., Adeoye, I. O., & Bello, O. S. (**2012**). Metal organic frameworks as adsorbents for dye adsorption: overview, prospects and future challenges. *Toxicological & Environmental Chemistry*, *94*(10), 1846–1863.
6. Levec, J., & Pintar, A. (**2007**). Catalytic wet-air oxidation processes: A review. *Catalysis Today*, *124*(3-4), 172–184.
7. Baughman, G. L., & Weber, E. J. (**1994**). Transformation of dyes and related compounds in anoxic sediment: kinetics and products. *Environmental Science & Technology*, *28*(2), 267–276.
8. Liu, G., Li, X., Zhao, J., Hidaka, H., & Serpone, N. (**2000**). Photooxidation Pathway of Sulforhodamine-B. Dependence on the Adsorption Mode on TiO_2 Exposed to Visible Light Radiation. *Environmental Science & Technology*, *34*(18), 3982–3990.
9. Wang, C., Li, J., Lv, X., Zhang, Y., & Guo, G. (**2014**). Photocatalytic organic pollutants degradation in metal–organic frameworks. *Energy Environ. Sci.*, *7*(9), 2831–2867.
10. Tsai, W., Hsu, H., Su, T., Lin, K., Lin, C., & Dai, T. (2007). The adsorption of cationic dye from aqueous solution onto acid-activated andesite. *Journal of Hazardous Materials*, *147*(3), 1056–1062.
11. Wang, C., Li, J., Lv, X., Zhang, Y., & Guo, G. (**2014**). Photocatalytic organic pollutants degradation in metal–organic frameworks. *Energy Environ. Sci.*, *7*(9), 2831–2867.
12. Van Dolah, F. M. (**2000**). Marine algal toxins: origins, health effects, and their increased occurrence. *Environmental Health Perspectives*, *108*(suppl 1), 133–141.
13. Konstantinou, I. K., & Albanis, T. A. (**2004**). TiO2-assisted photocatalytic degradation of azo dyes in aqueous solution: kinetic and mechanistic investigations. *Applied Catalysis B: Environmental*, *49*(1), 1–14.
14. Padmanabhan, P., Sreekumar, K., Thiyagarajan, T., Satpute, R., Bhanumurthy, K., Sengupta, P., Warrier, K. (**2006**). Nano-crystalline titanium dioxide formed by reactive plasma synthesis. *Vacuum*, *80*(11-12), 1252–1255.

15. Akpan, U., & Hameed, B. (**2009**). Parameters affecting the photocatalytic degradation of dyes using TiO_2-based photocatalysts: A review. *Journal of Hazardous Materials*, *170*(2-3), 520–529.

16. Jury, W. A., & Vaux, H. (**2005**). The role of science in solving the world's emerging water problems. *Proceedings of the National Academy of Sciences*, *102*(44), 15715–15720.

17. Bonaventura, C., & Johnson, F. M. (**1997**). Healthy environments for healthy people: bioremediation today and tomorrow. *Environmental Health Perspectives*, *105*(suppl 1), 5–20.

18. Gaya, U. I., & Abdullah, A. H. (**2008**). Heterogeneous photocatalytic degradation of organic contaminants over titanium dioxide: A review of fundamentals, progress and problems. *Journal of Photochemistry and Photobiology C: Photochemistry Reviews*, *9*(1), 1–12.

19. Arslan-Alaton, I. (**2003**). A review of the effects of dye-assisting chemicals on advanced oxidation of reactive dyes in wastewater. *Coloration Technology*, *119*(6), 345–353.

20. Wang, J. L., & Xu, L. J. (**2012**). Advanced Oxidation Processes for Wastewater Treatment: Formation of Hydroxyl Radical and Application. *Critical Reviews in Environmental Science and Technology*, *42*(3), 251–325.

21. Lee, W., Son, H. J., Lee, D., Kim, B., Kim, H., Kim, K., & Ko, M. J. (**2013**). Suppression of photocorrosion in CdS/CdSe quantum dot-sensitized solar cells: Formation of a thin polymer layer on the photoelectrode surface. *Synthetic Metals*, *165*, 60–63.

22. Spathis, P., & Poulios, I. (**1995**). The corrosion and photocorrosion of zinc and zinc oxide coatings. *Corrosion Science*, *37*(5), 673–680.

23. Wu, W., Changzhong Jiang, C. J., & Roy, V. A. L. (**2015**). Recent progress in magnetic iron oxide–semiconductor composite nanomaterials as promising photocatalysts. *Nanoscale*, *7*(1), 38–58.

24. Ramji, K. Ph.D. Dissertation, Seton Hall University, South Orange, NJ: (**2018)**.

25. Sullivan, J. MS Thesis, Seton Hall University, South Orange NJ: (**2016)**.

26. Dzinun, H.; Othman, M.H.D.; Ismail, A.F.; Puteh, M.H.; Rahman, M.A.; Jaafar, J. "Stability Study of PVDF/TiO_2 dual-layer hollow fiber membranes under long term UV irradiation exposure" *J. Water Process Eng.* (**2017)**, *15*, 78-82.

27. Azeez, A., Polio, L., Hanson, J. E., & Gorun, S. M. (**2019**). Photoreactive Superhydrophobic Organic-Inorganic Hybrid Materials Composed of Poly(vinylidene fluoride) and Titanium Dioxide-Supported Perfluorinated Phthalocyanines. *ACS Applied Polymer Materials*, *1*(6), 1514–1523.

28. a) Bench, B. A.; Beveridge, A.; Sharman, W. M.; Diebold, G. J.; Van Lier, J. E.; Gorun, S. M. "Introduction of Bulky Perfluoroalkyl Groups at the Periphery of Zinc Perfluorophthalocyanine: Chemical, Structural, Electronic, and Preliminary Photophysical and Biological Effects" *Angew. Chem., Int. Ed.* (**2002)**, *41*, 747-750. b) Pelmuş, M.;

Carrion, E. N.; Colomier, C.; Santiago, J.; Gorun, S. M. Group III Perfluoroalkyl Perfluoro Phthalocyanines, *J. Porphyr. Phthalocyanines* (**2016)**, *20*, 1401-1408.

29. a) Antonin, V. S., Garcia-Segura, S., Santos, M. C., & Brillas, E. (**2015**). Degradation of ***Evans Blue*** diazo dye by electrochemical processes based on Fenton's reaction chemistry. *Journal of Electroanalytical Chemistry*, *747*, 1–11. b) Ma, Y., & Yao, J. (**1998**). Photodegradation of ***Rhodamine B*** catalyzed by TiO_2 thin films. *Journal of Photochemistry and Photobiology A: Chemistry*, *116*(2), 167–170.

30. Wu, T., Liu, G., Zhao, J., Hidaka, H., & Serpone, N. (**1998**). Photo assisted Degradation of Dye Pollutants. V. Self-Photosensitized Oxidative Transformation of ***Rhodamine B*** under Visible Light Irradiation in Aqueous TiO_2 Dispersions. *The Journal of Physical Chemistry B*, *102*(30), 5845–5851.

31. Hu, C., Yu, J. C., Hao, Z., & Wong, P. K. (**2003**). Photocatalytic degradation of triazine-containing azo dyes in aqueous TiO_2 suspensions. *Applied Catalysis B: Environmental*, *42*(1), 47–55.

32. Wilhelm, P., & Stephan, D. (**2007**). Photodegradation of ***Rhodamine B*** in aqueous solution via SiO_2@TiO_2 nano-spheres. *Journal of Photochemistry and Photobiology A: Chemistry*, *185*(1), 19–25.

33. Zhao, X., Qu, J., Liu, H., & Hu, C. (**2007**). Photoelectrocatalytic Degradation of Triazine-Containing Azo Dyes at γ-Bi_2 MoO_6 Film Electrode under Visible Light Irradiation (λ > 420 Nm). *Environmental Science & Technology*, *41*(19), 6802–6807.

34. Zhang, Y., Xie, M., Adamaki, V., Khanbareh, H., & Bowen, C. R. (**2017**). Control of electrochemical processes using energy harvesting materials and devices. *Chemical Society Reviews*, *46*(24), 7757–7786.

35. Bhati, A., Singh, A., Tripathi, K. M., & Sonkar, S. K. (**2016**). Sunlight-Induced Photochemical Degradation of ***Methylene Blue*** by Water-Soluble Carbon Nanorods. *International Journal of Photoenergy*, *2016*, 1–8.

36. Kumar, A., & Pandey, G. (**2018**). Preparation and photocatalytic activity of TiO_2/PPy/GO for the degradation of ***Rose Bengal*** and Victoria Blue dye in visible light in aqueous solution. *DESALINATION AND WATER TREATMENT*, *114*, 265–284.

37. Li, X., Wang, Z., Li, X., & Wang, G. (**2012**). Synthesis of a super-hydrophilic conducting polyaniline/titanium oxide hybrid with a narrow pore size distribution. *Applied Surface Science*, *258*(10), 4788–4793.

38. Kaur, J., & Singhal, S. (**2014**). Heterogeneous photocatalytic degradation of ***Rose Bengal***: Effect of operational parameters. *Physica B: Condensed Matter*, *450*, 49–53.

39. Morita, Y. (**2005**). Curing of epoxy siloxane monomer with anhydride. *Journal of Applied Polymer Science*, *97*(3), 946–951.

40. Crivello, J. V., Song, K. Y., & Ghoshal, R. (**2001**). Synthesis and Photoinitiated Cationic Polymerization of Organic-Inorganic Hybrid Resins. *Chemistry of Materials*, *13*(5), 1932–1942.

41. Jang, M., & Crivello, J. V. (**2003**). Synthesis and cationic photopolymerization of epoxy-functional siloxane monomers and oligomers. *Journal of Polymer Science Part A: Polymer Chemistry*, *41*(19), 3056–3073.

42. Rosas-Barrera, K., Ropero-Vega, J., Pedraza-Avella, J., Niño-Gomez, M., Pedraza-Rosas, J., & Laverde-Cataño, D. (**2011**). Photocatalytic degradation of ***Methyl Orange*** using Bi_2MNbO_7 (M=Al, Fe, Ga, In) semiconductor films on stainless steel. *Catalysis Today*, *166*(1), 135–139.

43. Peng, D., Qin, W., & Wu, X. (**2015**). A study on resistance to ultraviolet radiation of POSS–TiO_2/epoxy nanocomposites. *Acta Astronautica*, *111*, 84–88.

44. Jiang, L., He, S., & Yang, D. (**2003**). Resistance to vacuum ultraviolet irradiation of nano-TiO_2 modified carbon/epoxy composites. *Journal of Materials Research*, *18*(3), 654–658.

45. Selvi, M., Devaraju, S., Vengatesan, M. R., Go, J. S., Kumar, M., & Alagar, M. (**2014**). The effect of UV radiation on polybenzoxazine/epoxy/OG-POSS nanocomposites. *RSC Advances*, *4*(16), 8238.

Chapter 6

Summary

The goal of this research effort was to design surfaces with two modes of self-cleaning activity: superhydrophobicity and catalytic photo-oxidation. Surface modification was performed on PVDF films by incorporation of NH_4HCO_3 thereby greatly enhancing a hydrophobic surface to a superhydrophobic surface with water contact angle $\theta = 159°$ via the generation of matrix voids by the CO_2, NH_3 and H_2O emitted by the thermally unstable NH_4HCO_3. The method is considered a bottom-up surface modification approach. The surfaces that were embedded with photoreactive inorganic catalysts were highly hydrophobic, the optimal material (NH_4HCO_3& $F_{64}PcZn \cup TiO_2) \in$PVDF surface having $\theta = 144°$. The films proved to have strong thermal resistance as evidenced by DSC and TGA data. The combined modified topographical morphology of the surface and photooxidation capacity imparted by the photosensitizer provide the resulting films with improved self-cleaning capabilities, demonstrated by the efficient degradation of the model dye ***Methyl Orange*** in solution. A comparison of the perfluorinated phthalocyanine photosensitizer supported on TiO_2-containing films with the just TiO_2-containing films, the perfluorinated phthalocyanine containing films revealed a 2.5 increase in the rate of ***Methyl Orange*** degradation. Most importantly, the polymer films incorporating the phthalocyanine photosensitizer supported on TiO_2 showed no signs of degradation, unlike the TiO_2-containing films.

Another set of surfaces were based on a robust organic-inorganic polymer; siloxane modified epoxy resin cross-linked with aminopropyltriethoxysilane. Incorporation of NH_4HCO_3 and its subsequent thermolysis was used to form a microstructured, rough surface. Two distinct surfaces obtained from (NH_4HCO_3 &$SiO_2 \cup F_{64}PcZn) \in$Siloxane epoxy and $NH_4HCO_3 \in$Siloxane epoxy, used to prepare films were characterized to determine and compare their thermal stability. The prepared films were thermally stable up to 300 °C, the embedded catalyst on the matrix of

siloxane modified epoxy did not change regardless of the thermal treatment. These favorable film characteristics suggest a broad range of applications.

The robust, polymer epoxy modified siloxane film with embedded perfluoro phthalocyanine photocatalyst was used to degrade a wide range of organic dyes in solution. In comparison with the PVDF, the epoxy modified siloxane coated proved to be stable under UV-Vis illumination, as established by SEM and FTIR study. The degradation of two dyes is worth further studies: ***Methylene Blue***, a cationic phenothiazine dye is degraded approximately 90% in 90 minutes, while ***Rose Bengal***, an anionic fluorescein dye was degraded approximately 90% in 30 minutes. Previous studies of the degradation rate of ***Rose Bengal*** revealed that this organic dye surprisingly is more resistant to photodegradation using the semiconductor TiO_2. This counterintuitive result remains to be explained via mechanistic studies. Organic dyes are also degraded when deposited as solids on the same films used in this Thesis. A comparison of the efficiency of degradation of dyes in solution vs. the solid-state is a logical next step in understanding in-depth the photocatalytic properties of the new materials. Nonetheless, the engineered surfaces described here, easy to produce and stable might be suitable for large scale applications.

Biography:

Abdul Azeez is from the San Francisco Bay Area, California. Attended San Francisco State University where he obtained a Bachelor of Science degree in Biochemistry, followed by a Master of Science in Chemistry with a focus in Analytical Chemistry. Worked at Evan Analytical Group formally known as PTRL West in the San Francisco area until 2014 before starting a Ph.D. program in Chemistry at Seton Hall University, Chemistry and Biochemistry Department in 2014, he earned a Master of Science in Chemistry with a focus in Engineering Superhydrophobic Surfaces at Seton Hall University in 2017 as he pursues his Ph.D. program.

PUBLICATIONS, INVENTION AND CONFERENCE PRESENTATIONS.

1. **Azeez, A**., Polio, L., Hanson, J. E., & Gorun, S. M. **2019**. Photoreactive Superhydrophobic Organic-Inorganic Hybrid Materials Composed of Poly(vinylidene fluoride) and Titanium Dioxide-Supported Perfluorinated Phthalocyanines. *ACS Applied Polymer Materials*, *1*(6), 1514–1523.
2. Hanson, J., **Azeez, A.,** Gorun, S. Photoactive Polymer Coatings. *US Provisional. Patent Application* No. 62/637,445, **2018.**
3. **Azeez, A.,** Hanson, J. E., & Gorun, S. M. Epoxy-Siloxane, Superhydrophobic Anticorrosion Coatings" *Gordon Conference on Aqueous Corrosion*, New London, NH, **2018**.
4. Hanson, J. E., **Azeez, A**., & Gorun, S. M. Surface Re-Engineered Reactive, Robust Polymer Hybrids" Presented by **A. Azeez** at the *Gordon Conference on Aqueous Corrosion*, New London, NH, **2018**.
5. **Azeez, A.,** Hanson, J. E., Gorun, S. M. Superhydrophobic, Self-cleaning Surfaces. *Petersheim Exposition*, Seton Hall University, **2017.**
6. **Azeez, A**., Hanson, J. E., Gorun, S. M. Surface Re-engineered Reactive, Robust Polymer Hybrids. *Petersheim Exposition*, Seton Hall University, **2018**.
7. Saway, J., **Azeez, A**., Hanson, J. E., Gorun, S. M. Evaluation of magnetic and photooxidative properties of zinc perfluorophthalocyanine nanocomposite. *Petersheim Exposition*, Seton Hall University, **2018**.
8. Prabh J Jassal., **Azeez, A**., Hanson, J. E., Gorun, S. M. Zinc Perfluorophthalocyanine: A Reactive Oxygen Species Induced Regulation of Microbial Growth. *Petersheim Exposition*, Seton Hall University, **2018**.
9. Polio, L., **Azeez, A**., Hanson, J. E., Gorun, S. M. The Control of Microbial Growth using the effects of Zinc Perfluorophthalocyanine as a Photosensitizer under Visible light. *Petersheim Exposition*, Seton Hall University, **2018**.
10. Jimenez, N., **Azeez, A**., Hanson, J. E., Gorun, S. M. Preparation and Photocatalytic Characteristics of Magnetically Reusable Fe_3O_4 nanoparticles coated with F_{64}PcZn. *Petersheim Exposition*, Seton Hall University, **2019**.
11. Bandala, J., **Azeez, A**., Hanson, J. E., Gorun, S. M. Degradation of Organic Dyes on F_{64}PcZn Supported on Silica. *Petersheim Exposition*, Seton Hall University, **2019**.